Paolo Verderio
N°: 744966

PhD thesis

Synthesis and Biofunctionalization of Novel Composite Nanocarriers for Targeted Detection and Treatment of Malignant Cells

---

Submitted for the degree of Doctor of Philosophy
at the University of Milano-Bicocca

School of Doctorate in Chemical Sciences
XXVI Course
University of Milano-Bicocca

Years 2011–2013

Synthesis and Biofunctionalization of Novel Composite Nanocarriers for Targeted Detection and Treatment of Malignant Cells

PhD thesis by
Paolo Verderio

University of Milano-Bicocca
Dept. of Biotechnology and Bioscience U3, building
P. za. Della Scienza, 2, 20126, Milano (Mi), Italy

Approved by:

Prof. Giorgio Moro
University of Milano-Bicocca, 20126 Milano (*Italy*) (School Coordinator)

International Reviewers:

Prof. Wolfgang Parak
Philipps Universität of Marburg, Biegenstraße 10, D-35032 Marburg (*Germany*)

Prof. Victor Franco Puntes
Institut Català de Nanociència, Universitat Autònoma de Barcelona, 08193 Bellaterra (*Spain*)

Advisory Committee

Prof. Francesco Nicotra
University of Milano-Bicocca, 20126 Milano (*Italy*)

Dr. Francesca Baldelli Bombelli
University of East Anglia, Norwich Research Park, NR4 7TJ Norwich (*United Kingdom*)

Dr. Ivano Eberini
University of Milan, Dipartimento di Scienze Farmacologiche, 20133 Milano (*Italy*)

Dr. Giorgio Colombo
ICRM, Instituto di Chimica del Riconoscimento Molecolare, 20131 Milano (*Italy*)

Dr. Carlo Morasso
Fondazione ONLUS Carlo Don Gnocchi, 20121 Milano (*Italy*)

Date of PhD Thesis submission: January 2014

“The Nature investigation resembles loads of unraveled intricate threads,
where a key combination is important
almost as well as the skill and the sharpness of observation.
The work of the scientist is exciting as it is for the hunter
to chase a unknown game in accidental circumstances”

Ernst Walfried Josef Wenzel Mach (1838−1916)

List of abbreviations

7AAD	7-aminoactinomycin D
ADCC	Antibody-dependent cellular cytotoxicity
A549	Adenocarcinomic human alveolar basal epithelial cells
APTMS	3-aminopropyl trimethoxy silane
APTES	3-aminopropyl triethoxy silane
ATF	Amino terminal fragment
B_2O_3	Boric oxide
BCA	Bicinchoninic acid
BSA	Bovine serum albumin
CH_3COOH	Acetic acid
$CHCl_3$	Chloroform
CH_2Cl_2	Methylene Chloride
CLSM	Confocal Laser scanning microscopy
CMC	Critical micelle concentration
CTAB	Cetyl trimethylammonium bromide
DAPI	4′,6-diamidino-2-phenylindole
DCS	Differential centrifuge sedimentation
DiD	Oil Red O Staining (confocal staining for membranes)
DLS	Dynamic light scattering
DMF	Dimethyl formamide
DMSO	Dimethyl sulfoxide
DMEM	Dulbecco's Modified Eagle's medium (cell cultures)
DNA	Deoxyribonucleic acid
DOX	Doxorubicin
DTT	Dithiothreitol
DTNB	5,5'-Dithio-*bis*-(2-nitrobenzoic acid)
EDBE	(2,2-(ethylenedioxy)bisethylamine
EDC	1-Ethyl-3-(3-dimethylaminopropyl)carbodiimide
EDTA	Ethylenediaminetetraacetic acid
EE (%)	Encapsulation efficiency in percentage
EGFR	Epidermal growth factor receptor
EPR	Enhanced permeation and retention effect
EtOH	Ethanol
EO	Ethylene oxide monomers
ER	Estrogen receptor
ErbB	The epidermal growth factor receptor (EGFR) is the founding member of the ErbB family
Et_2O	Diethyl ether
FACS	Fluorescence Activated Cell Sorting (in this)
Fc	The fragment crystallizable region (*Fc* region) is the tail region of an antibody
FDA	Food and drug Administration
FBS	Fetal bovine serum
Fe_3O_4	Magnetite
γ-Fe_2O_3	Maghemite
FITC	Fluorescein isothiocyanate
FRET	Förster resonance energy transfer
FT-IR	Fourier Transform Infra-Red spectra
G1	Growth 1 phase of the cell cycle
G2/M	Gap2 and mitosis cell cycle phase
g	Grams
GFD	Growth factor domain
GST	Glutathione S-transferase
HALO	Haloalkane dehalogenase protein designed to covalently bind to synthetic ligands
H_c	Coercive field
HCl	Hydrochloridic acid
HER2	Human Epidermal growth factor receptor 2
HepG2	Liver hepatocellular carcinoma cells
His_Tag	Oligohistidine affinity tag

HRP	Enzyme horseradish peroxidase
HSA	Human serum albumin
K	Kelvin (unit for temperature)
K_u	Anisotropy constant
IEP	Isoelectric point
IPTES	3-isocyanatepropyl triethoxy silane
ICAM1	Intercellular adhesion molecule 1
mAb	Monoclonal antibody
mg	Milligrams
µg	Micrograms
M	Molar concentration
mM	Millimolar concentration
µM	Micromolar concentration
MAPK	Mitogen-activated protein kinase
MCF7	Michigan Cancer Foundation-7; HER2 positive breast cancer cell line
MDA-MB231	Mammary gland/breast; derived from metastatic site: pleural effusion; HER2 negative
MDA-MB468	Mammary gland/breast adenocarcinoma; HER2 negative
MeOH	Methanol
MMPs	Matrix-metalloproteinase
MNPs	Magnetic iron oxide nanoparticles
MRI	Magnetic resonance imaging
MS−PEG4	Methyl-PEG4-NHS Ester
MTT	3-(4,5-dimethylthiazol-2-yl)-2,5-diphenyltetrazolium bromide
M_s	Saturation magnetization
M_R	Remanent magnetization
M_z	Magnetization
Mwco	Medium weight cut off
NaOH	Sodium hydroxide
NCBI	National Center for Biotechnology Information
NHS	*N*-hydroxysuccinimide
NMR	Nuclear magnetic resonance
NaH	Sodium hydride
NPs	Nanoparticles
NTA	Nitrilotriacetic acid
PBS	Phosphate buffer solution
PDI	Polydispersity index
PTX	Paclitaxel
PEG	Poly ethylene glycol
PLGA	Polylactide-co-glycolide acid
PCNPs	Polymeric curcumin nanoparticles
PMA	Poly(isobutylene-*alt*-maleic anhydride)
PR	Progesterone receptor
PVA	Polyvinyl alcohol
PVP	Polyvinyl pyrrolidone
PVC	Polyvinyl chloride
PNIPAM	poly(N-isopropylacrylamide-methacrylate)
RNA	Ribonucleic acid
RES	Reticulo endothelial system
ROS	Reactive oxygen species
r_{SP}	Superparamagnetic radius
RPMI	Cell culture medium used for the culture of human normal and neoplastic leukocytes
RT	Room temperature
SBB	Sodium borate buffer
scFV	Portion of the whole antibody
SDS-PAGE	Sodium Dodecyl Sulphate - PolyAcrylamide Gel Electrophoresis
SEM	Scanning electron microscopy
SiNPs	Silica nanoparticles
siRNA	short interfering RNA
SM−PEG8	NHS ester-PEG8-Maleimide
SPDP	3-(2-pyridyldithio)propionate
SPM	Superparamagnetic material
TCEP	tris(2- carboxyethyl)phosphine

TEM	Transmission electron microscopy
TEOS	Tetraethyl orthosilicate
THQ	1,2,3,4-tetrahydroquinoline
TNBS	2,4,6-Trinitrobenzene Sulfonic Acid
Tf	Transferrin
TfR	Transferrin receptor
THF	Tetrahydrofurane
TZ	Trastuzumab moloclonal antibody
T_1	Longitudinal relaxation
T_2	Trasversal relaxation
uPAR	Urokinase Plasminogen Activator receptor
U11	Small peptide of 11 amino acid implicated in uPAR recognition: VSNKYFSNIHW
U937	Human leukemic monocyte lymphoma cell line
u_e^-	Electrophoretic mobility
ε_{RS}	Relative permittivity of the electrolyte solution
VEGF	Vascular endothelial growth factor
VPNPs	Void polymeric nanoparticles
Vs.	Versus

SUMMARY

Contents

Background

My PhD research project which is discussed in this thesis, has been divided into two kinds of parallel studies that find applications in breast cancer diagnosis and therapy.

The first part has been focused on two types of inorganic nanoparticles, which exploit different chemical physical properties: superparamagnetic iron oxide nanoparticles (MNPs) and luminescent silica nanoparticles (SiNPs). These nanomaterials have been functionalized by different biologically active molecules towards over-expressed breast cancer cell receptors with the aim to achieve a specific recognition of human cancer cells, exploiting these systems for future applications in biological investigations and medical diagnosis.

Instead, the second part of the work has been focused on developing a biodegradable polymeric nanoparticle system endowed with drug delivery properties for the encapsulation of hydrophobic drugs, which are nowadays under investigation in preclinical and clinical trials for medicinal development.

For both subsets, chemical characterizations and biological studies on cells have been the framework to understand nanoparticles behavior towards their diagnostic or therapeutic goals. These studies have been accomplished in collaboration with my Biologist coworkers at the NanoBioLab in the research group of Dr. Davide Prosperi, Department of Biotechnology and Bioscience (University of Milano-Bicocca, Italy) and the Department of Biomedical and Clinic Science, Hospital “Luigi Sacco” (University of Milan, Italy). Part of this thesis has been carried out during the second year of the PhD school as a visitor at the CBNI, Center for Bio-Nano Interactions, Department of Chemical Biology (University College of Dublin, Ireland) under the supervision of Prof. Kenneth A. Dawson.

Briefly, in this summary, the reader could find an overlook within aims and how the research has been developed to run forward these goals. I hope the reader will find in my thesis elements that could elicit interest and curiosity; I will be very pleased if he/she will accurately inspected all fields in a critical point of view to take the cue for a scientific discussion about proposed results.

Multiple Presentation of Scfv800E6 on Silica Nanospheres Enhances Targeting Efficiency Toward HER2 Receptor in Breast Cancer

Nanomedicine, or Nanobiotechnology, defined as the biomedical application of materials at the nanometer scale, is a rapidly developing area of nanotechnology, which involves the creation and then use of materials and devices at the level of atoms and molecules. Nanomaterials within the range of 1–200 nm possess a great potential for biomedical application through the complementary combination of chemical/physical and size-dependent properties, which are not observed at the molecular level or in bulk phase but modulate significant interactions with biological molecular systems. The fabrication of high quality hybrid inorganic nanoparticles endowed with distinguished inherent magnetic and/or optical properties represents a promising new advance for the development of a

novel generation of diagnostic agents for biosensing, preclinical investigations and clinical use, in turn leading to a new discipline of nano-oncology [1].

At present, mammary carcinoma is the second most common type of malignant tumor in adult women after lung cancer, as more than one million women are diagnosed with breast cancer every year. Despite many advances in diagnosis and treatment [2−4], which have resulted in a decrease in mortality in recent decades, this pathology remains a major public health problem. One of the most significant unresolved clinical and scientific problems is the occurrence of resistance to clinical treatments and their toxicity (and how to predict, prevent and overcome them). Unfortunately, the heterogeneity of human breast cancer in terms of genetic features, molecular profiles and clinical behaviour represents a great hurdle obstructing the discovery of a resolved solution to the disease. It is currently considered that chances of success of therapies may increase if the tumor cells are selectively removed before they can evolve to their mature stages up to metastases production [5] (Figure. 1).

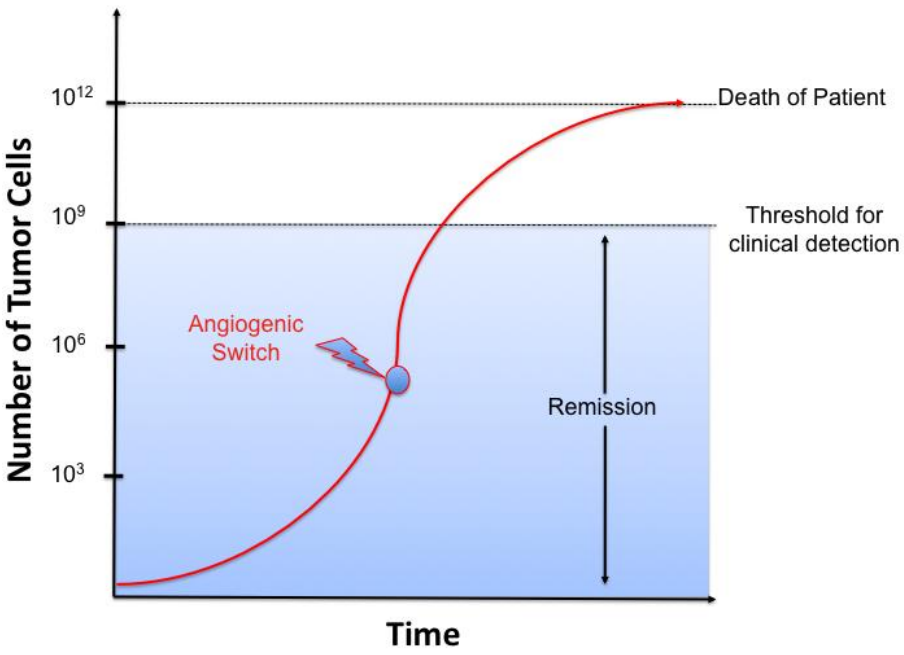

Figure 1: Gompertzian growth curve of a solid tumor and its relationship to cancer detection.
Number of malignant cells (ordinate) as a function of time (abscissa). The transition from first lag to log phase of growth, associated with the transition from diffusion-limited nutrition to neurovascularization, is labelled “angiogenic switch”. Remission is shown as the uncertainly of cell number ranging from zero to the current clinical treshold for cancer detection (approximately 10^9 cells growing as a single mass)

Therefore, novel and more sensitive diagnostic tools are being developed, with the aim of improving the early and not-invasive detection of rising malignancies and the accuracy of tumor tissue localization. In parallel,

there is an emerging use of targeted therapies in oncology, depending on the expression of specific proteins or genes recovered in tumor cells. Among the molecular targets considered for the treatment of breast cancer cells so far, our group chose to focus on examples involving over-expression and/or gene amplification of “Human Epidermal growth factor Receptor 2” (HER2) protein [6,7]. In current studies, various types of nanoparticles conjugated with the anti-HER2 monoclonal antibody, the so-called “trastuzumab”, are under investigation extensively due to promising results in biological and preclinical applications aimed at improving the treatment of breast cancer [8−11]. In this part of my PhD research I will present the preparation and development of small silica nanoparticles (SiNPs ≈ 60 nm) functionalized with a portion of the whole antibody Trastuzumab, named scFv800E6, preliminary engineered and produced in yeast *Pichia pastoris* [12], that recognizes the breast cancer membrane marker HER2. The chemistry of functionalization resulted by both localized histidine-tag recognition, leading to an oriented protein ligation, and glutaraldehyde cross-linking, exploiting a statistical reactivity of lysine amine groups in the primary sequence of the molecule (Figure. 2).

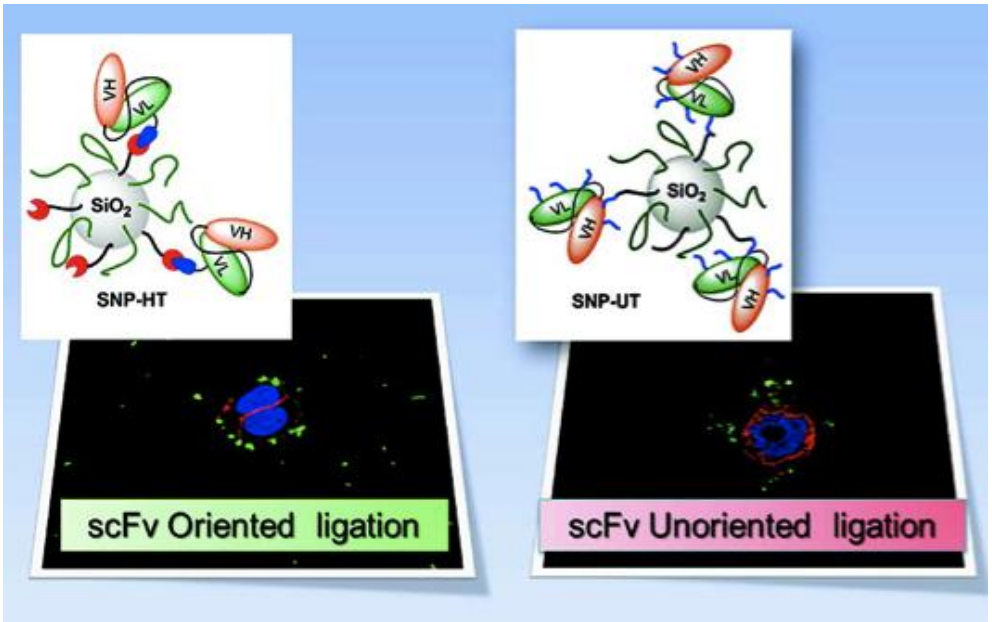

Figure 2: SiNPs synthesized and functionalized with anti-HER-2 scFv800E6 antibody
The chemical functionalization has been performed by both histidine-tag recognition (scFv oriented ligation) and glutaraldehyde cross-linking (unoriented ligation).

For instance, I would like to present a strategy to enhance scFvs target binding efficacy that makes use of silica nanoparticles as a multimerization scaffold. The aim of this work, was to correlate the chemical functionalization of SiNPs with their targeting capability; particular emphasis has been placed on the diagnostic potential of this generation of hybrid nanoparticles, exploiting the multifaceted mechanisms of action of small fragments of trastuzumab, in comparison with free scFv and the whole antibody, against malignant cells. In this way, the targeting efficiency of nanocomplexes has been evaluated using a HER2 antigen-positive MCF7 breast cancer cell line, exhibiting a 4-fold increase in scFv binding efficacy, close to the affinity of intact anti-HER2 monoclonal antibody, which suggests the effectiveness of presenting multiple scFv molecules on nanoparticles thus improving antigen recognition.

Development of a Fluorescent Silica Nanoparticles Platform for Transferrin Conjugations: Implications at the Bio-Nano Interface

The metabolism of iron by cancer cells often may lead to over-expression of transferrin receptor (TfR) [13], making transferrin (Tf), a 79 kDa glycoprotein that binds TfR at extracellular pH, [14] a potential targeting molecule. Previous investigations with Transferrin-targeted nanoparticles have sometimes given inconsistent results, and problems such as linker stability and protein flexibility have been identified [15,16]; in this way some nanoparticle types fail to target the relevant pathway, even though they enter cells efficiently.

The detailed (*in situ*) structure of the nanoparticle interface with the full biological environment (both target and biological milieu) is critical in determining this outcome. Prof. Kenneth Dawson's group, where this part of my work took place as a visiting student, has recently validated a method to discriminate this bio-nano interface, which could strongly influence the active targeting of TfrR. Using 50 nm transferrin-conjugated core-shell

fluorescent SiNPs, they found that proteins in the media can shield transferrin from binding to both its targeted receptors on cells and soluble transferrin receptors. In this way, the formation of a “protein corona” can be an example to “screen” the targeting molecules on the surface of nanoparticles and evaluate the loss of specificity in receptor targeting [17].

My work has been focused on the synthetic optimization of spherical 20−30 nm core−shell fluorescent SiNPs, prepared by the Stöber hydrolysis and co-condensation of tetraethyl orthosilicate with N-1-(3-trimethoxysilylpropyl)-N′-fluoresceyl thiourea (APTMS-FITC) followed by the growing of second silica shell (5 nm thickness) in order to further protect dye photo−bleaching. After NPs synthesis, the surface has been modified with a great amount of amino groups an external functionality. The reactive amount of amine with has been reduced gradually prior to SM-PEG_8 coupling by reaction with a short inert PEG composed by 4 units (called MS-PEG_4); the organic moiety has been attached with the usual peptide coupling while the opposite part of the linker exploited an inhert methoxyl group. Later on, a heterobifunctional PEG composed by 8 units (called SM-PEG_8) exploiting an *N*-hydroxysuccinimide (NHS) and a maleimide (MaL) ring, has been attached and used for the following protein conjugation. Human Tf modified with a thiol–PEG linker was conjugated to the PEGylated particle to give fluorescent bioconjugates. Cellular study of TfR binding revealed a correlation between the number of amino groups and the active targeting of the receptor. In this study, RNA interference was used in parallel to silence the expression of TfR in human A549 lung epithelial cells in order to determine the effect of TfR on nanoparticle uptake. I emphasize that the absolute uptake level does not give information on the specificity of these interactions. However, the difference in particle uptake in silenced and non-silenced cells is indicative of the relative contribution made by that pathway. I would like to point out that this subproject is ongoing and all my final considerations about the experimental details will need to be completed with further and more accurate results. Unfortunately, the lack of time did not allow me to complete the

whole experimental part during my visiting PhD collaboration at the CBNI and thus is now ongoing.

Orientation-Controlled Conjugation of Haloalkane Dehalogenase Fused Homing Peptides to Multifunctional Iron Oxide Nanoparticles for the Specific Recognition of Cancer Cells

Hybrid multifunctional iron oxide nanoparticles, which combine unique superparamagnetic properties and fluorescence emission, have been investigated as promising bimodal tracers for non-invasive diagnosis of cancer both *in vitro* and *in vivo* [18−21]. The design of ideal targeted iron oxide nanoparticles needs careful optimization of fundamental features including uniform size and shape [22], surface charge [23], optical and magnetic properties [24,25], and efficient functionalization with suitable homing ligands [26–28] to improve the signal amplification and target selectivity toward malignant cells. When the ligands are complex molecules, such as proteins, their proper orientation on the surface of nanoparticles becomes a crucial factor for maximizing the affinity for their molecular counterparts. According to this purpose, recently several different approaches have been explored to check ligand positioning, including oriented immobilization on MNPs driven by recombinant protein linkers [29,30]; conjugation mediated by affinity tags inserted into the protein primary sequence [31,32] and site-specific chemo-selective ligation [33,34].

A new modern approach, called Halo Tag technology, is being widely applied for cellular imaging, protein quantification and interaction analysis. It is designed for rapid, side-specific labeling of proteins in living cells*;* basically it is based on the efficient formation of a covalent bond between the Halo Tag protein and synthetic ligands [35]. The Halo-Tag protein is a catalytically inactive, genetically modified derivative of a hydrolase protein; this protein is used to generate N- or C-terminal fusions that can be efficiently

expressed in a variety of cell types. The Halo Tag ligands are small chemical tags, containing two crucial components: a common Halo Tag reactive linker that initiates formation of the covalent bond (chlorine) and functional reporter such as a thiol or amino-group for a fast and selective conjugation on the surface of a nanomaterial. The rate of the ligand-protein binding is remarkably fast and the covalent bond formed is highly specific and irreversible.

The goal of this subproject was to the design and the synthesis of a hybrid iron oxide nanoparticles (MNPs) conjugated to a Halo Tag functional ligand, in order to obtain a bioactive conjugate with a number of properties, such as stability in a wide pH range and physiological media, certain size and functionality. These particles should be able to be recognized by Halo Tag protein called HALO-U11, constructed by a genetic fusion with a small peptide of 11 amino acids (U11= VSNKYFSNIHW) as a targeting module for urokinase plasminogen receptor (uPAR) [36] which is over-expressed on the membrane of several metastasizing cancers [37]. In this way, the nanoparticle has the function of substrate for the “HALO capture model”; although the peptide, homed in the protein sequence, is the active targeting biomolecule towards the cell surface receptor (Figure. 3).

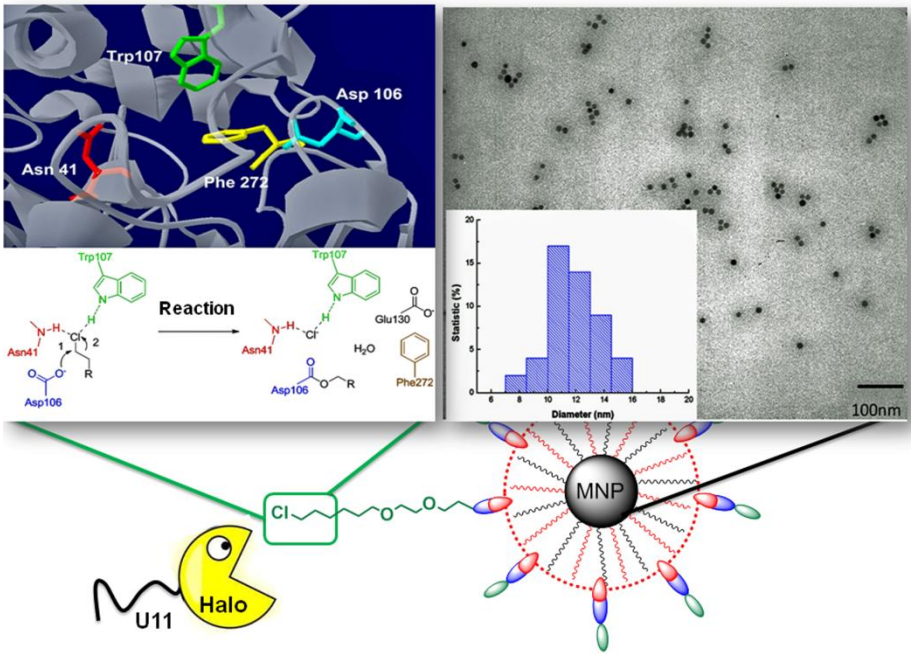

Figure 3: Schematic chemical conjugation of HALO protein to hybrid iron oxide nanoparticles.

A green fluorescent label has been chemically incorporated inside the nanoparticle polymer layer to check the affinity for cellular receptors by fluorescence intensity with flow cytometry. For this reason U937 cell lines were selected as the cellular model to assess the targeting efficiency of MNP-U11 conjugated. These cancer cell line is available both as uPAR-positive (U937_13) and as uPAR-negative (U937_10). The only difference between them was the membrane expression of a U11-specific receptor. Finally, cellular toxicity experiments has been evacuate on the same cell line after 24 h of exposure within MNPs which suggested that this system was nontoxic within a broad range of concentrations, making this nanoconstruct promising for future *in vitro* and *in vivo* applications

Intracellular Drug Release from Curcumin-Loaded PLGA Nanoparticles Induces G2/M Block in Breast Cancer Cells

Biodegradable organic polymers such as polylactide-co-glycolide acid (PLGA) have been used as carriers for drugs, peptides, proteins, vaccines, and nucleotides [38]. Nanoparticles formed by self assembly of polymer chains can protect drug moieties from degradation and provide sustained drug release in a time dependent way. For instance, PLGA nanoparticles are sometimes effective in facilitating intracellular delivery of bioactive materials and, according to this capability, they have been approved by Food and Drug administration (FDA) for parenteral administration of different molecules for applications in vaccination, cancer therapy, and the treatment of cerebral disorders [39]. In particular, these nanoparticles have been widely investigated for use in cancer therapy for two reasons: first of all, PLGA nanoparticles, if given intravenously, can extravasate into and accumulate within tumor tissues that have defective blood vessels and impaired lymphatic drainage [40]. This effect, called enhanced permeability and retention (EPR) effect, helps the internalization of nanoparticles in tumor sites [41]. Secondly, most of the chemotherapeutic molecules adopted for cancer therapy suffer from different hurdles such

as high toxicity rate, undesirable administration side effects, poor solubility in physiological media and difficult tumor accumulation. For these reason modern medicine needs efficient drug delivery systems which may effort sustainable medicinal tissue localization ad efficiency.

As a model of hydrophobic anticancer drug that can overcome these problems, I turned my attention to a natural chemical compound, 1,7-*bis* (4-hydroxy-3-methoxyphenyl)-1,6-hepadiene-3,5-dione, which is commonly referred to as curcumin. This compound has been shown to possess a wide range of pharmacological activities, including anticancer effects [42−44].

This part of the thesis, has been focused on developing uniform curcumin-bearing PLGA nanoparticles, synthesized by the single emulsion technique (about 120 nm), which exhibit a prolonged curcumin release over time. The loading ratio of encapsulated drug has been evaluated by UV-vis spectroscopy and it has been also provided an efficient protection of curcumin from environment by the polymer shell, as determined by fluorescence emission and Raman experiments. Within the following *in vitro* experiments, the intracellular degradation of nanoparticles associated with a specific G2/M blocking effect on MCF7 breast cancer cells caused by curcumin release in the cytoplasm, has provided direct evidence on the mechanism of action of this nanovector (Figure 4).

This study has been carried out using apoptosis cell-death analysis and an assessment of cellular proliferation. PLGA nanoparticles uptake has been assessed by flow cytometry and confocal laser scanning microscopy thanks to the fluorescence emission properties of the molecule. The pure PLGA nanoparticles (without drug) proved a safety profile, suggesting a potential utilization of this nanoconstruct to improve the intrinsically poor bioavailability of curcumin for malignant breast cancer therapy.

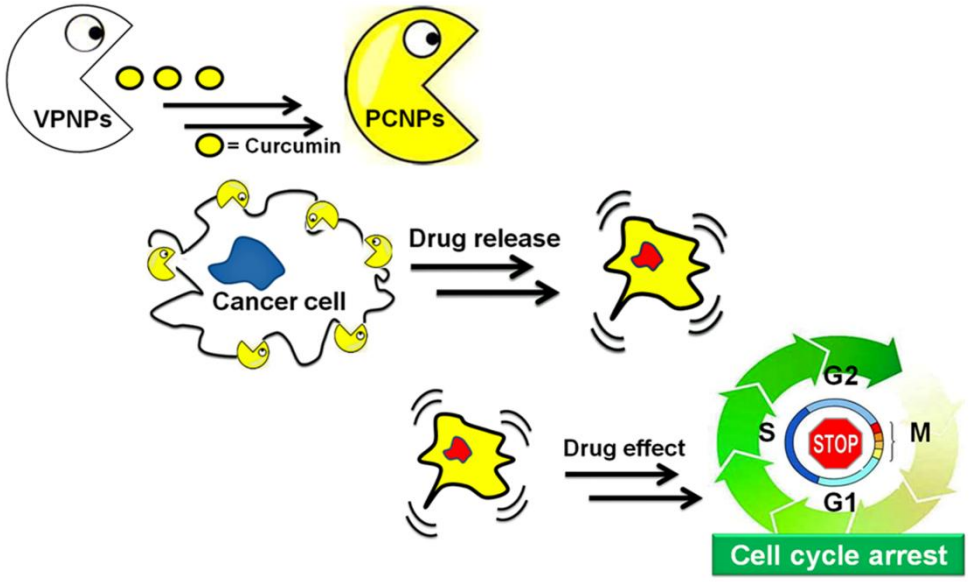

Figure 4: PLGA nanoparticles bearing Curcumin.
The mechanism of action is associated with a specific G2/M blocking effect on MCF7 breast cancer cells caused by curcumin release in the cell cytosol

Related References

[1] Riehemann, K.; Schneider, S. W.; Luger, T. A.; Godin, B.; Ferrari, M. and Fuchs, H.; *Angew. Chem. Int. Ed.* **2009**, *48*, 872−897.

[2] Veronesi, U.; Paganelli, G.; Galimberti, V.; et al.; *Lancet.* **1997**, *349*, 1864−1867.

[3] Silverstein, M. J.; *BMJ.* **1997**, *314*, 1736−1739.

[4] Noguchi, M.; *J. Surg. Oncol* **2003**, *84*, 94−101.

[5] Frangioni, J. V; *J. Clin. Oncol* **2008**, *26*, 4012−4021.

[6] Chae, A. W; Vandewalker, K. M.; Li, Y. J.; Beckett, M. A.; Ramsamooj, M.; Bold, M. J. and Kathri, V. P.; *Eur. J. Surg. Oncol* **2013**, *39*, 627−633.

[7] Swede, H; Moysich, K. B.; Freudenheim, J. L.; et al.; *Cancer Detect. Prev.* **2001**, *25*, 511−519.

[8] Swain, S. M.; Kim, S. B.; Cortés, J.; et al.; *Lancet. Oncol.* **2013**, *14*, 461−471.

[9] Freedman, R. A.; Huges, M. E.; Ottesen, R. A.; et al.; *Cancer* **2013**, *15*, 839−846.

[10] Pierga, J. Y.; Petit, T.; Delozier, T.; et al.; *Lancet. Oncol.* **2012**, *13*, 375−384.

[11] Chan, A.; Conte, P. F.; Pertuzelka, L.; et al.; *Anticancer Res.* **2013**, *33*, 2657−2664.

[12] Sommaruga, S.; Lombardi, A.; Salvadè, A.; et al.; *Appl. Microbiol. Biotechnol.* **2011**, *91*, 613−621.

[13] Daniels, T. R.; Delgado, T.; Helguera, G. and Penichet, M. L.; *Clin. Immunol.* **2006**, *121*, 159−176.

[44] Thorstensen, K.and Romslo, I.; *Biochem. J.* **1990**, *271*, 1−10.

[15] Barandeh, H.; Nguyen, P. L.; Kumar, R.; et al.; *PLOSone.* **2012**, *7*, e29424.

[16] Kumar, R.; Roy, I.; Ohulchanskyy, T. Y.; et al.; *ACSnano.* **2008**, *2*, 449−456.

[17] Salvati, A.; Pitek, A. S.; Monopoli, M. P.; et al.; *Nat. Nanotech.* **2013**, *8*, 137−143.

[18] Sah, H.; Thoma, L. A.; Desu, H. R.; Sah, E. and Wood, G. C.; *Int. J. Nanomed.* **2013**, *8*, 747−765.

[19] Park, K.; Lee, S.; Kang, E.; Kim, K.; Choi, K. and Kwon, I. C.; *Adv. Funct. Mater.* **2009**, *19*, 1553−1566.

[20] Lee, J. H.; Huh, Y. M.; Jun Y. W.; et al.; *Nat. Med.* **2007**, *13*, 95−99.

[21] Kim, K.; Park, S.; Lee, J. E.; et al.; *Angew. Chem. Int. Ed.* **2006**, *45*, 7754−7758.

[22] Corsi, F.; Fiandra, L.; De Palma, C.; et al.; *ACSnano.* **2011**, *5*, 6383−6393.

[23] Park, J.; An, K.; Hwang, Y.; et al.; *Nat. Mater.* **2004**, *3*, 801−805.

[24] Corsi, F.; De Palma, C.; Colombo, M.; et al.; *Small.* **2009**, *5*, 2555−2564.

[25] Yang, J.; Lim, E. K.; Lee, H. J.; et al.; *Biomaterials.* **2008**, *29*, 2548−2555.

[26] Chen, S.; Reynolds, F.; Yu, L.; Weissleder, R. and Josephson, L.; *J. Mater. Chem.* **2009**, *19*, 6387−6392.

[27] Lewin, M.; Carlesso, N.; Tung, C. H.; et al.; *Nat.Biotechnol* **2000**, *18*, 410−414.

[28] Simberg, D.; Duza, T.; Park, J. H.; et al.; *Proc. Am. Chem. Soc.* **2007**, *16*, 932−936.

[29] Thanh, N. T. K. and Green, L. A. W. *Nanotoday.* **2010**, *5*, 213−230.

[30] Mazzucchelli, S.; Colombo, M.; De Palma, C.; et al.; *ACSnano.* **2010**, *4*, 5693−5702.

[31] Garcia, I.; Gallo, J.; Genicio, N.; Padro, D. and Penadés, S. *Bioconjugate Chem.* **2011**, *22*, 264−273.

[32] Xu, C.; Xu, K.; Gu, H.; et al.; *J. Am. Chem. Soc.* **2004**, *126*, 3392−3393.

[33] Long, J. C. L.; Pan, Y.; Lin, H. C.; Hedstrom, L. and Xu, B. *J. Am. Chem. Soc.* **2011**, *133*, 10006−10009.

[34] Yu, C. C.; Lin, P. C. and Lin, C. C. *Chem. Commun.* **2008**, *1*, 1308−1310.

[35] Colombo, M.; Sommaruga, S.; Mazzucchelli, S.; et al.; *Angew. Chem. Int. Ed* **2012**, *51*, 496−499.

[36] Los, G. V.; Encell, L. P.; McDougall, M. G.; et al.; *ACS Chem. Biol.* **2008**, *3*, 373−382.

[37] Wang, M.; Löwik, D. W. P. M.; Miller, A. D. and Thanou, M.; *Bioconjugate Chem.* **2009**, *20*, 32−40.

[38] Blasi, F.and Sidenius, N.; *FEBS Lett.* **2010**, *584*, 1923−1930.

[39] Danhier, F.; Ansorena, E.; Silva, J. M.; Coco, R.; Le Breton, A. and Préat, V.; *J. Control. Release.* **2012**, *161*, 505−522.

[40] De Jong, W. A. and Borm, P. J. A.; *Int. J. Nanomed.* **2008**, *3*, 133−149.

[41] Acharya, S. and Sahoo, S. K.; *Adv Drug Deliv. Rev.* **2011**, *63*, 170−183.

[42] Sa, G. and Das, T.; *Cell. Division.* **2008**, *3*, 1−14.

[43] Bhattacharyya, S.; Mandal, D.; Sen, G. S.; et al.; *Cancer Res.* **2007**, *67*, 362−370.

[44] Lai, C. S.; Wu, J. C.; Yu, S. F.; et al.; *Mol. Nutr. Food. Res.* **2011**, *55*, 1819−1828.

[45] Yamashita, S.; Lai, K. P.; Chuang, K. L.; et al.; *Neoplasia.* **2012**, *14*, 74−83.

[46] Lai, K. P.; Huang, C. K.; Chang, Y. J.; et al.; *Am. J. Pathology.* **2013**, *182*, 460−473.

Complete List of Publications:

- Prencipe, G.; Maiorana, S.; **Verderio, P.**; Colombo, M.; Fermo, P.; Caneva, E.; Prosperi, D. and Licandro, E.; "Magnetic Peptide Nucleic Acid for DNA Targeting"; *Chem. Commun.* **2009**, *40*, 6017−6019.

- Colombo, M.; Corsi, F.; Foschi, D.; Mazzantini, E.; Mazzuchelli, S.; Morasso, C.; Occhipinti, E.; Polito, L.; Prosperi, D.; Ronchi, R. and **Verderio, P.**; "HER2 targeting as a two sided strategy for breast cancer diagnosis and treatment: outlook and recent implications in nanomedical approaches"; *Pharmacol. Res.* **2010**, *62*, 150−165.

- Mazzucchelli, S.; Colombo, M.; De Palma, C.; Salvadè, A.; **Verderio, P.**; Coghi, M. D.; Clementi, E.; Tortora, P.; Corsi, F. and Prosperi, D.; "Synthesis of single-domain Protein A-engineered magnetic nanoparticles: a step towards a universal strategy to site- specific labeling of antibodies for targeted detection of tumor cells"; *ACS Nano.* **2010**, *4*, 5693-5702.

- **Verderio, P.**; Occhipinti, E.;* Natalello, A.; Galbiati, E.; Colombo, M.; Mazzucchelli, S.; Salvadè, A.; Tortora, P.; Doglia, S. M. and Prosperi. D.; "Investigating the Structural Biofunctionality of Antibodies Conjugated to Magnetic Nanoparticles"; *Nanoscale.* **2011**, *3*, 387−390.

- Corsi, F.; Fiandra, L.; De Palma, C.; Colombo, M.; Mazzucchelli, S.; **Verderio, P.**; Allevi, R.; Tosoni, A.; Nebuloni, M.; Clementi, E. and Prosperi, D.; "HER2 Expression in Breast Cancer is downregulated upon active targeting by antibody-engineered multifunctional nanoparticles in mice"; *ACS Nano.* **2011**, *5*, 6383−6393.

- Morasso, C.; **Verderio, P.**; Colombo, M. and Prosperi, D.; Book Chapter: Chapter 5: "Strategies for the characterization of the saccharidic moiety in composite nanoparticle". In "Petite and Sweet: Glyco-Nanotechnology as a Bridge to New Medicines"; Huang, X., et al.; Publication Date (Web): December 13, 2011. ACS Symposium Series; © 2011American Chemical Society: Washington, DC, 2011.

- **Verderio, P.**; Mazzucchelli, S.;* Sommaruga, S.; Colombo, M.; Salvadè, A.; Tortora, P.; Corsi, F. and Prosperi, D.; "Multiple presentation of scFv800E6 on silica nanospheres enhances targeting efficiency toward HER2 receptor in breast cancer cells"; *Bioconjugate Chem.* **2011**, *22*, 2296−2303.

- Colombo, M.; Sommaruga, S.; Mazzucchelli, S.; Polito, L.; **Verderio, P.**; Galeffi, P.; Corsi, F.; Tortora, P. and Prosperi, D.; "Site-specific conjugation of scFvs to nanoparticles by bioorthogonal strain-promoted alkyne-nitrone cycloaddiction"; *Angew. Chem. Int. Ed.* **2012**, *51*, 496−499.

- Avvakumova, S.; **Verderio, P.**; Speranza, G. and Porta, F.; "Gold nanoparticles modified with guanine: study of conformational changes"; *J. Phys. Chem. C.* **2013**, *117*, 3002−3010.

- Mazzucchelli, S.; Colombo, M.; **Verderio, P.**; Rozek, E.; Andreata, F.; Galbiati, E.; Tortora, P.; Corsi, F. and Prosperi, D.; "Orientation-controlled conjugation of HALO-fused homing peptides to multifunctional nanoparticles for specific recognition of cancer cells"; *Angew. Chem. Int. Ed.* **2013**, *52*, 3121−3125.

- **Verderio, P.**; Bonetti, P.;* Colombo, M.; Pandolfi, L. and Prosperi, D.; "Intracellular drug release from curcumin-loaded PLGA nanoparticles induces G2/M block in breast cancer cells"; *Biomacromolecules.* **2013**, *14*, 672−682.

- **Verderio, P.**; Avvakumova, S.;* Alessio, G.; Belllini, M.; Colombo, M.; Galbiati, E.; Mazzucchelli, S.; Avila, J. P.; Santini, B. and Prosperi, D.; "Delivering colloidal nanoparticles to mammalian cells: a Nano−Bio interface perspective"; *Adv. Heathcare Mater.* **2014**, DOI: 10.1002/adhm.201300602..

(*) contributes equally

First Section

Chapter I

Inorganic Nanoparticles

Contents

1.1. Introduction

A considerable attention towards nanotechnology has raised, nowadays, as a growing impact to modern life; nanoparticle research has been exploited to the use of inorganic nanoparticles in different technological fields [1]; particularly, a significant factor is the development of a great number potential biological applications in biomedical science of nanoparticles, ranging from imaging [2] to biochemical sensing [3,4], targeting [5,6] and drug delivery [7,8]. The main advantage of inorganic

nanoparticles is attributed to their intrinsic physical properties including size-dependent optical, magnetic, electronic, and catalytic properties as well as some biological activities (*e.g.* anti-bacteria or specific interactions) [9]. In addition, a possible construction between inorganic nanoparticle, as physical supports, and biochemical building blocks lead to a broad selection of novel hybrid systems with interestingly properties. In this framework, new synthetic chemistry approaches continue to uncover more elaborate structures, which is expected to expand further the range of biomedical applications of inorganic nanomaterials [10]. The main challenge of these chemical approaches is the controlled synthesis of nanostructures such that they are uniform in size, shape, chemical composition, they are produced in high yields, and they are stable in biological environments. Many functional groups provide a wide range of potential interactions of organic moieties and biomolecules with nanoparticle surface, which can be easily used to compose a bio-nano structure with a specific biological function.

The modification of peptides, proteins and other complex molecules with specific anchoring groups facilitates the binding to nanoparticles *via* a site-specific linkage, introducing chemical functionalities that can provide recognition or affinity interactions between the biomolecules and antibodies or cell receptors. This approach has been widely used to design nanoparticle conjugates to be used in different applications [10]. Nowadays there is a huge part of research exploring these interactions, which may affects the structures at the molecular level thus affecting the biological function. For this reason, the challenge to use of bio-nano systems requires the joint efforts of interdisciplinary research groups to be adequately faced; one of the main issues to be considered concerns the design and optimization of effective functionalization strategies. At the same level, it is needed a detailed

understanding profile of biomolecule-nanoparticle interactions at their interface and with biological systems such as cells and tissues [11].

The present chapter focuses on some interesting inorganic nanoparticles, which enclose fascinating properties and promising applications for the biotechnological field. Different synthetic approaches of these inorganic nanoparticles will also be mentioned as well as their surface modifications with organic and active biomolecules; in addition are described some interesting applications for mammalian cancer diagnostics and therapy. These inorganic particles include iron oxides and silica nanoparticles, which have been also the starting materials of the applied research of this PhD thesis work.

1.2. Iron oxide nanoparticles: general aspects

The nanoscale, defined by the US National Nanotechnology Initiative, is a range from 1 to 1000 nm, including particles which are naturally occurring, such as particles in smoke, volcanic ash, sea spray, and from anthropogenic sources. In terms of biology, the nanoscale is the size range of important cellular components, such as double-stranded DNA (about 2.5 nm in diameter), proteins (hemoglobin is about 5 nm in diameter), cell walls, cell membranes, and compartments [12]. The SI prefix “nano” means a billionth (10^{-9}) part of a meter, or about one hundred thousandth the thickness of a sheet of paper.

Metal nanoparticles have a long history in terms of preparation, characterization, and application. Understanding the properties of iron based nanoparticles and exploring their potential applications are major driving forces behind the synthesis of a large variety of functional nanomaterials. Many properties of these nanoparticles arise from their large surface-area-to-volume ratio and the spatial confinement of electrons, phonons, and electric fields in and around the particles. These may cause deviations from the usual bulk atomic arrangements, such as higher reactivity; different elastic, tensile, and magnetic properties; increased conductivity; or increased tendency to reflect and refract light.

Iron is one of the most abundant metallic elements in living organisms, and is essential for various biological processes, such as oxygen transport by hemoglobin and cellular respiration by redox enzymes. Iron oxide nanoparticles (MNPs), which are usually magnetic susceptible, are one of the few nanomaterials that can be injected into the body and incorporated into natural metabolic pathways of human body; for these reasons, compared with many other nanoparticles, iron oxide nanoparticles are less toxic and more biologically tolerated in a broad range of

concentrations. The most common nanomaterials are pure iron magnetic oxides, such as Maghemite (γ-Fe_2O_3) and magnetite (Fe_3O_4). MNPs doped with magnetically susceptible elements (*e.g*. $MnFe_2O_4$ and $CoFe_2O_4$) and metal alloys nanoparticles (*e.g.* FeCo and FePt) are also available, but they are much less employed in biomedical applications because of their potential toxicity and rapid oxidation, even though the magnetism of these ferrites and metal alloys is stronger than that of the corresponding pure iron oxide. The metabolism, and pharmacokinetics of intravenously injected MNPs have been well studied [13] and, in addition to their superior biocompatibility, magnetic MNPs offer many important skills for biomedical applications, such as magnetic resonance imaging (MRI), drug delivery, cell tracking and hyperthermia [14] Currently, there are some iron oxide nanoparticle-based MR contrast agents that have already been used in clinical trials, or are undergoing clinical trials [15].

Most of these commercially available MNPs are covered by a specific organic and/or inorganic layer; this appropriate coating depends on the type of nanoparticle core and the proposed applications. Differently coated iron oxide nanoparticles will have different effects on cells and different fates in the body, depending on their size, the crystallinity of their core and the chemical composition of their coating layers. Hence, the suitable chemical design of both the core and shell of the nanoparticle is extremely important for future projected clinical practice [16].

1.3. Properties of Iron oxide nanoparticles

Magnetic materials are characterized by the presence of magnetic dipoles generated by the spinning of some of their electrons. Each of these polarized electrons can be aligned in a parallel or anti-parallel fashion with respect to the neighboring ones in the crystal lattice and this type of interaction is what gives rise to the macroscopic magnetic effect that we can measure. Depending on the magnetic response observed, it is possible to classify magnetic materials as paramagnets, ferromagnets, ferrimagnets or anti-ferromagnets. However, such behaviors are strongly size-dependent and consequently it is better to keep in mind that, at a particular temperature, the magnetic behavior of any material can be altered by tuning its size [17].

A material in a paramagnetic phase is characterized by uncouple (randomly oriented) magnetic dipoles, which can be aligned only in the presence of an external magnetic field and along its direction. This type of material has no coercivity nor remanence, which means that when the external magnetic field is switched off, the internal magnetic dipoles randomize again, no extra energy is required to demagnetize the material and hence the initial zero net magnetic moment is spontaneously recovered. A nanoparticle with such magnetic behavior is superparamagnetic (SPM) (Figure. 1.1).

Otherwise, single magnetic dipoles in a crystal may align parallel one to the other, hence exhibiting an enhanced collective response even in the absence of an external magnetic field; this phenomenon is known as ferromagnetism. In this case three main parameters can describe the strength and magnetization of the material: (a) the *Coercive Field* (H_C) which is the external field of opposite sign required to

reduce the magnetization back to zero; this parameter represents also the minimum energy required for the reversal of the magnetization of the material.

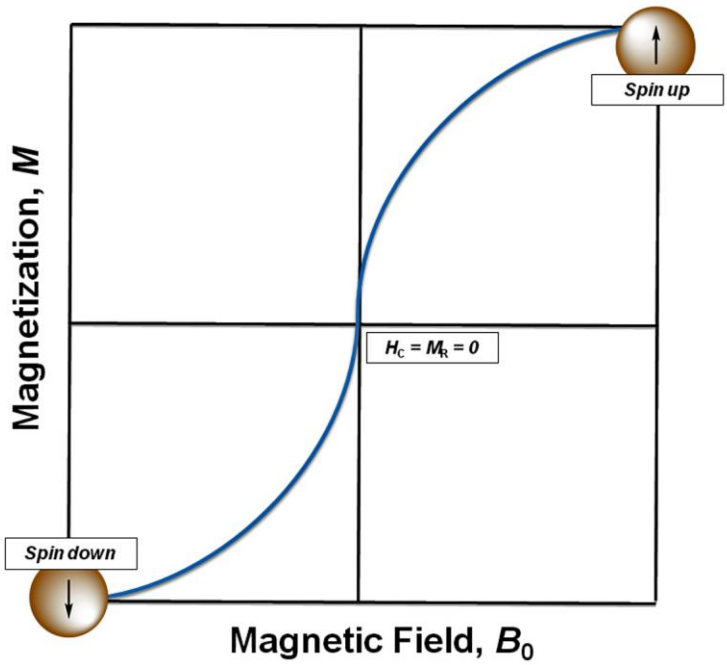

Figure 1.1: Theoretical magnetization versus magnetic field.
Curve for superparamagnetic nanoparticles, the saturation magnetization and the remanent magnetization (MR) parameters

H_C is strictly related to the magnetic anisotropy constant (K_u) that determines the energy to be overcome in order to invert the direction of the magnetic dipoles of the material; K_u can have different contributions such as the symmetry of the crystal lattice, the surface contribution with respect to the core of the nanoparticle, and finally the shape of the nanoparticle. (b) The *Saturation Magnetization* (M_S), which is the maximum value of magnetization that the material can reach under the effect of sufficiently high magnetic fields. (c) The *Remanent Magnetization* (M_R), which indicates the residual magnetization at zero applied field. These three parameters can be easily identified in the hysteresis loop generated in field-dependent magnetization measurements, see Figure. 1.1.

Bulk metals such as iron as well as some of its alloys (FePt, FeCo) are ferromagnetic materials. Differently to the ferromagnetic situation, neighboring magnetic dipoles can align anti-parallel in the lattice, which means that they will repulse each other. This type of magnetic exchange can lead to two different situations, namely *anti-ferromagnetism*, occurring when the magnetic dipoles or interacting spins have the same value and hence the material shows a net zero magnetization, and *ferrimagnetism* when the two coupled spins show different values; in this case a net magnetic dipole different than zero will still magnetize the material, even in the absence of an external magnetic field. The former case lacks of interest for biomedical applications due to the zero net magnetic moment arising in such materials. The latter instead is much more interesting and actually MNPs (both bulk magnetite and maghemite) belongs to the ferrimagnetic class of materials.

The size reduction of magnetic materials shows enhancing advantages that make them more suitable for therapeutic and diagnostic techniques compared to their bulk counterparts; for example magnetic parameters such as the H_C of particles can be tuned by decreasing their size and, consequently, the biomedical performance of the sample can be optimized to the practical requirements. Moreover, a further reduction of the size below a certain value of the radius (called superparamagnetic radius, r_{SP}), induces a magnetic transition in particles where both ferro- and ferri-magnetic nanoparticles become *superparamagnetic.* Superparamagetism is strictly associated to nanoformed magnetic materials and arises when the thermal energy is sufficiently high to overcome the magnetic stabilization energy of the particle [18] (Figure 1.2).

This last property translates into a considerable advantage, especially for *in vivo* experiments: the absence of H_C (the zero net magnetic moment) of the

nanoparticles after concluding the diagnostic measurement will prevent the potential aggregation of MNPs that could easily cause the formation of embolisms in the blood vessels.

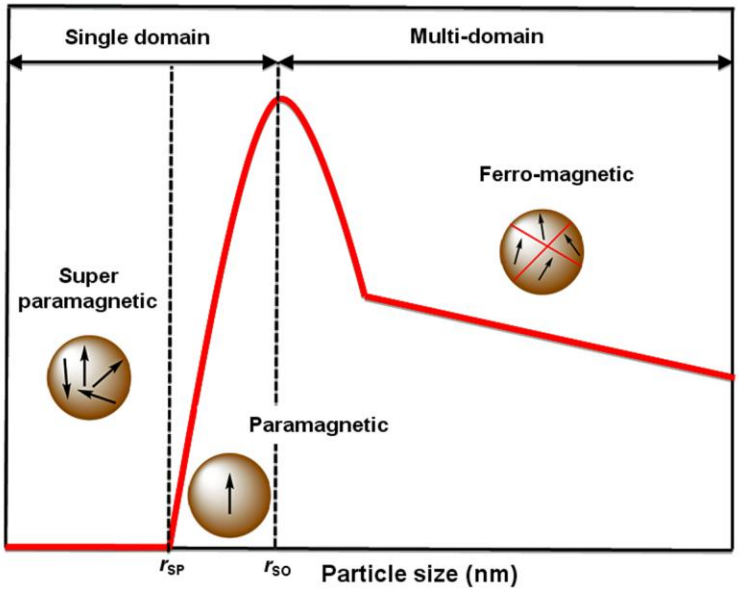

Figure 1.2: Size-dependent behavior.
Variation of the coercivity (HC) of magnetic nanoparticles with size.

1.4. Large-scale chemical synthesis of iron oxide nanoparticles

Up to now, a great number of physical and chemical methods have been applied to synthesize MNPs [19]. Physical methods [20] have advantages in that they can be adapted to mass production and high-purity nanomaterials can be obtained, but it is difficult to control the size and shape of the nanoparticles. To overcome these drawbacks, various chemical methods based on solution-phase colloidal chemistry have been investigated for the synthesis of high quality nanoparticles. These chemical methods include metal salt reduction, sol-gel process, reverse micelle technique, and thermal decomposition of iron organic precursors [21]. Nevertheless, to prepare iron oxide nanoparticles suitable for the intended medical applications, the use of "green chemistry" is highly recommended, which avoids the use of toxic chemicals. It is also desirable to have a synthetic process that is scalable to industrial applications, and should be reproducible from batch to batch. In this section, instead of compiling a list of all the chemical approaches to iron oxide nanoparticle synthesis, I briefly introduce typical and representative methods for the scalable synthesis of iron oxide nanoparticles for medical use.

1.4.1- Coprecipitation

Magnetite is prepared by reacting Fe(II) and Fe(III) salts in alkaline aqueous media in a molar ratio of 1:2; MNPs made by this method are commonly used for biomedical applications for two main reasons: 1) easy and large-scale production; 2) direct dispersion in water without further treatment. Massart first performed the coprecipitation process for the preparation of iron oxide particles by alkaline precipitation of $FeCl_3$ and $FeCl_2$ [22]. However, the synthesized magnetite particles from this process were highly polydisperse and unstable. To further improve the

stability, iron oxide nanoparticles prepared with the Massart method were coated in situ using various capping ligands such as hydroxamate, dimercaptosuccinic acid, phosphorylcholine, and citric acid [23,24]. However, the crystallinity of the synthesized iron oxide nanoparticles is very poor, which reduces their magnetic susceptibility; furthermore, the nanoparticles are generally quite polydisperse, and a size selection process is required to get uniform-sized nanoparticles.

1.4.2- Aerosol-vapor technology

The aerosol/vapor technology (*e.g*. flame-spray, laser pyrolysis) is another way to synthesize MNPs on a large scale. These technologies produce a wide range of iron oxide nanoparticles such as magnetite, maghemite, and wustite (FeO), which can be controlled by varying the fuel-to-air ratio during combustion, as well as by controlling the valence state of the iron precursors. In flame-spray pyrolysis, ferric salt and reducing agent, mixed together in an organic solvent, are sprayed into a series of reactors to condense the aerosol solute, followed by evaporating the solvent [25]. In laser pyrolysis, a laser is used to heat a gaseous mixture of an iron precursor and a flowing mixture of gases in order to produce well-dispersed fine nanoparticles [26]. The size of the nanoparticles can be tuned in the range from 2 to 7 nm by adjusting the pyrolysis conditions. Unfortunately, because of the difficulty of obtaining a uniform size for the initial droplets or gaseous mixture, the final nanoparticles made by this process have a very broad size distribution.

1.4.3- Solvothermal decomposition from organo-metallic precursors

Uniform-sized nanoparticles are preferred because they are easier to characterize both *in vitro* and *in vivo*, and thus they are more likely to get Food and Drug Administration (FDA) approval. The methods described previously have several intrinsic drawbacks, including the difficulty of producing highly uniform iron oxide

nanoparticles and low crystallinity. Highly uniform-disperse MNPs can be synthesized on a large scale by solvothermal decomposition of organometallic iron precursor such as iron pentacarbonyl [27], iron cupferron [28], iron oleate [29], or iron acetylacetonate [30,31] in a hot surfactant solution. Nanoparticles synthesized by solvothermal decomposition have high crystallinity and uniform size distribution; unfortunately, this synthetic procedure cannot readily be applied to large-scale and economic production because and expensive toxic reagents and complicated synthetic steps are employed in this process. Nanoparticles produced via this procedure often have particle size distributions with polidispersity (σ) ≈ 10%. A size-selection process is needed to narrow the size distributions to σ < 5%. Hyeon et al. reported the fabrication of highly uniform iron oxide nanoparticles by the thermal decomposition of iron oleate complex, which was prepared by the reaction of iron pentacarbonly with oleic acid [27]. Monodisperse iron oxide nanoparticles were obtained by mixing iron pentacarbonly precursor with oleic acid solution at low temperature and heating up the reaction mixture to high temperature. The initially produced iron nanoparticles were further oxidized to iron oxide nanoparticles by using trimethylamine N-oxide as a mild oxident. The size of the nanoparticles was controlled by adjusting the molar ratio of iron pentacarbonyl to oleic acid. Because the resulting iron oxide nanoparticles were highly monodisperse, a laborious and tedious size-selection process was not required to obtain uniform nanoparticles. The same author few years later reported a synthetic method of obtaining mono-disperse MNPs using an inexpensive and nontoxic iron chloride ($FeCl_3$) rather than toxic and expensive iron pentacarbonyl [32]; according to this purpose, this process has been also adopted to synthesize MNPs for my thesis work (Figure. 1.3).

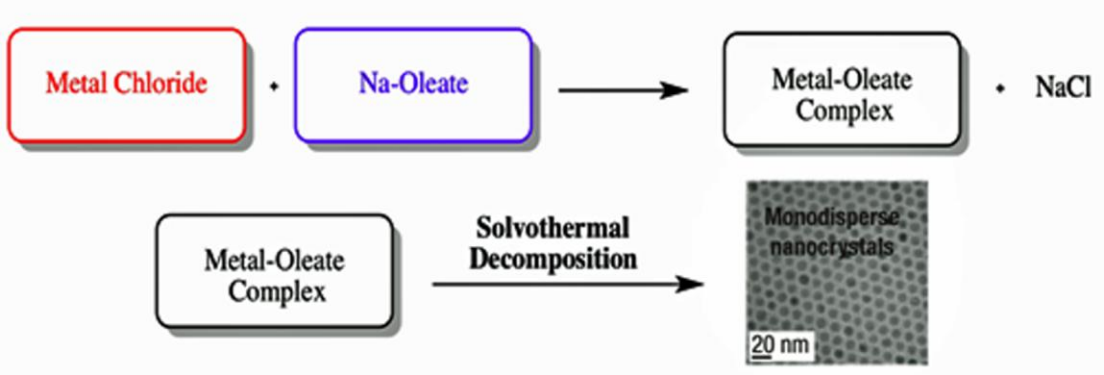

Figure 1.3: Scheme for the ultra-large-scale synthesis of monodisperse nanocrystals.
Metal–oleate precursors were prepared from the reaction of metal chlorides and sodium oleate. The thermal decomposition of the metal–oleate precursors in high boiling solvent produced monodisperse nanocrystals.

A dispersion containing the iron-oleate complex, generated from the reaction between $FeCl_3$ and sodium-oleate, is soaked in an high boiling solvent (1-octadecene); the mixture is slowly heated to the boiling point of the solvent to produce the mono-disperse nanoparticles. Because of the simplicity of the reaction and the stability of the iron–oleate complex, this method can readily be scaled up for mass production to yield grams of uniform iron oxide nanoparticles in a single reaction and, essentially, without the need for a size-selection process. The size of the iron oxide nanoparticles may be modulated by changing the aging temperature. When 1-hexadecene [boiling point (bp): 274 °C], octyl ether (bp: 287 °C), 1-octadecene (bp: 317 °C), 1-eicosene (bp: 330 °C), and trioctylamine (bp: 365 °C) were used as the solvent, 5-nm, 9-nm, 12-nm, 16-nm, and 22-nm iron oxide nanoparticles have been produced, respectively [33−35]. Very recently, uniform and extremely small iron oxide nanoparticles of less than 4 nm have been synthesized via the thermal decomposition of an iron–oleate complex in the presence of oleyl alcohol [36]. The use of oleyl alcohol reduced the reaction temperature by reducing the iron–oleate complex, resulting in the production of extremely small MNPs. This size could be finely controlled from 1.5 nm to 3.7 nm by changing the ratio of oleyl alcohol to oleic acid or by changing the aging temperature.

1.5. Applications of Iron Oxide Nanoparticles in Biomedical Research

The increasing applications of MNPs, has given rise to many concerns among public, scientific and regulatory authorities regarding their toxicological properties and long-term impact on human health. Hence, the *in vivo* behaviors and toxicology of iron oxide nanoparticles have been intensively studied for the safe design in the past decades. In this section will be discussed most of the applications of MNPs in biomedicine and their involvement into biological processes.

1.5.1- Magnetic Resonance Imaging (MRI): T_2 and T_1 contrast agent

'Contrast' refers to the signal differences between adjacent regions, which could be 'tissue and tissue', 'tissue and vessel', and 'tissue and bone'. Contrast agents for X-ray show contrasting effects according to the electron-density difference, and they produce direct contrast effects on their positions. However, the contrast mechanism is more complicated for MRI, where the contrast enhancement occurs as a result of the interaction between the contrast agents and neighbouring water protons, which can be affected by many intrinsic and extrinsic factors such as proton density and MRI pulse sequences. The basic principle of MRI is based on nuclear magnetic resonance (NMR) together with the relaxation of proton spins in a magnetic field [37]. When the nuclei of protons are exposed to a strong magnetic field, their spins align either parallel or anti-parallel to the magnetic field applied. (Figure. 1.4).

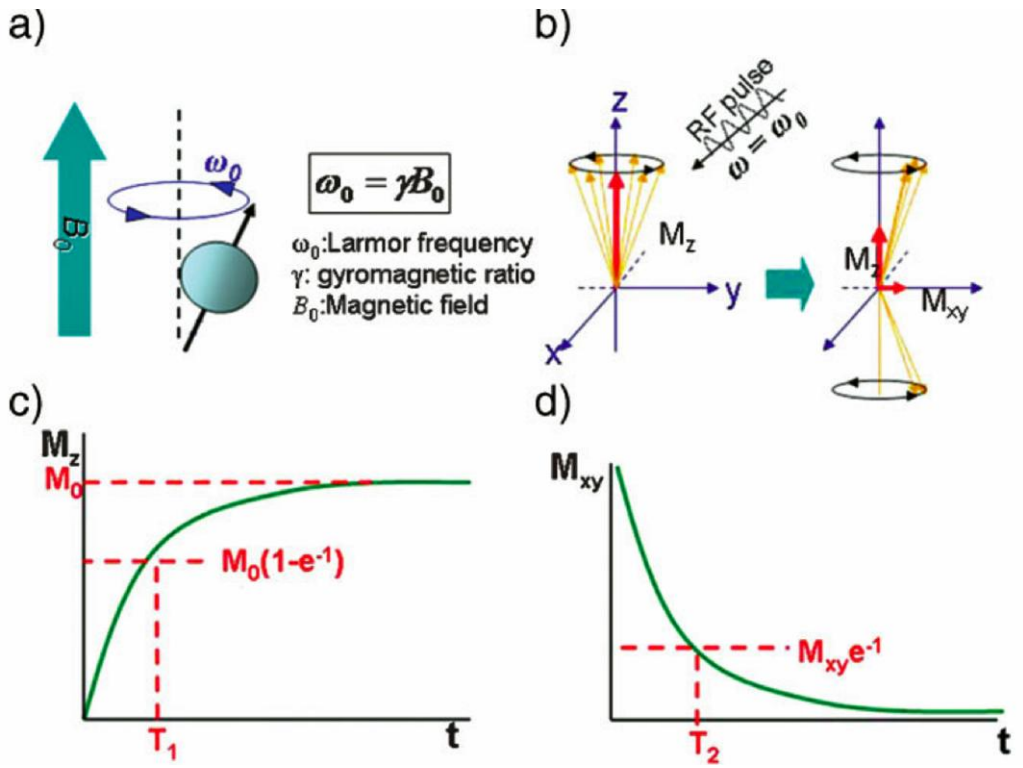

Figure 1.4: Principle of magnetic resonance imaging.
a) Spins align parallel or antiparallel to the magnetic field and precess under Larmor frequency (ω_0); b) After induction of RF pulse, magnetization of spins changes; c) Excited spins take relaxation process of T_1 relaxation and d) T_2 relaxation.

During their alignment, the spins precess under a specified frequency, known as the Larmor frequency (ω_0, Figure. 1.4a). When a 'resonance' frequency in the radio-frequency (RF) range is introduced to the nuclei, the protons absorb energy and are excited to the anti-parallel state. After the disappearance of the RF pulse, the excited nuclei relax to their initial, lower-energy state (Figure. 1.4b). There are two different relaxation pathways: the first, called longitudinal or T_1 relaxation, involves the decreased net magnetization (M_z) recovering to the initial state (Figure. 1.4c). The second, called transverse or T_2 relaxation, involves the induced magnetization on the perpendicular plane (M_{xy}) disappearing by the dephasing of the spins (Figure. 1.4d). Based on their relaxation processes, the contrast agents are classified as T_1 and T_2 contrast agents.

Commercially available T_1 contrast agents are usually paramagnetic complexes, while T_2 contrast agents are based on MNPs, which are the most representative nanoparticulate agents; therefore, it is reported in Table .1 some examples of T_2 contrast agents based on MNPs, commonly exploited in biomedical MRI.

Name	Core NPs	Surface	Diam (nm)	Magnetization [emu g^{-1}]	r_2 [mM^{-1} s^{-1}]	B_0 applied [T]	[Refs]
Feridex	Fe_3O_4	Dextran	4.96	45	120	1.5	[38]
Resovist	Fe_3O_4	Carboxydextran	4	60	186	1.5	[39]
Combidex	Fe_3O_4	Dextran	5.85	61	65	1.5	[40]
CLIO-Tat	Fe_3O_4	Dextran	5	60	62	1.5	[41]
MEIO	Fe_3O_4	DMSA	4	25	78	1.5	[42]

Table. 1: Commercially available T_2 contrast agent based on iron oxide nanoparticles.

1.5.2- Drug delivery

Magnetic iron oxide nanoparticle-based nanovectors have been intensively studied also as drug delivery vehicles [43−45]; this immediately upgrades the MRI imaging probes to theranostic agents that combine both diagnostic and therapeutic elements. One trick is to load MNPs, along with therapeutic agent, into polymer-based matrices [46] and, thus, various formulations employing iron oxide nanoparticles have been developed for theranostic applications. Recently, for instance, Nasongkla et al. [47] developed iron oxide nanoparticle-based theranostics, named SPIO-doxorubicin (Dox)-cRGD micelles for synchronous cancer imaging and traceable drug delivery. This approach showed the therapeutic modality of Doxorubicin and the diagnostic features of the cluster of MNPs which has been co-loaded into the cores of PEG-PLA micelles, while the targeting ligand, a cRGD peptide, has been attached onto the micelle surface for targeting the integrin $\alpha_v\beta_3$ overexpressed on tumor endothelial cells.

Aside from co-capsulation and/or chemical covalent coupling of drugs [48], therapeutics can also be loaded into hollow iron oxide nanoparticles via physical absorption. For instance, the Sun group developed porous iron oxide nanoparticles with a sizable cavity by controlled oxidation and acid etching of Fe particles [49]. In this work the authors loaded cisplatin, a powerful therapeutic agent against numerous solid tumors, into the cavities of the nanoparticles, and coupled Trastuzumab, a monoclonal antibody that interferes with the HER2/neu receptor, onto the nanoparticle surfaces to confer targeting specificity; in this way the functionalized iron oxide nanoparticles showed a selective affinity to HER2 receptors, overexpressed on breast cancer cells, and a sustained toxicity attributable to the release of cisplatin from the nanoparticles.

1.5.3- Nanosensors

MNPs offer desirable and unmatched characteristics for biomarker detection such as unique magnetic properties and significant surface area to volume ratio. Generally, the controlled clustering or aggregation of a few superparamagnetic iron oxide nanoparticles can greatly shorten T_2 relaxation time compared to single nanoparticles at the same iron concentration; thus, when magnetic nanosensors aggregate through affinity ligands to the biomarkers, a decrease in the T_2 relaxation time is observed, allowing the sensitive and accurate detection of biomarkers with excellent temporal and spatial resolution [50,51]. For instance, Colombo et al. [52] reported the accurate and reliable detection of anti-HSA (human serum albumin) antibodies by protein-functionalized magnetic nano-spherical probes due to the reversible alteration of their micro aggregation state induced by protein antibody specific interaction, sensed as changes in the T_2 relaxation time of surrounding water molecules.

El-Boubbou et al. [53] developed a magnetic nanosensor bearing carbohydrates to screen the carbohydrate-binding characteristics of cancer cells by MRI. The system consists of microcoils for radio-frequency excitation and signal detection, an on-board NMR spectrometer, a portable magnet, and micro-fluidic networks. Magnetic iron oxide nanoparticles were conjugated with antibodies to each biomarker, followed by incubation with samples of cancer cells. Significant differences in T_2 relaxation time could be observed for a variety of cancer cells using this system; in this way, this strategy with high sensitivity, specificity and high-throughput shows great potential for early cancer diagnosis in the clinic.

1.5.4- Hyperthermia

The cancer treatment by magnetic fluid hyperthermia has been explored extensively with iron oxide nanoparticles playing the key role as the local heaters. In the magnetic fluid thermo-therapy, magnetic fluids containing MNPs are delivered to the cancer and then heated by external alternating magnetic field, resulting hyperthermia of cancer tissue [54]. The underlying mechanism is that MNPs can act as antennae in an external alternating magnetic field to convert electromagnetic energy into heat; this feature holds promise in cancer therapy for cancer cells that are more susceptible to elevated temperature than normal cells.

Using MNPs and alternating magnetic fields, Zhao and co-workers [55] have found that head and neck cancerous tumor cells in mice can be killed in half an hour without harming normal cells; they basically injected a MNPs solution directly into the tumor site, with the mouse relaxed under anesthesia; they quickly placed the animal in a plastic tube wrapped with a wire coil that generated magnetic fields that alternated directions 100.000 times each second. The magnetic fields produced by the wire coil heated only the concentrated MNPs within the cancerous tumor and left

the surrounding healthy cells and tissue unharmed. In an analogue study amino silane coated MNPs have been injected into a subcutaneous tumor model in rats, which have been exposed to an alternating magnetic field [56]. The alternating magnetic field in conjugation with nanoparticles raised the temperature of tumor above 43 °C and caused tumor regression.

Nowadays, with the aim to engineer MNPs so as to enhance the stability and the tumor target capability, fragments of antigen-specific antibodies has been chemically anchored onto nanoparticle surfaces [57]; when MNPs have been administrated systemically into tumor-bearing mice; this novel nanoparticles platform should improve higher tumor uptake, presumably due to an antibody-antigen interaction, and they should induce better tumor hyperthermia when exposed to an alternating magnetic field (Figure. 1.5).

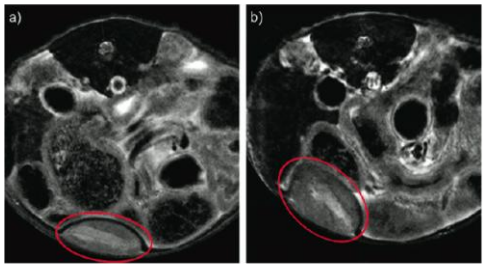

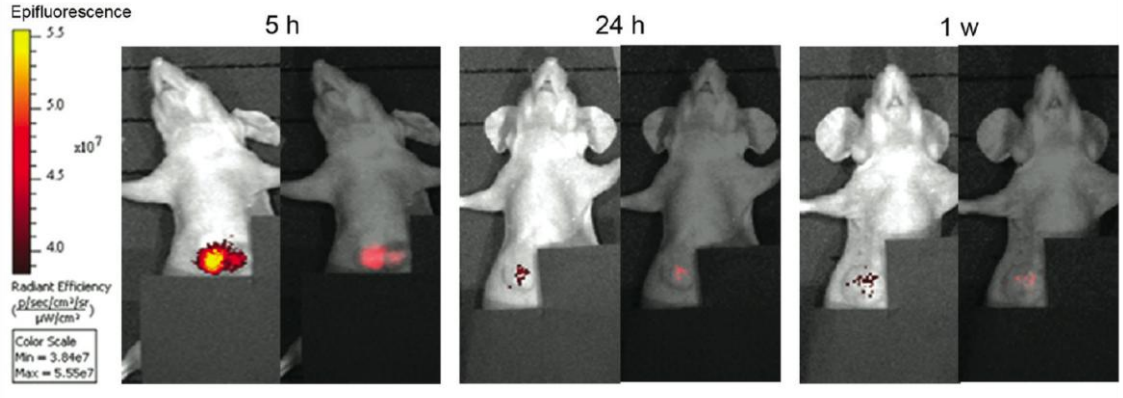

Figure 1.5: Monitoring MNPs uptake *in vivo* by MRI and Epifluorescence Camera.
(Upper inset) The axial T_2-weighted MR images have been obtained from MCF7 tumor-bearing mice (Left) before and (Right) 24 h after the injection of nanocrystals. The images, obtained by a T_2-mapping sequence, were acquired at 32.2 ms echo time.
(Lower Panels) CCD camera images of mice bearing MCF7 xenografts at 5 h, 24 h, and 1 week post-injection of fluorescent MNPs. Epifluorescence intensity images are reported on the left [57].

1.6. Silica based nanoparticles: general aspects

Proper silica nanoparticles (SiNPs) design and functionalization yields particularly stable colloids, even in physiological conditions, and provides them with multiple functions. A suitable choice of dyes could be coupled with SiNPs trough different synthetic strategies yielding a very bright and stable nanoconstruct. This subchapter discusses silica-based with a multi-component nanostructure involved in specific cellular applications, on which highly valued functions like light harvesting and signal amplification are needed.

In comparison to other NPs, SiNPs may appear mundane at first sight; however, from the practical viewpoint, this does not appear to be the case. In nanotechnologies, silica-based NPs have a dominant role because of their fundamental characteristics, such as size (generally from 5 to 1000 nm), unique optical properties, low density, adsorption capacity, capacity for encapsulation and low toxicity [58]. Consequently, intensive research has been performed to use SiNPs in diverse biomedical applications for diagnosing and controlling diseases, identifying and correcting genetic disorders and, most importantly, increasing longevity. Thus SiNPs offer considerable advantages and have opened new avenues of biomedical research in numerous leading edge applications, such as biosensors [59], controlled drug release and cellular uptake [60].

All these features are very appealing for analytical and quantitative applications in broad range of fields of great social and economical impact [61]. In this context, luminescent nanoparticles are particularly versatile components that have already been used in many fields thanks in part to their extreme brightness.

1.7. Controlled syntheses and properties of silica nanoparticles

Silica has attracted significant interest because its unique properties amenable for *in vivo* applications, such as hydrophilic surface favouring protracted circulation, versatile chemistry for surface functionalization and ease of large-scale synthesis with low cost production. In this context, in 2011 an Investigational New Drug Application for exploring an small nonporous silica NP for targeted molecular imaging of cancer was approved by the US Food and Drug Administration (FDA) for a first in human clinical trial [62], highlighting the great potential of clinical translation of SiNPs drug delivery platform.

1.7.1- Syntheses with size control

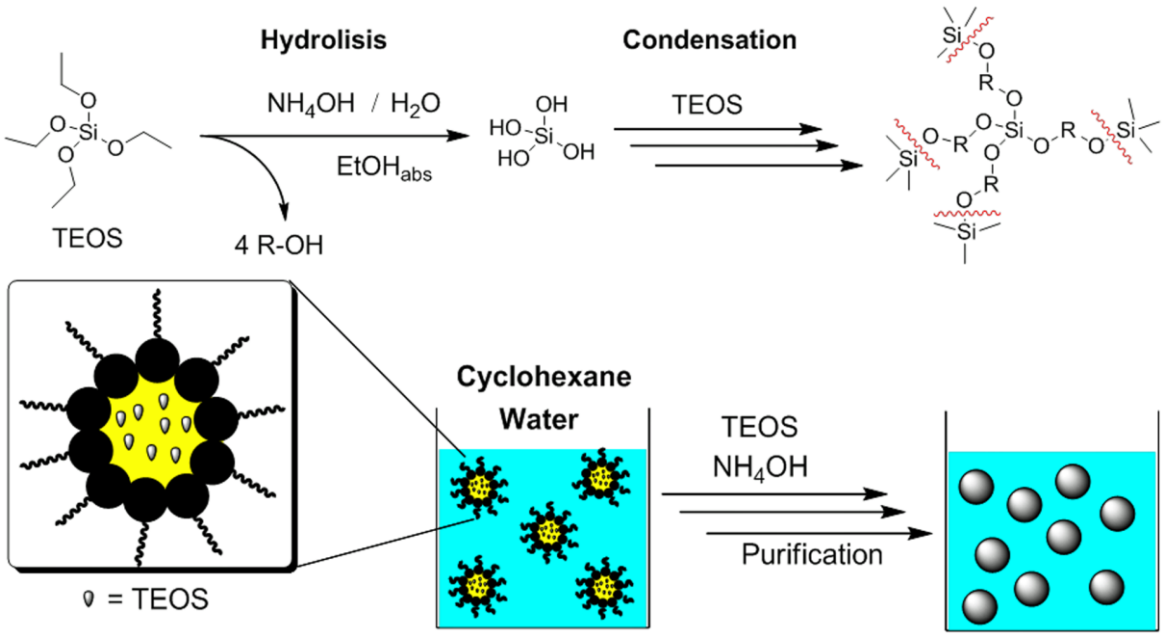

Figure 1.6: Strategies for the synthesis of silica nanoparticles.
(Upper Scheme) Stöber-van Blaaderen method; (Lower scheme) reverse microemulsion or water-in-oil method.

The first synthesis of size-controlled SiNPs has been reported by Stöber [63] in which monodisperse silica spheres with diameters ranging from 50 nm to 200 nm have been successfully prepared in a mixture of water, alcoholic solvent, ammonia, and tetra-alkoxysilane (Figure 1.6, upper scheme). The reaction parameters and

mechanism has been subsequently investigated [64,65], demonstrating that the growth proceeds through a surface reaction-limited condensation of hydrolyzed monomers or small oligomers. The particle nucleation proceeds through an aggregation process of siloxane substructures that is influenced strongly by the surface potential of particles and the ionic strength of the solvent. In this way, the rates of hydrolysis and condensation as a function of the mixture play the most important role in determining the final silica NP sizes [65]. The smallest homogeneous NPs that can be prepared by the Stöber method without aggregation have diameters of 20 nm and are more polydisperse (<10−20% St. Dev.) than 200 nm NPs (<3% St. Dev.).

Recently, in an important breakthrough 12 nm monodisperse SiNPs have been prepared in a heterogeneous reaction supplemented with L-lysine or L-arginine instead of ammonia (as a basic catalyst) in the aqueous phase and tetraethoxysilane in the organic layer [66].

In another modification organic modified SiNPs have been synthesized in an aqueous microemulsion supplemented with surfactants [67]; in this process the formulation of 20−300 nm silica NPs in a water-based emulsion has been accomplished with sodium dodecylbenzene sulfonate as surfactant. An alternative method for the production of uniform silica spheres involves the use of reverse microemulsions (Figure 1.6 lower scheme), in which particles form in inverse micelles compartmentalized by a suitable surfactant in a non−polar organic solvent. This synthetic approach works particularly well for SiNPs smaller than 100 nm in diameter [68] and permits eventually the encapsulation of active molecules in the reverse micelles during particle nucleation [69]. This methodology has also been widely used for coating other functional NPs with silica to produce core−shell structures [70].

1.7.2- Syntheses with shape control

The shape of SiNPs considerably affects their circulation into the bloodstream and tumor penetration behavior [71]; for example, it is noticeable that nanorods penetrate tumor tissues more rapidly than nanospheres likely because of improved transport through tumor vasculature pores [71]. These results suggest the importance of controlling the shape of SiNPs designed for nanomedicine to ameliorates their circulation and tissue penetration properties. Although there are many methods for the size-controlled preparation of silica nanospheres, only a handful of methods have been reported for the preparing of one-dimensional silica nanorods/nanotubes and other nanostructures [72−74]. The methods for shape control of silica NPs are mainly using templates and/or through polymer adsorption [72,74]. This facile shape control of SiNPs is important for essential studies of understanding the shape effect of nanomedicine in biological system and for optimizing these geometrical structures for improved diagnosis and therapy.

1.7.3- Syntheses with surface properties control

The surface properties of nanomaterials are known to play an important role in determining the interactions between particles and biological systems (*e.g.* cellular internalization and trafficking, biodistribution) [75]. Therefore, to achieve efficient disease targeting and improved therapy, it is fundamental to adjust the surface properties of desired nanomedicines. SiNPs have the advantage of easy surface modification via physical adsorption or covalent conjugation using siloxane chemistry; depending on the specific application, the surface property of silica NP might be easily tuned. For example the surface charge of SiNPs can be easily controlled with the addition of aminosiloxanes (3-aminopropyltriethoxysilane, 3-(trihydroxysilyl)-propylmethylphosphonate) or zwitterionic silanes, after the basic formulation of

SiNPs [76]. As a result, SiNPs with positive, negative, or both (zwitterionic surface) could be prepared [77]; in addition, many other different functional groups could be grafted to these surfaces using similar techniques because a large number of these siloxane compounds are commercially available [78,79].

SiNPs surface have been also functionalized with polymers either chemically, through covalent bonds, or physically, by physical adsorption [80]; the former is preferential due to stable covalent bonds between the two counterparts. For example, polyethylene glycol (PEG) has been conjugated to SiNPs surface via a ‘‘grafting-to’’ method [81] or, on the other hand, with a ‘‘grafting-from’’ [82].

The surface of silica NPs can also be functionalized with various targeting ligands for example, antibodies or aptamers; but detailed information will be discussed in following sections of this thesis according to the aims of my research study.

1.8. Applications of Silica Nanoparticles in Biomedical Research

Going into the concept of living cells and the whole body is very important to achieve a better understanding of the mechanism of NPs interacion and requires specialized imaging techniques. Functionalized silica nanoconstructs have the potential to match such needs through real-time and non-invasive visualization of biological events *in vivo*; in literature are present different studies talking about SiNPs as a platform for nanomedicine applications [83,84]. In addition, the possibility to incorporate SiNPs doped with fluorescent dyes appears to be an ideal and flexible program for developing fluorescence imaging techniques applied in living cells and the whole body [85]. It is possible to select and incorporate different dyes inside the silica matrix either noncovalently or covalently. All these techniques form the functionalized hybrid SiNPs, which support multiplex labeling and ratiometric sensing in living systems; since that the silica matrix protects its content from the external environment and degradation factors, this system enhances the photostability and biocompatibility of SiNPs as fluorescent probes.

1.8.1- Labeling and tracking cell surface receptors

In situ labeling and tracking cell surface receptors with high sensitivity and selectivity holds great potential for the diagnosis of early stage diseases and the monitoring of some life processes. By utilizing the enhanced properties of dye-doped SiNPs, researchers have been developed an immunofluorescence labeling and tracking technique platform for cell surface receptors involved in several diseases. Based on the specificity associated with the ligand–receptor recognition process, fluorescent SiNPs has been covalently conjugated with different ligands and then

applied to label antigens or receptors in several cell lines, such as HepG liver cancer cells [86], MDA-MB231, and MCF7 breast cancer cells [87].

Similarly, some cellular processes have also been monitored by tracking cell membrane surface receptors using biofunctionalized SiNPs [88]; for example, the externalization of phosphatidylserine, from the inner to the outer membrane, has been used to detect early stage apoptosis since that it is a major event in the apoptotic process. In this work [88], a novel fluorescent silica bioprobe based on Rhodamine-doped SiNPs modified with Annexin V has been explored, which, in addition of specifically labeling early stage apoptotic cells, it could but also track the physiological change process of phosphatidylserine. With the extension of culture time with paclitaxel (a mitotic inhibitor used in cancer chemotherapy), the number of the apoptotic cells labeled by SiNPs increased ever more. Meanwhile, red fluorescence of the SiNPs on the outer membrane of the recognized apoptotic cells changed from weak to strong, from partially to completely surrounding the cell membrane (Figure 1.7), which revealed a gradual translocation process of phosphatidylserine in the early stage apoptotic cell membrane.

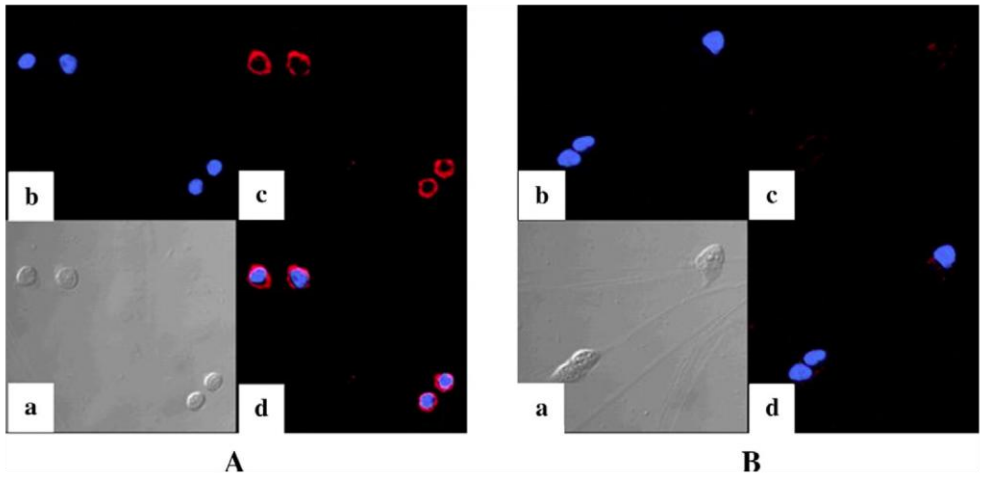

Figure 1.7: Dye doped SiNPs for cellular labeling and tracking.
Confocal microscopy images of (A) Early-stage apoptotic MCF-7 cells induced with paclitaxel and (B) MCF-7 cells untreated with paclitaxel, incubated with dye-SiNPs conjugated to Annexin V and then stained with Hoechst33258. Subpanels: a) optical image; b), c) are fluorescence images of Hoechst33258 and dye-SiNPs, respectively; d) is the merged images of b and c. [88]

1.8.2- Intracellular sensing

Dye-doped SiNPs has been adopted for real-time sensing of intracellular physiological parameters change [89]. In this work, a ratiometric pH nanosensor based on two-fluorophore-doped SiNPs containing a pH-sensitive indicator (FITC) and a reference dye (RuBpy) for noninvasive monitoring of intracellular pH changes (Figure 1.8). The pH nanosensor with an average diameter of 42 nm could easily be taken up by cells and exhibited excellent pH sensitivity, reversibility, and a dynamic range from pH = 4.0 to pH = 7.0 for biological studies. In this way, this novel pH nanosensor could be used in real time and with high pH sensitivity to monitor both lysosomal pH changes and the intracellular acidification occurring with early stages of apoptosis.

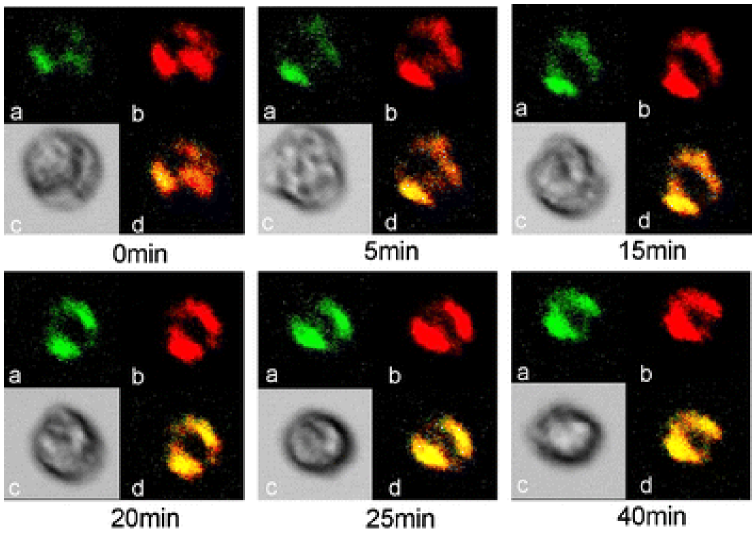

Figure 1.8: Cellular sensing using dye-doped SiNPs.
Change in lysosomal pH, as monitored by 2dyes-SiNPs, in murine macrophages after treatment with chloroquine. In a, lysosomal pH was plotted against time for increasing chloroquine concentrations. A) represents a control without chloroquine treatment. B) represent the effects of increasing conc. of chloroquine, respectively, on the lysosomal pH. Images labeled C) represent bright-field images of macrophages, and those labeled D) are images merges of A) and B) of chloroquine [89].

1.8.3- Small-molecule drug delivery and controlled release

Small active molecules might be encapsulated in the silica matrix during nanoparticle nucleation [90] or, in contrast, they could be linked covalently to the silica surface [91]. In the former strategy, as described before, SiNPs are formed by a

two-step inorganic poly-condensation reaction consisting of hydrolysis and condensation; at this stage, adding bioactive molecules during oxidative backbone formation facilitates their encapsulation within the oxide matrix, leading to the production of a composite nanomaterial with the active ingredients trapped inside the silica matrix; in this way, the release occurs by a combination of diffusion of the encapsulated molecules and dissolution of the silica matrix. According to this, there are many studies in literature describing the silica degradation over time under physiological conditions [92].

In order to increase the drug load amount, another kind of SiNPs, synthesized with large mesoporous, has been selected to fabricate stimuli-responsive intracellular release systems [93]. Recently have been constructed several controlled release systems that could be triggered by a range of stimuli, such as light, pH, and redox. As a title of example example, in the work cited above [93] by grafting a duplex DNA with a C–Ag^{+}–C structure as a smart molecule-gated switch, the authors have designed a mesoporous silica thiol-responsive system and they investigated its intracellular release behavior. In this way they demonstrated that the carriers could be internalized remarkably into the cells by endocytosis in a couple of hours and distributed predominantly into lysosomes; later on, the entrapped cargo molecule could be released from the pores, triggered by intracellular thiol-containing molecules, such as reduced L-Glutathione and L-Cystine.

For the latter strategy, various covalent conjugation strategies for coupling drugs on SiNPs have been explored [94,95]. Recently, Cheng and co-workers have developed a potentially clinically applicable drug-silica nanoconjugate with excellent control over particle size and drug loading and release profile [96]. The multialkoxysilane-coupled with different drugs have been synthesized with a

degradable ester linker between drug and trialkoxysilane group and then condensed with tetraalkoxysilane to allow the drug molecules to be incorporated into the resulting silica NPs; in this way, drugs can be released through the cleavage of the ester linker. In this paper several anticancer drugs (*e. g.* camptothecin, paclitaxel, and docetaxel) and fluorescence dyes (*e.g.* rhodamine, IR783) conjugated silica NPs with precisely controlled sizes can be prepared similarly (Figure 1.9).

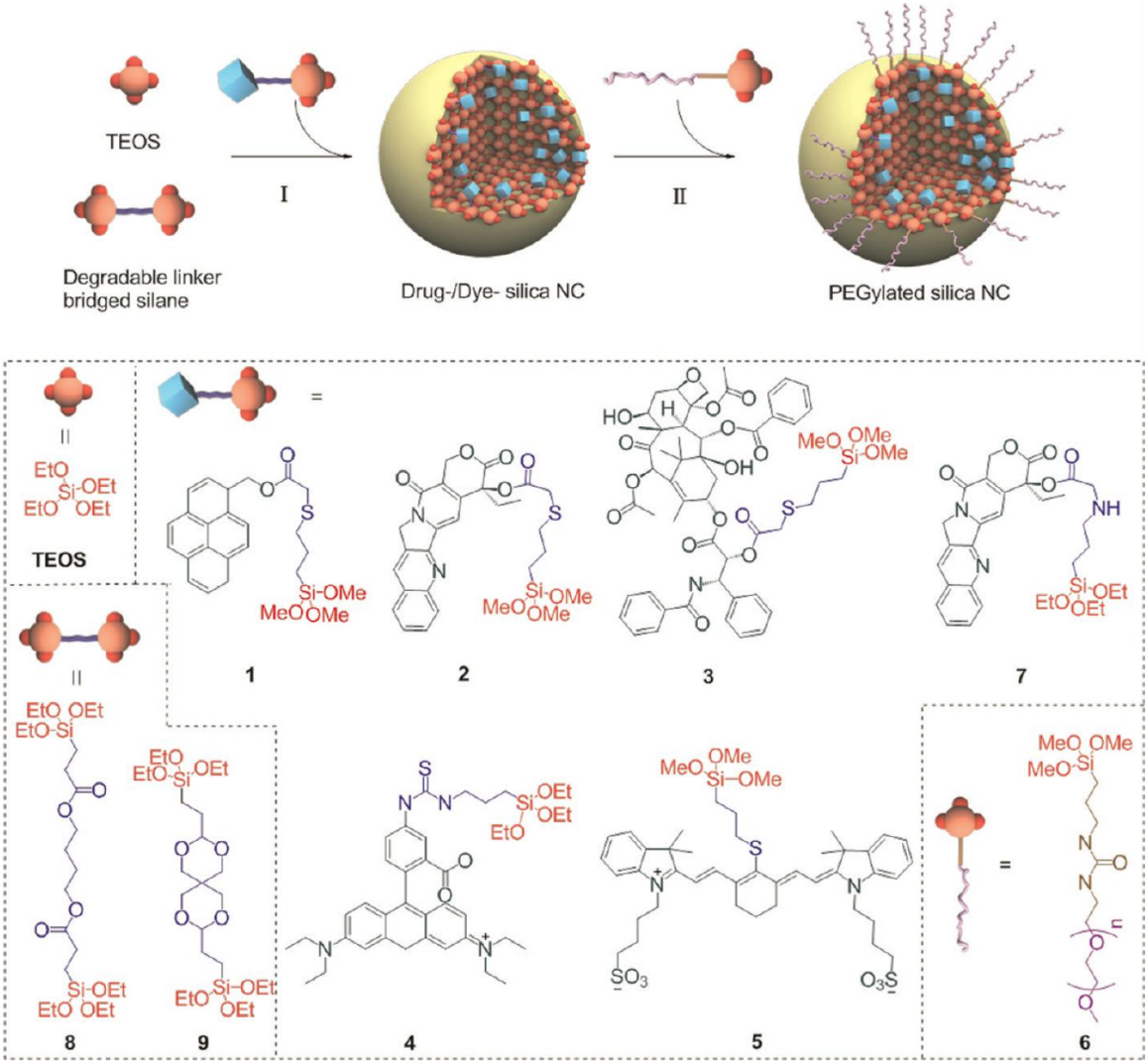

Figure 1.9: Drug loaded dye-doped SiNPs.
Size controlled drug−silica nanoconjugates for cancer therapy: schematic view showing the preparation of drug/dye−silica nanoparticles accomplished with anticancer drugs (camptothecin, paclitaxel) or fluorescence dyes (rhodamine, IR783); all nanoconjugates have been prepared and PEGylated *in situ* [96].

In conclusion, Silica offers a promising alternative to organic drug delivery systems and exhibit many unique properties, such as highly controllable size and shape. Nonporous silica NPs have found numerous biomedical applications for the delivery of drugs, proteins, and genes and for molecular imaging. However, before SiNPs can be used routinely in clinic, some major challenges must be overcome, including the need for improved drug incorporation efficiency, spatial and temporal control of drug release, highly efficient targeting of disease sites, scalable manufacturing, long-term stability, and well-understood biocompatibility and potential toxicity. Organo-silica hybrid NPs are expected to have both unique properties of SiNPs due to their functionalities. Furthermore, the possibility of directing SiNPs specifically to disease sites by means of targeting ligands, such as antibodies and aptamers, also needs to be further explored within a complete understanding of the toxicity profile and potential environmental impact of SiNPs. This hurdle will need to be a prerequisite for future clinical applications and safety when using these nancomplexes.

Related References

[1] Ladj, R.; Bittar, A.; Eissa, M.; et al.; *J. Mater. Chem. B*. **2013**, *1*, 1381–1396.

[2] Swierczewaska, M.; Lee, S. and Chen, X.; *Mol. Imaging*. **2011**, *10*, 3–16.

[3] Peng, G.; Tisch, U.; Adams, O.; et al.; *Nat. Nanotech*. **2009**, *4*, 669–673.

[4] Yeom, S. H.; Kang, B. H.; Kim, K. J. and Kang, S. W.; *Front. Biosci.* (Landmark Ed). **2011**, *16*, 997–1023.

[5] Nam, J.; Won, N.; Bang, J.; et al.; *Adv. Drug Deliv. Rev.* **2013**, *65*, 662–648.

[6] Hyon, B. N.; Song, I. C. and Hyeon, T.; *Adv. Mater.* **2009**, *21*, 2133–2148.

[7] Tan, S.; Li, X.; Guo, Y. and Zhang, Z.; *Nanoscale.* **2013**, *5*, 860–872.

[8] Kim, C. S.; Tonga, G. Y.; Solfiell, D. and Rotello, V. M.; *Adv. Drug Deliv. Rev.* **2013**, *65*, 93–99.

[9] Huang, H. C.; Barua, S.; Sharma, G.; Dey, S. K. and Rege, K.; *J. Control Release.* **2011**, *155*, 344–357.

[10] Sapsford, K. E.; Algar, W. R.; Berti, L.; et al.; *Chem. Rev.* **2013**, *113*, 1904–2074.

[11] Albanese, A.; Tang, P. S. and Chan, W. C. W.; *Annu. Rev. Biomed. Eng.* **2012**, *14*, 1–16.

[12] Sperling, R. A.; Gil, P. R.; Zhang, F.; Zanella, M. and Parak, W. J.; *Chem. Soc. Rev.* **2008**, *37*, 1896–1908.

[13] Bourinnet, P.; Bengele, H. H.; Bonnemain, B.; et al.; *Invest. Radiol.* **2006**, *41*, 313–324.

[14] Hao, R.; Xing, R.; Xu, R.; Hou, Y.; Gao, S. and Sun, S.; *Adv. Mater.* **2010**, *22*, 2729–2742.

[15] Jang, J.; Nah, H.; Lee, J. H.; Moon, S. H.; Kim, M. G. and Cheon, J.; *Angew. Chem. Int. Ed.* **2009**, *48*, 1234–1238.

[16] Figueroa, A.; Di Corato, R.; Manna, L. and Pellegrino, T.; *Pharm. Res.* **2010**, *62*, 126–143.

[17] O'Handley, R.C.; "Modern Magnetic Materials: Principles and Applications" **2000**, Publisher Wiley & Co. ©, New York (USA).

[18] Figueroa, A.; Di Corato, R.; Manna, L. and Pellegrino, T.; *Pharm. Res.* **2010**, *62*, 126–143.

[19] Huber, D. L.; *Small.* **2005**, *1*, 482–501.

[20] Skorvanek, I. and O'Handley, R. C.; *J. Magn. Magn. Mater.* **1995**, *140*, 467–469.

[21] Ling, D. and Hyeon, T.; *Small.* **2013**, *9*, 1450–1466.

[22] Massart, E.; *IEEE Trans. Magn.* **1981**, *17*, 1247–1248.

[23] Jolivet, J. P.; Tronc, E. and Chaneac, C.; *C. R. Chim.* **2002**, *5*, 659–664.

[24] Smolensky, E. D.; Park, H. E.; Berquò T. S. and Pierre, V. C.; *Contrast Media Mol. Imaging.* **2011**, *6*, 189–199.

[25] Kumpfer, B. M.; Shinoda, K.; Jeyadevan B. and Kennedy, I. M.; *J. Aerosol Sci.* **2010**, *41*, 257–265.

[26] De Castro, V.; Benito, G.; Hurst, S.; Serna, C. J.; Morales, M. P. and Veintemillas-Vergaguer, S.; *J. Nanosci. Nanotechnol.* **2008**, *8*, 2458–2462.

[27] Hyeon, T.; Lee, S. S.; Park, J.; Chung, Y. and Na, H. B.; *J. Am. Chem. Soc.* **2001**, *123*, 12798–12801.

[28] Thimmaiha, S.; Rajamanthi, M.; Singh, M.; et al.; *J. Mater. Chem.* **2001**, *11*, 3215–3221.

[29] Bronstein, L. M.; Huang, X.; Retrum, J.; Schmucker, A.; et al.; *Chem. Mater.* **2007**, *19*, 3624–3632.

[30] Gage, S. H.; Stein, B. D.; Nikoshvili, L. Z.; et al.; *Langmuir.* **2013**, *29*, 466–473.

[31] Luigjes, B.; Woudenberg, S. M. C.; de Groot, R.; et al.; *J. Phys. Chem. C.* **2011**, *115*, 14598–14605.

[32] Park, J.; An, K.; Hwang, Y.; Park, J. G.; Noh, H. J.; Kim, J. Y.; Park, J. H.; Hwang, N. and Hyeon, T.; *Nat. Mater.* **2004**, *3*, 891–895.

[33] Teng, X. and Yang, H.; *J. Mater. Chem.* **2004**, *14*, 774–779.

[34] Jana, N, R.; Chen, Y.; and Peng, X.; *Chem. Mater.* **2004**, *16*, 3931–3935.

[35] Huang, J. H.; Parab, H. J.; Liu, R. S.; et al.; *J. Phys. Chem. C.* **2008**, *112*, 15684–15690.

[36] Kim, B. H.; Lee, N.; Kim, H.; et al.; *J. Am. Chem. Soc.* **2011**, *133*, 12624–12631.

[37] Brown, M. A. and Senelka, R. C. "MRI: Basic Principles and Applications" **2010**, Publisher Wiley-Blackwell & Co. ©, New York (USA).

[38] Jung, C. W. and Jacobs, P.; *Magn. Reson. Imaging.* **1995**, *13*, 661–674.

[39] Wang, Y. X.; Hussain, S. M. and Krestin, G. P.; *Eur. Radiol.* **2001**, *11*, 2319–2331.

[40] Wunderbaldinger, P.; Josephson, L. and Weissleder, R.; *Acad. Radiol.* **2002**, *9*, S304–S306.

[41] Josephson, L.; Tung, C. H.; Moore, A. and Weissleder, R.; *Bioconjugate Chem.* **1999**, *10*, 186–191.

[42] Park, J.; Lee, E.; Hwang, N. M.; et al.; *Angew. Chem. Int. Ed.* **2005**, *44*, 2872–2877.

[43] Ho, D.; Sun, X. and Sun, S.; *Acc. Chem. Res.* **2011**, *44*, 875–882.

[44] Yoo, D.; Lee, J. H.; Shin, T. H. and Cheon, J.; *Acc. Chem. Res.* **2011**, *44*, 863–874.

[45] Huang, H. C.; Barua, S.; Sharma, G.; Dey, S. K. and Rege, K.; *J. Control Release.* **2011**, *155*, 344–357.

[46] Dilnawaz, F.; Singh, A.; Mohanty, C. and Sahoo, S. K.; *Biomaterials.* **2010**, *31*, 3694–3706.

[47] Nasongkla, N.; Bey, E.; Rey, J.; et al.; *Nano Lett.* **2006**, *6*, 2427–2430.

[48] Hwu, J. R; Lin, Y. S.; Josephrajan, T.; et al.; *J. Am. Chem. Soc.* **2009**, *131*, 66–68.

[49] Cheng, K.; Peng, S.; Xu, C. and Sun, S.; *J. Am. Chem. Soc.* **2009**, *131*, 10637–10644.

[50] Perez, J. M.; Grimm, J.; Josephson, L. and Weissleder, R.; *Neoplasia.* **2008**, *10*, 1066–1072.

[51] Grimm, J.; Perez, J. M.; Jospehson, L. and Weissleder, R.; *Cancer Res.* **2004**, *64*, 639–643.

[52] Colombo, M.; Ronchi, S.; Monti, M.; Corsi, F.; Trabucchi, E. and Prosperi, D.; *Anal. Biochem.* **2009**, *392*, 96–102.

[53] El-Boubbou, M.; Zhu, D. C.; Vasileiou, C.; Borhan, B.; Prosperi, D. and Huang, X.; *J. Am. Chem. Soc.* **2010**, *132*, 4490–4499.

[54] Lee, J. H.; Jang, J. T.; Choi, J. S.; et al.; *Nat. Nanotech.* **2011**, *6*, 418–422.

[55] Zhao, Q.; Wang, L.; Cheng, R.; et al.; *Theranostic.* **2012**, *2*, 113–121.

[56] Jordan, A.; Scholtz, R.; Maier-Hauss, K.; et al.; *J. Neuro. Oncol.* **2006**, *78*, 7–14.

[57] Corsi, F.; Fiandra, L.; De Palma, C.; et al.; *ACS Nano.* **2011**, *5*, 6383–6393.

[58] Halas, N. J.; *ACS Nano.* **2008**, *2*, 179–183.

[59] Tallury, P.; Payton, K. and Santra, S.; *Nanomedicine.* **2008**, *3*, 579–592.

[60] Chu, Z.; Huang, Y.; Tao, Q. and Li, Q; *Nanoscale.* **2011**, *3*, 3291–3299.

[61] Prodi, L.; *New. J. Chem.* **2005**, *29*, 20–31.

[62] Benezra, M.; Penate-Medina, O.; Zanzonico, P. B.; et al.; *J. Clin. Invest.* **2011**, *121*, 2768–2780.

[63] Stöber, W.; Fink, A.; Bohn, E; *J. Colloid. Interface. Sci.* **1968**, *26*, 62–69.

[64] Bogush, G. H.; Tracy, M. A.; Zukoski, C. F.; *J. Non-Cryst. Sol.* **1988**, *104*, 95–106.

[65] Van Blaaderen, A.; Van-Geest, J. and Vrij, A.; *J. Colloid. Interface Sci.* **1992**, *154*, 481–501.

[66] Yokoi, T.; Wakabayashi, J.; Otsuka, Y.; et al.; *Chem. Mater.* **2009**, *21*, 3719–3729.

[67] Bharali, D. J.; Klejbor, I.; Stachowiak, E. K.; et al.; *Proc. Natl. Acad. Sci.* **2005**, *102*, 11539–11544.

[68] Finnie, K. S.; Bartlett, J. R.; Barbè, C. J. A. and Kong, L.; *Langmuir.* **2007**, *23*, 3017–3024.

[69] Tang, L.; Fan, T. M.; Borst, L. B. and Cheng, J.; *ACS Nano.* **2012**, *6*, 3954–3966.

[70] Guerrero-Martinez, A.; Perez-Juste, J. and Liz-Maran, L. M.; *Adv. Mater.* **2010**, *22*, 1182–1195.

[71] Chauan, V. P.; Popovic, Z.; Chen, O.; Cui, J.; Fukumura, D.; Bawendi, M. G. and Jain, R. K.; *Angew. Chem. Int. Ed.* **2011**, *50*, 11417–11420.

[72] Kuijk, A.; van Blaarderen, A. and Imhof, A.; *J. Am. Chem. Soc.* **2011**, *133*, 2346–2349.

[73] Gao, C.; Lu, Z. and Yin, Y.; *Langmuir.* **2011**, *27*, 12201–12208.

[74] Liu, H. Y.; Chen, D.; Li, L. L.; Liu, T. L.; Tan, L. F. and Tang, F. Q.; *Angew. Chem. Int. Ed.* **2011**, *50*, 891–895.

[75] Kim, B.; Han, G.; Toley, B. J.; Kim, C. K.; Rotello, V. M. and Forbes, N. S.; *Nat. Nanotechnol.* **2010**, *5*, 465–472.

[76] Graf, C.; Gao, Q.; Schütz, I.; et al.; *Langmuir.* **2012**, *28*, 7598–7613.

[77] Rosen, J. E. and Gu, F. X.; *Langmuir.* **2011**, *27*, 10507–10513.

[78] Estephan, Z. G.; Jaber, J. A. and Schlenoff, J. B.; *Langmuir.* **2010**, *26*, 16884–16889.

[79] He, X. X.; Nie, H. L.; Wang, K. M.; Tan, W. H.; Wu, X.; and Zhang, P. F.; *Anal. Chem.* **2008**, *80*, 9597–9603.

[80] Karakoti, A. S.; Das, S.; Thevulthasan, S.; and Seal, S.; *Angew. Chem. Int. Ed.* **2011**, *50*, 1980–1994.

[81] Rio-Echevarria, I. M.; Selvestrel, F.; Segat, D.; et al.; *J. Mater. Chem.* **2010**, *20*, 2780–2787.

[82] Ohno, K.; Akashi, T.; Tsujii, Y.; Yamamoto, M. and Tabata, Y.; *Biomacromolecules.* **2012**, *13*, 927–936.

[83] Bitar, A.; Ahmad, N. M.; Fessi, H. and Elassari, A.; *Drug Discov. Today* **2012**, *17*, 1147–1154.

[84] Tang, L. and Cheng, J.; *Nano Today* **2013**, *8*, 290–312.

[85] Wang, K.; He, X.; Yang, X. and Shi, H.; *Acc. Chem. Res.* **2013**, *7*, 1367–1376.

[86] Bonacchi, S.; Genovese, D.; Juris, R.; Montalti, M.; Prodi, L.; Rampazzo, E. and Zaccheroni, N.; *Angew. Chem. Int. Ed.* **2011**, *50*, 4056–4066.

[87] He, X.; Duan, J.; Wang, K.; Tan, W.; Lin, X. and He, C.; *J. Nanosci. Nanotechnol.* **2004**, *4*, 585–589.

[88] Shi, H.; He, X.; Wang, K.; et al.; *Nanomed: Nanotechnol., Biol., Med.* **2007**, *3*, 266–262.

[89] Peng, J.; He, X.; Wang, K.; Tan, Wl.; Wang, Y. and Liu, Y.; *Anal. Bioanal. Chem.* **2007**, *388*, 645–654.

[90] He, X. X.; Hai, L.; Su, J.; Wang, K. M. and Wu, X.; *Nanoscale.* **2011**, *3*, 2936–2842.

[91] Stevens, E. V.; Carpenter, A. W.; Shin, J. H.; Liu, J. S.; Der, C. J.; and Schoenfisch, M. H.; *Mol. Pharm.* **2010**, *7*, 755–785.

[92] Mahon, E.; Hristov, D. R. and Dawson, K. A.; *Chem. Commun.* **2008**, *8*, 2483–2487.

[93] He, D.; He, X.; Wang, K.; Chen, M.; Cao, J. and Zhao, Y.; *J. Mater. Chem.* **2012**, *22*, 14715–14721.

[94] Georgelin, T.; Bombard, S.; Siaugue, J. M. and Cabuil, V.; *Angew. Chem. Int. Ed.* **2010**, *49*, 8897–8901.

[95] Della Rocca, J.; Huxford, R. C.; Costock-Duggan, E. and Lin, W.; *Angew. Chem. Int. Ed.* **2011**, *50*, 10330–10334.

[96] Tang, L.; Fan, F. M.; Borst, L. B. and Cheng, J.; *ACS Nano.* **2012**, *6*, 3954–3966.

Chapter II

Organic Nanoparticles

Contents

2.1. Introduction

Nanotechnology has the potential to transform the pharmaceutical field by offering the ability to encapsulate and strategically deliver drugs, proteins, nucleic acids, or vaccines thus improving their therapeutic index. Encapsulating pharmaceuticals in nano- and micro-particles offers a solution to multiple problems in medicine underscored by the relatively new boom in interests from chemist and biologists. NPs can be made from various materials including lipids [1]; inorganic materials such as gold, carbon, and iron oxide [2]; proteins [3]; and polymeric systems [4]. Lipids, which are widely used and well characterized in carrier systems, are especially advantageous for targeting, because their dynamic nature allows clustering of peptides or other ligands, enhancing the affinity of the interaction with target cells; nevertheless, this same dynamic nature also makes them less stable than other carriers. Inorganic materials provide the advantage of stability; but again,

this strength is also a disadvantage, especially in the case of gold, as their retention in the body could limit clinical applications.

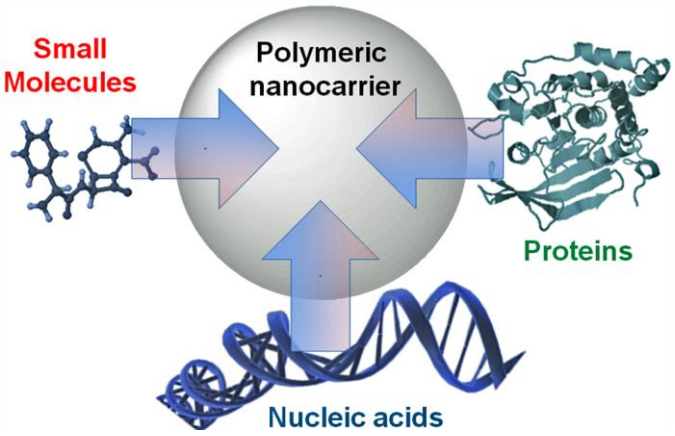

Figure 2.1: Polymeric nanoparticles in drug delivery. Small polymeric delivery systems in the nano and micro range can be used to deliver diverse therapeutics, including small molecules, proteins, nucleic acids, and diagnostic agents. The organic polymeric layer should prevent drug degradation, increase clearance and reduce undesired side effects.

Biodegradable polymeric nanoparticle systems offer many advantages for biocompatibility, superior controlled release, synthesis size control, and low toxicity. The ability of polymers to degrade into safe small components that can be cleared by the body is almost as important as the ability to formulate the particles. Biodegradable polymeric nanoparticles can be formulated in a variety of ways and modified to easily encapsulate, embed within, or bind drugs to the exterior of nanoparticles (Figure 2.1). For these reasons, this chapter is focused on polymeric nanoparticles as a possible platform to build new and more relevant carriers to deliver drugs with a particular attention to the treatment of mammary basal-cells carcinoma. These organic particles include PLGA [poly(lactide-co-glycolide)] nanoparticles, trough which I could develop part of my research of PhD thesis work dealing with drug delivery systems.

2.2. Polymeric nanoparticles: “playing” with chemistry

2.2.1 Ligands and antibodies

Nanotechnology field is starting to evolve and take advantage of biological, chemical, and physical properties. In this framework the chemical targeting of NPs involves multiple advanced strategies that may include materials that are cellular environment responsive. These multiple strategies can be applied independently or combined to improve therapeutic delivery.

Nanoparticle targeting with antibodies or ligands has been greatly applied in cancer and immunological diseases. For instance, several strategies take advantage of popular cell surface targets that are overexpressed by cancer cells. The most common targets include the epidermal growth factor receptor (EGFR), vascular endothelial growth factor, folate receptor, the transferrin receptor, and several glycoproteins, among others. EGFR, a receptor highly expressed in breast cancer, has been used with PLGA nanoparticles containing rapamycin that were surface-conjugated with an EGFR antibody [5]. Although in vitro results usually do not reflect what happens *in vivo*, current proof-of-concept experiments support the notion that targeting will help improve therapeutic delivery. Antibody-conjugated nanoparticles can also be used for the targeted delivery of nucleic acids. The use of siRNA as a therapeutic has shown a lot of promise, but the main obstacle is preventing it from degrading upon delivery and improved targeting. CALAA-01, a nanoparticle formulation to deliver siRNA in tumor cells, is the first nanoparticle of its type to enter human clinical trials [6] The nanoparticle consists of a cyclodextrin engulfed into a polymer and surrounded by PEG chains. Developments resulting from CALAA-01 clinical trials will help pave the way when considering the design, safety, and efficacy of targeted siRNA delivery systems

2.2.2 Stimuli−responsive nanocarriers

Using biological cues to creatively target pharmacological agents is always a good method to improve specificity and minimize side effects. An alternative method is to combine bioresponsive materials with internal or external physical *stimuli* as summarized in Table 2.

Trigger release	Target	Types of polymer	[Refs]
pH	Acidic compartments found at physiological pathological tissues (tumor sites) or within cells in the endosomes	Polyacrylamide	[7]
Thermal	Heat applied external or from physiologically changes	poly(*N*-isopropylacrylamide-*co*-((2-dimethylamino)ethylmethacrylate))	[8]
Light	External applied stimuli	Amphiphilic Poly(ethylene oxide)-poly(2-nitrobenzyl methacrylate)	[9]
Redox	Regions where reactive oxidative and reductive species are abundant (e.g. inflammation and tumor sites)	poly-(1,4-phenyleneacetone dimethylene thioketal)	[10]
Enzyme	Regions of high protease expression such as cancerous tissues	Polymers coupled with cell-penetrating peptides	[11]

Table. 2: Examples of stimuli responsive strategies.

pH-responsive systems can be applied for external (tumor sites) and internal (endosomes) cellular release. The extracellular matrix of tumor sites has a relatively low pH (pH = 6.5) due to the cell's high metabolic activity and limited oxygen availability; in addition, cancer cells respond to this microenvironment by undergoing anaerobic glycolysis resulting in higher production of lactic acid. Several studies have successfully developed and demonstrated the potential of using this particular pathological stimuli to deliver encapsulated drugs [7]. NPs can also be triggered to release drugs once they are taken up by cells *via* endocytosis [12]. As NPs are taken up by cells, they progress through the endocytic pathway and eventually to the

lysosome; the early endosome begins to acidify within minutes and progressively becomes more acidic as it moves toward the lysosomes where the pH can be as low as 4. The pH difference within endosomes is an attractive system because particles can be maintained in stable conditions until they enter the targeted cells. In addition, changes in ionic strength causes a proton "sponge" effect in certain cationic buffering polymers that can allow the endosome to release the encapsulated molecule (Figure 2.2).

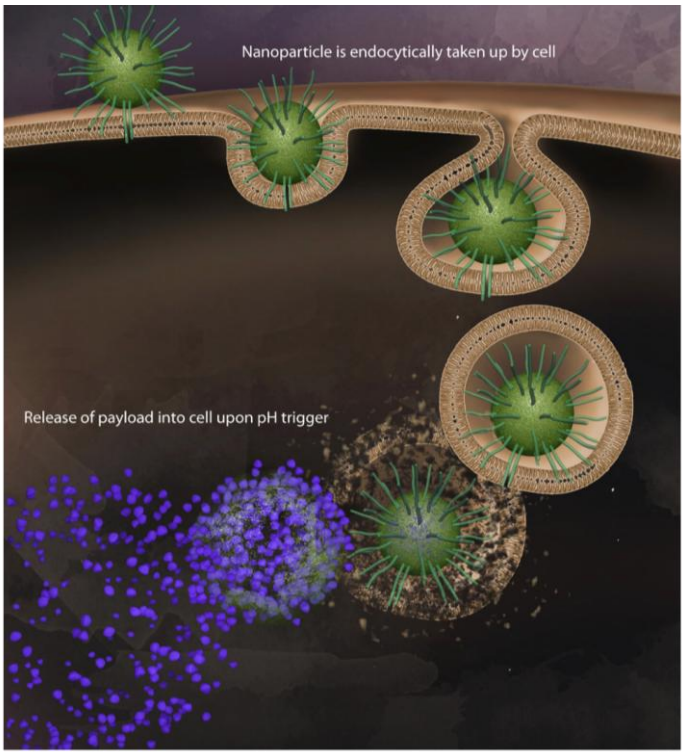

Figure 2.2: pH triggered release.
Polymeric pH-sensitive systems allow efficient entry into cells followed by cargo release in response to acid conditions of the endosome. Thus the drug is release and can accumulate into the cytoplasm of the cell exploiting its effect.

Thermally responsive polymeric nanoparticles can be used to take advantage of local temperature differences or via external heat application. NPs that contain temperature-sensitive polymers can shrink or expand when triggered by heat; indeed the balance between the hydrophobic and hydrophilic segments determines the sensitivity of heat. Recent *in vivo* studies are also beginning to show some promising results to treat cancer using thermosensitive nanoparticles based on PNIPAM, poly(N-isopropylacrylamide-methacrylate) copolymers [8].

Light-activated particles are created using optically active substances such as functional dyes, metals, and light-sensitive polymers that are capable of degrading or releasing their cargo [9]; these systems can incorporate a chromophore that can

absorb light, which is then dissipated locally as heat, ultimately altering the swelling of the particle. There are limitations, however, because most visible light cannot penetrate deep into tissue and the conversion of light into thermal energy is usually slow.

Furthermore, in cancer therapeutics tumor expansion followed by metastasis requires a breakdown of extracellular matrix by proteases. Matrix metalloproteases 2 and 9 are highly expressed in the tumor microenvironment and promote angiogenesis for the tumor. These proteases usually cleave a conserved peptide sequence and, for this reason, many polymeric nanocarriers have been developed to take advantage of this specific protease activity and implement a short cleavable sequence to target release of cargo or activate an additional targeting module such as a cell-penetrating peptide [11] Unfortunately, the tumor protease targeting activity revealed that metalloproteinase targeting is not as efficient is most likely due to cleavage in the vascular compartment rather than one's in tumor site; this is why it is so important enhanced this targeting within cell-penetrating peptides [11].

Finally, since redox changes associated with tumor cytoplasmatic compartment have been identified as a viable biomarker for tumor progression and cancer drug resistance, reductive species over-expressed in tumor microenvironments, such as glutathione, provide another way for selective tumor targeting. Hence, bioreductive polymers based for example on trimethyl-locked benzoquinone can be chemically transformed into lactone triggered by two-electron reduction [13]. From this rationale, prodrugs and bio-imaging molecules have been based on the bioreductive cleavage of the polymer by reductive molecules and suggested for solid tumor-selective drug delivery and imaging triggered by redox changes occurring in tumor hypoxia.

2.3. PLGA nanoparticles in therapeutics

PLGA (Poly(lactic-co-glycolic acid) is nowadays one of the most successfully biodegradable polymers on the nanomedical market because its natural decomposition leads to the production of metabolite monomers such as lactic acid and glycolic acid. Because these two monomers are easily metabolized by the body through the Krebs cycle, only minimal systemic toxicity is usually associated with the use of PLGA as drug delivery systems [14]. The chemical nature of this polymer gives an amphiphilic character because of the hydrophilic branch of poly(lactide) and the other hydrophobic branch composed by poly(glicolide); this structural property allows the formation of spherical nanomicelles in aqueous solution, usually in a range between 100 and 500 nm according to the chemical synthetic route adopted. In addition, it is possible to encapsulate both hydrophobic and hydrophilic molecules with the aim to increase time−dependent drug bioavailability and preferential transport.

PLGA NPs are internalized in cells partly through fluid phase pinocytosis and also through clathrin-mediated endocytosis. NPs rapidly escape the endo-lysosome apparatus and enter the cytoplasm within few time of incubation (Figure 2.3). This facilitates interactions of nanoparticles with the vesticular membranes leading to transient and localized destabilization of the membrane, resulting in the escape of nanoparticles into the cytosol [15]. The polymer degradation time can differ from days, several months or several years, depending on the molecular weight and copolymer ratio [16,17]; for example PLGA is usually identified by the monomers ratio used (50:50 identifies a copolymer composed by 50% lactic acid and 50% glycolic acid. *In vivo*, the binding of opsonin proteins in the bloodsteam leads to

attachment onto macrophages and subsequently their internalization mediated by phagocytosis [18].

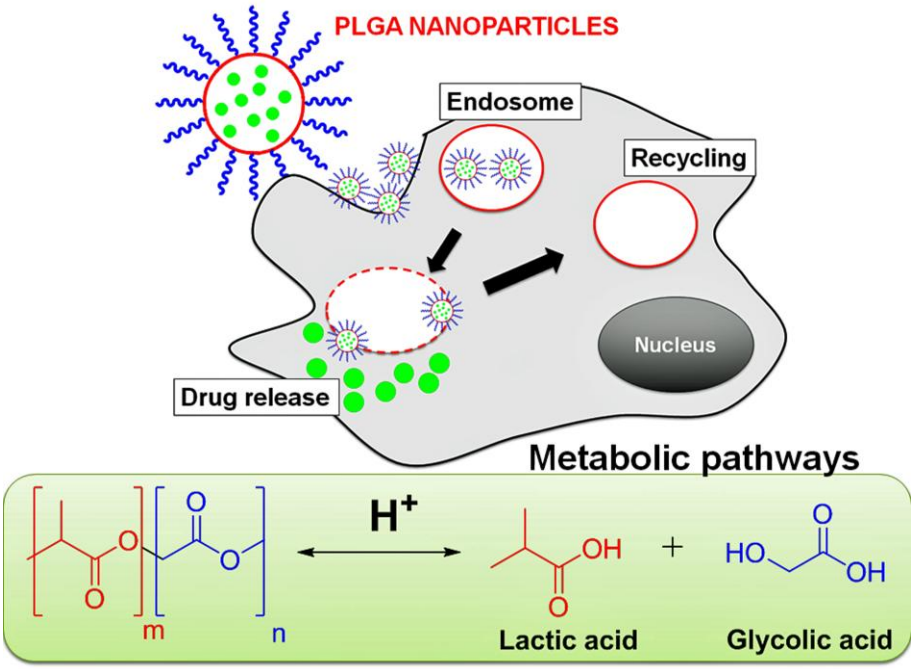

Figure 2.3: Schematic representation of PLGA nanoparticle internalization in cells.
Polymeric PLGA NPs allow efficient entry into cells followed by cargo release in response to acid conditions inside endosomes. Thus the polymer is decomposed trough metabolic compounds and drug can accumulate into the cytoplasm of the cell.

To threshold these phenomenon, several methods of surface modifications have been developed to produce “stealthness” and many work converged to the surface modification with PEG, which exhibits excellent biocompatibility and low toxicity. A sufficient PEG coating is essential for avoiding recognition by the reticulo−endothelial system [19], while targeting ligands should be extended away from the nanoparticle surfaces to avoid shielding by the PEG chains [20]. Also surface charge of nanoparticle should be modulated to avoid too many non−specific interactions; PLGA NPs have negative charges but they might be shifted to neutral or positive charges by surface modification by PEGylation [21] or chitosan coating [22], respectively.

2.3.1 Formulations of PLGA NPs

The drug is entrapped inside the core of a “nanocapsule” as well as adsorbed on the surface of a matrix “nanosphere”. The nanosized droplets are induced by sonication or homogenization and, later, the solvent is evaporated or extracted and the nanoparticles collected after centrifugation [23]. Another method, called water/oil/water double emulsion synthesis is instead used to encapsulate hydrophilic drugs, such as peptides, proteins and nucleic acids [24]. PLGA NPs can also be formulated by the nanoprecipitation method [25]: the drug and the polymer are soaked into an organic solvent (such as acetone or ethanol) and added dropwise to water; the organic solvent is then allowed to evaporate and NPs are collected by centrifugation. Unluckily, even if this technique is the easiest to reproduce, it doesn’t allow to obtain a monodisperse suspension of NPs and also drug encapsulation yield is not very high.

2.3.2 Advantages and drawbacks of PLGA formulations

Formulations need to have a high percentage of loaded drug but a precise determination of the drug content is not easy since that NPs are colloidal systems. One of the major pitfalls of PLGA-based carriers relates to the poor loading; indeed, while PLGA-based nanoparticles often present high encapsulation efficiency, the final drug loading is generally poor (≈ 1 wt.% which means that NPs content 1 mg active ingredient each 100 mg of polymers). A second important drawback consists in the high burst release of drug from the polymer matrix and this phenomenon is common for most of PLGA-based construct. Consequently, the drug might not be able to reach the target tissue or cells, leading to a loss of efficacy. Considering the application of NPs in sustained drug delivery, drug release mechanisms are also very important to understand. Kumari and colleagues [14] describes five mechanisms of drug release: (i) desorption of drug bound to the surface, (ii) diffusion through the

polymer matrix, (iii) diffusion through the polymer wall of nanocapsules, (iv) nanoparticles matrix erosion and (v) a combined erosion−diffusion process. These five mechanisms depend on the polymer used and on the loading efficiency; generally, the burst release effect is endorsed to adsorbed drug to the nanoparticles surface [14]. Moreover, toxicological studies and regulations will be necessary in order to fully classify the biocompatibility of PLGA nanocarriers in humans. In most of case, *in vitro* studies provide encouraging results and currently there are many examples in clinical trials of PLGA drug delivery systems for the treatment of different pathologies (Table 3).

Therapeutic Compounds	Targeted nanoparticles / Ligands	Development level	[Refs]
Paclitaxel	Untargeted	Preclinical (mice)	[26]
siRNA AnxA2	Untargeted	Preclinical (mice)	[27]
Doxorubicin	ICAM-1 / cLABL	*In vitro*	[28]
Paclitaxel	Folate receptor / Folate	Preclinical	[29]
Cisplatin	Prostate specific receptor / PSMA	Preclinical	[30]
Paclitaxel	Nucleolin / AS1411	*In vivo*	[31]
PE38KDL	HER2 / rhuMabHER2	Preclinical (mice)	[32]

Table. 3: Developed PLGA-nanoparticles in advanced preclinical models.

2.4. Cancer treatments with PLGA-based nanoparticles

2.4.1 Passive and active tumor targeting

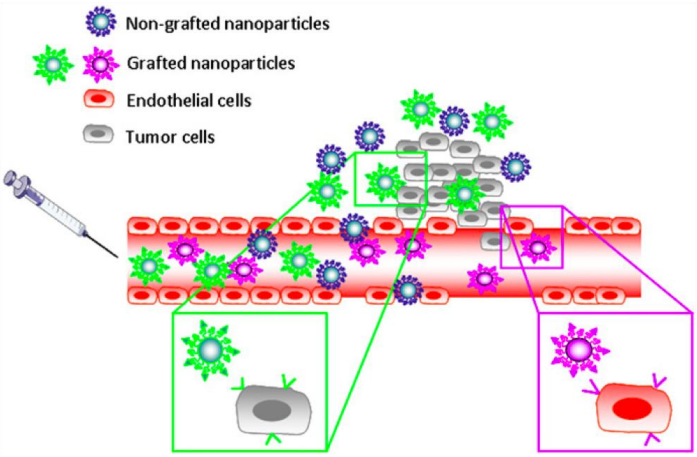

Figure 2.4: Passive and active cancer targeting. Nanocarriers can reach tumors selectively through the leaky vasculature surrounding the tumors. Ligands grafted on their surface bind to receptors expressed by cancer cells (green) or angiogenic endothelial cells (pink).

Chemotherapeutic agents damage healthy tissues, leading to systemic toxicity and adverse effects that greatly limit the maximum tolerated dose of anticancer drugs and thus restricts their therapeutic efficacy. In general, nanoparticles can achieve tumors via an active or passive targeting. The **Passive targeting** (Figure 2.4) takes advantage of the size of nanoparticles and exploits the unique anatomical and pathological abnormalities of the tumor vasculature. NPs can extravasate and accumulate inside the interstitial space: this contributes to an “enhanced permeability”. Moreover, lymphatic vessels are absent or ineffective in tumors, leading to inefficient drainage of the tumor tissue: this contributes to an “enhanced retention”. Taken together these two phenomena constitute the “Enhanced Permeability and Retention” *(EPR) effect* [33].

In **Active targeting** (Figure 2.4), targeting ligands are grafted at the nanoparticles surface [21]. The ligand is chosen to bind specific receptors over−expressed by tumor cells or tumor vasculature and not−expressed by normal cells. Another important factor in the choice of targeting ligands is the homogeneity of the expression of the receptor on all targeted cells. Nevertheless, this information is often deficient. Two cellular targets can be distinguished: (i) cancer cells and (ii) tumoral endothelial cells. To target cancer cells, several over−expressed receptors

have been investigated (*e.g.* the transferrin receptor, the folate receptor, glycoproteins, the epidermal growth factor receptor (EGFR) or integrins). Thus in this strategy, targeted nanocarriers aimed to directly kill angiogenic blood vessels and indirectly kill tumor cells [21].

Moreover, the enhanced cellular internalization rather than an increased tumor accumulation is responsible of the anti tumoral efficacy of actively nanocarriers. This is the base of the design of delivery systems targeted to endocytosis-prone surface receptors [34]. Therefore, this receptor−mediated internalization constitutes a major advantage of targeted nanoparticles in addition to the specific targeting of nanoparticles.

2.4.2 Cancer Chemotherapy

Many small anti-cancer drugs have been encapsulated in PLGA- based nanoparticles and have been evaluated *in vitro* and *in vivo* to treat various cancers.

Doxorubicin (DOX), a highly potent anthracycline approved for use against a wide spectrum of tumors, is the first example of drug encapsulated in PLGA NPs because of its toxicity which can cause dangerous cardiomyopathies and heart failures. PLGA nanoparticles have shown to decrease drastically the cardiomyopathies compared to Doxil ®, a liposomal formulation of DOX currently commercially available [35]. Paclitaxel (PTX), a mitotic inhibitor used in the treatment of different cancers, presents a low therapeutic index and a low aqueous solubility. Its current commercialized form, Taxol®, contains PTX at a concentration of 6 mg mL^{-1} solubilized in a mixture of Cremophor® EL and ethanol (1:1). However, serious side effects are associated with Cremophor® EL. In this case, PTX encapsulation into PLGA NPs strongly enhanced its cytotoxic effect as compared to Taxol® both *in vitro* and *in vivo* [26].

PLGA NPs targeting the tumor cells or tumor endothelium have been shown to be usually more active in preclinical studies than non−targeted nanoparticles. A cyclic peptide, Cyclo-(1,12)-penITDGEATDSGC (cLABL), has been shown to inhibit LFA-1/ ICAM-1 via the binding to ICAM-1 and it is internalized after binding ICAM-1 receptor. The cytotoxicity study of cLABL-nanoparticles and non-targeted nanoparticles compared to free DOX showed similar IC_{50} values suggesting that the activity of DOX was maintained [28]. Although numerous studies are described in the literature about PLGA NPs, only few papers describe active targeting using PLGA. Additionally, most of these papers illustrate the characterization of their system only *in vitro*; few articles report actively targeted PLGA NPs both *in vitro* and *in vivo*.

2.4.3 Cancer Theragnostic

Theragnostics combine passive and active targeting, environmentally responsive drug release, molecular imaging and other therapeutic functions into a single platform [36−38]. DOX has been encapsulated into magnetic nanoparticles that were embedded in PLGA through hydrophobic interactions. DOX was released sustainably without any inhibition. These magnetic nanocapsules have been tested in mice, rats and in human [39]. More recently, MNPs embedded in PLGA matrices have been designed as dual drug delivery and imaging system able to encapsulate both hydrophilic (carboplatin) and hydrophobic drugs (PTX and rapamycin). Magnetic resonance imaging have showed, both *in vitro* and *in vivo*, that these nanoparticles present a better contrast effect than commercial contrast agents [40].

Related References

[1] Buse, J. and El-Aneed, A.; *Nanomedicine*. **2010**, *5*, 1237–1260.

[2] Huang, H. C.; Barua, S.; Sharma, G.; Dey, S. K. and Rege, K.; *J. Control*. *Release.* **2011**, *155*, 344–357.

[3] Maham, A.; Tang, Z.; Wu, H.; Wang, J. and Lin, Y.; *Small*. **2009**, *5*, 1706–1721.

[4] Nicolas, J.; Mura, S.; Brambilla, D.; Mackiewicz, N. and Couvreur, P.; *Chem. Soc. Rev*. **2013**, *42*, 1147–1235.

[5] Acharia, S.; Dilnawaz, F. and Sahoo, S. K.; *Biomaterials*. **2009**, *30*, 5737–5750.

[6] Davis, M. E.; *Mol*. *Pharm.* **2009**, *6*, 659–668.

[7] Acharia, S.; Dilnawaz, F. and Sahoo, S. K.; *Biomaterials*. **2009**, *30*, 5737–5750.

[8] Peng, C. L.; Tsai, H. M.; Yang, S. J.; Luo, T. Y.; Fin, C. F.; Lin, W. J. and Shieh, M. J.; *Nanotechnology*. **2011**, *22*, 265608.

[9] Fomina, N.; McFearin, C.; Sermsadki, M.; Edigin, O. and Almutairi, A.; *J. Am. Chem. Soc*. **2010**, *132*, 9540–9542.

[10] Wilson, D. S.; Dalmasso, G.; Wang, L.; Sitaraman, S. V.; Merlin, D. and Murthy, N.; *Nat. Mater*. **2010**, *9*, 923–928.

[11] van Duijnhoven, S. M. J.; Robillard, M. S.; Nicolay, K. and Grüll, H.; *J. Nucl. Med*. **2011**, *52*, 279–286.

[12] You, J. O. and Augusta, D. T.; *Nano. Lett*. **2011**, *52*, 279–286.

[13] Cho, H.; Bae, J.; Garripelli, V. K.; Anderson, J. M.; Jun, H. W. and Jo, S.; *Chem. Commun*. **2012**, *48*, 6043–6045.

[14] Kumari, A.; Yadav, S. K. and Yadav, S. C.; *Colloids. Surf. B Biointerfaces*. **2010**, *75*, 1–18.

[15] Prokop, A. and Davisdon, J. M.; *J. Pharm. Sci*. **2008**, *97*, 3518–3590.

[16] Vert, M.; Mauduit, J. and Li, S.; *Biomaterials*. **1994**, *15*, 1209–1213.

[17] Vasir, J. K. and Labhasetwar, V.; *Adv. Drug. Deliv. Rev*. **2007**, *59*, 718–728.

[18] Owens, D. E. and Peppas, N. A.; *Int. J. Pharm*. **2006**, *307*, 93–102.

[19] Wang, M. and Thanou, M.; *Pharmacol. Res*. **2010**, *62*, 90–99.

[20] Karakoti, A. S.; Das, S.; Thevuthasan, S. and Seal, S.; *Angew. Chem. Int. Ed.* **2011**, *50*, 1980–1994.

[21] Danhier, F.; Feron, O. and Préat, V.; *J. Control*. *Release*. **2010**, 1*48*, 135–146.

[22] Tahara, K.; Sakai, T.; Yamamoto, K.; et al.; *Int. J. Pharm*. **2009**, *382*, 198–204.

[23] Cartiera, M. S.; Ferreria, E. C.; Caputo, C.; Egan, M. E.; Capian, M. J. and Salzman, W. R.; *Mol. Pharm*. **2010**, *7*, 86–96.

[24] Jain, A. K.; Swarnakar, N. K.; Das, M.; Godugu, C.; Singh, R. P.; Rao, P. R. and Jain, S.; *Mol. Pharm*. **2011**, *8*, 1140–1151.

[25] Barichello, J. M.; Morishita, M.; Takayama, N. and Nagay, T.; *Drug. Dev. Ind. Pharm*. **1999**, *25*, 471–476.

[26] Danhier, F.; Lecouturier, N.; Vroman, B.; Jerome, C.; Feron, O. and Préat, V.; *J. Control. Release*. **2009**, *133*, 11–17.

[27] Braden, A. R.; Kafka, M. T.; Cunningham, L.; Jones, H. and Vishwanatha, J. K.; *J. Nanosci. Nanotechnol.* **2009**, *9*, 2856–2865.

[28] Chittasupho, C.; Xie, S. X.; Baoum, A.; Yakovleva, T.; Siahaan, T. J. and Berkland, C. J.; *Eur. J. Pharm. Sci*. **2009**, *37*, 141–150.

[29] Liang, C.; Yang, Y.; Ling, Y.; Huang, Y. and Li, X.; *Bioorg. Med. Chem.* **2011**, *19*, 4057–4066.

[30] Dhar, S.; Gu, F. X.; Langer, R.; Farokhzad, O. C. and Lippard, S. J.; *Proc. Natl. Acad. Sci*. **2008**, *105*, 17356–17361.

[31] Guo, J.; Gao, X.; Su, L.; et al.; *Biomaterials*. **2011**, *31*, 8010–8020.

[32] Chen, H.; Gao, J.; Lu, Y.; et al.; *J. Control. Release*. **2008**, *128*, 209–216.

[33] Matsumura, Y. and Maeda, H.; *Cancer Res.* **1986**, *46*, 6387–6392.

[34] Kirpotin, D. B.; Drummond, D. C.; Shao, Y.; et al.; *Cancer Res*. **2006**, *66*, 6732–6740.

[35] Park, J.; Fong, F. M.; Lu, J.; et al.; *Nanomedicine*. **2009**, *5*, 410–418.

[36] Danhier, F.; Ansorena, E.; Silva, J. M.; Coco, R.; Le Breton, A. and Préat, V.; *J. Control. Release*. **2012**, *161*, 505–532.

[37] Martin−Banderas, L.; Lobato, M.; Rubio, I.; et al.; *Rev. Med. Chem*. **2013**, *13*, 58–69.

[38] Morachis, J. M; Mahmoud, E. A. and Almutairi, A.; *Pharmacol. Rev*. **2012**, *64*, 505–519.

[39] Janib, S. M; Moses, A. S. and Mackay, J. A.; *Adv. Drug. Deliv. Rev*. **2010**, *62*, 1052–1063.

[40] Singh, A.; Dilnawaz, F.; Mewar, S.; Sharma, U.; Jagannathan, N. R. and Sahoo, S. K.; *ACS Appl. Mater. Interfaces*. **2011**, *3*, 842–856.

Second Section

Chapter III

Materials and Methods

Contents

3.1 Characterization challenges

A rational characterization strategy for bioconstructed NPs contains three elements: physicochemical characterization, *in vitro* assays, and finally *in vivo* studies. Physicochemical characterization plays a key role in the interpretation of *in vitro* or *in vivo* biological data; while testing *in vitro* might give an initial estimate of formulation efficacy and, eventually, toxicity. These approaches traditionally used for small molecules to ascertain their physicochemical properties, can be perfectly applied for nanoconjugates: for instance, techniques like nuclear magnetic resonance (NMR), fluorescence spectroscopy, UV-vis spectroscopy, infrared spectroscopy (IR) can be run in a high-throughput fashion to analyze the molecule-nanoparticle interactions. The nanoconjugates properties can influence biological activity, and may depend on parameters such as particle size, size distribution, surface area, surface charge, surface functionality, shape, and aggregation state. Additionally, since many nanoparticle concepts are multifunctional (with targeting, imaging, and therapeutic components), the stability and distribution of these components can have dramatic effects on nanoparticle biological activity as well.

Furthermore, another important and challenging area of nanoparticle characterization is measurement under physiological conditions that resembles or mimics the physical state *in vivo*. Many NPs properties are environment dependent; for example, the particle's hydrodynamic size at physiological pH and ionic strength may differ from the size in water. Surface charge may also depend on the pH and ionic strength of the suspending solution. While *in vitro* characterization is performed to elucidate mechanisms and biocompatibility of nanomaterials, making use of numerous immortalized cell lines.

3.2 Nanoparticle core size, shape and properties

All reagents and solvents have been purchased from Sigma-Aldrich (St. Louis, MO, USA), Fluka (St. Gallen, Switzerland) and Riedel-de Haën (Seelze, Germany) and used as received without further purification. Whole antibodies (mAb) (Roche Products Ltd.,UK) have been received as a powder lyophilized for intravenous administration; before reactions they have been purified from additives by dialysis membrane (MWCO 12-14000 Da) in 20 mM phosphate buffer solution (PBS), pH = 7.4, 150 mM NaCl, 5 mM EDTA. Water has been deionized and ultrafiltered by a MilliQ apparatus (Millipore Corporation, Billerica, MA). Ultrasounds have been generated by S15H Elmasonic Apparatus (Elma, Singen, Germany).

3.2.1- Transmission and Scanning electron microscopy

In present work, TEM micrographs of MNPs, SiNPs and PLGA NPs have been obtained using an TEM (Zeiss EM-109 microscope, Oberkhochen, Germany) operating at 80 kV, available at the "Centro di Microscopia Elettronica per le Nanotecnologie applicate alla medicina" (CMENA, University of Milan). The samples have been prepared by evaporating a drop of NPs suspension (5 µg mL^{-1}, either in water or organic solvent) onto carbon-coated copper grid and allowing it to dry on the air. The histograms of the particle size distribution and the average particle diameter have been obtained by measuring about 100 particles by using Image−J software analysis (Mircosoft).

3.2.2- Dynamic light scattering (DLS)

Dynamic Light Scattering is one of few techniques capable of determining the size of nanoparticles in solution, providing an accurate measure of nanoparticle hydrodynamic size. In DLS, the nanoparticle solution is illuminated by a monochromatic laser and its scattering intensity is recorded with a photon detector at

a fixed or variable scattering angle with time. Generally, nanoparticle samples contain a distribution of sizes as a result of imperfections in synthesis and due to natural conformational variations in the large number of atoms involved. A metric for size variability is the polydispersity index (PDI) equivalent to the relative variance of the distribution.

In the present work DLS measurements have been performed, using a 90 Plus Particle Size Analyzer from Brookhaven Instrument Corporation (Holtsville, NY) operating at 15 mW of a solid-state laser (λ = 661 nm), using a scattering angle of 90°. Plastic (or eventually glass) disposable cuvettes with 1 cm optical path length have been used for the measurements. Viscosity and refractive index of water have been used to characterize the solvent. All materials have been previously cleaned with Milli-Q water and EtOH 40 vol.% in deionized water and then allowed to dry with a nitrogen flow. Samples have been prepared by dilution with the solvent or 1.0 mM NaCl water solution in a final concentration range typically close to 20 µg mL^{-1}. Each sample has been allowed to equilibrate for 2 min prior to the measurement and five independent measurements of 1 min duration have been performed at 25°C. The calculations of hydrodynamic diameter have been performed using Mie theory, considering absolute a PDI index accepted below 0.350.

3.2.3- Sight distribution spectra

Sight distribution spectra have been collected by NanoSight LM10 from NanoSight Limited (Amesbury, UK) and analyzed with Nanoparticle Tracking Analysis (NTA) software, version 2.2 Build 0363; samples have been in a range of concentration around 10.0×10^8 NP mL^{-1} working at 23 °C. All measurements have been performed in triplicate and the average values have been taken.

3.2.4- ζ-potential measurements (Zeta-potential)

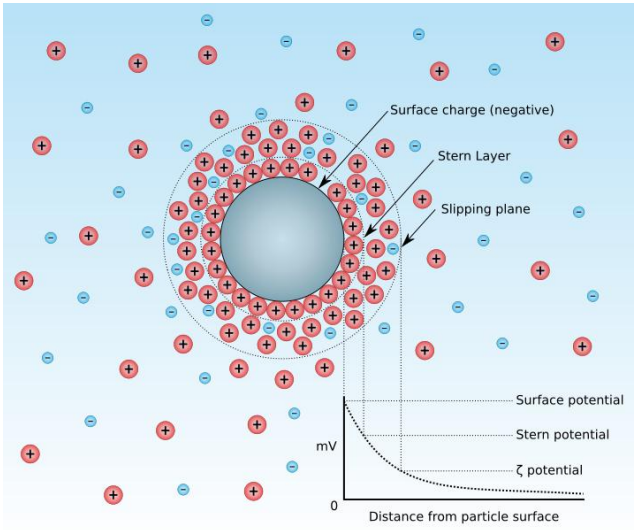

Figure 3.1: ζ-potential theory.
Electrical double layer of a negatively surface charged nanomaterial

In an ionic solution, NPs with a net charge have two surrounding layers: a layer of ions of opposite charge strongly bound to their surface, and a diffuse outer layer of loosely associated ions. These two layers are collectively called the electrical double layer. As the particle moves, a distinction is created between ions in the diffuse layer that move with the nanoparticle and ions that remain with the bulk dispersant. The electrostatic potential at this "slipping plane" boundary is called the zeta potential and is related to the surface charge of the nanoparticle (Figure 3.1). In zeta potential measurements, an electrical field is applied across the sample and the electrophoretic mobility of nanoparticles is measured by laser doppler velocimetry [1]. Nanoparticles with a zeta potential between −10 and +10 mV are considered approximately neutral, while nanoparticles with zeta potentials greater than +30 mV or less than −30 mV are considered strongly cationic and anionic, respectively [2]. In this thesis ζ-potential has been determined at 25°C using a 90 Plus Particle Size Analyzer from Brookhaven Instrument Corporation (Holtsville, NY) equipped with an AQ-809 electrode, operating at applied voltage of 120 V. The samples for measurements have been prepared by dilution of NPs in 1.0 mM NaCl aqueous solution pH = 7.25 up to 20 µg mL^{-1}. A minimum of three runs (for ten measures) have been acquired to establish measurement reproducibility. The Zeta-potential has been automatically calculated from electrophoretic mobility based on the Helmholtz-

Smoluchowski theory (Equation 1). A viscosity of 0.891 cP, a dielectric constant of 78.6, and Henry function of 1.5 have been used for calculations.

$$u_e = \frac{\varepsilon_{rs} \cdot \varepsilon_0 \cdot \zeta}{\eta} \qquad \text{(eq. 1)}$$

where u_e- electrophoretic mobility, ε_{rs}- relative permittivity of the electrolyte solution, ε_0 –electric permittivity in vacuum, η-dynamic liquid viscosity, ζ-zeta-potential [2].

3.2.5- Differential Centrifuge Sedimentation (DCS)

Particle size, size distribution and extent of aggregation have been analyzed by analytical centrifugation on a CPS disc centrifuge DC24000 (CPS Instruments Inc., UK). The CPS Disc Centrifuge separates particles by size using centrifugal sedimentation in a liquid medium. The sedimentation is stabilized by a slight density gradient within the liquid. The particles sediment within an optically clear, rotating disc. Approaching the outside edge of the disc, they scatter a portion of a light beam that passes through the disc. The change in light intensity is continuously recorded, and converted by the operating software into a particle size distribution.

As a gradient fluid, 8 and 24 wt.% Sucrose solution in Milli-Q water (or PBS 20 mM in used for NPs protein conjugates) have been adopted and filled successively in nine steps into the disc, starting with the dilution of highest density. For analysis, the disc rotation speed has been set to 22 000 rpm. Calibration has been performed using poly-vinylchloride (PVC) particles (0.460 µm) as calibration standard (Analytik Ltd., UK). Colloidal NPs have been sonicated 3 min before injection into the disc centrifuge.

3.2.6- UV-vis spectroscopy

UV-vis spectroscopy can be a useful tool in fast and real-time monitoring of MNPs and fluorescent SiNPs agglomeration and concentration. UV-visible spectra

have been recorded by using a Nanodrop 2000C spectrophotometer (Thermo Fisher Scientific, Wilmington, Germany) in a wavelength range between 190 and 700 nm, with 1 cm path length quartz cuvettes and a solution obtained by diluting the original NPs suspension with the appropriate solvent, which has been used as a blank. The results of the experiment are expressed as average of three different analyses. To calculate NPs concentration, 1 mL of suspension has been allowed to dry in the oven (T= 150°C) for 2 hs and then the residual fine powder weighted. The calculated amount of NPs gives the concentration in mg mL^{-1}; in this way the resultant NPs suspension has been diluted several times and samples have been analyzed with UV-vis spectrophotometer at the following wavelength: MNPs (λ= 450 nm) broad peak; FITC-labeled SiNPs (λ= 485 nm) fluorescein absorption peak. Calibration curves of NPs concentration have been created (Figure 3.2) and, at the end of any single functionalization step, the NPs concentration have been checked.

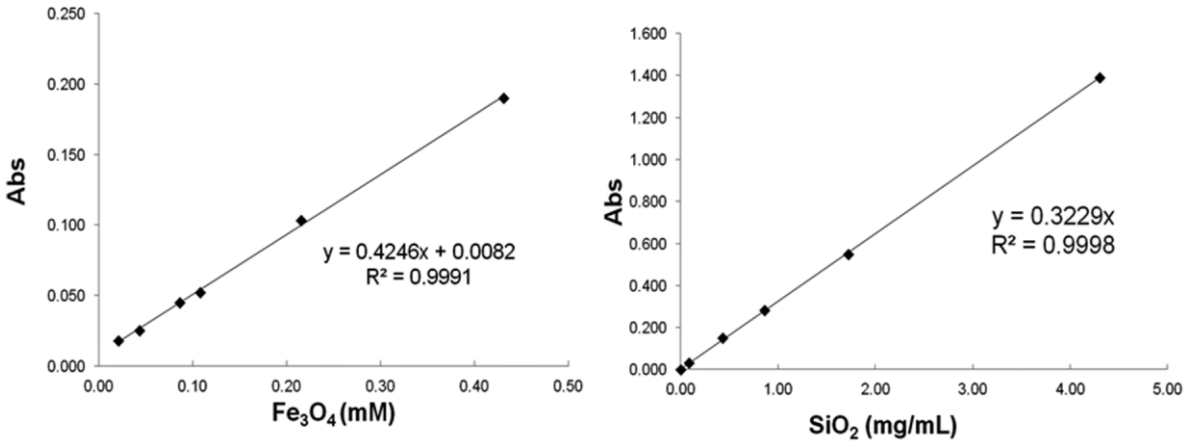

Figure 3.2: Calibration curves by UV-vis spectroscopy.
(Left) Iron oxide NPs in deionized water (λ=450nm); (right) Fluorescent FITC-labeled 20nm SiNPs in deionized water (λ=485nm).

3.2.7- Fluorescence spectroscopy

In the case of fluorescent-labeled SiNPs and PLGA NPs, fluorescence spectroscopy has been used to check the relative fluorescent intensity of NPs, which is fundamental for further cellular imaging quantification and localization (Figure 3.3).

Fluorescence spectra have been recorded by using Fluoromax-4P spectrofluorometer from Horiba Scientific (New Jersey,USA). Samples have been excited at a fixed wavelength (FITC λ_{ex} = 480 nm; Curcumin λ_{ex} = 450 nm) and spectra have been collected in a wavelength range between 480 and 700 nm. The fluorescence emission of FITC and Curcumin have been detected at 520 nm and 500 nm respectively; slit widths (for controlling magnitude and resolution of transmitted light) have been standardized at 3 and 3 nm for excitation and emission wavelength. The results of the experiment are expressed as average of three different analyses.

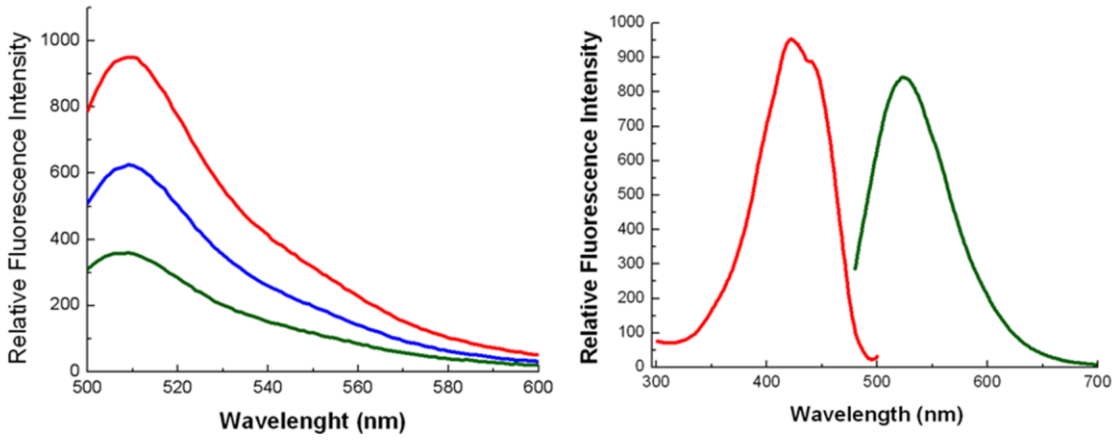

Figure 3.3: Fluorescence spectra analyses.
(Left) Core-shell SiNPs-fluorescein labeled; 100 µg mL^{-1} (red curve), 50 µg mL^{-1} (blue curve), 25 µg mL^{-1} (green curve); (rigt) Fluorescence excitation and emission spectra of Curcumin [5 µM] in EtOH.

3.2.8- Magnetization studies: T_2 relaxation times evaluation

As anticipated in the introduction, MNPs have strong magnetic properties and might be adopted as contrast agents for *in vivo* MRI. Indeed Relaxometric measurements to determine the T_2 enhancing capability of magnetite synthesized nanocrystals have been evaluated and compared to commercially available T_2 MRI contrast agent. T_2 relaxation times have been monitored at temperature of 313 K using a Bruker Minispec mq20 system (Ettlingen, Gerrmany) working with 1H at 20 MHz magnetic field (1.47 *T*) with the following parameters: Carr-Purcell-Meiboom-Gill pulse sequence, 1000 echoes with a 20 ms echo times and 2 s repetition time.

Samples of MNPs suspension in water have been introduced using a 10 mm NMR spectroscopy tubes. Before T_2 measurements, the tubes have been pre-warmed at 40°C for 10 min in order to obtain thermal equilibration and T_2 values have been acquired on the samples at this stage. Relaxivity has been determined as the slope of a T_2^{-1} plot as function of iron concentration, expressed in mM. This value has been compared with the one's of commercially available T_2 contrast agents based on polymer-coated iron oxides, such as Endorem ® (Guerbet), Ferumoxytol ® (Adv. Magnetics) and Resovist ® (Schering).

3.3 Nanoparticle ligand characterizations

3.3.1- Picrylsulfonic acid (TNBS) assay: quantification of amino groups onto SiNPs

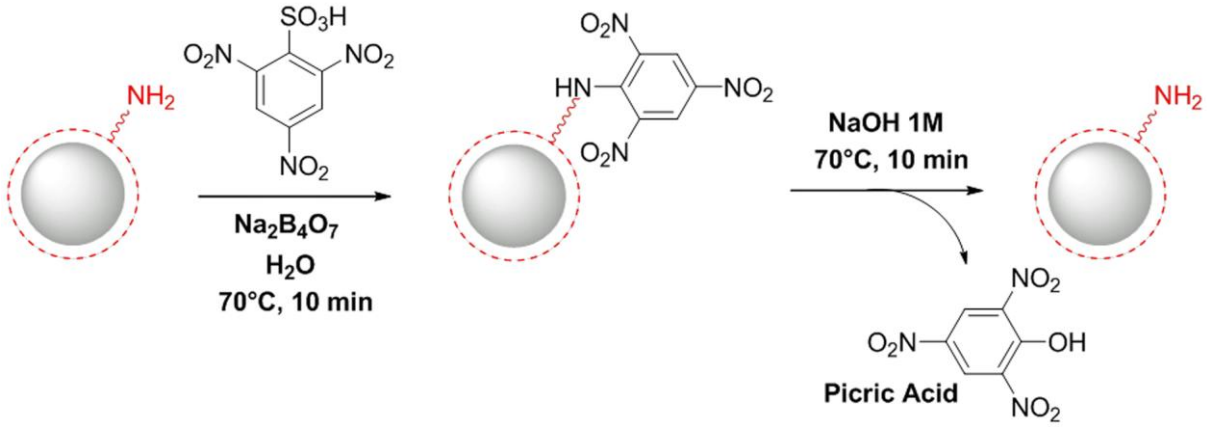

Figure 3.4: TNBS assay.
Amino functionalyzed SiNPs react with picrylsulfonic acid; the stable intermediate is finally broken by hydrolysis. The yellow picric acid released can be estimated by UV-vis spectroscopy.

Following a method described in the literature [3] (Figure 3.4), an aqueous mixture containing 1 M TNBS (10.0 µL) and 0.05 M $Na_2B_4O_7$ (1.5 mL) has been added to a sample of aminated SiNPs (6.0 mg). The suspension has been sonicated for 1 min and then heated at 70 °C for 10 min. At the end of reaction, the mixture has been cooled to RT; SiNPs have been then separated from the supernatant by centrifugation (11200 rcf) and washed with deionized water (1.0 mL), 50% acetone in water (1.0 mL), 100% acetone (1.0 mL) and water (twice 1.0 mL). SiNPs have been then suspended in 1 M NaOH (5.0 mL) and heated to 70 °C under vigorous stirring for 10 min. The suspension has been cooled to RT and SiNPs separated by centrifugation. An aliquot of particle-free supernatant (1.0 mL) has been withdrawn and its absorbance read with UV-vis spectrophotometer at 410 nm. Each particle contained silica (d = 2.2 × 10^6 g m^{-3}) with an average radius of 40 nm = 4.0 × 10^{-8} m. The average volume and mass of SiO_2 nanoparticles is 2.68 × 10−22 m^3 and 5.90 × 10^{-16} g, respectively. Hence, 1 mg of SiO_2 contained 1.02 × 10^{14} particles. By

determination of residual absorbance due to picric acid released from reaction it has been established that 0.012 µmol of ligand APTMS has been immobilized on the particle surface corresponding to about 0.07 NH_2 / nm^2.

3.3.2- Ninhydrin assay: quantification of amino groups onto SiNPs

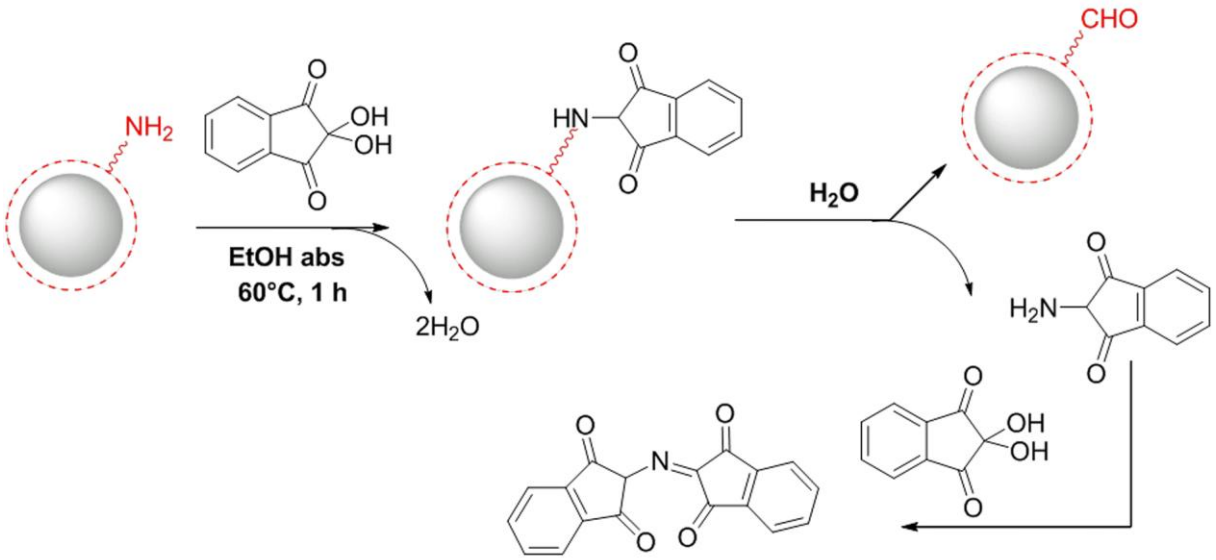

Figure 3.5: Ninhydrin assay.
The amino group of SiNPs is condensed with a molecule of ninhydrin to give a Schiff base. Thus only ammonia and primary amines can proceed past this step. At this step, there must also be an alpha proton for Schiff base transfer, so an amine adjacent to a tertiary carbon cannot be detected by the ninhydrin test. The reaction of ninhydrin with secondary amines gives an iminium salt which is also yellow-orange colored.

This method has been adapted as described in literature [4] (Figure 3.5). Briefly, aminated SiNPs (3 mg) equilibrated twice in absolute EtOH (1 mL) and then have been resuspended in the same solvent (1.0 mL). Meanwhile a Ninhydrin stock solution (3.5 mg mL^{-1}) has been prepared obtaining a clear pale green solution. An aliquot of Ninhydrin stock solution (0.250 mL) has been added to SiNPs suspension and, after 1 min of sonication, heated at 60 °C for 1 h in the oven. At the end of reaction, the mixture has been cooled to RT; SiNPs have been then separated from the supernatant by centrifugation (11200 rcf) and an aliquot of particle-free blue supernatant (0.2 mL) read with UV-vis spectrophotometer at 588 nm. Standard calibration curve has been created using Ethanolamine in a concentration range

between 0−3 mM in absolute EtOH The same calculations used for TNBS assay have been performed to estabilished the particle surface NH_2 coating corresponding to about 2.16 NH_2 / nm^2.

3.3.3- Elmman's reagent: quantification of sulphydryl groups reactivity [5]

SiNPs with external maleimide functionalization (5.0 mg) have been reacted within a known concentration of a reagent bearing thiol groups (*e. g.* MeO-PEG_4-SH) 2 h at RT. At the end of the reaction, NPs have been separated with centrifugation and an aliquot of the clear supernatant (50.0 µL) has been poured in 0.1 M PBS, 1 mM EDTA pH=8 (250.0 µL). A 5,5'-Dithio-*bis*-(2-nitrobenzoic acid) (DTNB) stock solution (4.0 mg mL^{-1}) previously prepared in the same solvent has been added to the reaction mixture (5.0 µL). After 15 min of incubation at RT, the color of the solution has turned yellow according to the amount of free sulphydryl groups in the mixture. Free thiol groups concentration have been estimated by UV-vis-spectroscopy (λ_{max}=412 nm) before and after reaction with maleimide functionalized NPs to discriminate the number of effective reactants (Figure 3.6).

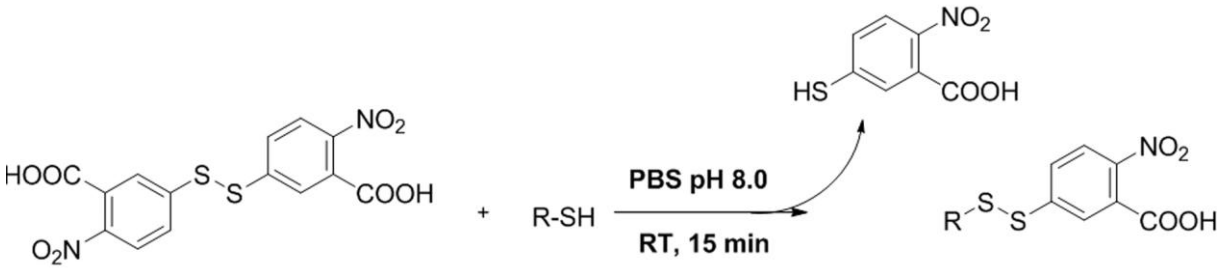

Figure 3.6: Ellman's reagent.
Thiols react with DTNB, cleaving the disulfide bond to give 2-nitro-5-thiobenzoate (NTB^-), which ionizes to the NTB^{2-} dianion in water at alkaline pH. This NTB^{2-} ion has a yellow color and can be quantify by UV-vis.

3.3.4- MicroBCA assay Protein assay Kit

The technique utilizes bicinchoninic acid (BCA) as the detection reagent for Cu^I, which is formed when Cu^{II} is reduced by protein in an alkaline environment [6]. A purple-colored reaction product is formed by the chelation of two molecules of BCA

with one cuprous ion (Cu^{I}). This water-soluble complex exhibits a strong absorbance at 562 nm that is linear with increasing protein concentrations in a range between 2−40 µg mL^{-1}. This procedure has been adapted from the company general schedule (Pierce Biotechnology, Rockford, IL, USA)

Kit contents: Reagent A (MA)

Reagent B (MB)

Reagent C (MC)

A solution of reagents (5 mL) has been prepared mixing MA : MB : MC in these proportions 50 : 48 : 2. In a 96-multiwell plate reader an aliquot of previous mixture (100.0 µL) and an aliquot of Transferrin-conjugated SiNPs (100.0 µL, corresponding to 100.0 µg of NPs) have been added to each well and mixed thoroughly on a plate shaker for 30 seconds. Samples have been incubated in the oven at 60°C for 1 h and then cooled at RT. The absorbance of samples and protein BSA calibration standards in a range of concentrations between 0-40 µg $mL^{-1.}$ Purple colored solutions have been read at 562 nm with a plate reader and the protein loading onto silica surface has been reported as µg / mg_{NP} and protein / NP.

3.4 Organic molecules characterization

3.4.1- $^{1}H-NMR$ spectroscopy

^{1}H-NMR experiments have been carried out on a Bruker BioSpin FT-NMR Avance 400 MHz equipped with a 11.7 *T* superconducting ultrashield magnet. Samples (5 mg) have been dissolved in suitable NMR solvents such as $CDCl_3$ or $DMSO_d$ and analyzed. All measures have been recorded at temperature of 300 K and spectra processed with Mnova NMR software (MestreLab research, S.L., Spain).

3.4.2- Critical micelle concentration (CMC) of polymeric PLGA nanoparticles

CMC of PLGA NPs has been estimated by fluorescence spectroscopy using pyrene as a fluorescence probe [7]. A solution of pyrene (6.0 mM) in acetone has been prepared and added to deionized water to reach a pyrene concentration of 12.0 μM; later, the organic solvent has been evaporated (acetone-free pyrene solution) in the air. Solutions of PLGA NPs (1.0 mL) in a concentration range between 5.0×10^{-5} to 1.0 mg mL^{-1} have been prepared and mixed together with acetone-free pyrene solution (1 mL) in order to gain a final concentration of pyrene in each sample solution of 6.0 μM. Fluorescence spectra of pyrene have been recorded monitoring the excitation fluorescence behavior at 334 and 338 nm. The CMC has been estimated and plotted following the cross-point when extrapolating the intensity ratio I_{338} / I_{334} at low and high concentration regions.

3.4.3- Drug content and encapsulation efficiency (E.E.%)

Both UV−vis and fluorescence spectroscopies have been used to determine the amount of drug encapsulated in PLGA NPs. A known amount of dry NPs (250.0 μg) has been dispersed in deionized water and chloroform has been added to the water phase. After 3 h under stirring, residual curcumin released from nanoparticles has been determined by both UV−vis and fluorescence emission. Empty PLGA NPs

and polyvinyl alcohol (PVA) don't interfere with the analysis of curcumin. The encapsulation efficiency has been calculated (Equation 2) as:

$$E.E.(\%) = \frac{drug_{loaded}\,(\mu g_{drug} \cdot mg^{-1}{}_{NPs})}{drug_{initial}\,(\mu g_{drug} \cdot mg^{-1}{}_{NPs})} \cdot 100 \qquad \text{(eq. 2)}$$

UV−vis quantification has been detected at λ_{max} = 420 nm and fluorescence emission spectra have been recorded in a wavelength range between 480 and 700 nm, exciting all samples at fixed wavelength (λ_{ex} = 450 nm). The fluorescence emission of curcumin has been detected at 500 nm; the slit widths (for controlling magnitude and resolution of transmitted light) have been standardized at 3 and 3 nm for both excitation and emission wavelength. The results of the experiment are expressed as average of three different analyses.

3.4.4- Encapsulated drug: fluorescence stability analysis

Fluorescence emission of curcumin in different biological milieu has been analyzed to show the efficacy of nanoparticle protection of the drug from external biological environment and degradation. Acetate buffer, 20 mM (pH = 4.75), phosphate buffer, 20 mM (pH = 7.40), ammonium buffer, 20 mM (pH = 9.25), and cell culture Dulbecco's Modified Eagle's medium (DMEM; pH = 7.40) have been prepared. Free curcumin (10 mM in DMSO) has been diluted in all buffers above described (5.0 μM); however, drug-loaded PLGA have been dispersed directly in the medium (25 μg mL^{-1}, drug content 5.0 μM) and the empty PLGA at the same concentration as a reference. Fluorescence emission spectra have been recorded using with the same instrument described above in a wavelength range from 490 to 700 nm (λ_{ex} = 480 nm).

3.4.5- Raman Spectroscopy analysis

Raman spectra have been recorded using an Aramis Horiba Jobin-Yvon micro-Raman spectrometer equipped with solid state lasers operating at 532 nm, 633 nm and 785 nm and with a DuoScan mapping mode configuration.

The analysis of Curcumin as free compound or encapsulated in PLGA has been recorded on dry powder using a 633 nm laser line (12.5 mW of power) and a 50X objective.

3.4.6- In vitro drug release profiles

In vitro drug release of curcumin from PCNPs has been evaluated by the dissolution technique [7,8]. Release studies have been performed at 37 °C in either acetate buffer, 20 mM (pH = 4.75), phosphate buffer, 20 mM (pH = 7.40) and ammonium buffer, 20 mM (pH = 9.25); each buffer has been supplemented with 2 wt.% albumin bovine serum to mimic a biological environment and enhance drug dissolution. A nanoparticulate dispersion of drug-loaded PLGA NPs (1 mg mL^{-1}) has been solubilized in all buffers at 37 °C in a closed glass tube, to prevent evaporation of the solvent, under mild stirring. Samples have been withdrawn (1.0 mL) at regular time intervals and, after nanoparticle centrifugation, solubilized curcumin in each sample analyzed. Subsequently, NPs have been inserted again in the reactor with fresh medium (1.0 mL) to create a sink condition; the medium has been completely replaced with fresh medium every 24 h. Samples have been spectrophotometrically quantified at 420 nm; all measurements have been performed in triplicate and the average values taken. The kinetic analysis of the release data has been processed using Peppas−Korsmeyer's model (Equation 3) [8]:

$$f_t = k \cdot t^n + [b]$$

$$\log f_t = \log k + n \cdot \log(t) + [\log b] \qquad \text{(eq. 3)}$$

where f_t is the fractional amount of drug release, *k* is the release constant, *n* is the release exponent, *t* is the time of release and *b* is coefficient of drug “burst effect release”; this last parameter must be inserted in all calculations because the release kinetic from PLGA NPs is critically affected by the burst effect in particular during the first 8 h of incubation.

3.5 Cell cultures

Breast cancer MCF7 (HER2+) and MDA-MB468 (HER2−) and lung cancer A549 (TfR+) have been used respectively. Cells have been cultured in 50 vol.% Dulbecco's Modified Eagle's Medium (DMEM) and 50 vol.% F12, supplemented with 10 wt.% fetal bovine serum, L-glutamine (2 mM), penicillin (50 UI mL^{-1}), and streptomycin (50 mg mL^{-1}) at 37 °C and 5% CO_2 in a humidified atmosphere and subcultured prior to confluence using trypsin/EDTA.

Promonocitic U937−13 cell clones and U937−10 have been used as uPAR positive and uPAR negative targets, respectively [9]. Cells have been cultured at 2×10^5 cells mL^{-1} in RPMI 1640 medium supplemented with 10 wt.% fetal bovine serum, L-glutamine (2 mM), penicillin (50 UI mL^{-1}) and streptomycin (50 mg mL^{-1}) at 37 °C and 5% CO_2 in a humidified atmosphere.

3.5.1- Flow cytometry (FACS)

To assess the efficiency of targeted delivery of NPs bearing antibodies, proteins and peptides, the binding toward cancer cells receptors (HER2, TfR and uPAR) has been evaluated by flow cytometry [10,11]. Cells have been cultured on a 12-multiwell plate until subconfluence (80%). Then, equal aliquots have been incubated 15 min at 37 °C in the presence of one of the following: (i) positive control dye-labeled free targeting ligand (5.0 µg mL^{-1}); (ii) dye-labeled fully PEGylated NPs without targeting ligand, (around 100 µg mL^{-1} NPs); (iii) dye-labeled active bioconjugated NPs, (around 100 µg mL^{-1} NPs). After different incubation times, cells have been washed once with culture medium (1.0 mL), twice with PBS (1.0 mL) and then, treated with typsin for 5 min at 37°C. Digestion with trypsin has been stopped with culture medium and cells have been transferred in FACS tubes and fixed with paraformaldehyde solution 4 wt.% in PBS (0.5 mL) for 20 min in the dark at RT.

Later, cells have been washed once with PBS (1.0 mL) and finally resuspended in PBS (0.5 mL) for FACS analyses.

On the contrary, when NPS haven't been dye labeled, cells have been incubated for 30 min at 4 °C in a blocking solution (PBS, 2 wt.% with Bovine Serum Albumin) and immunodecorated with FITC-conjugated antibody (1.0 µL) to whole murine IgG (MP Biomedicals) for 30 min at 4 °C. The excess of secondary antibody has been removed by washes six times with PBS (1.0 mL). Labeled cells have been resuspended with PBS (0.5 mL) and analyzed on a FACS Calibur flow cytometer (Becton Dickinson). Twenty thousand events have been acquired for each analysis, after gating on viable cells, and isotype-control antibodies have been used to set the appropriate gates.

3.5.2- Confocal laser scanning microscopy (CSLM)

Cells have been cultured on collagen (Sigma Aldrich, Germany) precoated coverglass slides until subconfluence.(80%). Then, cells have been incubated at fixed time points at 37 °C with free dye-labeled free targeting ligands (5.0 µg mL^{-1}) and with equal amounts targeting ligand immobilized onto NPs. Later on, cells have been washed with PBS (1.0 mL), fixed for 20 min with 4 wt.% paraformaldehyde solution in PBS and treated for 10 min with 0.1 M glycine in PBS. A blocking step has been performed for 1 h at RT with a PBS solution supplemented with 2.0 wt.% bovine serum albumin and 2.0 wt.% goat serum. Nuclei have been stained with DAPI (4′,6-diamidino-2-phenylindole) diluted in PBS (200 ng mL^{-1}) supplemented with 0.1 wt.% Saponin for 20 min at RT. Membranes have been stained with DiD oil at a 1:300 dilution in PBS by incubating 30 min at 37 °C. Microscopy analyses have been performed with a Leica SP2 AOBs microscope confocal system; images have been

recorded with 63× magnification oil immersion lenses at 1024 × 1024 pixel resolution; picture's scale bar has been set at 10 µm.

3.5.3- Cellular toxicity evaluation

To test NPs toxicity, MTT assay was performed. Cells (1.5×10^3) have been seeded in 96-multiwell plate and, 24 h after plating, incubated with different NPs concentrations (e. g., 50 and 100 µg mL^{-1}); the culture media has been removed and the toxicity has been monitored after until to 72 h of NPs exposure. According to the manufacturer's instructions (CellTiter 96 Non-Radioactive Cell Proliferation Assay, Promega), at the end of each exposure time, the tetrazolium salt has been added and the formazan product has been detected after 4 h incubation, by means of a plate reader at fixed wavelength (λ= 595 nm). Results are normalized with untreated control and expressed as the mean absorbance of ± SEM of three independent biological replicates.

3.5.4- Cell death analysis: Apoptosis measurement

Cells have been incubated 24 h at 37 °C in the presence of different NPs concentrations (e.g., 20 µg mL^{-1} or 100 µg mL^{-1}). After the incubation time, cells have been washed twice with PBS (1.0 mL) and treated for FACS analysis according to PE Annexin V Apoptosis Detection Kit I manufacturer's protocol (Becton Dickinson Biosciences). Briefly, cells have been resuspended in 20 mM Binding Buffer and incubated 15 min in presence of Annexin-PE (5.0 µL) and 7-aminoactinomycin D (5.0 µL). Furthermore, cells have been washed with PBS (1.0 mL) and subsequently analyzed at the flow cytometer. Twenty thousand events have been recorded for each analysis, after gating on viable cells and analyzed with CellQuest Pro Software (BD). Therefore, we consider cell death as the populations positive for Annexin V and

for 7AAD staining alone and together. The results are expressed as means ± standard deviation of the mean of 3 individual experiments.

3.5.5- Determination of drug release by FACS analysis

MCF7 cells have been seeded in 6-multiwell plates (1.0×10^5 cells each well) and, 24 h after plating, cells have been incubated with curcumin-PLGA NPs (100 μg mL^{-1}, corresponding to 20 μM drug), free curcumin (20 μM) or left untreated as negative control. After 24 h incubation, cell culture medium containing NPs or free curcumin has been removed and cells have been washed three times with PBS (1.0 mL); freshly culture medium without either NPs or curcumin has been added. Total cell fluorescence has been monitored sampling cells at 24, 48, or 72 h after incubation by FACS analysis. Cells have been washed with PBS (1.0 mL), trypsinized, and collected in FACS tubes in PBS (0.5 mL). Sample acquisition has been performed and analyzed with CellQuest Pro Software (BD), recording at least twenty thousand events. The results are expressed as means of 3 individual experiments.

3.5.6- Cell cycle analysis

MCF7 cells have been cultured in 6-multiwell plates and incubated with drug-loaded PLGA NPs (100 μg mL^{-1}, corresponding to 20 μM drug), empty PLGA NPs (100 μg mL^{-1}) and free curcumin at 20 μM for 24, 48, and 72 h. Later, cells have been collected and fixed in 70 vol.% ethanol in PBS (2.0 mL). For DNA staining, after ethanol removal, cells have been incubated overnight at 4 °C with propidium iodide 10 (μg mL^{-1}) and RNAse-A (18 μg mL^{-1}). Sample acquisition has been performed using the flow cytometer equipped with doublet-discriminator module (FACS Calibur; Becton Dickinson, San Jose, USA), and the DNA content has been analyzed by Flowjo software (TreeStar Inc. OR, USA).

Related References

[1] Scott, E.; “Characterization of nanoparticles intended for drug delivery”; McNeil, © Humana Press. New York (NY, USA), **2011**.

[2] Delgado, A. V.; Gonzales-Caballero, F.; Hunter, R. J.; Koopal, L. K. and Lyklema, J.; *J. Colloid. Interf. Sci*. **2007**, *309*, 194–224.

[3] Halling, P. L. and Dunhill, P.; *Biotechnol. Bioeng*. **1979**, *21*, 393–416.

[4] Soto-Kantu, E.; Cueto, R.; Koch, J. and Russo, P. S.; *Langmuir*. **2012**, *28*, 5562–5569.

[5] Riddles, P. V.; Blakeley, L. R.; and Zerner, B.; *Anal.Biochem*. **1979**, *94*, 75–91.

[6] Wiechelman, K. J.; Braun, R. D. and Fitzpatrick, J. D.; *Anal. Biochem*. **1988**, *175*, 231–237.

[7] D’Souza, S. S. and DeLuca, P. P. *Pharm. Res*. **2006**, *23*, 460–474.

[8] Costa, P. and Sousa Lobo, J. M.; *Eur. J. Pharm. Sci*. **2001**, *13*, 123–133.

[9] Laemmli, U. K.; *Nature*. **1970**, *227*, 680–685.

[10] Mazzucchelli, S.; Colombo, M.; De Palma, C.; et al.; *ACS Nano*. **2010**, *4*, 5693–5702.

[11] Salvati, A.; Pitek, A. S.; Monopoli, M. P.; *Nat*. *Nanotech.* **2013**, *8*, 137–143.

Third Section

Chapter IV

Multiple Presentation of ScFv800E6 on Silica Nanospheres Enhances Targeting Efficiency Toward HER2 Receptor in Breast Cancer Cells

Contents

4.1 The Human Epidermal Growth Factor Receptor HER2: Action and Signaling Inhibition

Some breast cancers produce protein biomarkers (*e.g.* estrogen receptor, progesterone receptor, and HER2), on which therapeutic decisions are made. The use of NPs is expected to allow for the simultaneous detection and quantification of several proteins in small tumor samples, which will ultimately enable the tailoring of specific anticancer treatment to an individual patient's specific tumor protein profile, potentially leading to a personalized medicine [1]. To design a diagnostic approach to breast carcinoma using nanoagents in humans, it is necessary to fulfill several

criteria for their utilization. These include high resolution and the accuracy and sensitivity of detection, which might be provided by using NPs coated with specific monoclonal antibodies against protein biomarkers overexpressed by breast cancer cells, such as HER2 receptor. The human epidermal growth factor receptor 2 (HER2) is a transmembrane tyrosine kinase receptor overexpressed in 25−30% of human breast cancers. HER2 includes an extracellular domain at which ligand binding occurs, an α-helical transmembrane segment and an intracellular protein tyrosine kinase domain [2]. An essential requirement for its function and signaling activity is the receptor dimerization (pairing) [2,3]. Indeed, after ligand binding to the extracellular domain, a conformational rearrangement occurs, exposing the dimerization domain that forms the core of the dimer interface with another receptor (Figure 4.1-A). The receptor dimerization is responsible for the transactivation of the tyrosine kinase portion of the dimer moiety as each receptor activates its partner by phosphorylation.

In many tumor cells, HER2 is overexpressed or constitutively activates and stimulates many intracellular signaling proteins and physiological pathways, such as the mitogen-activated protein kinase (MAPK), phosphoinositide 3 kinase/Ak transforming factor (PI3K/Akt), mammalian target of rapamycin (mTOR), Src kinase, and STAT transcription factors (signal transducers and activators of transcription) [5,6]. However, pathology arises here whereas the usual negative regulatory loops that function in normal cells are impaired [7]. Two key signaling pathways activated by the ErbB family dimers are the MAPK pathway, which stimulates proliferation, and the PI3K/Akt pathway, which promotes tumor cell survival. The activation of the MAPK pathway leads to the transcription of genes that drive cellular proliferation, migration, differentiation and angiogenesis [2,3].

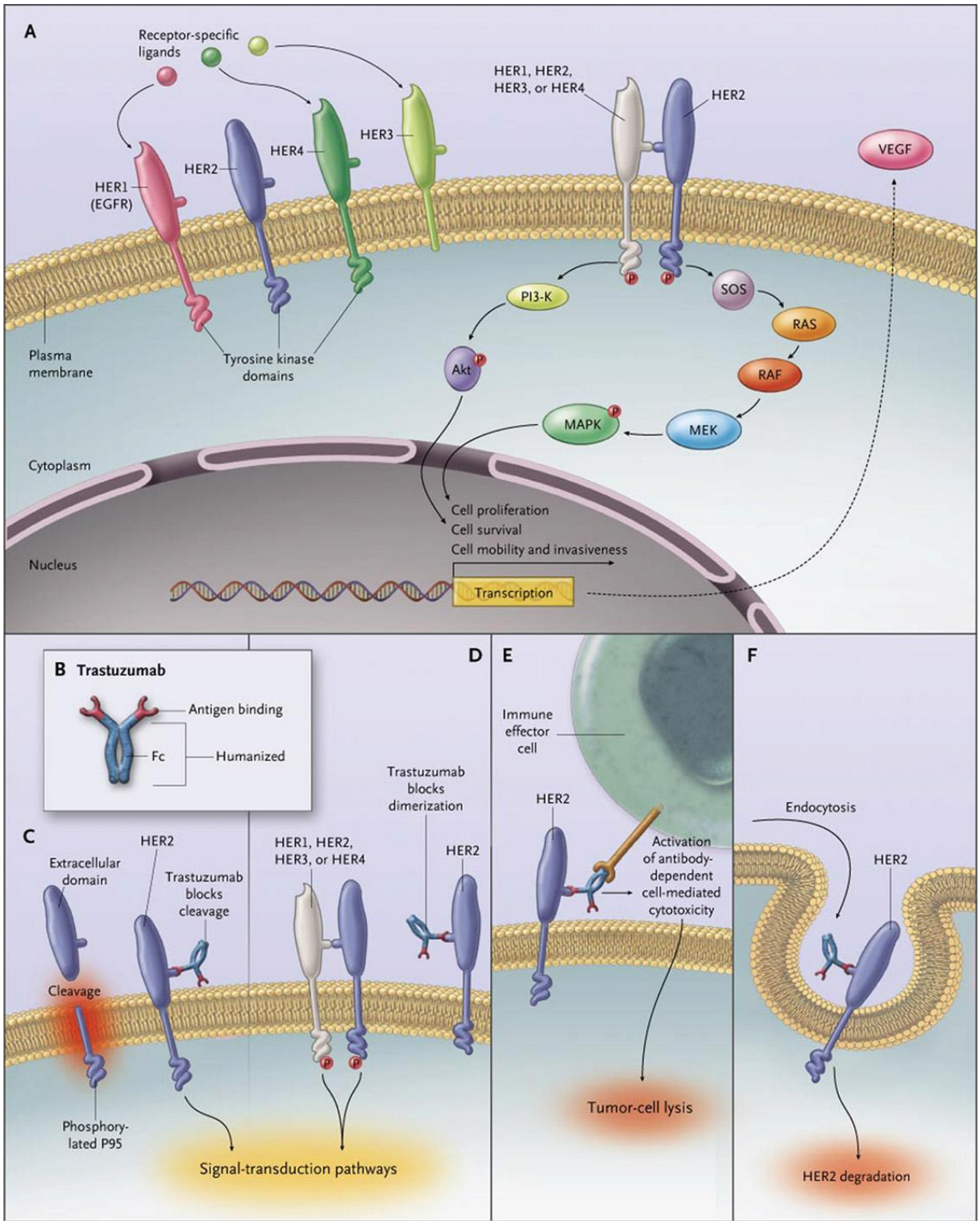

Figure 4.1. Signal transduction by the HER2 family and mechanism of action of Trastuzumab.
Panel A) The four members of the ErbB family: HER1, HER2, HER3, HER4. Panel B−F) The most well-documented potential mechanisms of action of Trastuzumab-®. [4]

Signaling through the PI3K/Akt pathway leads to the activation, through phosphorylation, of many other proteins that initiate processes to enable cell survival, suppression of apoptosis and cell cycle control.

Extracellular domain of HER2 has been the target of several monoclonal antibodies created in order to inhibit the proliferation of human cancer cells. The most popular **Trastuzumab-®** (Genetech-Roche) is a humanized monoclonal antibody consisting of two antigen-specific sites that bind to the juxtamembrane portion of the extracellular domain of the HER2 receptor preventing the activation of its intracellular tyrosine kinase [8] (Figure 4.1-B−F). There are several possible mechanisms through which trastuzumab may decrease HER2 signaling. Some works showed that trastuzumab mediates the activation of antibody-dependent cellular cytotoxicity (ADCC). The presence of ADCC is mainly due to the activation of natural killer (NK) cells, expressing the Fc gamma receptor, which can be bound by the Fc domain of trastuzumab [9,10]. However, Molina and coworkers demonstrated that, in HER2 overexpressing breast cancer cell lines, trastuzumab may follow an alternative mechanism of action involving blockage of the proteolytic cleavage of HER2 extracellular domain and p95 serum-release by inhibiting metalloproteinase activity [11]. A diminished signaling mechanism may result from trastuzumab-mediated internalization and degradation of the HER2 receptor [12]. Finally, trastuzumab treatment provokes cell cycle arrest during the G1 phase, with a concomitant reduction of proliferation. This event is accompanied by the reduced expression of proteins involved in the sequestration of the cyclin-dependent kinase inhibitor p27kip1, including cyclin D1. This results in the release of $p27_{kip1}$ including cyclin D1. This results in the release of $p27_{kip1}$, allowing it to bind and inhibit cyclin E/cdk2 complexes [13].

4.2 Efficient Production of anti-HER2 scFv Antibody Variant for Targeting Breast Cancer Cells

A recent approach alternative to the combination of chemotherapeutics with entire IgGs consists in conjugating antibody portions, including diabodies, scFv fragments, V_H/V_L domains and affibody small molecules, with drugs and/or diagnostic markers with the aim to achieve an efficient delivery to the injured site through selective targeting of tumor cells. In particular, scFv variants have been utilized to target molecular processes associated with carcinogenesis, as well as to improve gene transfer efficiency, and are thus becoming increasingly popular due to the high target selectivity and reduced immunogenicity compared to whole antibodies. Several ongoing clinical trials are exploiting various phage display-derived scFvs for targeting breast cancer [14,15].

In a recent paper from our group [16] the authors described the production and purification of a soluble anti-HER2 scFv antibody secreted by the yeast *Pichia Pastoris*. The gene encoding scFv800E6 with an additional 6× His_tag tail at the 3′-end was inserted into the expression vector pPICZα and transformed in *P. pastoris* (Figure 4.2).

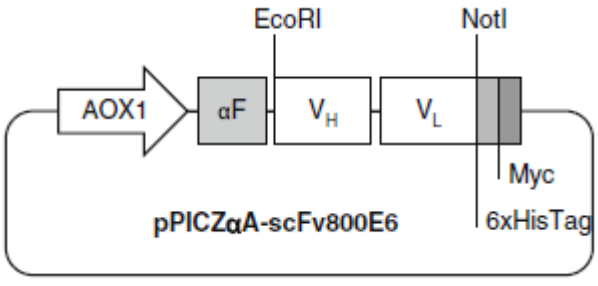

Figure 4.2: Schematic diagram of the pPICZαA-scFv800E6 expression vector.
The recombinant gene encoding scFv800E6 is inserted into the pPICZαA vector under the control of the alcohol-oxidase-1 (AOX1) promoter, in frame with the prepro α-factor signal sequence (α*F*) and with myc and histidine (6xHis) tags [16]

The highest expression of scFV800E6 was obtained in the culture medium after 48 h of induction; moreover, the use of the yeast *P. pastoris* proved very valuable as an expression system, allowing the isolation of almost 10 mg L^{-1} of highly purified antibody, remarkably higher than previously reported data. The functionality of purified anti-HER2 scFv has been assessed by flow cytometry and confocal laser scanning microscopy on HER2(+) MCF7 breast cancer cells, showing good affinity and high selectivity for the target membrane receptor (Figure 4.3).

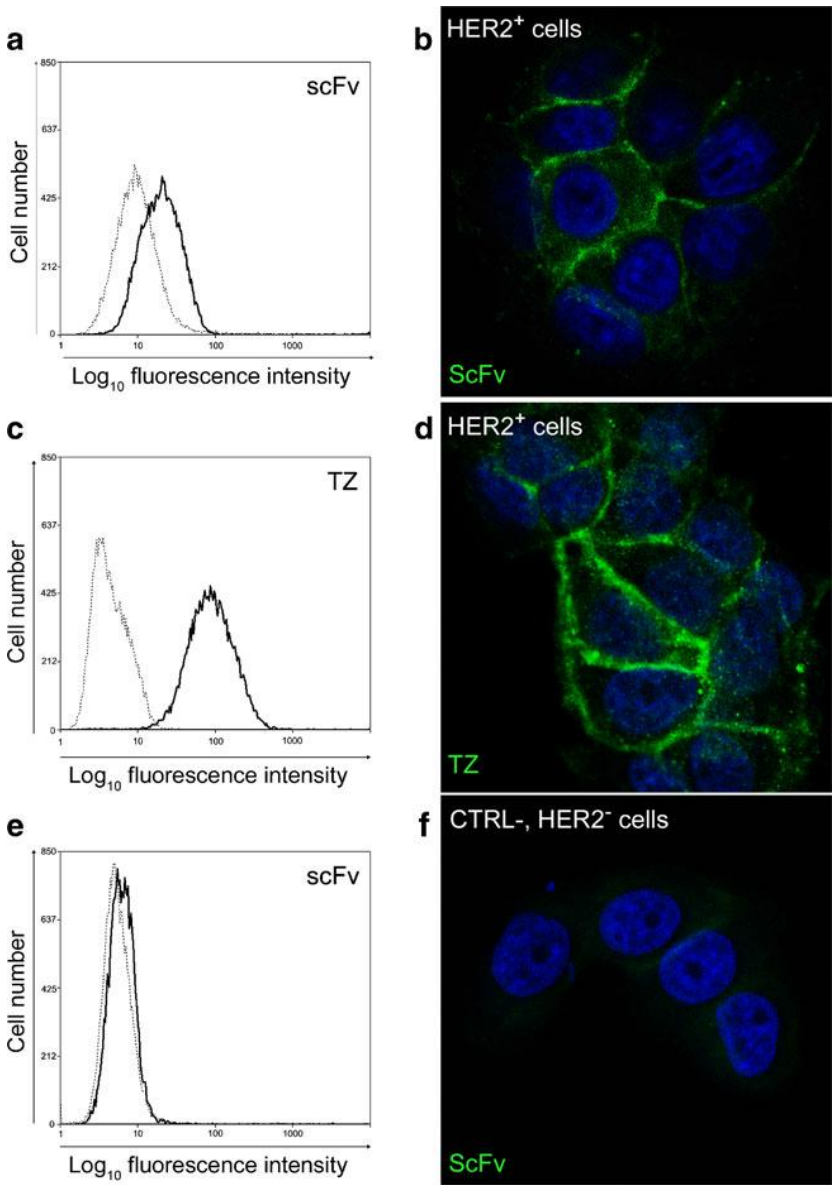

Figure 4.3: ScFv800E6 binding specificity to HER2.
Cells are incubated with scFv or Trastuzumab (Tz) and processed for flow cytometry (a, c, e) and for immunofluorescences (b, d, f). TZ incubation on HER2+ cells was used as positive control (c, d), while scFv incubation on HER2− cells as negative control (e, f). ScFv is revealed by a FITC-conjugated antibody to whole

murine IgG (a–b, e–f) and TZ by an anti-human Alexa fluor 488 (c–d). In panels (a), (c), and (e), dashed lines represent the isotype-control antibodies, while continuous lines represents scFv (a, e) or TZ (c). Nuclei were stained with DAPI (b, d, f). Scale bar=10. [16]

These results confirm that antibody fragments can highlight the potential role of scFv800E6 in diagnostic and therapeutic applications. Starting from these interesting findings, even if this work is not the main synthetic contents of this thesis, I exploited to highlight our biotechnological knowledge to better understand the role of antibody-functionalized NPs in breast cancer diagnosis. In addition, the schematic design of such biomolecules represents a capital awareness for the specific construction of several potential nanobioconjugate systems. For this purpose, the current research in our laboratory is aimed at developing different nanoconstructs based on multifunctional NPs for targeted detection of breast cancer cells, where the particle is basically the source of the signal, meanwhile the targeted recognition is primarliy implemented by the presence of selected biomolecules properly attached on the surface of the nanovector.

According to this goal, I envisioned to develop this project involving antibody fragments such as single-chain antibodies, which are of particular interest as partners of nanoparticles capable of specifically targeting tumor cells. ScFv800E6 is a single-chain variable fragment specific for the HER2 oncogene product. In particular, I reasoned that two important feature could be combined to these aim: 1) many literature data demonstrated its specificity and high affinity comparable, yet lower, to that of the parental monoclonal antibody Trastuzumab [17,18]; 2) the presence of a His_Tag at the C terminus is suitable to be further exploited for scFv conjugation with diagnostic agents and nanostructured delivery systems to develop an scFv nanoconjugate for the detection of breast cancer.

4.3 Multimodal synthesis: different functionalization of silica nanospheres

Spherical silica nanoparticles (termed here SNP) have been synthesized and separately functionalized with an anti-HER2 scFv800E6 antibody as anticipated in the previous paragraph, by two different strategies: 1) localized His_Tag recognition, leading to an oriented protein ligation, and 2) glutaraldehyde cross-linking, exploiting a statistical reactivity of lysine amine groups in the primary sequence of the molecule. Our goal has been the targeting efficiency of both nanoconstructs in comparison with free scFv800E6 and the whole Trastuzumab antibody, using MCF7 cells as a model HER2 positive breast cancer cell line.

Bare **SNP** have been prepared using the Stöber process, [19] which has been well-known to produce spherical SiNPs with relatively narrow size distributions. In this work, SNP has been synthesized with an average diameter of 60 nm, as determined by TEM and SEM (Figure 4.4).

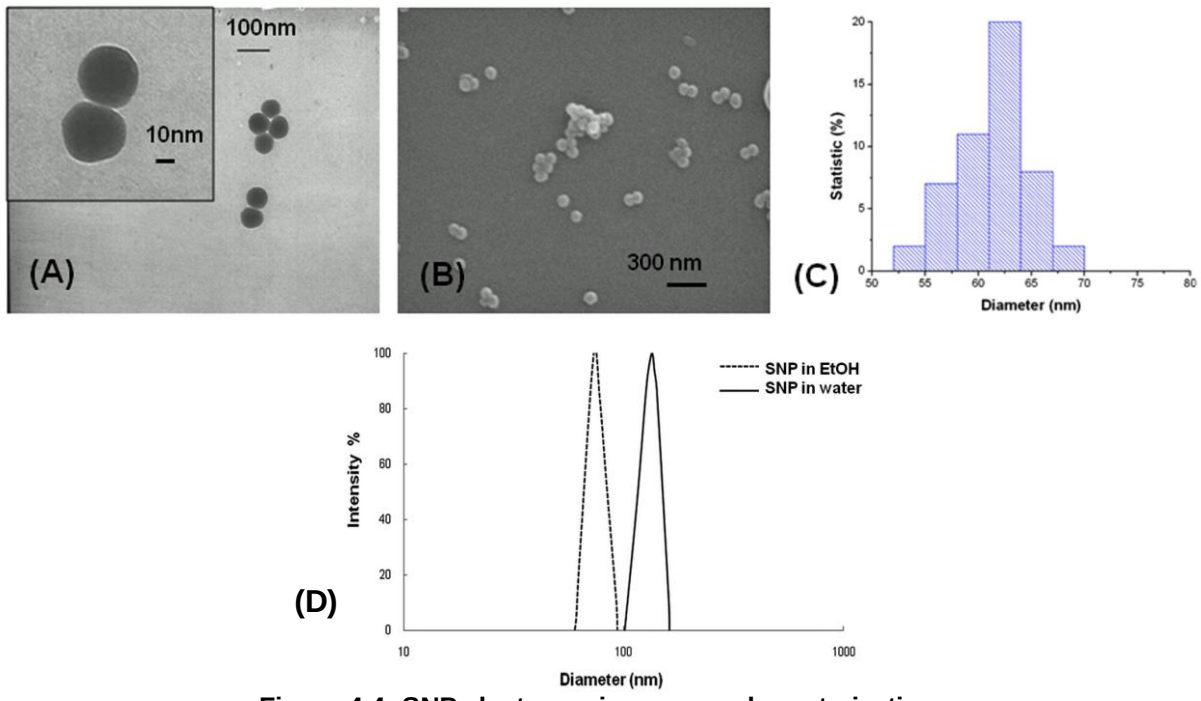

Figure 4.4: SNP electron microscopy characterization.
(a) Transmission Electron Microscopy image; (b) Scanning Electron Microscopy picture; (c) Statistic geometrical distribution analysis; (d) Dynamic light scattering distribution of SNP in ethanol (dashed line) and water (bold line).

Hydrodynamic diameter of SNP after the synthesis has been evaluated both in ethanol (78.3 ± 2.2 nm; PDI 0.132) and in deionized water (133.8 ± 20.9 nm; PDI 0.232) respectively; the NPs resuspension in water causes a little bit of NPs aggregation since that NPs have been dried after from the ethanol phase, as reported in several experimental papers (see exp. part). Unfortunately, by our experience completely SNP dryness influences negatively about the colloidal stability, thus inducing the formation of some NPs aggregates (which have been removed by a quick centrifugation at low speed before any SNP functionalization), The surface charge is strongly negative since that at physiological pH (ζ −35.85 ± 0.64 mV in 1 mM aqueous NaCl, pH 7.25) surface acidic silanols, exposed to the solvent, are completely deprotonated. This condition allows for a long term stability of this suspension in water due to an electrostatic repulsion.

The surface functional groups of SNP, *e.g.* silanol (Si−OH) and ethoxy silanol (Si−OEt), have been converted to different functionalities with the same silane chemisty of catalytic hydrolysis and condensation. A selection of ligands have been chosen to achieve first a fully inhert pegylated surface (**SPEG**), secondly a surface exploiting a specific coordination ligand for an oriented conjugation of His_Tagged proteins (SNP1) and finally an aminated surface for an unoriented conjugation of proteins (SNP2). To this purpose, at first several organic linkers have been synthesized as carefully described in the experimental section at the end of this chapter.

In the first method (Figure 4.5), a solution of APTS-PEG2000 complex has been prepared and reacted in a molar ratio 1:1 with a second heterobifunctional linker namely APTS-NTA under alkaline condition. According to literature data [20], PEG increases the particle solubility in buffered media and, at the same time,

reduces nonspecific adsorption of proteins. The second linker instead has the role to conjugate NPs surface through silanol groups and, in the counterpart, the nitriloacetic acid groups (NTA) generate the **SNP1** nanoconjugate that promotes the active chelation of bivalent $NiCl_2{-}6H_2O$ (Ni^{2+}-NTA).

The 6 × His-affinity tag, constructed at the tail of ScFv800E6 protein, is the ligand which has been chosen to achieve the effective oriented conjugation, forming **SNP−HT**. The oligohistidine affinity tag (His_Tag) is widely used for the purification of his-tagged protein over nickel nitrilotriacetic acid (Ni-NTA) beads, [21] and affinity labeling of his-tagged proteins with a fluorophore-conjugated NTA system (note, a small molecule, not a nanoparticle) has been reported to give proteins that retain their activity and can be used in FRET assays. For example in a recent paper a Cy5-NTA system has been used to label a His−Tagged protein site specifically and obtained good results from fluorescence anisotropy measurements and FRET experiments [22].

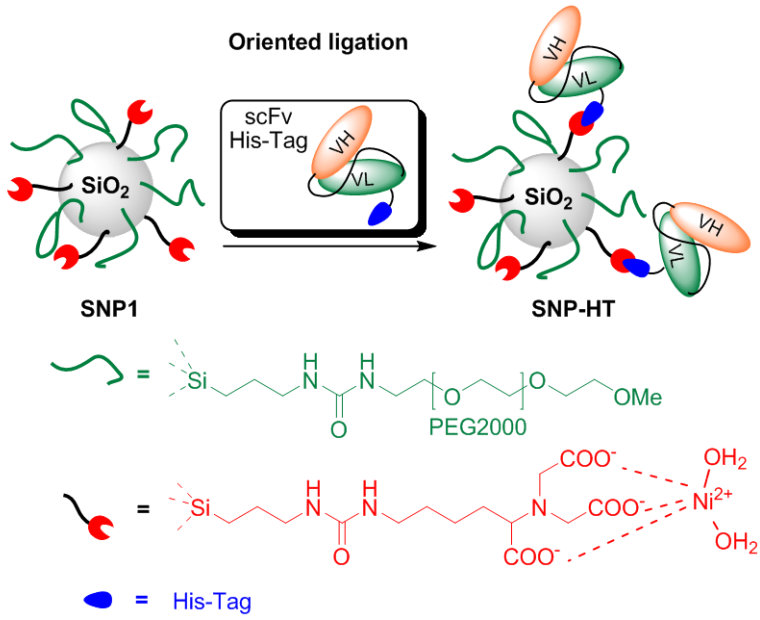

Figure 4.5: SNP functionalization: Method 1.
SNP1 functionalized with Ni-NTA groups tightly and specifically interact with scFv histidine tag leading to an oriented protein immobilization (SNP-HT).

In the second method (Figure 4.6), a mixture of the same APTS-PEG2000 complex in a molar ratio 1:1 with APTES (3-aminopropyl-triethoxysilane) have been condensed on the surface of SNP, generating the intermediate **SNP2** [23]. The estimation of free amino groups exposed on the surface of NPs has been performed with a colorimetric test described in the literature for this class of compounds, involving the reaction of picrylsulfonic acid [24]; this molecules could be covalently attached to the free amino groups but, at the same time, the electron substitution, activated on secondary amine bond by three nitro groups on the phenyl ring, can be easily reconverted to the primary amine by NaOH catalytic hydroxylation. The product derived from this reaction is picric acid, and by its determination of residual absorbance, it is possible to calculate the effective amino groups available for following NPs biofunctionalization.

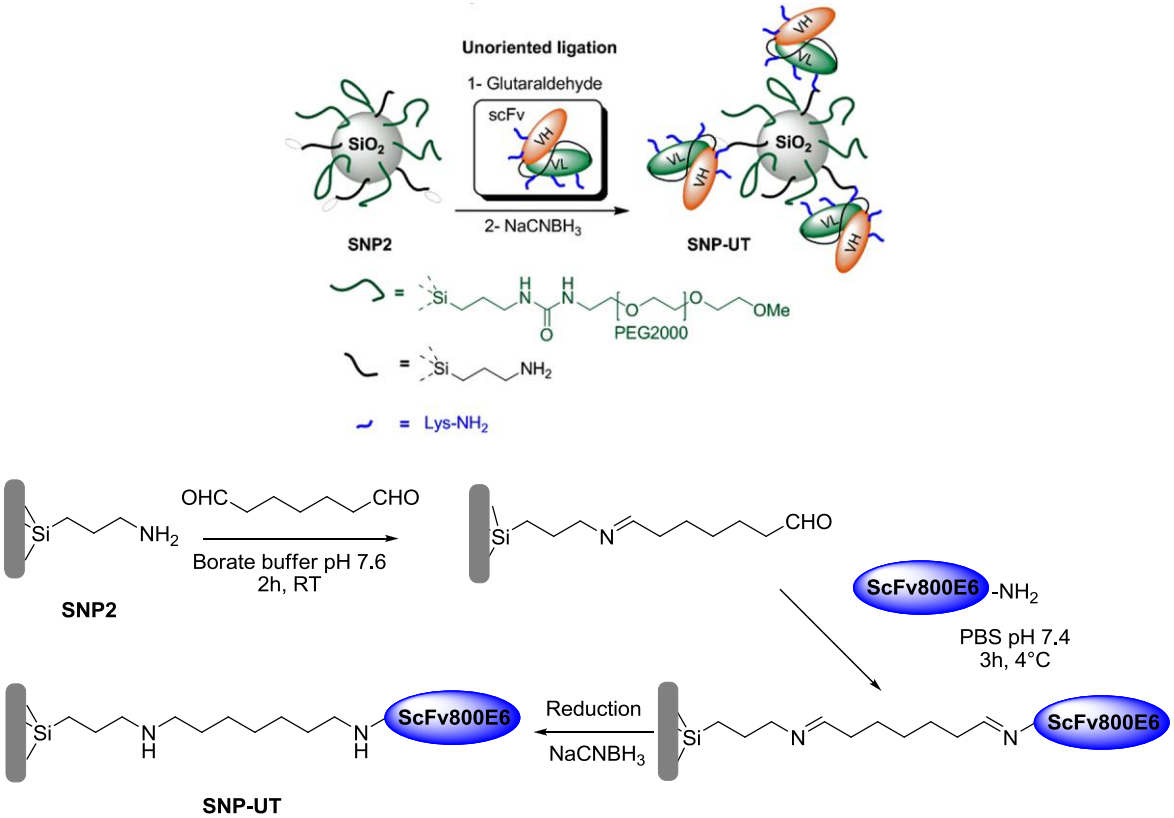

Figure 4.6: SNP functionalization: Method 2.
SNP2 are functionalized with free exposed available amino groups groups. Glutaraldehyde addition creates an intermediate imine between SNP2 amine and available amine of lysine residues of scFv. The intermediate is reduced by $NaCNBH_3$ generating a stable secondary amine (SNP-UT).

In the final step, in order to generate an unoriented silica bioconjugate (**SNP−UT**), SNP2 have been reacted with amino groups exposed on the surface and the one's of lysine residues of scFv800E6 by glutaraldehyde cross-linking reaction, followed by imine reduction with $NaCNBH_3$, forming a stable secondary amine [25].

The hydrodynamic diameter and the colloidal stability during time, of all kind of functionalized SNP, have been evaluated determined by dynamic light scattering (Figure 4.7). Hence, the pH dependent behavior of SNP, SNP1, SNP2, and SPEG has been investigated in the 2−9 pH range; all nanosilica preparation have been tested once a day for a whole week. All samples tested did not exhibit the formation of critical aggregates in particular between the physiological buffers pH 4−9, however in some cases a little bit of aggregation has been observed (PDI ≈ 0.240, results expressed in figure are indicated as the mean average population in Intensity%). Also ζ-potential of SNP, SPEG, SNP1, and SNP2 in water in the 2−9 pH range has been also investigated. From pH 5 to 9, SNP were strongly negatively charged (−35.85 ± 0.64 mV), whereas at pH 4 and lower, the charge approached neutrality (−6.40 ± 1.77 mV). Similar behavior has been observed for SPEG, −25.01 ± 0.38 mV at pH 7 due to the charge-shielding effect of the PEG layer on the nanoparticle surface. SNP1 showed, on the contrary, a remarkably low surface charge at pH 7 (−13.64 ± 0.74 mV), in accordance with the presence of the Ni^{2+} ions chelated on the carboxylic groups of NTA; The charge did not appreciably change in the pH range tested but, this effect caused a little bit of NPs aggregation; however eventually formed bigger particulates have been removed by NPs centrifugation at low speed before the conjugation with the biomolecules scFV800E6. SNP2 were negatively charged (−25.23 ± 1.03 mV) at pH 7−9; nevertheless, below pH 5, a gradual shift of

the charge to positive values has been observed, in line with the presence of protonated amino groups of APTES in acidic conditions.

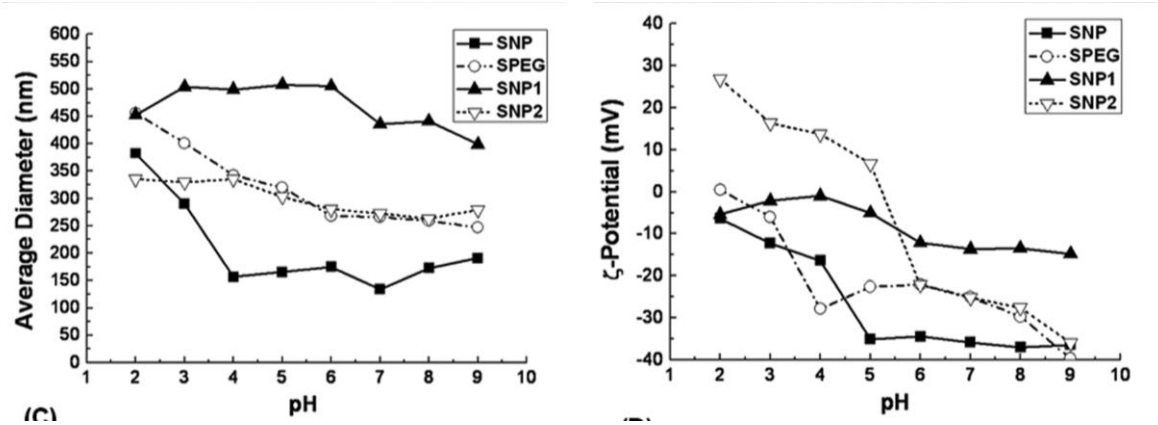

Figure 4.7: Colloidal suspension behavior.
DLS (left)and ζ-potential measurements (right) of SNP, SPEG, SNP1, and SNP2 as a function of pH in aqueous solution.

4.4 ScFv600E6 bioconjugations: assessing targeting efficiency towards HER2 receptor

After bioconjugations, the amount of scFv800E6 has been evaluated by protein assay of supernatants at 280 nm, by using a calculated ε at 280 nm of 55 600 M^{-1}. With this assay it has been estimated that 26 μg mg_{NP}^{-1} for SNP−HT (6 molecules per nanoparticle) and 43 μg mg_{NP}^{-1} for SNP−UT (10 molecules per nanoparticle). The immobilization of scFv on SNP−HT has been also confirmed by dot-blot assay (Figure 4.8) where different amount of scFv and SNP−HT have been immobilized onto a membrane and then probed with anti-Myc-HRP antibody. Intensities of immunoreactive spots of SNP−HT and 0.1 μg of free scFv could be compared; this result reasonably fits with the amount of bound scFv estimated by the protein assay in solution. Moreover, to exclude the release of chelated scFv from SNP−HT thus assessing the stability of this synthetic method, the previous immunostaining have been performed incubating SNP−HT from 1 to 48 h at 37 °C. Nanoparticle-free supernatants have been filtered onto the membrane and probed with an anti-Myc-HRP antibody. The negative result of this experiment confirmed that His_Tag scFv conjugation on SNP−HT is stable within 48 h of incubation at 37 °C. The same test has been performed with SNP−UT exploiting the same result.

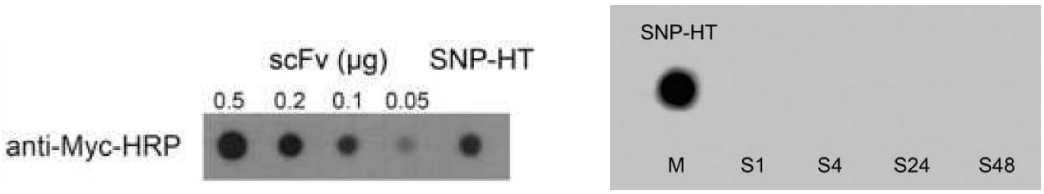

Figure 4.8: Dot-Blot assay of SNP-HT complex.
(Left panel) Different amounts of scFv800E6 (0.5, 0.2, 0.1, and 0.05 μg) and an aliquot of SNP-HT have been filtered onto a PVDF membrane; then probed with anti- Myc-HRP antibody and revealed with an ECL substrate. (Right panel) The same assay has been tested for on SNP-HT and particle-free supernatant until to 48 hs of incubation at 37°C.

Furthermore, to assess the outcome of multivalent presentation of scFv on silica, flow cytometry has been used to evaluate SNP−HT and SNP−UT binding toward HER2 receptor in a breast cancer cell line model (MCF7). Therefore, free scFv800E6, the whole anti-HER2 Trastuzumab (TZ) and both types of SiNPs, containing equal amounts of conjugated scFv, have been exposed with HER2 positive MCF7 cells for 15 min at 37°C.

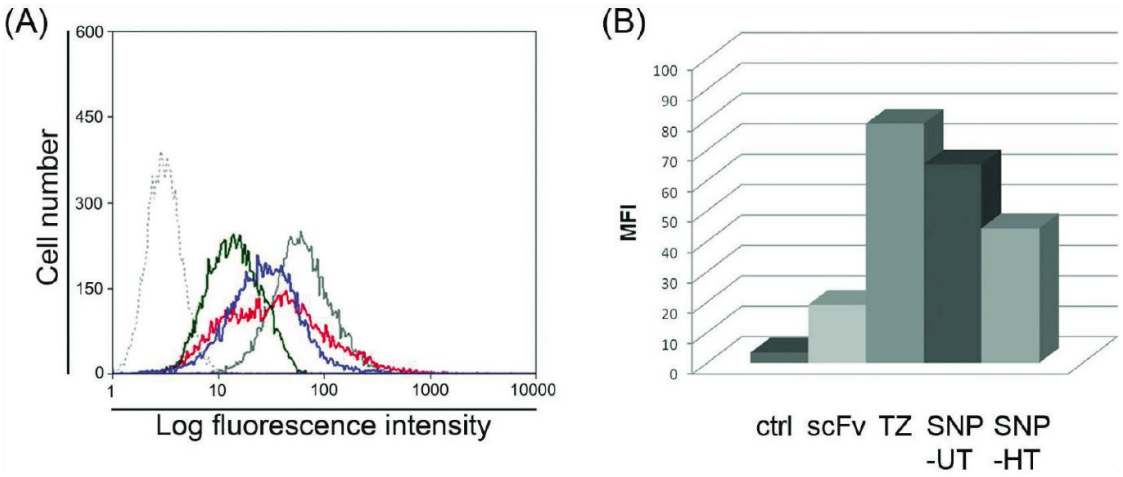

Figure 4.9: Receptor Binding efficiency by FACS analysis.
(Panel A) MCF-7 cells profiles after incubation with scFv (green line), SNP-HT (blue line), SNP-UT (red line), trastuzumab (TZ; gray continuous); untreated cells are the negative control (gray dashed line). (Panel B) Mean fluorescence intensity histograms evaluated considering the mean fluorescence intensity (MFI) of the whole cell population.

I would like to point out that, the fluorescence signal has been revealed not properly by the NPs complex, but by staining cells with a FITC-conjugated secondary antibody to whole murine IgG commercially available. For instance the green signal has been revealed only from the direct recognition of the specific immunodecoration of the NPs antibody. A huge shift of fluorescence signal has been observed accounting for an increase in scFv binding efficacy upon multimerization due to SNP conjugation; Gaussian curves have been analyzed and normalized within the whole population of cells (100%) and histogram values of the fluorescent positive cell population have been reported (Figure 4.9).

Both NPs conjugates showed substantial improvement of receptor binding rather then free scFv800E6. Surprisingly, SNP−UT sample showed more than a 3-fold increase in mean fluorescence intensity in comparison with free scFv at the same ligand concentration and, in addition, multimerized scFv exhibited a mean fluorescence intensity very close to that of whole antibody TZ, indicating that a significant improvement in receptor binding capability occurred.

On the other hand, in this case the conjugation strategy exploited for scFv multimerization on SNP (method 1 *vs.* method 2) did not prove to be crucial in enhancing scFv binding efficiency; SNP−HT and SNP−UT exhibited similar profiles by flow cytometry. To account for this unexpected result, the localization of lysines in scFv sequence has been inspected: multiple sequence alignment of scFv800E6 with other scFv sequences available in the NCBI database has revealed that all lysine residues are abundantly preserved. This last fair analysis might indicate that most of these residues are not directly involved in HER2 binding but, more probably, they play a basic structural role in the ligand construction; this hypothesis could explain both the higher amount of scFv conjugated to NPs by glutaraldehyde cross-linking and the unexpected lack of interference towards HER2 receptor binding.

To visually validate flow cytometry data, confocal microscopy has been performed (Figure 4.10). HER2 positive MCF7 cells have been treated with scFv as a positive control, SNP−HT and SNP−UT at a scFv concentration of 25 μg mL^{-1} for 1 h at 37 °C. In parallel, in order to discriminate between specific binding to the membrane receptor thus excluding possible nonspecific adsorption of SNP, MDA-MB468 (HER2 negative) cells have been tested. As HER2 is a transmembrane receptor, we expected and verified that, after a short incubation time, a huge accumulation of SNP−HT and SNP−UT at the level of the cell membrane of HER2

positive cells only have been observed. This result confirmed that nanoparticle capture has been assessed mostly trough specific membrane receptor-mediated internalization.

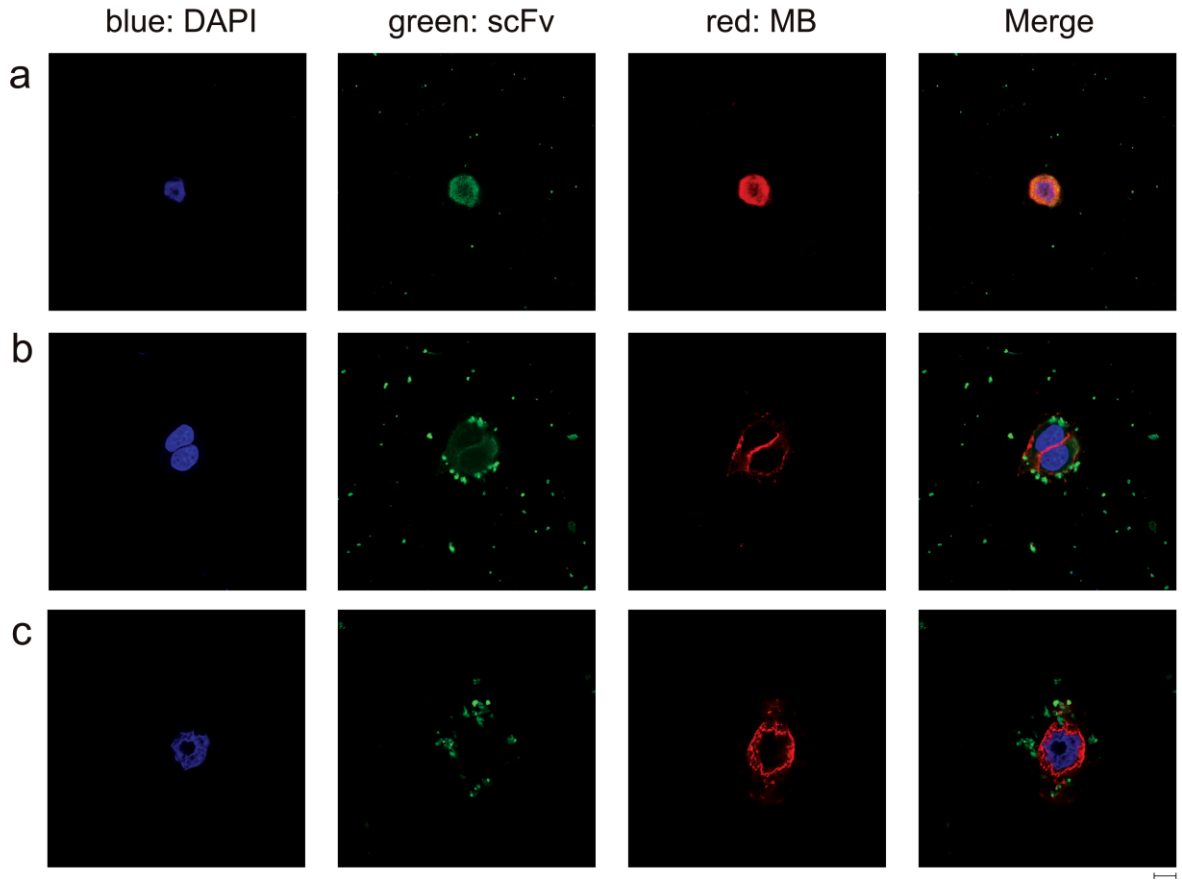

Figure 4.10: Receptor Binding efficiency by CLSM on HER2(+) cells.
SNP-HT (Panels B), SNP-UT (Panels C) and free scFv (Panels A) have been incubated. Nuclei were stained with DAPI (Blue), membranes (Red) and Merge images are shown. Scale bar: 10 µm..

4.5 Conclusions and outlooks

In this chapter a nanoparticle-based multimerization strategy has been presented, with the aim of enhancing the specific binding affinity of engineered scFvs toward cancer cell receptors. So far, a substantial increase in binding efficiency of an antibody fragment has been primarily obtained by either covalently linking the individual scFv unit or by the construction of a multivalent variant by connecting antibody fragment with oligomerization domains. Our strategy has proved of capital interest for the easy and reliable development of a multifunctional hybrid nanoparticles, allowing for multiple presentation of scFv molecules on their spherical surface. Such multifunctional nanoconstruct has been demonstrated very selective in binding a specific transmembrane receptor overexpressed in living cells, namely HER2. These results suggest that the use of controlled inorganic nanoparticles as a multimerization scaffold is capable of enhancing the targeting efficiency to high levels, which could run together with monoclonal antibodies currently adapted in clinical diagnostic practice.

4.6 Nanomaterials Experimental section

4.6.1 Synthesis of Silica Nanospheres (SNP)

Monodisperse silica nanospheres have been obtained as described in previously [1]. Briefly, in a plastic tube a 25% NH_4OH solution in water (12.5 mL) and absolute EtOH (250.0 mL) have been mixed under vigorous magnetic stirring. To the above solution a mixture of TEOS (6.25 mL, 28.0 mmol) dissolved in absolute EtOH (7 mL) has been added at a rate of 1 mL min^{-1} through a dropping funnel. The reaction has been stirred 20 h at RT; at the end of the reaction, the solution has turned milky and the product has been collected from the suspension by centrifugation (8300 rcf, 30 min) and the supernatant discarded. The white particulate has been washed several times with ethanol (4 × 100 mL) and finally dried SNP (100 mg) has been redispersed in EtOH (4 mg mL^{-1}) for further experiments.

4.6.2 Synthesis of Fully PEG-coated Silica (SPEG)

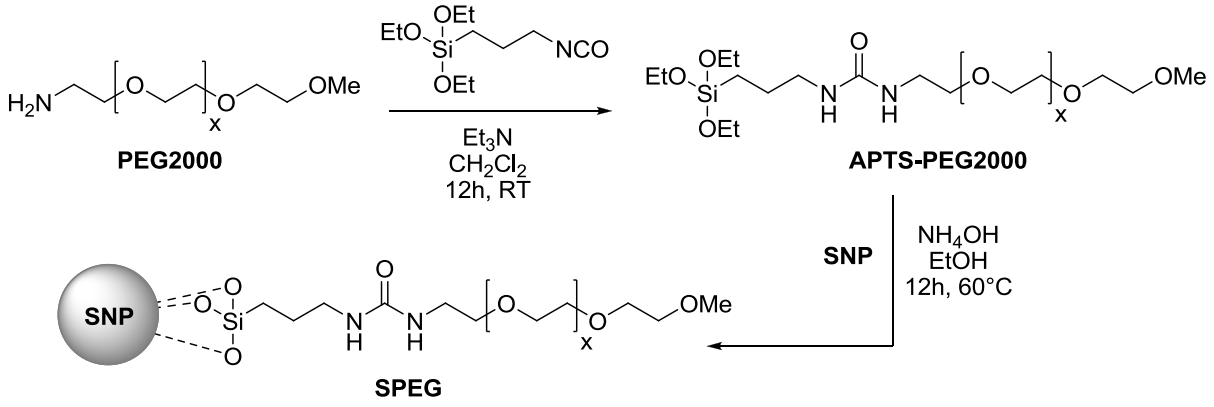

(Inhert atmosphere, Nitrogen flow)

In a dried round-bottom flask, *O*-(2-aminoethyl)-*O'*-methylpolyethylene glycol 2000 Da (100 mg, 50 µmol) has been dissolved in anhydrous CH_2Cl_2 (1.0 mL); subsequently, Et_3N (8 µL, 55 µmol) and 3-(isocyanatopropyl)triethoxysilane (15 µL, 60 µmol) have been added to the mixture; the reaction run overnight at RT under vigorous stirring. Once the reaction has been completed, the solution has been filtered and the clear filtrate has been evaporated under reduced pressure. The resultant yellow pale oil has been redissolved in a minimum amount of CH_2Cl_2 (300 µL), and cold Et_2O (10.0 mL) has been added to precipitate the product as a fine white solid. The product has been washed twice with Et_2O (10.0 mL) and finally dried under vacuum. APTS-PEG_{2000} (98 mg) has been used immediately without further purification. The conjugation reaction was performed as follows [26,27]; a suspension of SNP in EtOH (20.0 mL, 1 mg mL^{-1}) has been warmed at 60 °C; next, 25% NH4OH (50.0 µL) and APTS-PEG2000 (20 mg, 10 µmol) have been added under vigorous magnetic stirring and lasted overnight. The particulate has been collected by centrifugation (8300 rcf, 15 min) and

washed twice with EtOH (10.0 mL) and water (10.0 mL). The resultant SPEG have been redispersed in water (10.0 mL) for analyses.

4.6.3 Synthetic route to N^{α},N^{α}-Bis[cerboxymethyl]-L-lysine (NTA)

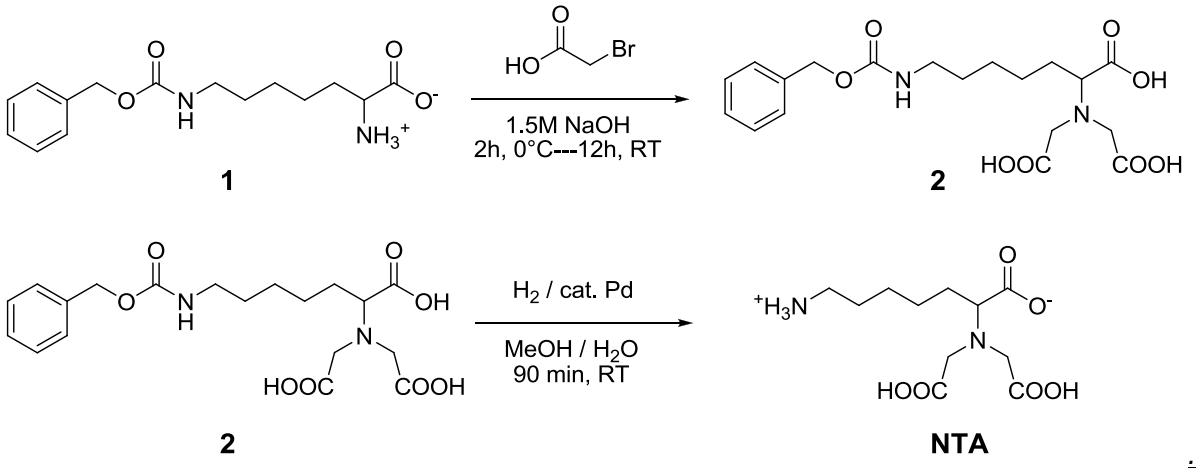

4.6.3.1 Synthesis of (N^{α},N^{α}-Bis[cerboxymethyl]-N-[benzyloxycarbonyl]-L-lisine (**2**)

In a round-bottom flask, Bromoacetic acid (4.17 g, 30.2 mmol) has been dissolved in 1.5M NaOH (15 mL) and cooled at 0°C on ice. Compound **1** (2 g, 15.1 mmol) dissolved in 1.5M NaOH (25 mL) has been added dropwise to this solution. After 2 h cooling has been stopped and the reaction has been stirred overnight at RT. The following day, after heating at 50°C for 2 h and cooling at RT, 1M HCl (45 mL) has been added dropwise and a white precipitate formed. The product **2** has been filtered off and finally died in vacuum (3.4 g, 8.5 mmol)

Yield (%)= 56%

^{1}H-NMR (DMSO), δ: 7.11 (*m*, 5H, Ar), 5.15 (*s*, 2H, Phenyl-CH_2-O), 3.50 (*s*, 4H, N-CH_2-COO), 3.32 (*t*, 1H, CH_2-C*H*-N), 1.81-1.25 (*m*, 8H, CH_2-alkyl chain) ppm. Data are consistent with reported values [28].

4.6.3.2 Synthesis of (N^{α},N^{α}-Bis[cerboxymethyl]-N-L-lisine (**NTA**)

The compound **2** (1.5 g, 3.75 mmol) has been dissolved in 20:1 MeOH / H_2O mixture (25 mL) and, after the addition of a spatula tip of 5 % Pd/C, hydrogenated at RT and normal pressure for 90 min. At the end of the reaction, NTA has been achieved by filtering off the catalyst and removing the solvent by evaporation under reduce pressure. The resulting precipitate has been dissolved in deionized water (2.5 mL) and EtOH (100 mL). The product **NTA** has been collected as white fine crystals after 2 days at 0°C and dried in vacuum (0.75 g, 2.85 mmol)

Yield (%)= 70%

^{1}H-NMR (D_2O), δ: 3.80 (*s*, 3H, N-CH_2-COO), 3.10 (*t*, 1H, CH_2-C*H*-N), 1.60-1.20 (*m*, 8H, CH_2-alkyl chain) ppm. Signals are consistent with literature data [28].

4.6.4 Synthesis of Silica-NTA conjugate (SNP1)

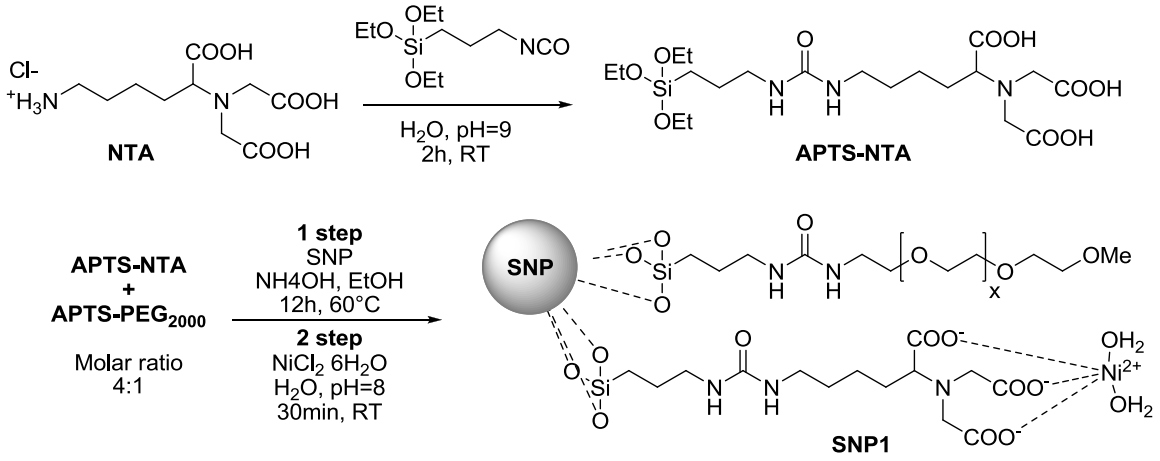

(Inhert atmosphere, Nitrogen flow)

N_{α},N_{α}-Bis(carboxymethyl)-L-lysine (NTA) has been synthesized according a previous work [28] .NTA (100 mg, 380 µmol) has been dissolved in deionized water at pH=9 (8.0 mL); subsequently, Et_3N (211 µL, 1.52 mmol) and 3-(isocyanatopropyl)triethoxysilane (113 µL, 456 µmol) have been added to the mixture and the reaction lasted 2h at RT with magnetic stirring. The product APTS-NTA has been used immediately without further purification. For the conjugation reaction [26,27], a suspension of SNP in EtOH/H2O 1:1 (20.0 mL, 1 mg mL^{-1}) has been warmed at 60 °C; 25% NH_4OH (50 µL), APTS-NTA (10 mg, 20 µmol), and APTS-PEG_{2000} (10 mg, 5 µmol) have been added under vigorous stirring; the reaction has been reacted at 60 °C overnight. Next, the particulate has been collected by centrifugation (8300 rcf, 15 min) and washed twice with EtOH (10.0 mL) and water (10.0 mL). Nanoparticles have been resuspended in deionized water (20.0 mL) for further chelation with nickel ions. A green solution of 0.1 M $NiCl_2{\cdot}6H_2O$ in deionized water (2.0 mL) has been added to the above suspension of nanoparticles; the pH has been adjusted to pH 8.0 with 0.1 N NaOH, and the resultant mixture have been stirred 30 min at RT. Particles have been collected by centrifugation and the pale blue supernatant discarded. The pale green particulate have been washed thrice with deionized water (10.0 mL) and, finally, SNP1 have been resuspended in deionized water (5.0 mL) and stored for further conjugation with His-tagged scFv800E6.

4.6.5 Synthesis of Silica-aminated conjugate (SNP2)

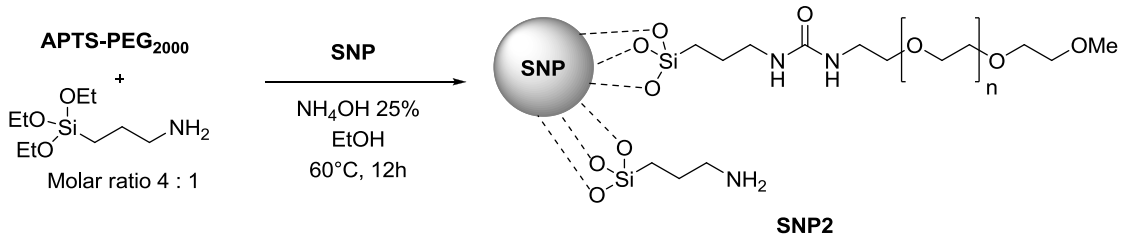

A suspension of SNP in EtOH (20 mL, 1 mg mL^{-1}) has been warmed at 60 °C; NH_4OH 25vol.% (50 µL) and 3-aminopropyl-triethoxysilane (5 µL, 20 µmol), and APTS-PEG_{2000} (10 mg, 5 µmol) have been added and tho the suspension; the resultant mixture has been kept under vigorous magnetic stirring at 60 °C overnight. The particulate has been collected by centrifugation and washed twice with EtOH (10 mL) and water (10 mL). The resultant SNP2 have been stored in water (10 mL) supplemented with HCl 0.5 M (10 µL) for further conjugation with scFv.

4.6.6 Determination of amino groups on SNP2

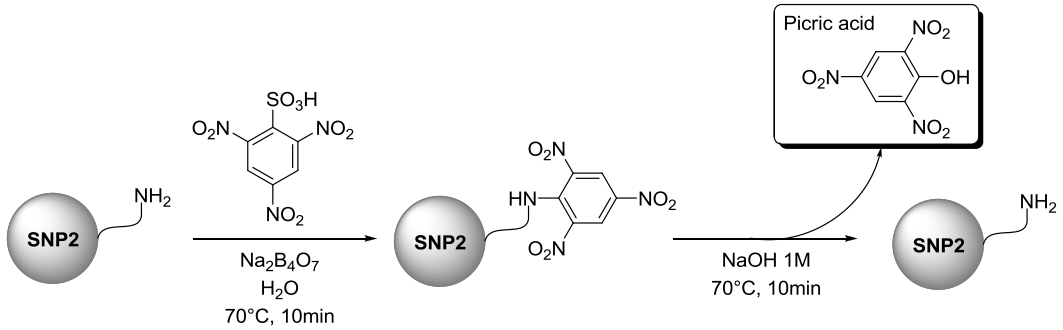

Following a method described in the literature [24], an aqueous mixture containing 1M picrylsulfonic acid TNBS (10 µL) and 0.05 M $Na_2B_4O_7$ (1.5 mL) have been added to aminated SNP2 (6 mg); the suspension has been sonicated 1 min and then heated at 70 °C for 10 min. Next, the mixture has been allowed to cool at RT and SNP2 has been separated from the supernatant by centrifugation high speed centrifugation. Several washings have been performed: water (1 mL), 50 vol.% acetone in water (1 mL), 100% acetone (1 mL), and twice water (1 mL). NPs have been then suspended in an aqueous solution 1 M NaOH (5 mL) and heated to 70 °C for 10 min. The yellow colored suspension has been cooled to RT and NPs have been separated and discarded from the supernatant. An aliquot of this particle-free solution (1 mL) has been taken and its absorbance read at 410 nm. Each particle contained silica (d = 2.2 × 106 g m−3) with an average radius of 30 nm = 3.0 × 10^{-8} m. The average volume and mass of SiO_2 nanoparticles are 2.68 × 10^{-22} m^3 and 5.90 × 10^{-16} g, respectively. Hence, 1 mg of SiO_2 contained 1.02 × 10^{14} particles. By determination of residual absorbance due to picric acid released from reaction, our estimation is that 0.012 µmol of

ligand APTS were immobilized on the particle surface corresponding to about 708 NH_2 groups/particle (Figure 4.11).

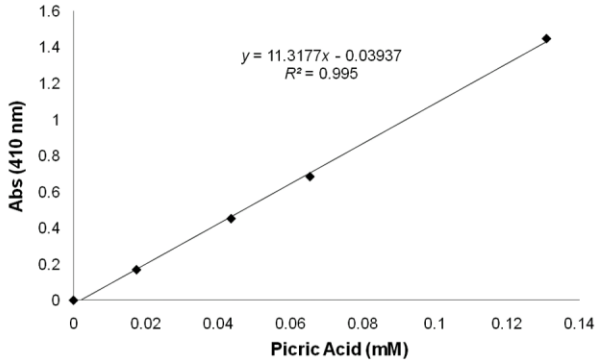

Figure 4.11. Calibration curve of Picric acid in aqueous NaOH 1 M (λ_{max} = 410 nm).

4.6.7 Oriented ligation of His-Tag scFv800E6 (SNP−HT)

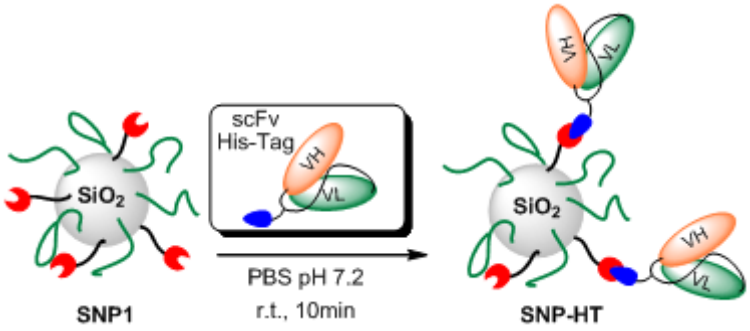

In a plastic sterile tube, SNP1 (1 mg) have been mixed with purified scFv800E6 (50 µg, 2 nmol) in 20 mM PBS pH 7.2 (final volume of 1 mL) and the mixture has been stirred on the orbital shaker 10 min at RT. SNP-HT have been isolated from unreacted scFv800E6 by three centrifugation cycles and washes with fresh PBS (500 µL). The final product have been finally stored in PBS at 4 °C for further experiments. By measuring the absorbance at 280 nm, the amount of scFv800E6 immobilized on nanoparticles has been evaluated of 26 µg mg^{-1} of SNP-HT, corresponding about 6 molecules NP^{-1}.

4.6.8 Ligation of scFv800E6 through reductive amination (SNP−UT)

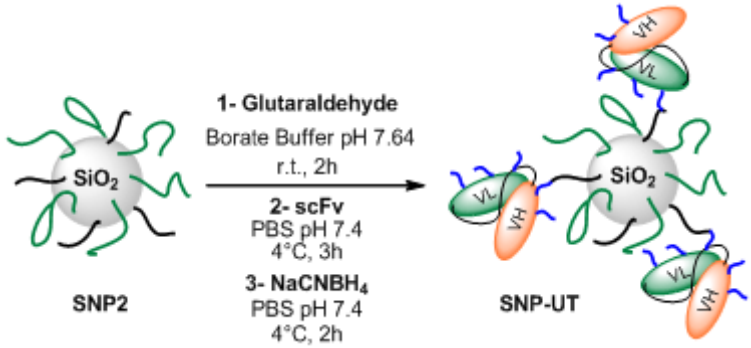

Particle-glutaraldehyde cross-linking, [29] followed by imine reduction [30] with $NaCNBH_3$ have been performed as follows. In a sterile plastic tube, amino SNP2 (1 mg) have been dispersed in borate buffer pH 7.6 (600 µL). A 5 mM glutaraldehyde solution in the same buffer (400 µL, 20 µmol) has been added under stirring at RT and after 2 h of reaction, aldehyde-conjugated NPs have been isolated by centrifugation and washed once with borate buffer pH 7.6 (1 mL) and twice with PBS pH 7.4 (1 mL). NPs have been then resuspended (1 mg mL^{-1}) in the same buffer (1 mL) and the suspension cooled at 4 °C with an ice bath; scFv800E6 (50 µg, 2 nmol) in PBS was added to the suspension and the resultant mixture has been stirred on the orbital shaker for 3 h at 4 °C. ScFv-functionalized nanoparticles have been recovered after centrifugation and washed twice with PBS pH 7.2 (1 mL). Subsequently, a $NaCNBH_3$ solution (10 µL, 1 mg mL^{-1}) in PBS pH 7.2 has been added to the previous mixture and incubated for 3 h at 4 °C. After centrifuging, SNP-UT have been washed three times with PBS (1 mL) and finally stored in the same buffer at 4 °C for further experiments. By measuring the absorbance at 280 nm, we determined an amount of scFv800E6 43 µg mg^{-1} of SNP-HT, corresponding about 10 molecules NP^{-1}.

4.6.9 Stability assay of scFv conjugation on SNP−HT

Immobilized-scFv on SNP-HT (5 µg estimated) have been incubated at 37 °C with 0.1 mL of cell culture medium. After incubation time, SNP-HT have been centrifuged 15 min at high speed at 4 °C and subsequently supernatants (S1, S4, S24, and S48) have been filtered onto a PVDF membrane utilizing a Manifold I dot blot apparatus (GE Healthcare). The membrane has been incubated in a blocking solution composed by 5 vol.% skim milk in PBS and Tween 0.05 vol.%, for 1 h at RT; the membrane has been then probed 1 h at RT in the blocking solution using rabbit anti-Myc-HRP antibody (Invitrogen) at a 1:5000 dilution. The Membrane has been rinsed thrice in 0.05 vol.% Tween in PBS for 10 min. Immunoreactive spots have been revealed using ECL Western blotting reagent (GE Healthcare). Five micrograms of scFv immobilized on SNP-HT and 0.1 mL of culture medium were used, respectively, as positive and negative control.

Related References

[1] Jain, K.; *Expert Opin. Pharmacother*. **2005**, *6*, 1463–1476.

[2] Olayioye, M. A..; Neve, M. R.; Lane, H. A. and Hynes, M. E.; *EMBO J*. **2000**, *19*, 3159–3167.

[3] Ferguson, K. M.; Berger, M. B.; Mendroia, J. M.; et al.; *Mol. Cell*. **2003**, *11*, 507–517.

[4] Colombo, M.; Corsi, F.; Foschi, D.; et al.; *Pharmacol. Res*. **2010**, *62*, 150–165.

[5] Sharma, S. V. and Setteleman, J.; *Exp. Cell. Res*. **2009**, *315*, 557–571.

[6] Wieduwilt, M. J. and Moasser, M. M.; *Cell Mol. Life Sci*. **2008**, *65*, 1566–1584.

[7] Amit, I.; Wides, R. and Yarden, Y.; *Mol. Syst. Biol*. **2007**, *3*, 151.

[8] Faltus, T.; Yuan, J.; Zimmer, B.; et al.; *Neoplasia*. **2004**, *6*, 786–795.

[9] Cooley, S.; Burns, L. J.; Repka, T. and Miller, J. S.; *Exp. Hematol*. **1999**, *27*, 1533–1541.

[10] Lewis, G. D.; Figari, I.; Fendly, B.; et al.; *Cancer Immunol. Immunother*. **1993**, *37*, 255–263.

[11] Molina, M. A.; Codony-Servat, J.; Albanell, J.; Royo, F.; Arribas, J. and Baselga, J.; *Cancer Res*. **2001**, *61*, 4744–4749.

[12] Sarup, J. C.; Johnson, R. M.; King, K. L.; et al.; *Growth Regul*. **1991**, *1*, 72–82.

[13] Lane, H. A.; Matoyama, A. B.; Beuvink, I. and Hynes, N. E.; *Ann. Oncol*. **2001**, *12*, S21–S22.

[14] Marlind, J.; Kaspar, M.; Trachsel, E.; et al.; *Clin. Cancer Res*. **2008**, *14*, 6515–6524.

[15] Zhang, G.; Liu, Y. and Hu, H.; *Eur. J. Inflamm*. **2010**, *8*, 75–82.

[16] Sommaruga, S.; Lombardi, A.; Salvadé, A.; et al.; *Appl. Microbiol. Biotechnol*. **2011**, *91*, 613–621.

[17] Galeffi, P.; Lombardi, A.; Donato, M. D.; et al.; *Vaccine*. **2005**, *23*, 1823–1827.

[18] Lombardi, A.; Sperandei, M.; Cantale, C.; Giacomini, P. and Galeffi, P.; *Protein Expr. Purif*. **2005**, *44*, 10–15.

[19] Stöber, W.; Fink, A. and Bohn, E.; *J. Colloid. Interface. Sci*. **1968**, *26*, 62–65.

[20] Lin, W.; Garnett, M. C.; Schacht, E.; Davis, S. S. and Illum, L.; *Int. J. Pharm*. **1999**, *189*, 161–170.

[21] Kim, S. H.; Jeyakumar, M. and Katzenellenbogen, J. A.; *J. Am. Chem. Soc*. **2007**, *129*, 13254–13264.

[22] Kapanidis, A. N.; Ebright, Y. W. and Ebright, R. H.; *J. Am. Chem. Soc*. **2001**, *123*, 12123–12125.

[23] Cantu, E. S.; Cueto, R.; Koch, J. and Russo, P. S.; *Langmuir*. **2012**, *28*, 5562–5569.

[24] Halling, P. J. and Dunnill, P.; *Biotechnol. Bioeng*. **1979**, *21*, 393–416.

[25] Hu, F.; Wei, L. Zhou, Z.; Ran, Y.; Li, Z. and Gao, M.; *Adv. Mater*. **2006**, *18*, 2553–2556.

[26] Wu, T.; Zhang, Y.; Wang, X. and Liu, S.; *Chem. Mater*. **2008**, *20*, 101–109.

[27] Kim, S. H.; Jeyakumar, M.; and Katznellenbogen, J. A.; *J. Am. Chem. Soc*. **2007**, *129*, 13254–13264.

[28] Schmitt, L.; Dietrich, C. and Tampè, R.; *J. Am. Chem. Soc*. **1994**, *116*, 8485–8491.

[29] Corsi, F.; De Palma, C.; Colombo, M.; et al.; *Small*. **2009**, *5*, 2555–2564.

[30] Han, H. J.; Kannan, R. M.; Wang, S.; Mao, G. and Romero, R.; *Adv. Funct. Mater*. **2010**, *20*, 409–412.

Chapter V

Development of a Fluorescent Silica Nanoparticles Platform for Transferrin Conjugation: Implications at the Bio-Nano Interface

Contents

5.1. The role of Transferrin receptor in human cancers

Transferrin (Tf) is considered the essential iron transport system in vertebrates and invertebrates [1]. Most of the transferrins and mainly human serum transferrin consist of a single polypeptide chain of roughly 700 amino acids organized in two lobes (C and N). Each lobe contains an iron binding cleft in which iron is coordinated to four protein ligands and a synergistic carbonate anion [2]. In mammals, soluble Tf solubilizes Fe^{3+} in neutral biological media. When it becomes iron-loaded on the C-site only or on both sites (holo-soluble Tf), it is recognized by transferrin receptor 1 (TfR1) and to a much lesser extent by TfR2 [1]. The iron-loaded Tf-TfR adduct that is formed is then internalized in the cytoplasm by receptor-mediated endocytosis. Later

on, upon acidification of the endosome at pH 5.5, the iron-loaded soluble Tf-TfR adduct loses its content of iron and is recycled back to the cell surface where TfR has no affinity anymore for iron-free Tf (apo-soluble Tf) [3]. Therefore, iron-loaded Tf in its interaction with TfR constitutes the system for transport of iron from the blood stream to the cytosol (Figure 5.1).

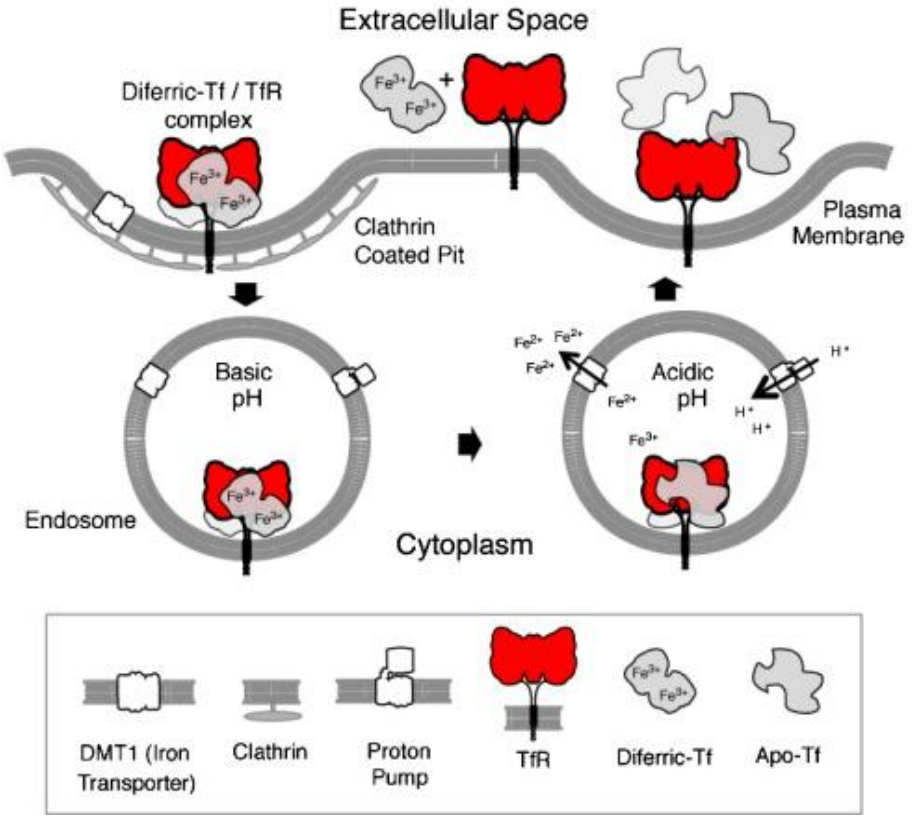

Figure 5.1: Transferrin Endocytosis of the diferric Tf/TfR1 complex
Endocytosis of the diferric Tf/TfR1 complex occurs via clathrin-coated pits and the complex is delivered into endosomes. Protons are pumped into the endosome resulting in a decrease in pH that stimulates a conformational change in Tf and its subsequent release of Fe^{2+}. The iron is then transported out of the endosome into the cytosol by the divalent metal transporter 1 (DMT1). Apotransferrin remains bound to the TfR1 while in the endosome is released only once the complex reaches the cell surface. TfR1 is found on the cell surface as a homodimer consisting of two monomers linked by disulfide.

Complete TfR was isolated from human placenta and identified in the 1980s [4]. TfR is a homodimeric 190 kDa glycosylated transmembrane protein composed of two identical subunits which are linked by two disulfide bonds [5]. The TfR dimer has a butterfly-like shape. Each of the two subunits possesses a transmembrane endodomain and an ectodomain of nearby 700 amino acids directed toward the

biological fluid. The latter contains the transferrin binding sites [4,5]. Each of these subunits can interact with one iron-loaded protein (Figure 5.2) [6,7].

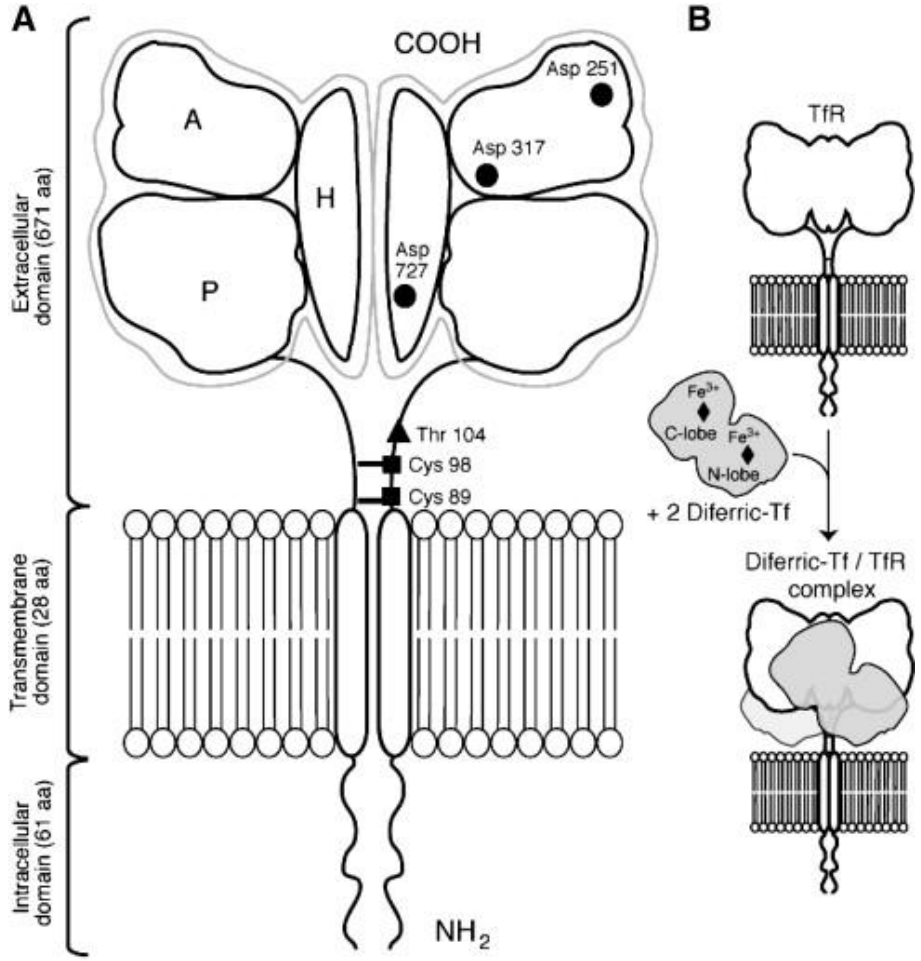

Figure 5.2: Transferrin receptor complex: schematic structure

(Panel A) TfR1 is found on the cell surface as a homodimer consisting of two monomers linked by disulfide bridges at cysteines 89 and 98 (■). The TfR1 contains an intracellular domain, a transmembrane domain, and a large extracellular domain. There is an O-linked glycosylation site at threonine 104 (▲) and three N-linked glycosylation sites on asparagine residues 251, 317 and 727 (●). The extracellular domain of one the TfR1 consists of three subdomains: apical (A), helical (H) and protease-like domain (P).
(Panel B) Each receptor monomer binds one Tf molecule that consists of two lobes (N and C lobes). Each lobe of Tf binds one iron molecule and thus two Fe^{2+} Tf molecules bind to the receptor with high affinity.

The receptor for transferrin (TfR), referred to as TfR1, is ubiquitously expressed at low levels in most normal human tissues. A second member of the TfR family is TfR2, a protein that is homologous to TfR1 but whose expression is largely restricted to hepatocytes [8]. Even if TfR expression in normal tissues is restricted at the level of liver and intestine, it has been observed that TfR is frequently overexpressed in tumor cell lines. Particularly frequent is its expression in ovarian cancer, colon cancer and glioblastoma cell lines; less frequent is its expression in leukemic and melanoma

cell lines [9]. Interestingly, in these tumor cell lines experiments of *in vitro* iron loading or iron deprivation provided evidence that TfR is modulated in cancer cell lines according to cellular iron levels following two different mechanisms: (i) in some cells, iron loading caused a downregulation of total TfR levels; (ii) in other cell types, iron loading caused a downmodulation of membrane-bound TfR, without affecting the levels of total cellular TfR content. Although these observations suggest that, the metabolism of iron by cancer cells may lead to over-expression of TfR1, which is expressed on malignant cells at levels several fold higher than those on normal cells and its expression can be correlated with tumor stage or cancer progression. Unfortunately, even if TfR expression is modulated by iron through different biochemical mechanisms, their molecular basis remains to be determined [10–12].

Despite its ubiquitous expression the high expression of the receptor on malignant cells, its ability to internalize, and the necessity of iron for cancer cell proliferation, make this receptor a widely accessible portal for the delivery of drugs into malignant cells and, thus, an attractive target for cancer therapy.

With nanotechnology, the binding of ligands such as Tf to the surface of the micelles has been used for the direct targeting of these structures as carriers of antineoplastic drugs or genetic material to tumors [13]. These complex micelles have been used for the delivery of antisense DNA into cancer cells, meanwhile, inorganic and polymeric nanoparticles are now emerging as promising drug vehicles because of their multi−modular structure that enables them to actively target discrete cells through multiple barriers and to simultaneously carry multiple drugs of various chemical natures [14−17].

5.2 The bio−nano interface outlines the biological identity

In recent years, Tf-conjugated nanoparticles have experienced and matured from simple devices to multifunctional, biodegradable, less-toxic, and less-immunogenic constructs. Unluckily despite all these promising results, previous investigations with Tf-targeted NPs have sometimes demonstrated controversial results, and highlighted severe problems such as linker stability and protein flexibility [18−20]. To understand the behavior of multifunctional colloidal nanoparticles capable of biomolecular targeting is still a charming challenge in materials science and has fundamental implications in view of a possible clinical translation. In several circumstances, assumptions on structure-activity relationships have failed in determining the expected responses of these complex systems in a biological environment. In a recent paper involving the Tf-targeted NPs, Salvati *et al*. [21] describe the complex interactions between silica NPs and the biological environment: the authors have basically demonstrated that the targeting ability of such functionalized nanoparticles may disappear when NPs are soaked in a full biological environment. Therefore, using Tf-conjugated 50 nm SiNPs, they have found that many soluble proteins in the milieu can shield Tf from binding to both its target receptors on cells and soluble TfR. Although, SiNPs continue to enter cells, the targeting specificity of Tf is completely lost. These results suggest that, in a complex biological environment, interactions with other proteins dissolved in the medium [22,23] can ‘screen’ the targeting biomolecule on the surface of NPs causing the loss of specificity in targeting.

To better understand this concept, a recent review from our group [24] highlights that most available studies correlate these interactions towards the bio−nano interface at different levels. For example many works connect these

phenomena with surface properties of nanomaterials, including size, shape and curvature, roughness, porosity and cristallinity [25−27]. Other works deal with the properties of the solid-liquid interface originated when nanoparticles are suspended in the surrounding medium, including for instance the effective surface charge, [28] the state of aggregation and the stability of the suspension over time and at different cellular pH values. In addition, the solid-liquid contact zone with biological substrates might be influenced by the nature of the chemical functionalization of NPs [29]. Also the contact with hydrophobic or charged regions of cells determines the nanoparticle preferential pathway of interaction with the cellular external environment and, moreover, the formation of stable or transient complexes with their binding molecules and the route of internalization and metabolism of nanoparticles [30]. Several recent works suggest that adsorbed proteins are not uniformly bound to the nanoparticle surface and the strength of the interaction is dependent on the protein affinity toward that material, giving a proper “protein corona” (Figure 5.3) [31,32].

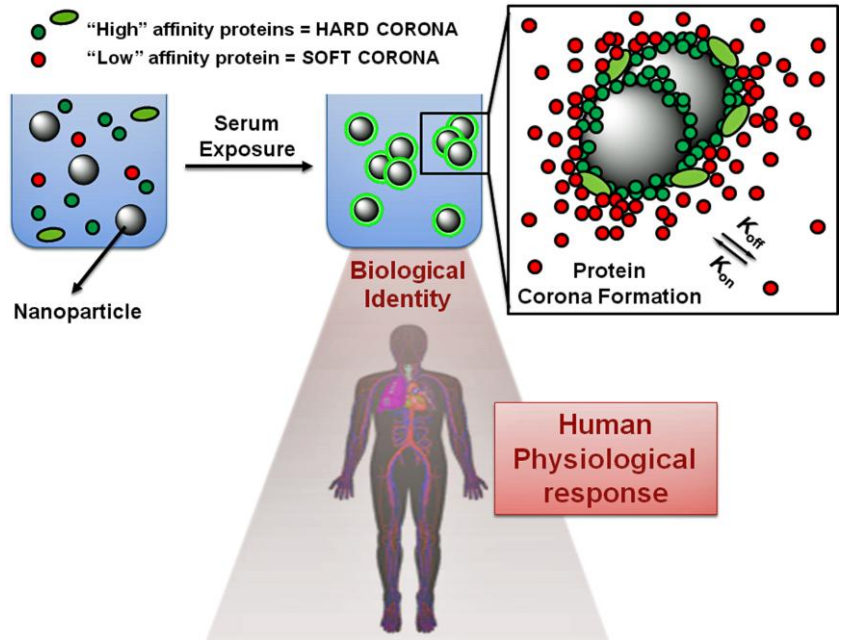

Figure 5.3: The “biological” identity: formation
Biomolecules with high affinity (green) and low affinity (red) form a thin layer of molecules on the nanomaterial surface, which can be tightly bound (“hard” corona) or reversibly adsorbed (“soft” corona), or both. The protein corona is one of the key factors managing the cellular response in terms of uptake, accumulation, and elimination.

Distinctively, molecules adsorbed with high affinity form the "*hard*" corona, consisting of tightly bound proteins that do not easily desorb, while molecules adsorbed with low affinity assemble the "*soft*" corona, consisting of loosely bound proteins. The general hypothesis defines that the *hard* corona binds directly with the nanoparticle surface, whereas the *soft* corona interacts preferentially with the hard corona via weak protein-protein interactions. Moreover, the corona probably consists of multiple layers: since most of plasma proteins have very small hydrodynamic size (range 3−15 nm), the average corona usually detected on nanoparticles is too thick to be accounted for by a single layer of adsorbed proteins [23,32].

As a result, nowadays the scientific community is trying to understand the role of the protein corona at the cellular level and it means to investigate its possible outcomes when using nanomaterials *in vivo* [33]. Therefore, the results that I am going to present in this chapter are focused on the creation of a small fluorescent silica NPs platform (20−30 nm), and of the optimization of the surface chemistry to assess high targeting efficiency of TfR with Tf protein; finally I have started to study if there is a strong negative correlation between the serum protein binding capacity on the surface of nanomaterials and their influence towards Tf-functionalized NPs at the rate which they are taken up by cells *in vitro*.

5.3 Development of a fluorescent-based silica nanoparticles platform

It has been finely described in the second chapter that fluorescent SiNPs have numerous applications in science ranging from protective layers for quantum dots to drug delivery platforms, and for technology in the electronics, paints and many other industries. They are also potentially useful as biological targeting platforms, practicable for a wide range of internal labeling techniques and surface modifications. I have started to investigate approaches to covalently (internally) dye label silica nanoparticles with fluorescein isothiocyanate (FITC) as fluorescent probe, using a fluorescent dye–alkoxysilane conjugate. In this chemical synthesis, the dye is covalently attached to an alkoxysilane, which can be hydrolyzed and condensed together with TEOS, in alkaline ethanol with the classical Stöber synthesis, as described in the previous chapter. To test the efficiency of this chemical approach, three spherical but size-different fluorescent silica nanoparticle (FSNP) have been synthesized, by tuning the temperature and the concentration of reactants [34], corresponding to 20 nm **FSNP**, 40 nm **FSNP** and 90 nm **FSNP** (see Table 7 in the experimental section). It is interesting to note the role played by the temperature, which is inversely proportional with the size, meanwhile increasing the concentration of NH_4OH, gives bigger FSNP.

As observed by electron microscopy (Figure 5.4), the dye-labeled Stöber synthesis has proved very efficient in producing monodisperse FSNP with high yield (more than 300 mg of FSNP from a single reactor). Previous reports have shown that, even if the overall particle size is unchanged, shape and morphological changes, including the selective etching of the core of silica nanoparticles, can occur at physiological

conditions.[35]. This can be particularly significant for biological applications, since that the biological interaction is determined at the surface [36].

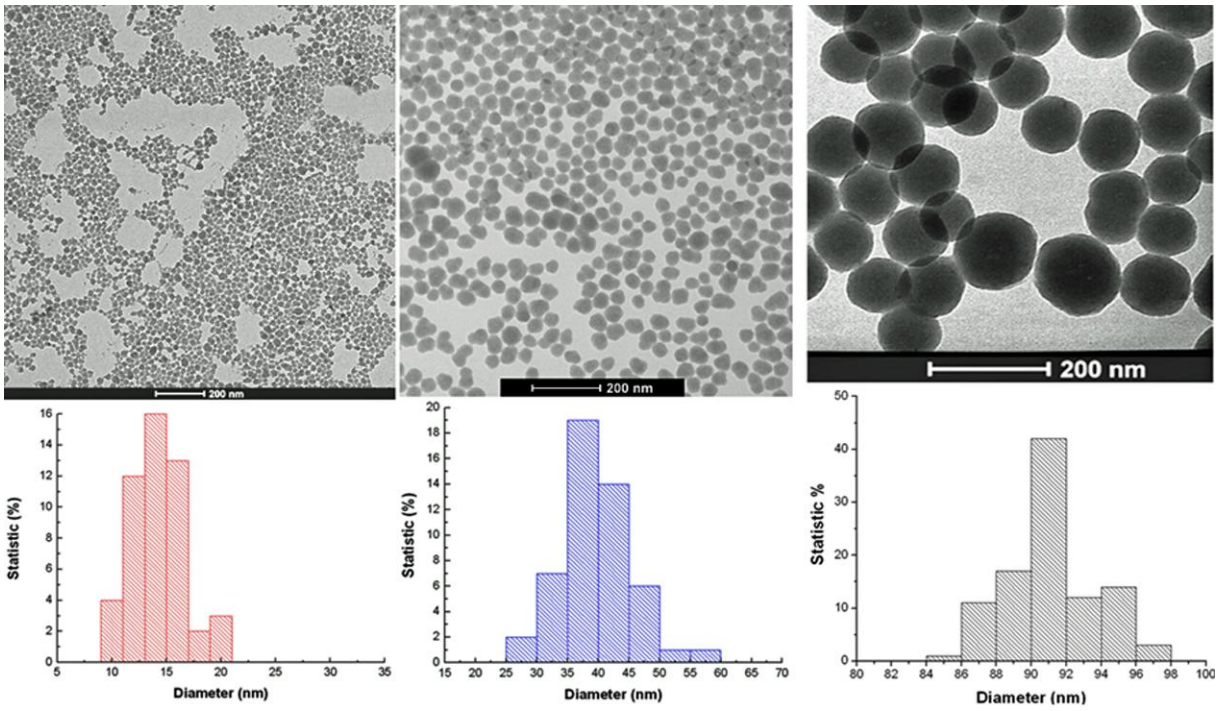

Figure 5.4: Geometrical size and shape of FSNP.
TEM pictures of as synthesized 20, 40 and 90 nm FSNP

As a solution of these problems, core–shell architectures have been prepared in which the highly fluorescent core is surrounded by a silica shell using methods derived from biosilicification, in which one uses amino acid residues, typically arginine, to control the reaction [37,38]. In making such particles, no effort needs to be made to limit the fluorescence intensity of the core, as this is no longer a significant element of the structural integrity of the nanoparticle. On the contrary, it has been previously demonstrated that stabilization of FSNP by growing a secondary silica shell under the classical Stöber conditions does not confer improved stability to degradation [39]. In this way, a layer of silica (10 nm, **SFSNP**) has been created on FSNP and verified with TEM and DLS (Figure 5.5). As noticed in the Table 5, FSNP and SFSNP are very stable in deionized water and also in 20 mM PBS pH7.4, the

behavior is the same: **SFSNP 30 nm**: Z-ave, 67.8 nm; PDI, 0.233; **SFSNP 50 nm**: Z-ave, 72.9 nm; PDI, 0.135; **SFSNP 100 nm**: Z-ave, 120.4 nm; PDI, 0.108.

Particle	DLS				DCS (wt. ave)	TEM (nm)
	Z-ave (nm)	PDI	Intensity (nm)	Number (nm)		
FSNP 20 nm	24.4 ± 1.1	0.231	45.6	19.3	23.7	15.1 ± 4.5
SFSNP 30 nm	35.8 ± 5.6	0.210	55.3	29.4	34.7	26.9 ± 4.2
FSNP 40 nm	55.6 ± 3.2	0.042	61.9	53.2	45.2	39.5 ± 3.5
SFSNP 50 nm	69.2 ± 4.5	0.088	75.6	68.4	51.4	52.3 ± 1.2
FSNP 90 nm	108.7 ± 4.8	0.055	99.8	95.2	94.8	92.1 ± 2.5
SFSNP 100 nm	116.9 ± 2.8	0.072	120.5	108.3	104.1	96.7 ± 5.2

Table. 5: Chemico-physical characterization of FSNP and SFSNP in deionized water

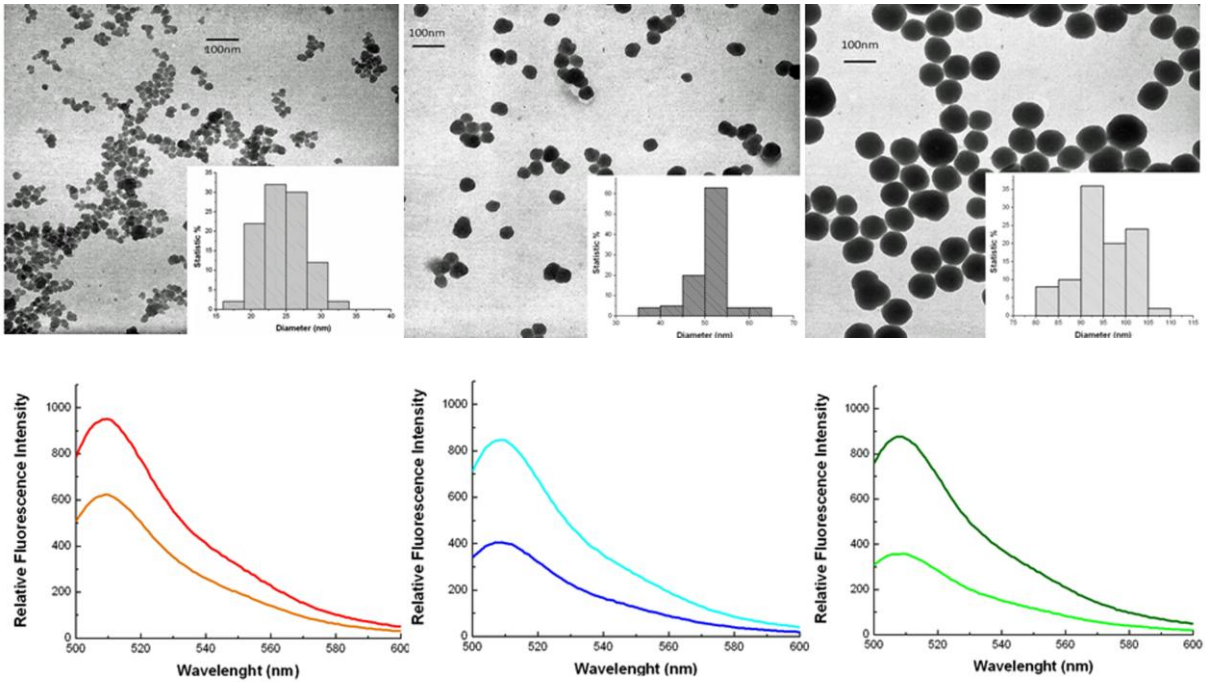

Figure 5.5: Geometrical size and shape of SFSNP.

(Upper level) TEM pictures and statistic distribution (inset) of as synthesized 30, 50 and 100 nm SFSNP after growing a shell of 10 nm (estimated by equation 4, see experimental section).
(Lower level) Relative fluorescence emission of SFSNP at two different concentration: 100 and 50 mg L^{-1} in PBS at pH 7.4. λ_{ex}= 488 nm

The fluorescence emission of FITC−encapsulated SFSNP in PBS pH 7.4 solution within 100 and 50 mg L^{-1} has basically showed promising results about the possibility to further visualize these nanovectors in cells by FACS and CLSM, thus validating the success of NPs synthetic chemistry to this purpose.

5.4 Silica surface functionalizations

After the basic NPs synthesis, 30 nm SFSNP has been chosen. to investigate the effects of the surface functionalization chemistry towards the Tf bio-conjugation and, as a consequence, for the specific TfR binding. A high density of amino groups have been introduced over the external silanol of SFSNP accomplished within the usual hydrolysis and condensation in water using CH_3COOH as acid catalyst. The reaction has lasted in a couple of hours yielding **HA-SNP**; the rate of amination has been estimated with the Ninhydrin assay meanwhile the iso-electric point (IEP) of the system has been calculated by ζ-potential titrations from pH 3 to pH 11 (Figure 5.6).

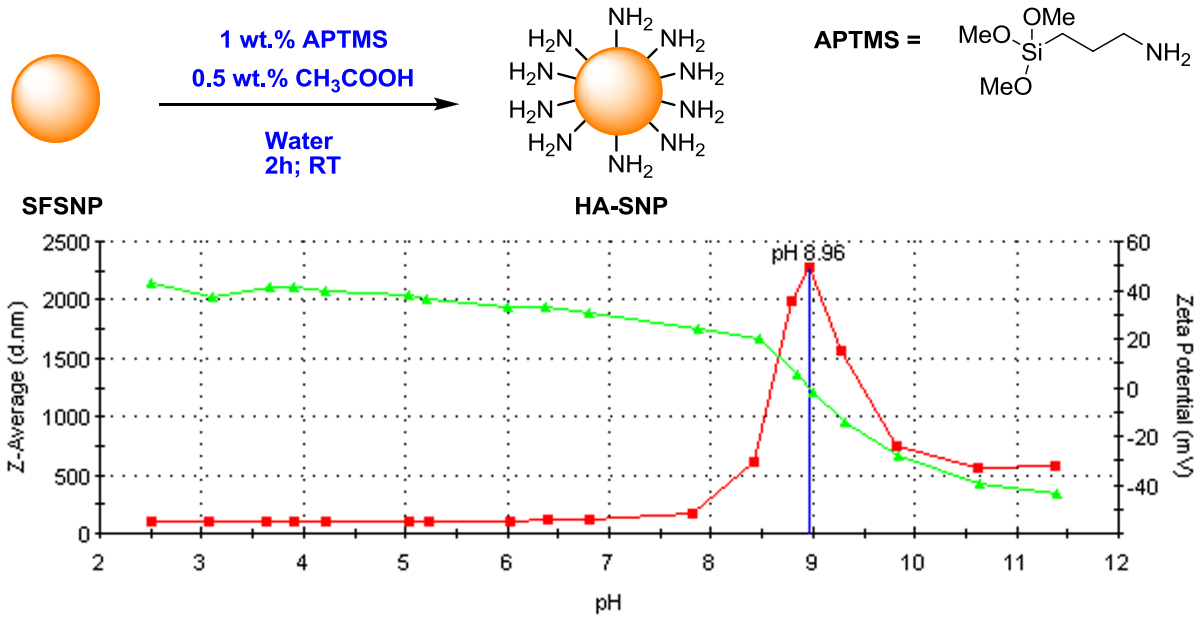

Figure 5.6: Amination of HA-SNP and ζ-potential titration.
(Upper scheme) Schematic synthesis of HA-SFSNP .
(Lower level) ζ-potential titration graph from pH=3 to pH 11 by addition of NaOH 0.1 M
(Green line= zeta potential curve; Red Line= average diameter of NPs).

It has been established that 2.16 NH_2 $(nm^2)^{-1}$ (corresponding to 0.070 μmol_{NH2} per mg of NPs) are exposed on the surface of HA-SNP corresponding to an IEP of 8.96. Since the basic synthetic idea for Tf conjugation has been focused on the direct fuctionalization of the amine moieties, it has been very important to correlate and discriminate the number of reactive groups for the following functionalization steps

and, of course, to optimize the nanoparticle construct for protein conjugation without altering NPs suspension over time.

The large number of NH_2 groups gives a high IEP of the NPs complex; as a result, performing an amide coupling at physiological pH should be very difficult because the uncompleted deprotonation of positive charges (NH_3^+) could result in a lack of NPs reactivity and, in addition, NPs severe aggregation caused by the reaction condition very close to the IEP of the system. To solve these problems and find possible connections with Tf activity on the NPs surface, a first inhert pegylation step (short PEG_4, named MS-PEG_4) has been conducted to reduce gradually the number of amine on the surface and, further, the value of IEP (Figure 5.7).

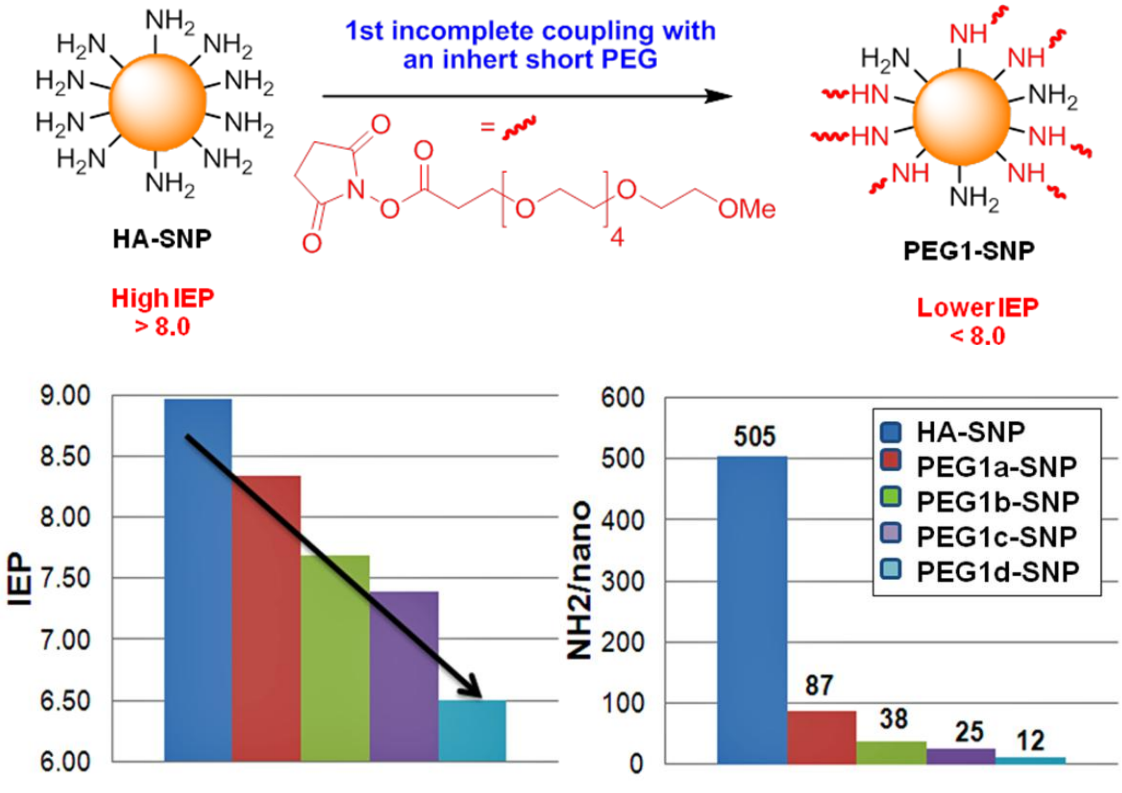

Figure 5.7: First inhert pegylation.
(Upper scheme) Schematic synthesis of PEG1a-d-SNP .
(Lower level) ζ-potential titration behavior graphs (from pH=3 to pH 11 by addition of 0.1 M NaOH). The IEP has been calculated by the software of the instrument (Z-sizer)

Different **PEG1-SNP** obtained (a-d) by gradually increasing of the molar ratio between calculated NH2 and MS-PEG_4 have been synthesized and, at the end of

reactions, residual surface amine have been estimated again by the ninhydrin assay while IEP points have been monitored by ζ-potential titrations. It has been observed a huge decrease of amino moieties on the surface by growing the molar ratio of PEG, however it is interesting to note that even at 10 molar excess of PEG, few amino groups are still free on the surface. Moreover, it should be considered also how the IEP of NPs has been affected by the pegylation reaction: for instance the system has gone throught IEP of 8.96 from HA-SNP to gradually reach the final value of 6.50 for Peg1d-SNP (PEG1a-SNP, 8.34; PEG1b-SNP, 7.69; PEG1c-SNP, 7.27). As a proof of concept, in this way the properties of colloidal suspension at physiological pH should be ameliorate and, most important, the reactivity of residual NH_2 groups should be improved due to the complete deprotonation of the NPs charge.

In conclusion five different compounds have been constructed for the optimization of Tf protein bioconjugation and, in parallel, taking into consideration how the properties of the surface functionalization could affect the protein conjugation and its reactivity toward the receptor.

5.5 Transferrin bioconjugation

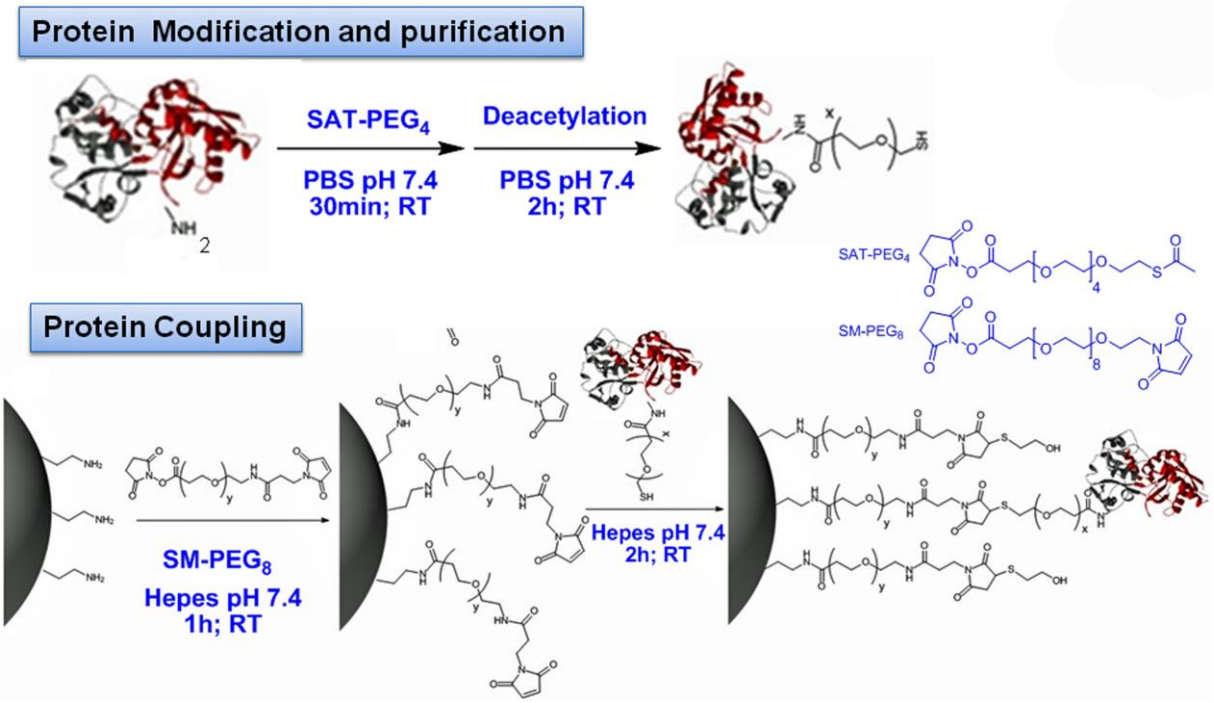

Figure 5.8: Schematic view of protein modification and conjugation (Tf-SNP).
(Upper scheme) Tf protein is modified with a short heterolinker (SAT-PEG4) giving free sulphydryl groups which have been chosen to react with NPs system.
(Lower level) NPs modification is accomplished in two steps: after the first coupling of heterobifuctional PEG (MS-PEG8), later the protein is conjugated by Michael addition to maleimide rings.

In the present investigation Human Tf modified with a thiol–PEG (named SAT-PEG_4) linker has been conjugated to the PEGylated particle in a two steps synthesis to give a final fluorescent bioconjugates. Optimal design for Tf-decorated silica nanoparticles (**$Tf_{1\text{-}5}$–SNP**) has been achieved with heterobifunctional PEG_8 spacers (named SM-PEG_8), as illustrated above (Figure 5.8). As noticed, the length of the PEG spacer is two times longer (8 EO monomers) compared with the previous inhert pegylation (4 EO monomers) with the aim to display prominently maleimide rings towards the Michael addition with the thiol-free modified Tf. It is important to note that all these functionalization steps have been achieved at physiological pH (7.4) using 20 mM Hepes buffer and 20 mM PBS; for instance, one key factor to check during the reaction is the maintenance of the colloidal stability for all the time requested for the reactions. Hence, a intermittent ultrasound treatment during the reaction has

been essential to homogenize HA-SNP and PEG1a-SNP and PEG1b-SNP suspensions which possess an IEP higher (or very close to) than pH 7.4; on the contrary, this treatment has not been necessary for PEG1c-d-SNP suspensions. At the end of Tf coupling, all NPs have been resuspended in 20 mM PBS pH 7.4 and stored at 4 °C for further analyses, both chemical characterizations and biological receptor recognition. Tf-SNP complexes behavior in solution has been characterized by both DLS, ζ-potential and DCS (Figure 5.9) and the results are summarized below (Table 6).

Particle	DLS and ζ-potential				DCS (wt. ave)
	Z-ave (nm)	PDI	Number (nm)	ζ-potential (mV)	
Tf1−SNP (H amino)	126.5 ± 2.1	0.160	76.1	−6.18	58.2
Tf2−SNP (PEG1a)	139.1 ± 0.5	0.161	93.6	−6.31	55.5
Tf3−SNP (PEG1b)	135.3 ± 1.3	0.178	80.9	−6.32	50.5
Tf4−SNP (PEG1c)	120.4 ± 1.9	0.200	70.7	−0.89	43.3
Tf5−SNP (PEG1d)	145.3 ± 2.8	0.225	58.5	+1.68	37.6

Table. 6: Chemico-physical characterization of Tf-SNP conjugates in PBS pH 7.4

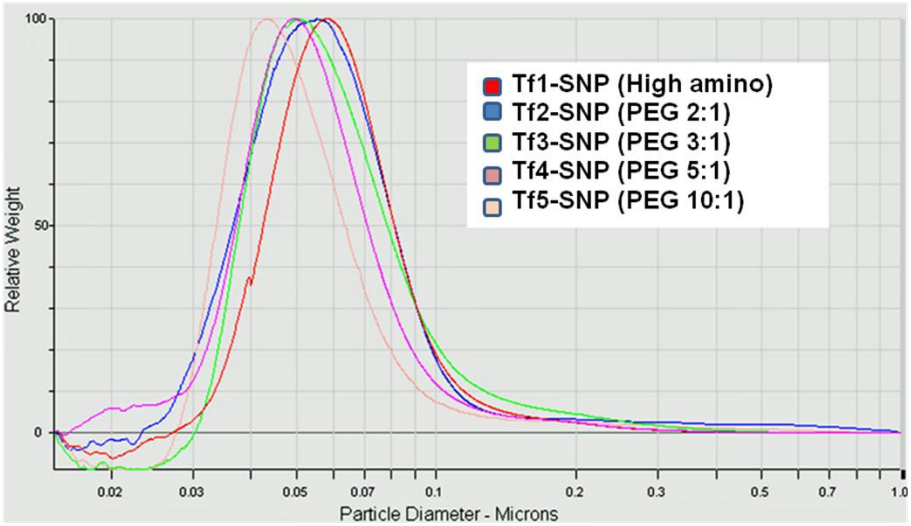

Figure 5.9: DCS behavior of Tf-SNPs in PBS.
Distribution profiles of $Tf_{1\text{-}5}$-SNPs in PBS pH 7.4.

The amount of protein immobilized onto SNPs has been quantified by microBCA protein assay: in this case, the loading quantity of protein has demonstrated to be proportional to the number of amino groups available on the

surface, even if I hypothesized that for HA-SNP most of the protein is passively adsorbed on the particle surface caused by the initial positively charges of the system (at pH 7.4), taking into consideration that the IEP of Human transferrin is in the range of pH 5.2 and 5.9 [40]. It has been found that 12 molecules of Tf have been conjugated to **Tf1-SNP** per nanoparticle (89 µg mg_{NP}^{-1}) instead after for samples treated with the first inhert MS-PEG_4 on SNP, the quantity of protein has slowly decreased; **Tf2-SNP**, (69.8 µg mg_{NP}^{-1}) 9 molecules per NP; **Tf3-SNP**, (62.6 µg mg_{NP}^{-1}) 8 molecules per NP; **Tf4-SNP**, (49.1 µg mg_{NP}^{-1}) 6 molecules per NP; **Tf5-SNP**, (36.7 µg mg_{NP}^{-1}) 5 molecules per NP.

5.6 Nanocomplex activities towards TfR

RNA interference has been used to silence the expression of TfR in A549 lung cancer epithelial cells in order to determine the effect of TfR on NPs uptake. I would like to emphasize that the absolute uptake level does not give information on the specificity of these interactions. However, the difference in particle uptake in silenced and non-silenced cells is clearly indicative of the relative contribution made by TfR mediated pathway. This silenced cell model has been then used to determine the contribution of Tf in the uptake of different NPs; I used to test the capacity of different Tf-conjugated nanoparticles to be recognized by TfR in simple buffer or serum-free medium to exclude the contribution of other proteins dissolved in the medium. Analyses have been performed by FACS, within cell-fluorescence intensity profiles exploited by time-increasing internalization of SNP (Figure 5.10).

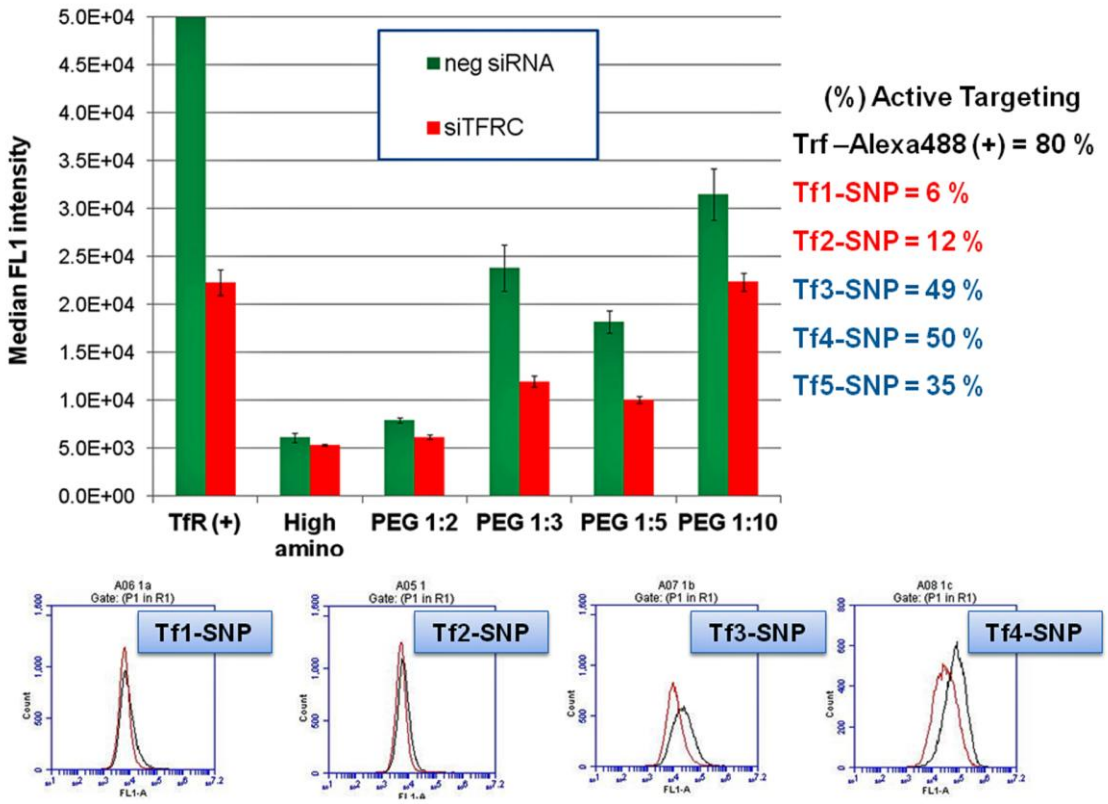

Figure 5.10: TfR recognition by FACS analysis.
(Graph) Histogram profiles of $Tf_{1\text{-}5}$-SNPs and Tf-Alexa488 (as positive control) after 4 h incubation at 37°C in serum-free conditions. (Lower graphs) Examples of FACS profiles of as synthesized NPs.

As showed by the graph, Tf-SNPs have different activities towards TfR-mediated uptake and there is a strong impact of the first PEGylation step; an high amination of SNP gives a superior protein loading amount but a very high non-specific uptake, while the first PEGylation within 3 and 5 molar excess of MS-PEG_4 guarantees the maximum targeting specificity (50%) beside a lower amount of protein conjugated; however, too much inhert PEG maybe has revealed negative effect as well, because few amine are free to react with the protein and maybe Tf-conjugated is not enough to be highly specific towards TfR (See Tf5-SNP).

The kinetic uptake experiment has been repeated in the completed cell culture medium (cMEM) supplemented with 10 wt.% FBS (tot proteins 4 mg mL^{-1}).

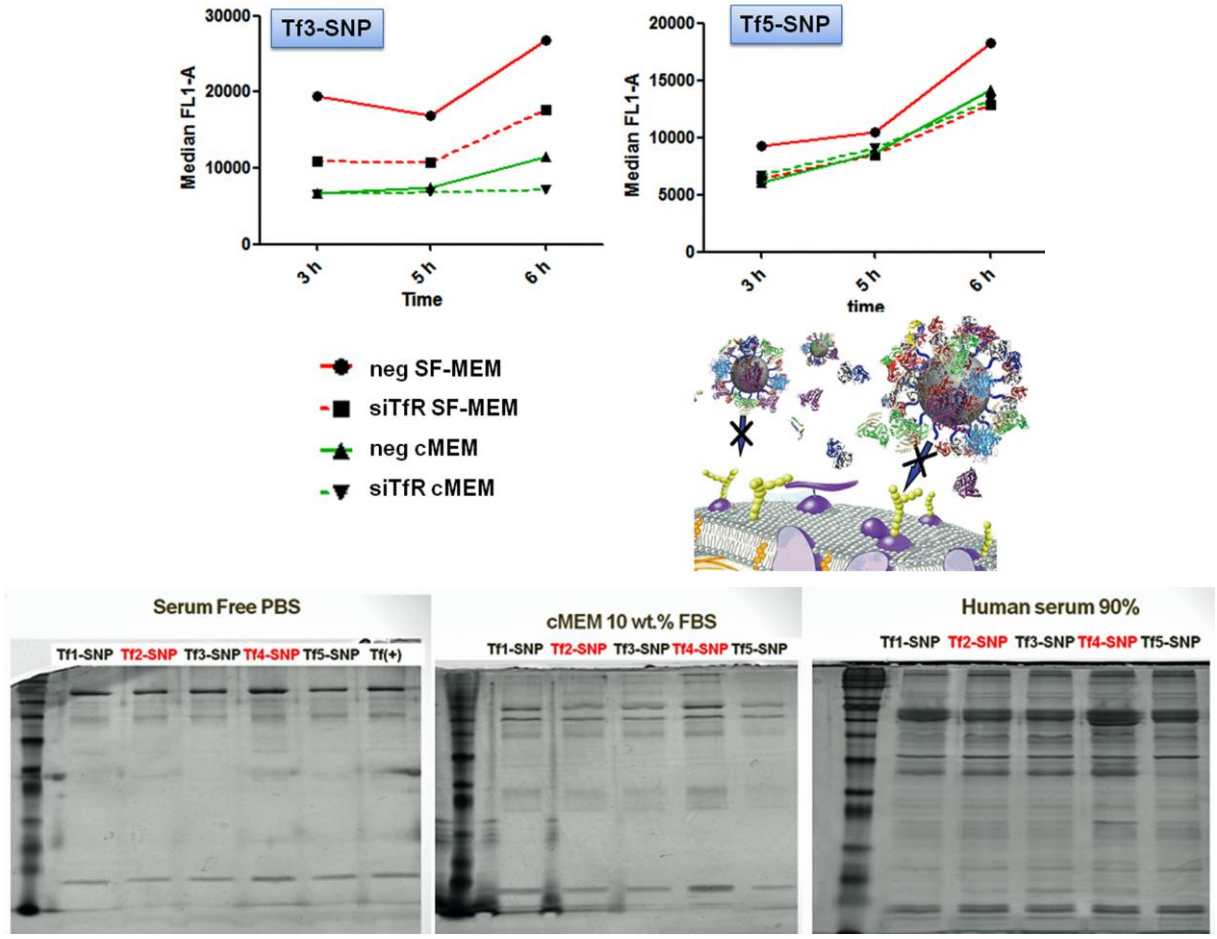

Figure 5.11: TfR recognition by FACS analysis and evaluation of "protein corona".
(Upper level) Uptake kinetic profiles of Tf4-SNP and Tf5-SNP after incubation at 37°C in cMEM.
(Lower level) Protein separation by 1D-SDS-PAGE in PBS, in cMEM 10wt.% FBS, in human serum 90 wt.%: .

This kinetic uptake experiment has revealed that all proteins dissolved in biological milieu play a critical role in the formation of the protein corona, thus masking completely the activity of Tf in the recognition of its receptor (Figure 5.11). This is why NPs that have worked perfectly in serum free conditions, lose completely their targeting capabilities when a biomolecule corona adsorbs on the surface. This result has found validations within the protein separation by SDS-page after incubation of NPs in different media 1 h at 37 °C. For instance, the single line corresponding to Tf in the first gel (left) is gradually associated to other proteins included in the corresponding milieu (center and right gels). However, only by this experiment; I cannot assess great differences between Tf-SNP protein coronas. Unfortunately, my restricted time of my visiting work did not allow me to conclude this project; hence this final consideration needs to be carefully validated with more complex assays.

5.7 Perspectives

Using transferrin-conjugated nanoparticles, first I have found that studying and tuning finely the chemistry of surface functionalization is a basic element to achieve a good targeting module protein-NP mediated. Secondly, I have observed that protein in the media can shield Tf from binding its targeted receptors on cells. My results suggest that when nanoparticles are placed in a complex biological environment, interactions with other proteins at the bio-nano interface strongly influenced NPs activity in targeting efficiency.

Nevertheless, these studies focus only on a single receptor (TfR) so that all mechanisms involved are of a general nature and suggest future deep investigation of the ligand targeting machinery towards the TfR and its relationship to specific biological outcomes [41]. Anyway, all the approaches outlined here may be of general value; in this way this study could be consider an example that could be readily extended to evaluate and screen different nanocomplexes as to their targeting recognition efficiency.

5.8 Nanomaterials Experimental section

5.8.1 Synthesis of Core-Fluorescent Silica Nanospheres (FSNP)

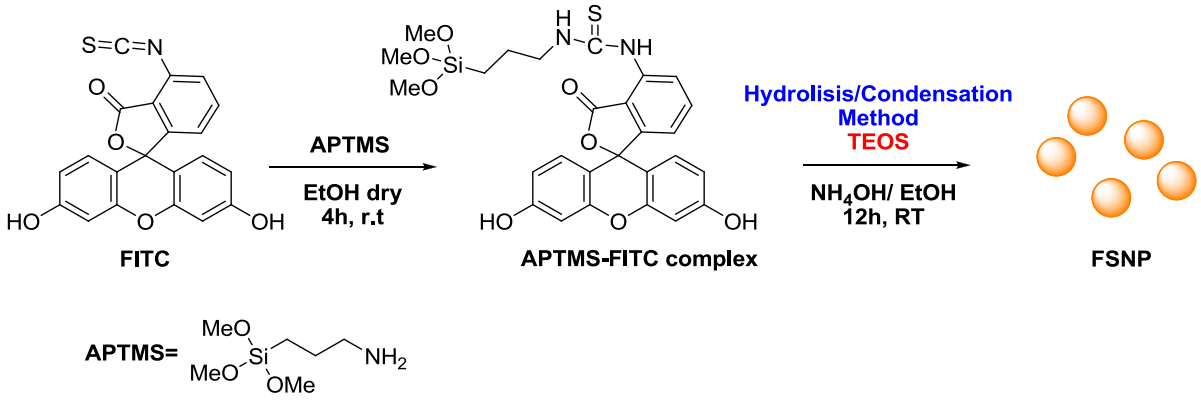

(Inhert atmosphere, Dry solvents)

*5.8.1.1 Synthesis of N-1-(3-trimethoxysilylpropyl)-N'-fluoresceyl thiourea (***FITC-APTMS***)*

Monodisperse silica nanospheres have been obtained as described in literature [34]. First of all the conjugate solution has been prepared by dissolving FITC (2 mg. 5.0 µmol) in anhydrous ethanol (2.0 mL). 3-Aminopropyl)trimethoxysilane (APTMS,10.0 µL, 55.0 µmol) has then added immediately to this solution with the mixture and then shaken at RT in darkness for 4 hr. This reaction has been monitored by ^{1}H-NMR (CD_3OD) where a shift in the signal from the proton adjacent to the amine group ($Si(OCH_3)_3CH_2CH_2CH_2NH_2$) δ: 3.80 (*t*, 2H) upon coupling FITC has reached an integration value constant and equal to the aromatic FITC signal δ: 7.15 (*d*, 2H). The reaction deemed complete after 4 h.

*5.8.1.2 Synthesis of Fluorescent core silica nanoparticles (***FSNP***)*

20nm FSNP has been prepared as soon as the dye-complex has been arranged, according with the Stöber synthesis. In a propylene plastic tube, to aqueous NH_4OH 28 wt.% (728 mg, 0.46 M) has been added dry EtOH to a total volume of 50 mL and the mixture has been rapidly stirred. FITC-APTMS (1 mL of the conjugate solution) has been then added to this mixture followed 1 minute later by TEOS (1.4 mL, 0.17 M). The reaction has been sealed and stirred at 55°C overnight. The solvent has been then evaporated under reduce pressure by half of its volume (25 mL) and deionized water has been added (40 mL). The remaining organic solvent has been removed completely under reduce pressure in order to gain a **FSNP** aqueous suspension; at the end of this step, FSNP have been filtered on a cotton filter to remove only large aggregates. Instead, FSNP have been then washed by the excess of dye with high speed centrifugation (20000 rcf, 30 min) and resuspension in deionized water (40 mL) three times. Following final resuspension in water (35-40 mL), the final volume has

been adjusted to give a final particle concentration of 10 mg/mL for further functionalization experiments (concentration measured by vacuum drying at 60°C overnight). Particle size can be modulated through aqueous ammonia concentration [M] as described in the table below.

Particle Diameter	[NH_4OH]	[H_20]	[TEOS]	FITC-APTMS	T (°C)
20 nm	0.46	1,232	0.17	20 µg mL^{-1}	55
40 nm	0.58	1.456	0.17	20 µg mL^{-1}	20
90 nm	0.85	1.900	0.17	20 µg mL^{-1}	20

Table. 7: Developed FSNP-nanoparticles

5.8.2 Synthesis of Core-shell fluorescent silica nanoparticles (SFSNP)

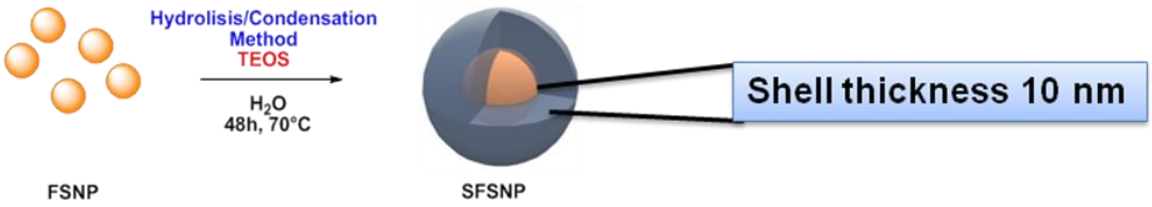

Core shell particles (30 nm, 50 nm and 100 nm) have been prepared following a method similar to previously published to produce nanosilica using methods derived from biosilicification to control the reaction [37,38] and increase the particle stability. In a propylene plastic tube, to a cleaned aqueous FSNP dispersion (10.0 mg mL^{-1}) has been added L-Arginine (0.5 mg mL^{-1}). The required amount of TEOS has been estimated according to equation below (equation 4). It has been then added to the mixture and the two-phase reaction has been left incubating at 70°C in darkness for 2 days under very gentle stirring, to homogenize the lower aqueous phase. The resultant dispersion, now one homogenous phase, has been then centrifuged at high speed rate (20000 rcf, 30 min) followed by resuspension of the pellet in deionized water. This cleaning cycle has been then repeated three times and finally **SFSNP** have been resuspended at a concentration of 10 mg mL^{-1} for further functionalization.

$$r_{final} = \sqrt[2]{\left(\frac{3V_{SiO_2}}{4\pi \cdot N} + r_{core}{}^3\right)} \qquad \text{(eq. 4)}$$

5.8.3 Amination of Core-shell fluorescent silica nanoparticles (HA-SNP)

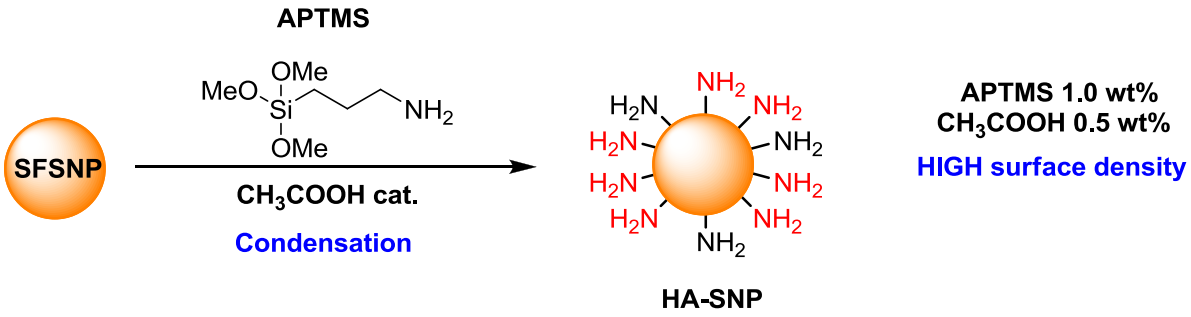

High density of amino groups on 30 nm SFSNP has been prepared with catalytic hydrolysis of 3-Aminopropyl)trimethoxysilane. In a propylene plastic tube, glacial acetic acid (5.0 µL) has been added to an aqueous SFSNP dispersion (10.0 mg mL^{-1}, 1 mL); the mixture should be equilibrated for 5 min. Later, APTMS (10.0 µL, 55 µmol) has been added to NPs suspension; the dispersion becomes turbid and needs an ultrasound treatment to disaggregate NPs clusters; when the suspension has became clear again, the reaction has been stirred for 2h at RT on the orbital shaker with vigorous stirring. The resultant dispersion, now one homogenous phase, has been then centrifuged at high speed rate (20000 rcf, 30 min) followed by resuspension of the pellet in absolute ethanol twice. An aliquot of aminated NPs (2 mg) has been withdrawn for amino quantification assay, while the cleaning cycle continued three times with deionized water; finally **HA-SNP** have been resuspended in water at a concentration of 10 mg mL^{-1} for further experiments.

5.8.4 Determination of amino groups on HA-SNP: Ninhydrin assay

This technique has been adapted as described in literature [42]. Briefly, HA-SNP (1 or 2 mg) have been equilibrated twice in dry EtOH (1 mL) and then resuspended in the same solvent (1.0 mL). Meanwhile a pale green Ninhydrin stock solution (3.5 mg mL^{-1}) has been prepared in dry ethanol as well. An aliquot of Ninhydrin stock solution (0.250 mL) has been added to HA-SNP suspension and, after ultrasound assisted equilibration, heated at 60 °C for 1 h in the oven. HA-SNP, after cooling to RT, have been then separated from the supernatant by centrifugation (11200 rcf) and an aliquot of particle-free blue supernatant (0.2 mL) read with UV-vis spectrophotometer at 588 nm. Standard calibration curve has been created using Ethanolamine in a concentration range between 0−3 mM in dry EtOH. The same calculations have been performed to estabilished the particle surface NH2 coating corresponding to about 2.16 NH_2 / nm^2, roughly 800 aminos for nanoparticles.

5.8.5 First inhert pegylation (PEG1-SNP)

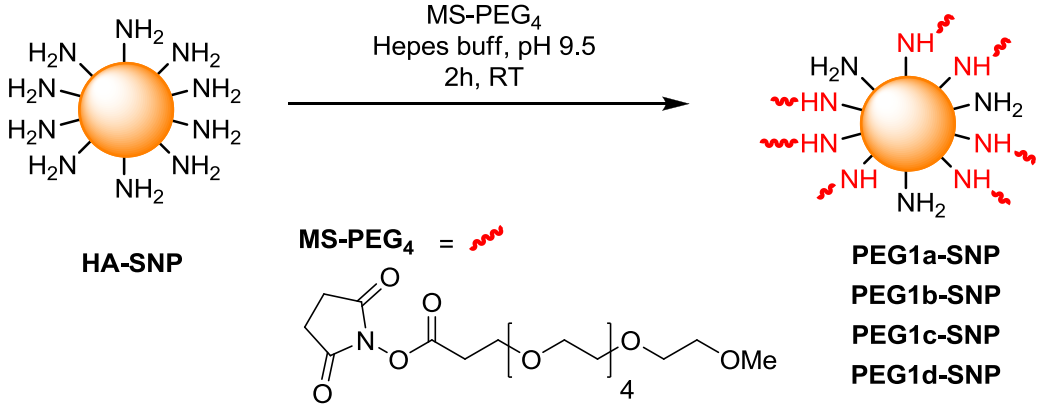

In a plastic tube, an aqueous suspension of HA-SNP (10.0 mg mL^{-1}, 1 mL, 0.790 µmol NH_2 total) have been equilibrated twice in 20 mM HEPES buffer pH 9.5 and then resuspensed in the same buffer (1 mL). An aliquot of a stock solution of MS-PEG_4 in DMSO (corresponding to 1.58 µmol, 2 molar eq. excess) has been added to HA-SNP dispersion. NPs dispersion has become turbid an ultrasound equilibration occurred to homogenize NPs suspension until to obtain a clear yellow suspension. The reaction has left to react for 2h at RT on the orbital shaker with vigorous stirring. At the end of the reaction, the resultant PEG1-SNP have been then centrifuged at high speed rate (20000 rcf, 30 min) followed by washings cycle with deionized water (1 mL, thrice); PEG1-SNP have been finally resuspended in water at a concentration of 10 mg mL^{-1} for analyses and transferrin bioconjugation.

The molar ration of inhert PEG has been modulated in order to obtain different inhert PEGylated surface. In this way the following product library has been created for Transferrin bioconjugation:

PEG1a-SNP = MS-PEG4 2 molar eq. excess;

PEG1b-SNP = MS-PEG4 3 molar eq. excess;

PEG1c-SNP = MS-PEG4 5 molar eq. excess;

PEG1d-SNP = MS-PEG4 10 molar eq. excess;

The ninhydrin assay has been repeated (5 mg of PEG1-SNP) for each product and residual amino groups on nanoparticle surface have been estimated:

PEG1a-SNP = 0.051 $\mu mol_{NH2}\, mg_{NP}^{-1}$, 220 molecules NH_2 per nanoparticle;

PEG1b-SNP = 0.010 $\mu mol_{NH2}\, mg_{NP}^{-1}$, 40 molecules NH_2 per nanoparticle;

PEG1c-SNP = 0.008 $\mu mol_{NH2}\, mg_{NP}^{-1}$, 30 molecules NH_2 per nanoparticle;

PEG1d-SNP = 0.004 $\mu mol_{NH2}\, mg_{NP}^{-1}$, 16 molecules NH_2 per nanoparticle;

5.8.6 Transferrin bioconjugation onto silica nanoparticles (Tf-SNP)

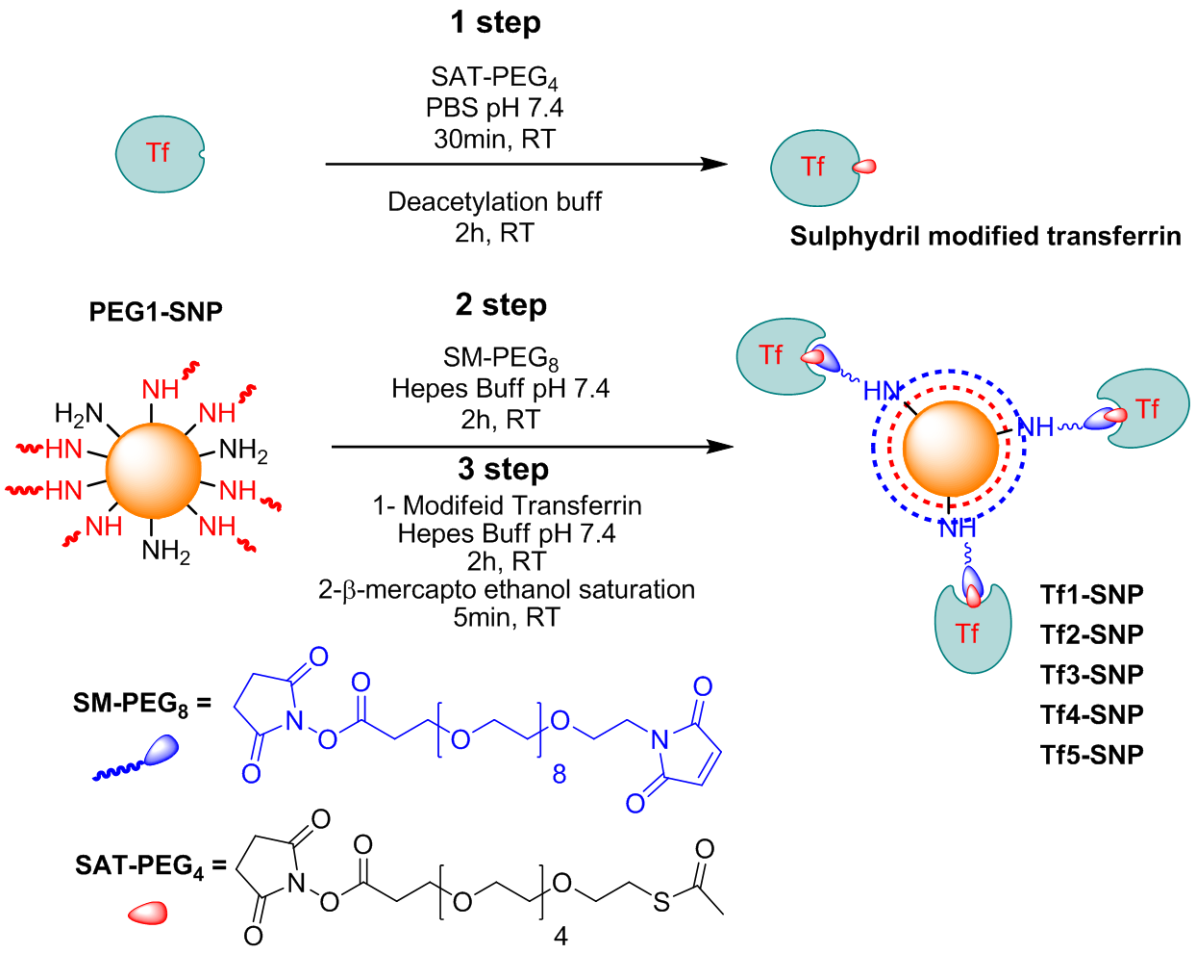

5.8.6.1 Suphydril modified Transferrin (**SAT-PEG$_4$**): *1st Step*

This protocol has been modified from a previous work [21] and is suitable for 5 mg of HA-SNP and PEG1-SNP. Transferrin, Tf (2.5 mg, 0.0312 µmol) has been dissolved in degassed 20mM PBS pH 7.4 (1 mL). To this solution has been added SAT-PEG$_4$ dissolved in DMSO (10 µg, 0.023 µmol). At this time, particle modification (2nd step) has been started at this time. After 30 minutes of gentle shaking at room temperature, deacetylation buffer (0.5M Hydroxylamine, 25mM ethylenediaminetetraacetic acid (EDTA) in 20 mM PBS, pH 7.4), (50 µL) has been added. The reaction has been allowed to continue for 2 hours without shaking, followed by addition with 1 mM tris(2- carboxyethyl)phosphine (TCEP) (0.023 µmol) just 1 min before cleaning on a Sephadex G25 spin column exchanging in deoxygenated HEPES buffer (pH 7.4). Column loading: 2.5 mL of reaction buffer, collecting Tf-modified fractions following the red band which elutes from the column.

5.8.6.2 protein coupling onto silica-modified nanoparticles (**SM-PEG$_8$**): *2nd Step*

The HA-SNP and PEG1$_{(a-d)}$-SNP (5 mg each batch) have been equilibrated twice with 20 mM HEPES buffer pH 7.4 (500 µL), before resuspension in the same buffer at a concentration of 10 mg mL^{-1}. To this suspension has been added an equal volume solution (500 µL) of SM-PEG$_8$ in 20 mM HEPES buffer pH 7.4 (which corresponds to 5 molar excess of calculated amino groups) with mixing. With high rate amination samples (not with PEG1c-SNP and PEG1d-SNP), the initially clouding reaction has been shaken 2 h with intermittent bath sonication (twice 30 sec) resulting in a clear suspension. At the end of the reaction nanoparticles have been then centrifuged down (14000 rcf, 30min) followed by two washes with deionized water (1 mL) and then finally resuspended in deoxygenated 20 mM HEPES buffer pH 7.4 (500 µL, final concentration of 10 mg mL^{-1}).

5.8.6.3 Silica second hetero bifunctioonal pegylation (**Tf-SNP**): *3rd Step*

The work has been timed so that the modified protein solution and modified particle dispersion would be ready simultaneously and have been then combined (2.0 mg protein each 5 mg nanoparticles. The resultant mixture has been shaken gently 2 h at RT. 1 mM 2-Mercaptoethanol (5 µg, 0.023 µmol) has been then added to saturate all unreacted malemide rings; later on, after 5 min, the **Tf$_{1-5}$-SNP** has been then cleaned of unreacted proteins and excess mercaptoethanol by centrifugation and resuspension three times in filtered 20 mM PBS pH 7.4 (1 mL). Finally all products have been resuspended in the same buffer and stored at 4°C for cellular experiments and analyses (500 µL, 5 mg mL^{-1}).

5.8.7 Cell silencing and flow cytometry

Cell silencing and flow cytometry have been adapted from literaure data [21]. A total of 20000 cells have been seeded in 12-well plates, and incubated for 24 h before silencing of the gene coding for transferrin receptor (TfR). Cells have been then transfected with a Silencer Select siRNA (30 pmol) using Oligofectamine (Invitrogen) according to the manufacturer's instructions; an the contrary, Neg1 silencer was used as a negative control. Cells have been transfected with siRNAs for 72 h in all experiments before exposure to nanoparticles or labelled transferrin. After 72 h silencing, cells have been washed twice 10 min serum-free cell cuture medium (MEM, 1 mL). The buffer has been then replaced by the Tf$_{1-4}$-SNP dispersions in serum free medium (100 µg mL^{-1}, 500 µL), freshly prepared by diluting the nanoparticle stock in serum-free MEM (or cMEM, supplemented with 10% FBS, depending on the experiment). Similar experiments have been performed by exposing cells to Alexa 488-labelled human transferrin (5 µg mL^{-1}, from Molecular Probes) in serum-free MEM.

For flow cytometry analysis, cells have been washed thrice with PBS (1 mL) and harvested with trypsin (400 µL). Cell pellets were then fixed at room temperature with 4% formalin (400 µL) for 20 min in the dark and then resuspended in PBS (500 µL) before cell-associated fluorescence (10000−15000 cells acquired each sample) has been measured using an Accuri C6 reader (BD Accuri Cytometers). Results are reported as the median of the distribution of cell fluorescence intensity, averaged over two to three independent replicates. Error bars represent the standard deviation between replicates. Each experiment has been performed at least two times.

5.8.8 Protein separation by 1D-SDS-PAGE

The nanoparticle-protein complexes have been separated and denatured by boiling for 5 minutes in loading buffer (62.5 mM Tris-HCl, pH 6.8 at 25 °C; 2 wt.% sodium dodecyl sulfate (SDS); 10 wt.% glycerol; 0.01 wt.% bromophenol blue; 40 mM dithiothreitol (DTT). Samples have been then separated by size in the moiety of porous 10% polyacrylamide gel (1D SDS polyacrylamide gel electrophoresis), in an electric field using a Mini-PROTEAN Tetra electrophoresis system from Bio-Rad. The electrophoresis has been run under constant voltage (130 V, 45 minutes). Gels have been silver stained using 2D Silver Stain Kit II (Cosmo Bio Co., Ltd) and scanned using Bio-Rad GS-800 Calibrated Densitometer.

Related References

[1] Aisen, P.; Enns, C. and Wessling-Resnick, M.; *Int. Biochem. Cell Biol.* **2001**, *10*, 940–959.

[2] Moore, S. A.; Anderson, B. F.; Groom, C. R.; Haridas, M. and Baker, E. N.; *J. Mol. Biol.* **1997**, *274*, 222–236.

[3] Lebron, J.A.; Bennett, M.J.; Vaughn, D.E.; et al.; *Cell.* **1998**, *93*, 111–123.

[4] Turkewitz, A. P.; Amatruda, J. F.; Borhani, D.; Harrison, S. C. and Schwartz, A. L.; *J. Biol. Chem.***1988**, *263*, 8318−8325.

[5] Enns, C. A. and Sussman, H. H.; *J. Biol. Chem.***1981***, 256,* 9820−9823.

[6] Lawrence, C. M.; Ray, S.; Babyonyshev, M.; Galluster, R.; Brhani, B. W.; and Harrison, S. C.; *Science* **1999**, *286*, 779−782.

[7] Cheng, Y.; Zak, O.; Aisen, P.; Harrison, S. C. and Walz, T.; *Cell* **2004**, *116*, 565−576.

[8] Daniels, T. R.; Delgado, T.; Rodriguez, J. A.; Helguera, G. and Penichet, M. L.; *Clin. Immunol.* **2006**, *121*, 144–158.

[9] Calzolari, A.; Oliviero, I.; Deaglio, S.; et al.; *Blood. Cel.Mol. Disease* **2007**, *39*, 82–91.

[10] Daniels, T. R.; Bernabeu, E.; Rodriguez, J. A.; et al.; *Biochim. Biophys. Acta* **2012**, *1820*, 291–317.

[11] Hemadi, M.; Kahn, P. H.; Miquel, G. and El Hage Chahine, J. M.; *Biochemistry* **2004**, *43*, 1736–1745.

[12] Yang, D. C.; Wang, F.; Elliott, R. L.; Head Daniels, J. F.; Bernabeu, T. R. and Rodriguez, E.; *Anticancer Res.* **2001**, *21*, 521–549.

[13] Gaucher, G.; Dufresne, M. H.; Sant, V. P.; Kang, N.; Maysinger, D. and Leroux, J. C.; *J. Control. Release.* **2005**, *109*, 169–188.

[14] Guo, W.; Zheng, W.; Luo, Q.; et al.; *Inorg. Chem.* **2005**, *109*, 169–188.

[15] Yang, P. H.; Sun, X.; Chiu, J. F.; Sun, H. and He, Q. Y.; *Bioconjugate Chem.* **2005**, *16*, 494–496.

[16] Yhee, J. Y.; Lee, S. J.; Lee, S.; et al.; *Bioconjugate Chem.* **2013**, *24*, 1850–1860.

[17] Sahoo, S. K.; Ma, W. and Labhasetwar, V.; *Int. J. Cancer.* **2004**, *112*, 335–340.

[18] Ferrari, M.; *Trends Biotechnol.* **2010**, *28*, 181–188.

[19] Kumar, R.; Roy, I.; Ohulchanskyy, T. Y.; et al; *ACS Nano.* **2008**, *2*, 449–456.

[20] Hogemann, D.; Bos, E.; Blondet, C.; et al.; *Neoplasia.* **2003**, *5*, 495–506.

[21] Salvati, A.; Pitek, A. S.; Monopoli, M. P,; et al.; *Nat. Nanotech*. **2013**, *8*, 137–143.

[22] Shapero, K.; Fenaroli, F.; Lynch, Y.; Cottell, D. C.; Salvati, A. and Dawson, K. A.; *Mol. BioSyst.* **2011**, *7*, 371–378.

[23] Del Pino, P.; Pelaz, B.; Zhang, Q.; Maffre, P.; Nienhaus, G. U. and Parak, W. J.; *Mater. Oriz.* **2014**, DOI: 10.1039/C3MH00106G.

[24] Verderio, P.; Avvakumova, S.; Bellini, M.; et al.; *Adv. Heathcare Mater.* **2013**, adhm.201300602R1.

[25] Albanese, A.; Tang, P.S. and Chan, W. C. W.; *Annu. Rev. Biomed. Eng.* **2012**, *14*, 1−15.

[26] Oh, W. K.; Kim, S.; Kwon, O. and Jang, J.; *J. Nanosci. Nanotechnol.* **2011**, *11,* 4254−4259.

[27] Florez, L.; Herrmann, C.; Cramer, J. M.; et al.; *Small* **2012**, *8*, 2222−2225.

[28] Hünh, D.; Kantner, K.; Geidel, C.; et al.; *ACS Nano* **2013**, *7*, 3253−3258.

[29] Sapsford, K. E.; Algar, W. R.; Berti, L.; et al.; *Chem. Rev.* **2013**, *113*, 1904−2074.

[30] Liu, W.; Rose, J.; Plantevin, S.; Auffan, M.; Bottero, J. and Vidaud, C.; *Nanoscale.* **2013**, *5*, 1658−1669.

[31] Dell'Orco, D.; Lundqvist, M.; Oslakovic, C.; Cedervall, T. and Linse, S.; *PlosONE.* **2010**, *5,* e10949.

[32] Monopoli, M. P.; Walczyk, D.; Campbell, A.; Elia, G.; Lynch, I.; Baldelli Bombelli, F.; Dawson, K. A. *J. Am. Chem. Soc.***2011**, *133*, 2525−2530.

[33] Pilar, G. L.; De Aberasturi, D. J.; Wulf, V.; et al.; *Acc. Chem. Soc.* **2013**, *6*, 743−749.

[34] Mahon, E.; Hristov, D. R. and Dawson, K. A.;*Chem. Commun*. **2012**, *48*, 7970–7972.

[35] Wong, Y. J.; Zhu, L. F.; Teo, W. S.; et al.;*J. Am. Chem. Soc.* **2011**, *133*, 11422–11425.

[36] Monopoli, M. P.; Baldelli Bombelli, F. and Dawson, K. A.;*Nat. Nanotech*. **2011**, *6*, 11–12.

[37] Hartlen, K. D.; Athanasopoulos, A. P. T. and Kitaev, V.; *Langmuir.* **2008**, *24*, 1714–1719.

[38] Yokoi, T.; Sakamoto, Y.; Terasaki, O.; Kubota, Y. and Tatsumi, T.; *J. Am. Chem. Soc.***2006**, *128*, 13664–13666.

[39] Larson, D. R.; Ow, H.; Vishwasrao, H. D.; et al.; *Chem. Mater.* **2008**, *20*, 2677−2684.

[40] Moguilevsky, N.; Rategui, L. A.and Masson, P. L.; *Biochem. J.* **1985**, *229*, 353−359.

[41] Casals, E. and Puntes, V. F.; *Nanomedicine.* **2012**, *7*, 1917–1930.

[42] Cantu, E.; Cueto, R.; Koch, J. and Russo, P. S.; *Langmuir.* **2012**, *28*, 5562–5569.

Chapter VI

Orientation-Controlled Conjugation of Haloalkane Dehalogenase Fused Homing Peptides to Multifunctional Iron Oxide Nanoparticles for the Specific Recognition of Cancer Cells

Contents

6.1 Engineering Halo protein for uPAR receptor targeting

This is the last example of NPs model to accomplish active targeting of tumor cellular biomarkers. The present project focuses on the utilization of iron oxide nanoparticles (MNPs) with the purpose of targeting urokinase Plasminogen Activator receptor (uPAR), a membrane protein over-expressed in several kinds of cancer, such as breast, ovarian, prostate, renal and pancreatic.

uPA is a 50 kDa serine protease that plays an important role in the progression of tumor, angiogenesis, metastasis and inflammation. All these effects are accomplished by the interaction with its receptor (uPAR). Basically, the binding of uPAR activates the proteolytic domain of uPA that is so able to trigger the cleavage of plasminogen into plasmin, which leads the degradation of the extracellular matrix by matrix-metalloproteinase (MMPs) thus releasing several growth factors [1].

uPA is composed of a carboxy-terminal serine protease domain and a modular amino terminal fragment (ATF) which is directly involved in the interaction with uPAR. ATF is in turn constituted of a kringle domain, which is supposed being involved in the stabilization of uPA-uPAR interaction, and a growth factor-like domain (GFD), which contains the amino acids physically involved in such interaction. In particular, there is a sequence of 11 amino acids (**VSNKYFSNIHW**), commonly named **U11** peptide, that forms a loop on GFD and finds accommodation in a precise pocket of uPAR. The most important residues are Ser21, Asn22, Lys23 and Tyr24 that make hydrogen bonds and polar interactions at the interface (Figure 6.1) [2].

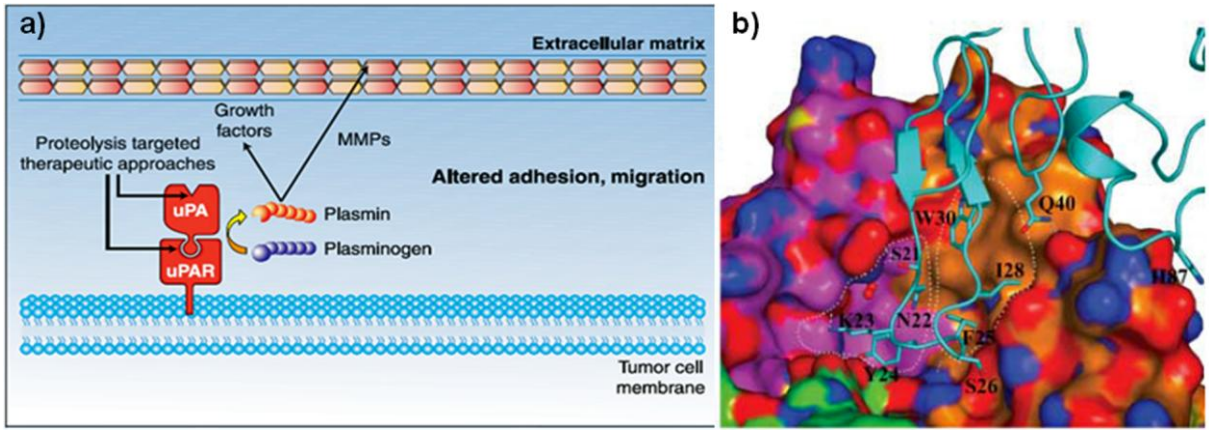

Figure 6.1: uPAR and its role in tumor biology.
(Panel A) The ligand for uPAR, uPA, is a serine protease that mediates the activation of plasminogen to plasmin and this process occurs with greater catalytic efficiency when bothmolecules are bound to the cell surface. Once activated, plasmin unleashes several cascades leading to the degradation of extracellular matrix, the activation of pro-matrix metalloproteinases, and the activation and release of growth factors such as vascular endothelial growth factor that are deposited in the matrix.
(Panel B) Aminoacid residues present in U11 sequence, important for the interaction with uPAR.

With the aim to recognize uPAR in this work two different strategies have been employed to guide the mechanism of action of this peptide. The first method consisted in the direct linkage of the peptide to the surface of NPs modulated by the interaction of a specific terminal cysteine which is used for MNPs conjugation by means of a thiol-based covalent reaction; whereas, the latter describes the design of a fusion protein model. Recently, a new modern approach, called **Halo Tag**

technology, applied for cellular imaging, protein quantification and interaction analysis has been developed [3]. It is designed to provide new options for rapid, site-specific labeling of proteins in living cells and *in vitro,* and based on the efficient formation of a covalent bond between the Halo Tag protein and synthetic ligands. The Halo Tag protein is a catalytically inactive, genetically modified derivative of a hydrolase protein [4]. This 33 kDa monomeric protein can be used to generate N- or C-terminal fusions that can be efficiently expressed in a variety of cell types. The Halo Tag ligands are small chemical tags capable of covalently coupling with the Halo Tag protein. The rate of the ligand-protein binding is remarkably fast because is like an enzymatic-oriented reaction (Figure 6.2). The covalent bond forms rapidly under physiological conditions, is highly specific and essentially irreversible yielding a stable complex even under denaturing conditions. Several requirements are needed for specific ligand to be active for the interaction with Halo Tag protein: the linker between halide and functional group should be 14 atoms long and contain 6 carbon atoms proximal to the terminal chloride [5].

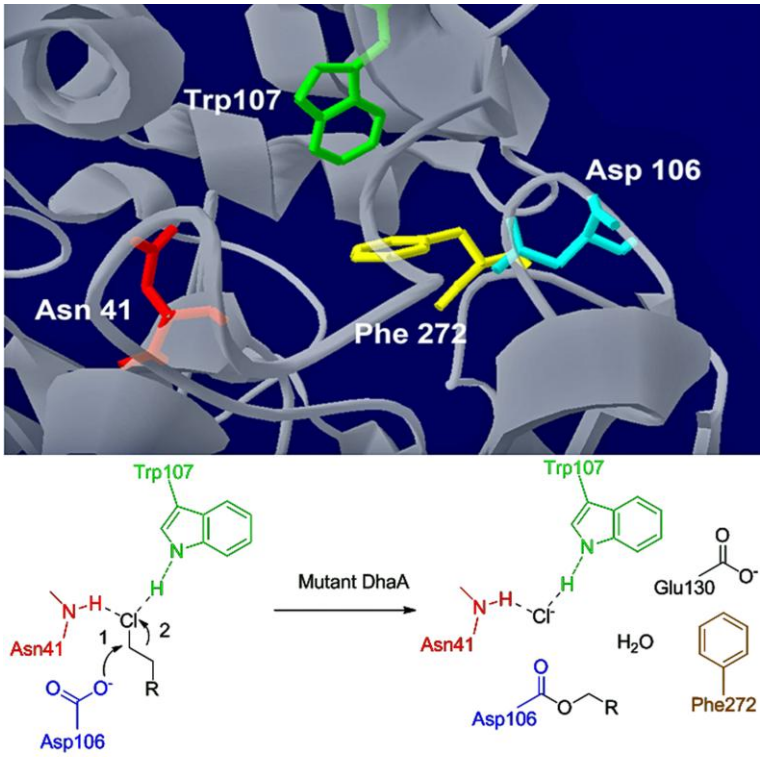

Figure 6.2: Overview of the HALO system.
(Upper level) The HaloTag protein (model) close-up of the ligand tunnel with covalently bound the specific chloroalcane ligand. (Lower level) Reaction mechanism of HALO. Nucleophilic displacement of the terminal chloride with Asp106 leads to a covalent alkyl-enzyme intermediate. The substituted Phe272 is ineffective as a base, thereby trapping the reaction intermediate as a stable covalent adduct.

In general, the structure of a nanoparticle bioconjugate affects its function, and the controlled display of biomolecules on NPs is critical in order to obtain conjugates with well-defined and reproducible properties [6]. Hybrid multifunctional MNPs, which combine unique superparamagnetic properties and fluorescence emission, have been envisaged as promising bimodal tracers for noninvasive diagnosis of cancer both *in vitro* and *in vivo* [7,8]. The design of ideal targeted NPs needs careful optimization of fundamental features including uniform size and shape, surface charge, optical and magnetic properties [9,10] and efficient functionalization with suitable homing ligands [11,12] to improve the signal amplification and target selectivity toward malignant cells. When the ligands are complex molecules, such as proteins, their proper orientation on the surface of nanoparticles becomes a crucial factor for maximizing the affinity for their molecular counterparts [13]. Recently, our group have proposed a novel approach that relies on engineered proteins consisting of a receptor-targeting domain genetically fused with a nanoparticle-capture domain, in which the capture module should be an enzyme capable of irreversibly reacting with a suicide inhibitor covalently anchored on MNPs [14]. In principle, this bimodular orthogonal bioreaction could present two important advantages when the homing ligand is a short peptide (*e.g.* 5–30 amino acids): i) the peptide is separated from the nanoparticle surface by a protein spacer; ii) the introduction of globular proteins enhances the solubility of the nanoconstruct.

This is the explanation of creating the HALO capture module for oriented-specific conjugation with MNPs, moreover, the addition of the U11 peptide sequence guarantees at the same time the targeting module for uPAR. Within this context, the peptide sequence take the lead of a double advantage: at first, the HALO covalent enzyme-catalyzed immobilization furnishes very high reaction specificity in few times;

secondly, the targeting peptide is sufficiently spaced apart (and oriented toward the counterpart while opposed to the particle) from the NPs surface in a way that it does not suffer too much from the physicochemical properties of the rigid metallic particle surface [15−17]. The capability of both methods to assure the recognition of the specific target uPAR, on uPAR(+) cancer cells (and uPAR(−) as a negative control) has been validated by FACS and CLSM.

In details, to construct the HALO sequence my biologist colleagues modified by selective mutagenesis the native protein as reported in literature [4] and, in addition, two restriction sites have been inserted at the 5'- and 3'-positions, respectively, and the modified gene was cloned in a pGEX-6-P-1 vector to express HALO in BL21(DE3) codon plus *E. coli* strain (Figure 6.3).

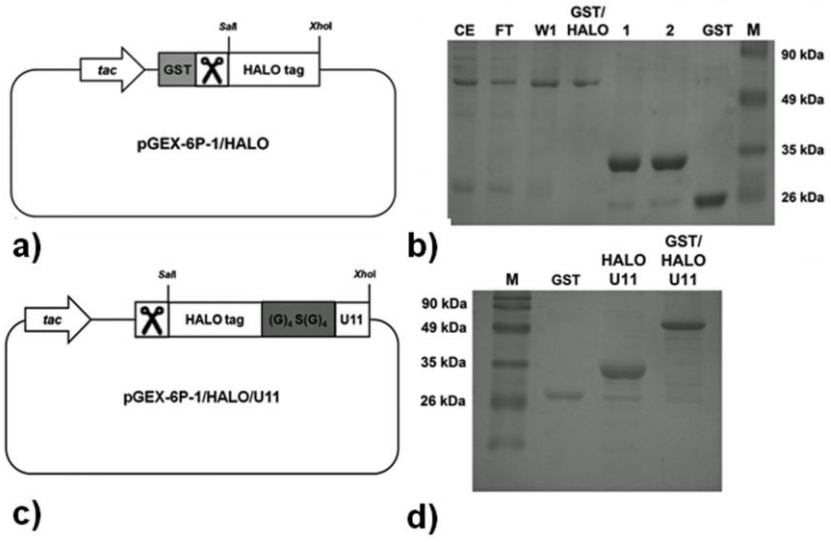

Figure 6.3: HALO protein engineering construction.
(Panel A and C) Schematic diagram of the pGEX-6P-1/HALO and HALO/U11 expression vectors.
(Panel B) Glutathione-affinity purification of HALO by SDS-page: crude extract (CE), flow trough (FT), wash (W1), glutathione elution (GST-HALO), fractions obtained by GST Pre Scission cleavage (1 and 2) visualized by Coomassie staining. M: protein markers (kDa); GST: glutathione S-transferase standard.
(Panel D) Glutathione-affinity purification of HALO/U11 by SDS-page: glutathione elution (GST-HALO/U11), fraction obtained by GST Pre Scission cleavage (HALO/U11).

A HALO capture model HALO capture module has been engineered in the same way by the introduction of a U11 targeting element involved in uPAR recognition, through a C-terminal insertion of a GGGGSGGGG loop, which should

provide sufficient freedom to the peptide. Both Conjugates have been isolated from the crude extract by using a glutathione–sepharose column showing an excellent degree of purity.

6.2 Synthesis and preliminary functionalization of magnetic nanocrystals

10 ± 1.3 nm magnetic iron oxide nanoparticles capped by oleate surfactant (MNC0) have been obtained by solvothermal decomposition in high boiling organic solvents [18] (Figure 6.4).

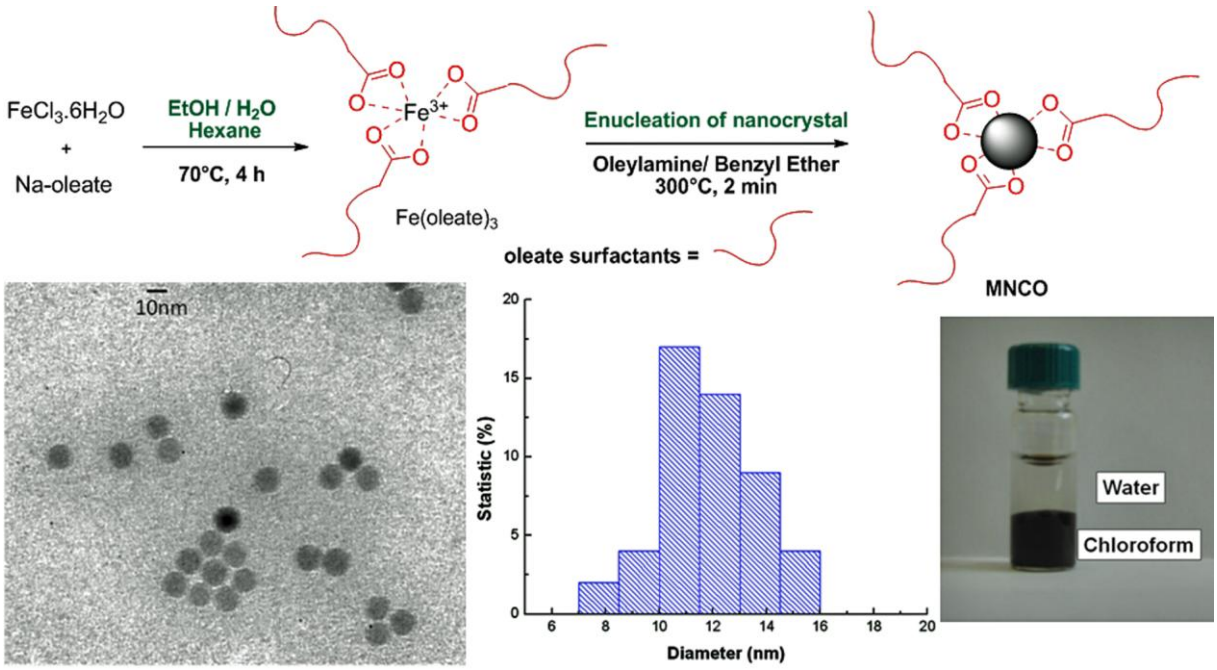

Figure 6.4: Iron oxide nanoparticles synthesis .
(Upper level) Schematic synthesis of MNC0, first, generation of the irox oleate complex and then nucleation of nanocrystals in high boiling solvents.
(Lower kevel) TEM image of as synthesized MNPs and histrogram geometrical distributions; finally the picture shows that NPs capped with oleate complex are soluble in nonpolar organic solvents.

The choice of an organic phase approach for the synthesis of the magnetite core nanostructure, has provided highly uniform and crystalline MNPs endowed with strong intrinsic relaxivity and narrow size distribution. This approach, while effective, has a main limitation, which is the lack of solubility of the resulting surfactant coated nanoparticles in aqueous solution. Hence, to be useful for biological application and biofunctionalization, **MNC0** have been transferred into water by mixing them with an amphiphilic polymer, obtained by condensation of poly(isobutylene-*alt*-maleic anhydride) and dodecylamine, named **PMA**; the concept of this polymer has been

successfully demonstrated in several work of Parak's group [19,20] (Figure 6.5): maleic anhydrides of the polymer are functionalized at 75% with dodecylamine, whereas 25% are left unreacted for following NPs functionalization. The long chains of dodecyamine can intercalate the first hydrophobic surfactant layer with their hydrophobic portion while water solubility of the nanocrystals is allowed by their hydrophilic groups. The nanocomplex results in the highly stable and dispersible (also fluorescent in the case of PMA-FITC used for cellular experiments) **MNP1**.

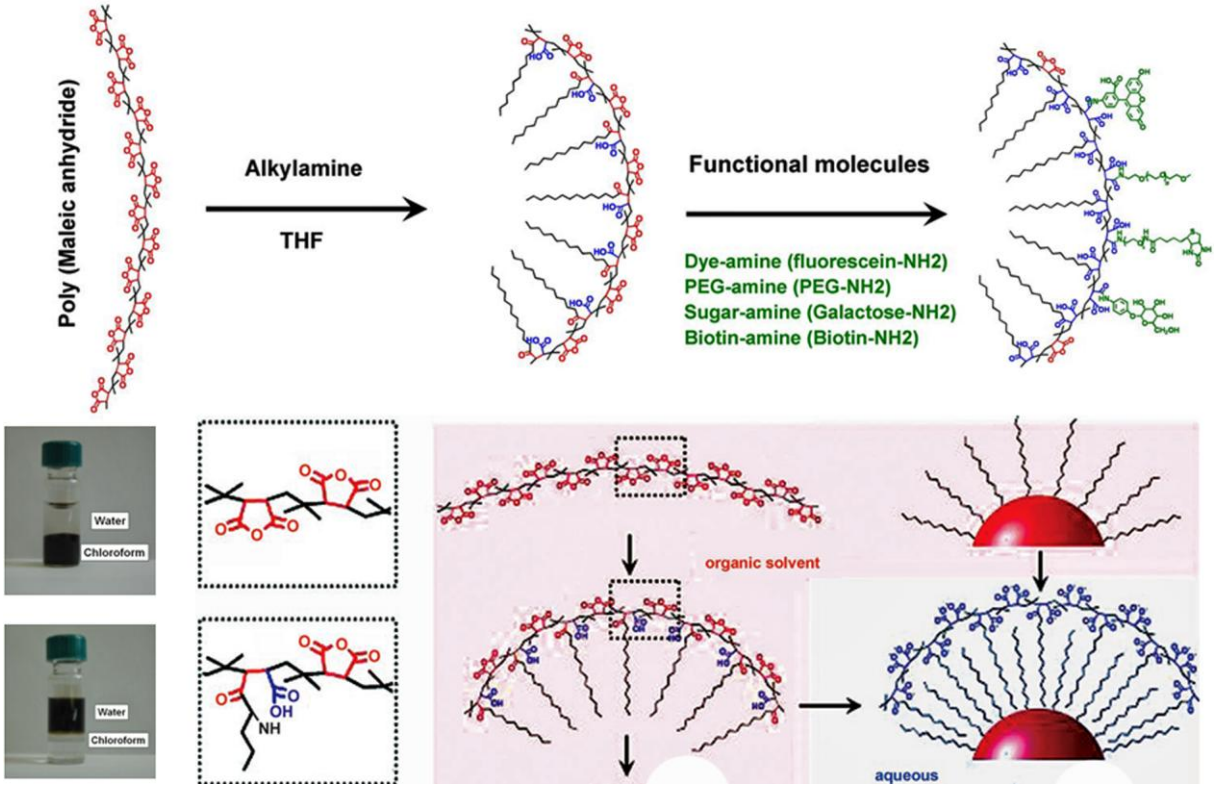

Figure 6.5: The concept of the phase transfer .
(Upper level) Schematic view of the PMA polymer functionalization.
(Lower level) The polymer is associated in organic phase within hydrophobic-coated NPs; the long alkyl chains intercalate together with the oleate chains forming a compact organic layer; instead; meanwhile the external hydrophilic groups is deprotonated in alkaline aqueous buffers thus maintaining NPs solubility [20].

Briefly, the polymer solution and MNPs suspension in chloroform (100 polymer units per nm^2 of NPs surface) are sonicated together and later the organic solvent is completely evaporated; the black solid is then resuspended in a diluted 20 mM sodium borate buffer, SBB (pH 12). After 5 min of sonication, the water soluble **MNP1** dissolves completely and the clear suspension is filtered onto an Amicon filter

concentrator tube to remove the excess unbound polymer. Within this excellent technique, NPs suspension maintains all features of as synthesize MNPs; for example, hydrodynamic diameter, ζ-potential and magnetic T_2 relaxivity have been compared to values recorded for clinical MRI commercial ferrofluids.(see Table 1 inside the chapter 1) (Figure 6.6).

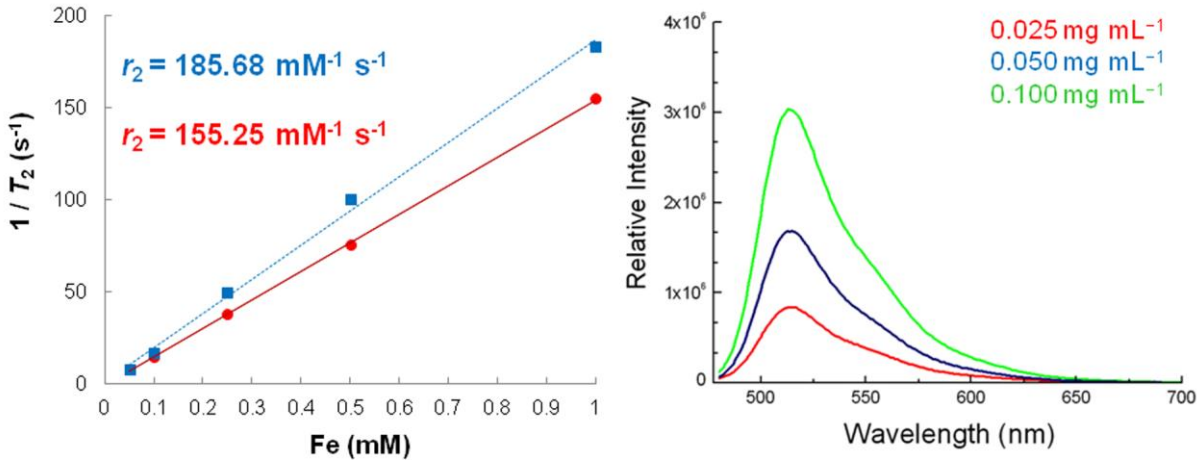

Figure 6.6: MNP0 and MNP1 magnetic and fluorescence properties .
(Left) Relaxivity (r_2) profiles of MNP0 (blue line) in hexane and MNP1 (red line) in water after PMA coating; values have been recorder increasing iron concentration in the solvent and the r_2 calculated as the slope of the curve. (Right) Fluorescence intensity of PMA-FITC coated MNP1, at three different concentrations: 20, 50 and 100 mg L^{-1} (after excitation at 488 nm)

As measured by DLS, MNP0 had a size of 21.7 ± 2 nm in hexane (PDI 0.0115) while MNP1 have been 25.1 ± 3 nm in size in 20 mM PBS, pH 7.4 at 5 mg L^{-1}, with a ζ-potential of −38 ± 6 mV (in NaCl 1 mM, pH 7.25), and exhibited a maximal dose dependent fluorescence emission at 515 nm (in the case of PMA-FITC coating) after excitation of FITC at 488 nm. The relaxivity r_2 calculated by T_2 measurements in deionized water at increasing amount of MNPs, has been calculated as the slope of curves and it has been of 185.68 mM^{-1} s^{-1} for MNP0 and 155.25 mM^{-1} s^{-1} for MNP1 respectively, showing theoretically good contrast power if compared to commercially available T_2 MRI contrast agent. Amino groups have been later introduced on MNP1 by using a homobifunctional linker (2,2-(ethylenedioxy)bisethylamine; EDBE) to give **MNP2**; the number of amino groups has

been optimized in order to gain a sufficient number of NH_2 without altering the colloidal stability of MNP2: for instance, by ninhydrin assay 20 NH_2 for nanoparticle have been calculated, which turns in a ζ-potential of −15.7 ± 3.4 mV and a size of 35.3 ± 3.4 nm (PDI, 0.174) by DLS in NaCl 1 mM, pH 7.25.

The **HALO ligand L1** has been synthesized according to the procedure reported in a previous paper [4] in three steps: at first the alkoxylated salt generated from 2,2-aminoethoxy ethanol has been reacted in a Wittig reaction accomplished by 1-chloro-6-iodohexane obtaining the compound **1** (see experimental section for details). In a second step *p*-nitrophenyl chloroformate has been coupled to triethylenglycol with the aim to achieve the di-substituted *p*-nitrophenyl carbonate product, named compound **2**. The former amino-chloroalkane **1** and the latter NPs spacer **2** have been matched together by formation of amide coupling. In this way, the generated organic HALO linker (**L1**) has been linked to the primary amino groups on the polymer through nucleophilic addition to the second *p*-nitrophenyl carbonate group by incubation overnight at 4 °C.

The **MNP3** nanocomplex has been characterized by DLS and exhibited a mean hydrodynamic size of 40.1 ± 2.7 nm in PBS pH 7.4 and a zeta potential of −28.5 ± 3.0 mV (in 1 mM NaCl, pH 7.2). It should be mentioned that MNP3 are very stable in PBS buffer and formed a dark transparent solution; compound MNP3 has been stored at 4 °C until further bioconjugation with the HALO and HALO/U11 proteins.

6.3 Bioconjugation of U11 peptide, HALO and HALO/U11 proteins

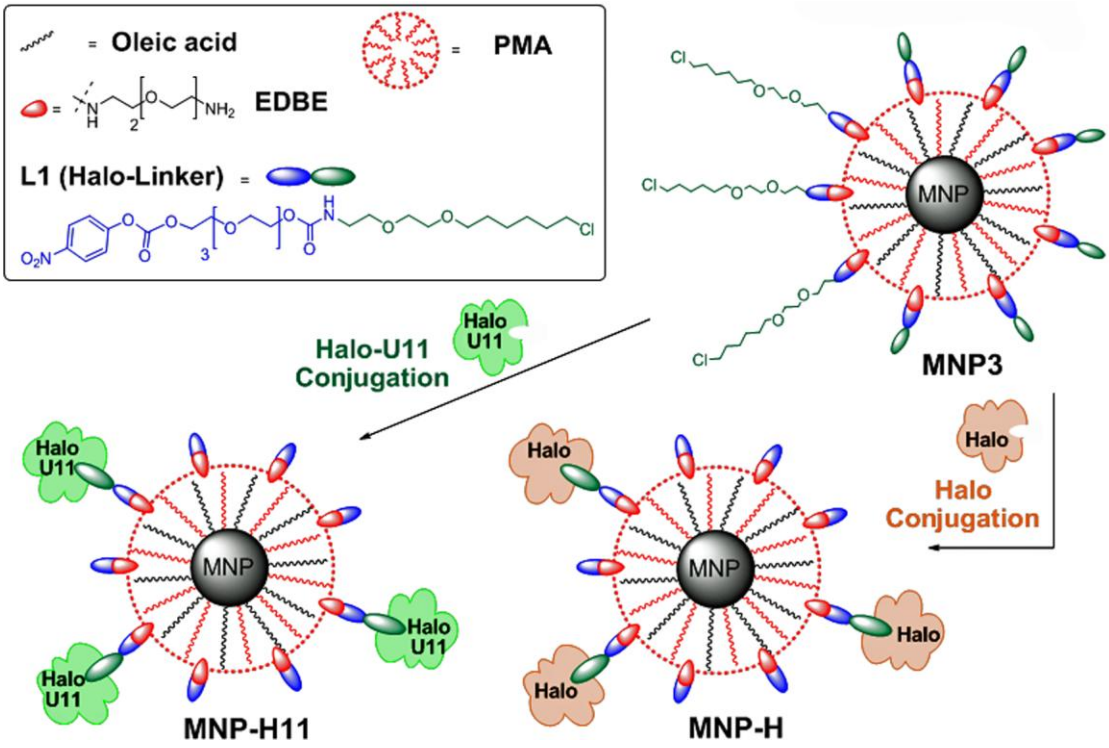

Figure 6.7: HALO functionalizations onto MNP3.
HALO and HALO/U11 have been reacted with MNP3 gaining MNP-H and MNP-H11 respectively.

HALO-functionalized MNP (**MNP-H**) have been preliminary optimized by treating purified fluoresceine isothiocyanate (FITC) labeled HALO with MNP3 in a 1:1 (w/w) ratio at physiological conditions (Figure 6.7). The unconjugated protein has been removed by centrifugation using amicon concentrator tubes and concentrated nanoparticles have been further reacted with an inhert α-methoxy-γ-amino-PEG (2 kDa, MeO-PEG_{2000}-NH_2), after activation of the carboxylate groups of the polymer by EDC, to minimize possible nonspecific protein adsorptions. MNP-H have been then washed three times with PBS and stored for biological experiments at 4 °C. The amount of unreacted dye-labeled HALO has been calculated fluorometrically after first establishing a standard calibration curve, which provided the number of HALO molecules attached to each nanoparticle. The presence of an average of about 5

HALO molecules per MNP-H has been determined. Subsequently, HALO–U11 FITC-labeled has been coupled with MNP3 to confirm the number of reacting proteins for nanoparticles and it has been demonstrated that again 5 HALO/U11 molecules reacted with MNPs. Finally by using the conjugation protocol illustrated before, HALO/U11 has been conjugated to fluorescent labeled MNP3 (using PMA-FITC coating polymer) to give **MNP-H11** (size = 67.6 ± 3.1 nm, ζ-potential = −27.8 ± 2.6 mV). In this case, I preferred to covalently incorporate the dye inside the polymer layer to avoid any contact with the external environment, which could affect the nanoparticle affinity for cellular receptors.

To assess the influence of the controlled orientation of ligand presented HALO–U11, and to verify also that the presence of the protein could increase the affinity of the peptide for the receptor, fluorescent labeled MNP2 have been also directly conjugated with U11 peptide (4–6 molecules per MNP) by introducing a Cys residue at the C-terminal to gain the product (**MNP-U11**).

All conjugates have been stored at 4 °C for further biological experiments in uPAR(+) and uPAR(−) breast cancer cells.

6.4 Binding specificity to uPAR in cell cultures

U937 cell lines have been selected as the cellular model to assess the targeting efficiency of our nanoconstruct since these cancer cells are available both as uPAR(+) (U937_13) and as uPAR(−) (U937_10). The difference between them is the membrane expression of the specific receptor for U11 targeting. U937_13 cell lines have been preliminary treated in parallel with dye-labeled MNP2 and HALO-FITC to evaluate nonspecific interactions of the pegylated nanoparticles and the capture protein alone with uPAR; this test has evidenced that in both cases, no of cell labeling has been detected by FACS.

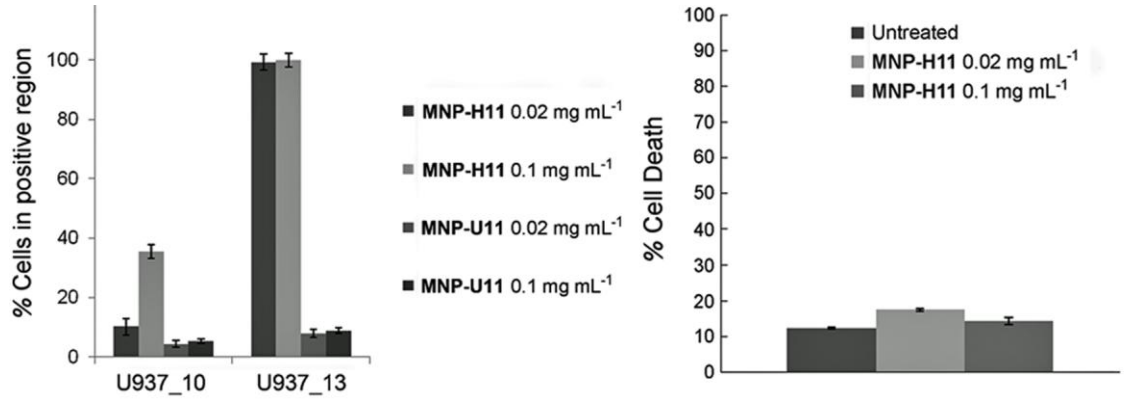

Figure 6.8: MNP-H11 and MNP-U11 Binding of uPAR and cell death evaluation.
(Left) Positive U937_13 and negative U937_10 cells have been incubated at 37 °C with MNP-H11 and MNP-U11 at two different concentrations (20 mg L^{-1} and 100 mg L^{-1}) for 1 h and then processed for flow cytometry. (Right) Annexin-V analysis with MNP-H11 (20 mg L^{-1} and 100 mg L^{-1}) in U937_13 cells, which evidenced no signs of cell damage.

Later on, MNP-H11 and MNP-U11 have been each incubated for 1 h at 37 °C with both cell lines at two different concentrations (20 mg mL^{-1} and 100 mg mL^{-1}) (Figure 6.8). FACS profiles on the U937_13 cells evidenced that the treatment with MNP-H11 showed a 20-fold increase in the percentage of cell's labeling compared to MNP-U11-treated cells. Quite surprisingly, the peptide alone has not been able to be specific to bind uPAR, probably owing to a low availability of the short peptides for recognition if the number of peptide ligands is low (in this case 5−6 molecules per NP

have been calculated). However, after MNP-H11 treatment the negative U937_10 cells remained mostly unlabeled, even at the highest exposure concentration.

Moreover, Annexin-V cell-death experiment has been performed on U937_13 cells after 24 h incubation with MNP-H11 at 20 mg L^{-1} and 100 mg L^{-1}, suggesting that our nano-protein complex is nontoxic within this range of concentrations; this finding is significant for *in vitro* and *in vivo* applications.

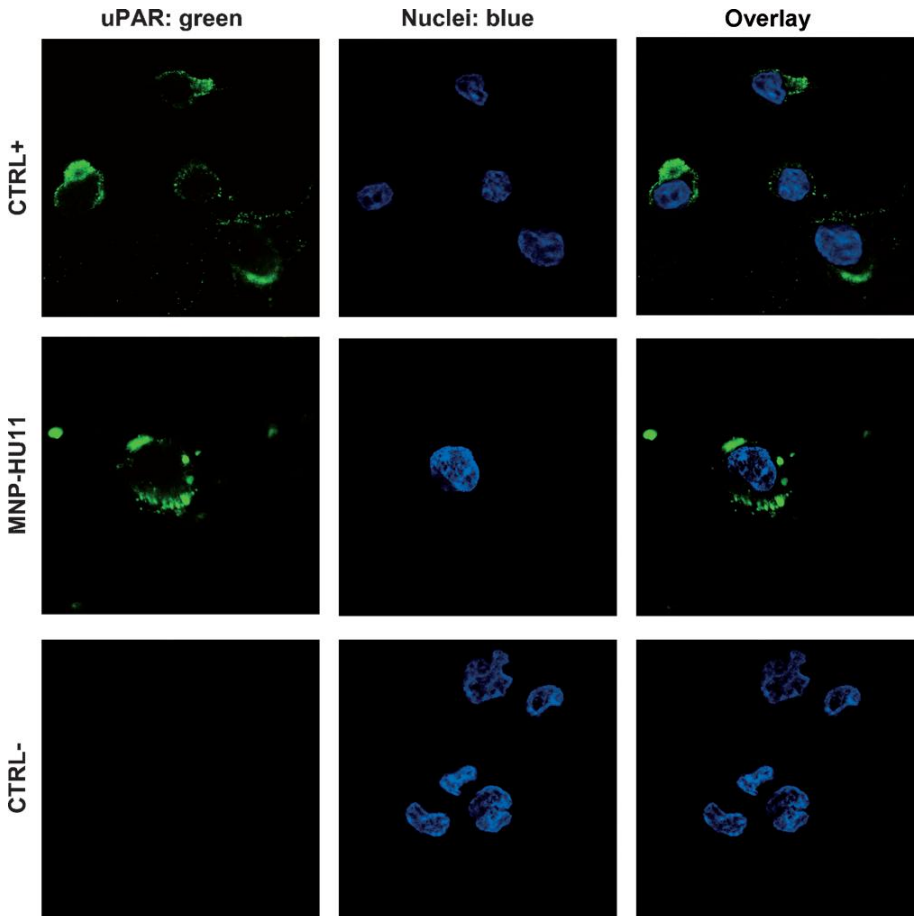

Figure 6.9: CLSM of U937_13 and U937_10 cells .
Cells have been incubated with MNP-H11 (100 mg mL^{-1}, green) 1 h at 37 °C. As a positive uPAR-expression control (CTRL+), U937_13 have been immunodecorated with anti-uPAR primary antibody, revealed with an anti-mouse secondary antibody labeled with Alexa-488 dye. Nuclei have been stained with DAPI. Scale bar: 10 mm.

Finally, the specificity of uPAR binding has been visually confirmed by CLSM (Figure 6.9). MNP-H11 have been localized on the cell membrane and also inside the cytoplasm of uPAR+ cells only, showing a uPAR recognition pattern similar to the positive control, where cells have been immunodecorated with anti-uPAR antibody.

6.5 Concluding remarks

In summary, we have demonstrated that oriented-controlled ligation of a HALO protein homing U11 peptide allows for a rapid and ultra effective recognition of breast cancer cell receptor within a uPAR *in vitro* model. The concept to create different multifunctional nanoparticles, combining, for example, optical and magnetic properties, leads to improved effectiveness of these diagnostic tools for selectively malignant receptor targeting in living cells. Moreover, at the same time, the finely construction of long−term highly water-stable, bioengineered, targeted nanoparticles exhibited a complete conservation of protein functionality.

As the structural motif of short peptides involved in tumoral biomarker targeting is highly conserved, other kinds of nanoparticles might be modified identically with the same polymer used herein [19,20], therefore, this approach is expected to be of general utility and may become a universal strategy for the development of a new generation of targeted nanoparticles.

6.6 Nanomaterials Experimental section

6.6.1 Procedure for the synthesis of the Halo linker (L1)

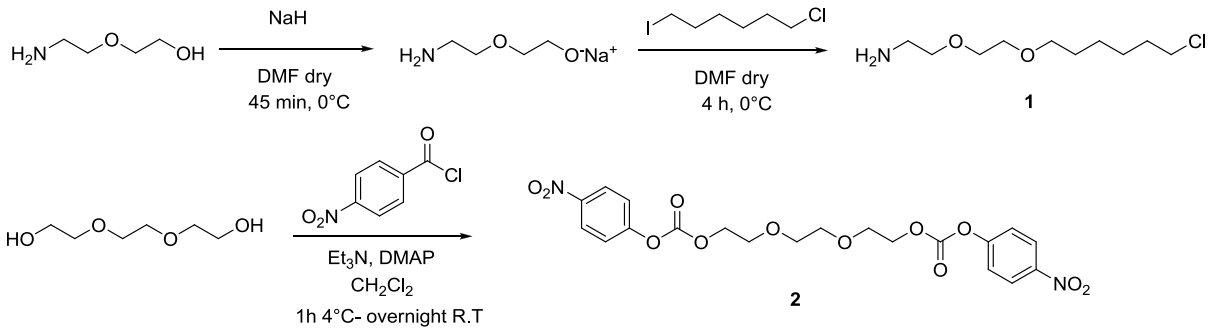

(Inhert atmosphere, Dry solvents)

6.6.1.1 Synthesis of 2,2-[2-(6-chloro-hexyloxy)-ethoxy]-ethylammonium hydrochloride (**1**)

In a centrifuge tube, a dispersion of NaH 60 wt.% in mineral oil (240 mg, 6 mmol) has been suspended and vortexed in freshly distilled dry hexane (3 mL). After centrifugation, the solvent has been removed and the white residue washed in the same way thrice and finally dried under vacuum. The dry NaH has been then suspended in dry dimethylformamide (DMF, 4 mL) and the suspension has been transferred with a metallic double-needle tube into a round bottom flask. Later on, the suspension has been cooled to 0 °C 2,2-aminoethoxy ethanol (520 µL, 5 mmol) has been added dropwise. The reaction mixture has been stirred 45 min to create the sodium alkoxylated intermediate . Furthermore, 1-chloro-6-iodohexane (835 µL, 5.5 mmol) dissolved in dry DMF (4 mL) and cooled at 0 °C, has been transferred dropwise by use of a wide bore cannula into the reaction and left under stirring at 0 °C for 4 h. Later on, the suspension has been filtered through celite and the solvent quickly removed under vacuum. The yellow residue has been dissolved in CH_2Cl_2 (10 mL) and washed with aqueous saturated $NaHCO_3$, followed by two washes with water. The organic layer has been dried with Na_2SO_4, filtered, and the solvent distilled under vacuum. The crude product has been cooled down to –78 °C and dried under high vacuum for 2 h. Subsequently, the yellow oil obtained has been dissolved in CH_2Cl_2 (2 ml) at 0 °C and 2 M HCl gas in Et_2O (4.5 mL) has been added to the mixture and stirred for 1 h. After solvent removal, the orange residue has been purified by silica flash column chromatography. The compound **1**, a sticky yellow oil, was collected. Yield: 45% overall.

^{1}H NMR ($CDCl_3$): δ= 8.04 (bs, 3H exchangeable, NH_3^+), 3.55−3.42 (m, 8H,-CH_2-O), 3.33 (t, 2H, CH_2-Cl), 2.29 (t, 2H, -CH_2-N), 1.78 (q, 2H, -CH_2-), 1.42 (q, 2H, -CH_2-), 1.28 (q, 4H, -CH_2-) ppm.

(Inhert atmosphere, Dry solvents)

6.6.1.2 Synthesis of 2,2'-(ethane-1,2-diylbis(oxy))bis(ethane-2,1-diyl)bis(4-nitrophenyl)-carbonate (**2**)

In a round bottom flask, 4-nitrophenyl chloroformate (4.4 g, 22 mmol) has been dissolved in dry CH_2Cl_2 (40 mL) and cooled at 0 °C with an ice bath. Triethylene glycol (1.33 mL, 10 mmol) dissolved as well in CH_2Cl_2 (20 mL) has been added dropwise by a funnel. Triethylamine (3.4 mL) and a catalytic amount of dimethylaminopyridine (63 mg, 0.52 mmol) have been added subsequently. The reaction has been stirred at 0 °C for 1 h and then allowed to warm to RT overnight. The mixture has been diluted with CH_2Cl_2 (50 mL) and washed twice with H_2O (50 mL). The organic layer has been dried and the solvent concentrated to the minimum volume by evaporation under reduced pressure. The yellow oil has been purified using flash chromatography using a gradient from 25 vol.% to 100 vol.% ethyl acetate in hexane. The product **2** has been collected as colorless oil. Yield: 55%.

^{1}H NMR ($CDCl_3$): δ = 8.20 (d, 4H, Ar), 7.40 (d, 4H, Ar), 4.43−4.32 (t, 4H), 3.82−3.56 (t, 4H), 3.34 (s, 4H) ppm.

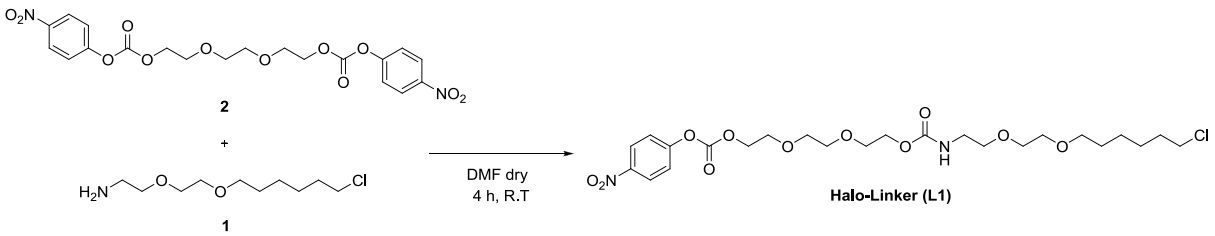

(Inhert atmosphere, Dry solvents)

6.6.1.3 Synthesis of 2-(2-(2-((4-nitrophenoxy)carbonyloxy)ethoxy)ethoxy)ethyl 2-(2-(6-chlorohexyloxy) ethoxy) ethylcarbamate (**L1**)

In a round bottom flask, the compound **2** (540 mg, 2.4 mmol) has been dissolved in dry DMF (10 mL) and the resultant solution has been carefully added to a solution of **3** (1.56 g, 3.25 mmol) in dry DMF (25 mL) under gentle stirring at room temperature. The mixture turned yellowish quickly due to the nucleophilic substitution and to the following release of *p*-nitrophenol. In this way, the reaction has been allowed to proceed to completion at room temperature for 4 h. After removal of DMF by evaporation under reduce pressure, the crude product has been purified by flash chromatography using a gradient from 40 vol.% to 100 vol.% ethyl acetate in hexane. Pale yellowish oil has been collected. Yield: 350 mg, 26%.

^{1}H-NMR ($CDCl_3$), δ= 8.24−8.22 (*d*, 2H, Ar), 7.36−7.34 (*d*, 2H, Ar), 5.29 (*bs* exchangeable, 1H, N*H*), 4.41−4.39 (*t*, 2H, C*H*$_2$-O-C(O)), 4.20−4.17 (*t*, 2H, *CH*$_2$-C(O)-O), 3.66 (*m*, 2H, *CH*$_2$-O), 3.56−3.47 (*m*, 14H, *CH*$_2$-O), 3.43−3.40 (*t*, 2H, *CH*$_2$-Cl), 3.33−3.31 (*d-d*, 2H, *CH*$_2$-N), 1.76−1.69 (*q*, 2H, -*CH*$_2$-), 1.59−1.52 (*q*, 2H, -*CH*$_2$-), 1.43−1.32 (*m*, 4H, -*CH*$_2$-) ppm.

6.6.2 Synthesis of 10 nm iron oxide nanoparticles (MNPs)

(Inhert atmosphere, Dry solvents)

The metal–oleate complex has been prepared by reacting metal chlorides and sodium oleate. In a typical synthesis, of iron chloride $FeCl_3 \cdot 6H_2O$ (1.8 g, 4 mmol) and of sodium oleate (3.65 g, 12 mmol) has been dissolved in a mixture solvent composed of ethanol (8 mL), distilled water (6 mL) and hexane (14 ml). The resulting solution has been heated to 70 °C and kept at that temperature 4 hours. At the end of the reaction, the upper organic layer containing the iron–oleate complex has been washed thrice with deionized water (5 mL) in a separatory funnel. After washing, hexane has been evaporated off, resulting in iron–oleate complex in a waxy dark red solid form (2.6 g).

The Synthesis of surfactant-coated (oleate surfactants) Fe_3O_4 nanoparticles has been performed by solvothermal decomposition of iron-organometallic precursors in high boiling apolar organic solvents as reported in literature [18]. Briefly, $Fe(oleate)_3$ (3.6 g, 4 mmol) has been dissolved in a mixture of oleylamine (2 mL) and dibenzyl ether (2 mL). The mixture has been heated at 110 °C for 1 h under argon, then refluxed at 300 °C for 2 h, and finallly cooled to room temperature. Ethanol (100 mL) has been added to precipitate the black MNPs by centrifugation. The supernatant has been discarded and the product has been washed several times with ethanol to remove the unbound surfactant. The resulting 10 nm oleylamine-coated magnetite nanocrystals (MNP0) have been finally dispersed in chloroform at a concentration of 10 mg mL^{-1} and stored at RT until further functionalization. MNP0 concentration has been gained by UV-vis calibration curve (in chloroform) diluting the mother solution and reading sample's relative absorbance at λ=450 nm

6.6.3 MNPs Phase transfer in water: polymer coating

(Inhert atmosphere, Dry solvents)

6.6.3.1 Synthesis of fluorescent dye-grafted co-polymer: (24% Anhydride-75% C_{12}COOH-1% Dye]

The maleic anhydride groups of the poly(isobutylene-*alt*-maleic anhydride), named **PMA** backbone have been assumed to be 100% reactive to primary amino-ligands through spontaneous amide linkage, which converts one maleic anhydride group into one corresponding amide and one free carboxylic acid group. For this synthesis, as reported in literature [19] is defined as a polymer of which 75% of its maleic anhydride rings have been reacted with dodecylamine and of which 1% of its maleic anhydride rings have been reacted with fluorescein-amine, leaving 24% of the anhydrides unreacted and available for further MNPs functionalizations.

Briefly, of fluorescein-amine (2.78 mg, 8 µmol) have been dissolved in anhydrous THF (1 mL) to obtain a 8 mM fluorescein-amine stock solution. This solution has been further diluted 10 times with anhydrous THF before modification. of 0.8 M monomer units of 25% Anhydride-75% C_{12}COOH (50 µL) have been mixed vigorously with of 0.8 mM fluorescein-amine (500 µL); the mixture have been reacted overnight under stirring at room temperature. The solvent have been then evaporated under reduce pressure and the crude yellow powder has been dissolved in of anhydrous chloroform (1 mL), to yield a final monomer concentration of 40 mM fluorescein-polymer (**FITC-PMA**).

6.6.3.2 Polymer coating: MNPs phase transfer into aqueous environment

Synthesis of PMA-FITC-coated fluorescent iron oxide nanoparticles has been performed following a procedure described in literature [19,20]. An aliquot of PMA-FITC solution (63 µL) was added to MNP0 (4.6 mg in $CHCl_3$); the mixture has been homogenized with an ultrasound bath and later the solvent has been completely evaporated under reduced pressure. Sodium borate buffer (SBB, pH 12, 10 mL) has been added obtaining a black aqueous nanoparticle dispersion (**MNP1**), which have been concentrated in Amicon tubes (filter cutoff 100 kDa) by centrifugation at 3500 rpm for 1 h. MNP1 have been washed several times diluting with SBB in the same way and concentrated (each centrifuge cycle was 20 min at 3500 rpm) to a final volume of 500 µL.

[The protocol used to obtain MNP1 without a fluorescent polymer coating has been performed in the same way apart the polymer PMA of which composition has been maintained 25% Anhydride-75% C_{12}COOH**]**.

6.6.4 PMA-coated iron oxide nanoparticles functionalized with Halo Ligand (MNP3)

MNP1 (4.6 mg) in deionized water (500 µL), have been reacted with 0.1 M EDC in water (18 µL) for 2 min and then aqueous 0.05 M 2,2-(ethylenedioxy)bis(ethylamine) (EDBE) (9 µL) has been added to the mixture and stirred for 2 h. Next, the **MNP2** dispersion have been concentrated in Amicon tubes (100 kDa filter cutoff) by centrifugation at 3500 rpm for 1 h. MNP2 have been washed twice with water (10 mL) in the same way to remove the excess of reagent and NPs have been finally concentrated at the final volume of 1 mL.

MNP2 (amino terminated) dispersion has been shaken overnight at 4 °C in the presence of L1 (460 µL, 10 mg mL^{-1} stock solution in DMSO), concentrated and washed twice with water as described above (**MNP3**).

6.6.5 Synthesis of iron oxide nanoparticles directly functionalized with U11 (MNP-U11)

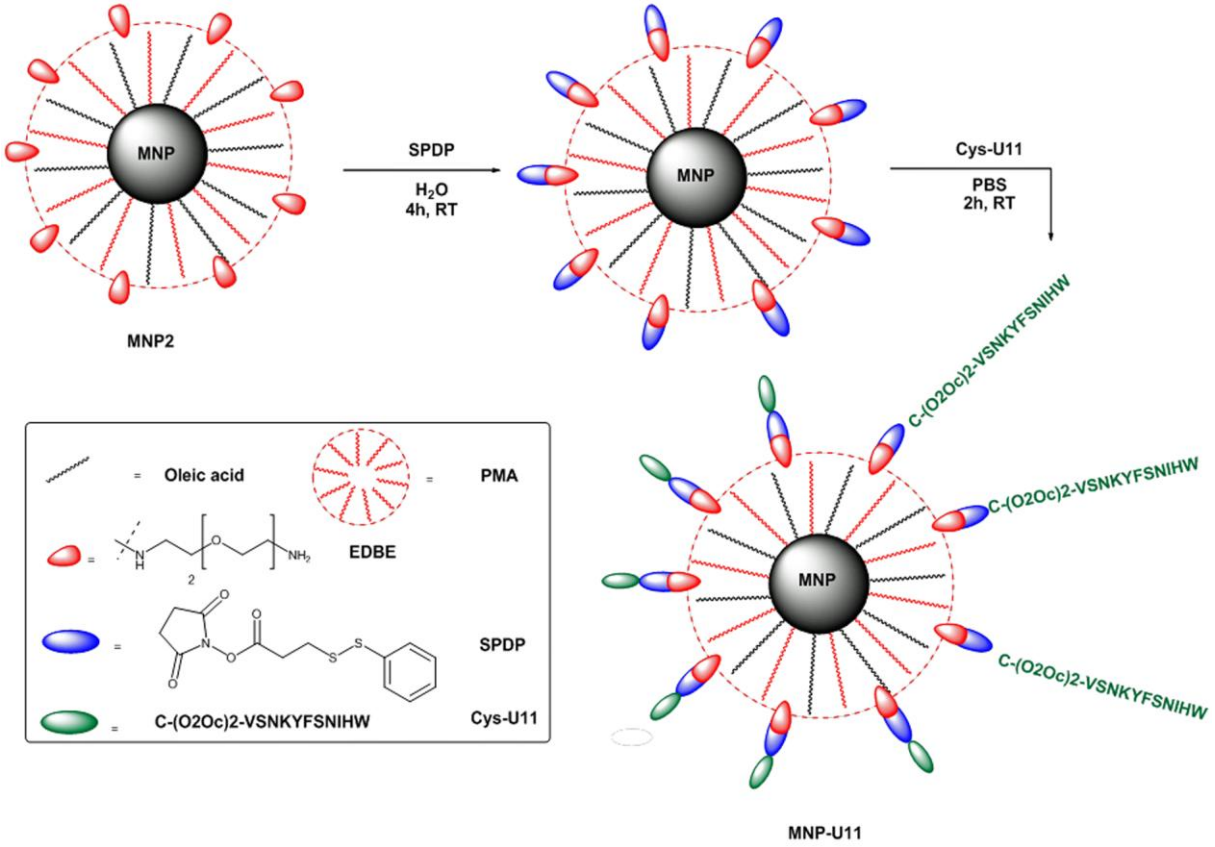

Synthetic conditions have been optimized in order to obtain an average conjugation of about 5 peptides (U11) per MNP, a number of ligands comparable to that of protein Halo-U11 conjugated (MNP-H11). An aliquot of MNP2 in water (2.3 mg mL^{-1}) have been shaken 4 h in the presence of *N*-succinimidyl-3-[2-pyridyldithio]-propionate (SPDP) (345 µL, 10 mg mL^{-1} stock solution in DMSO). At the end of the reaction, NPs have been concentrated and washed twice with water to remove excess of SPDP. Next, a solution of thiol terminated U11 C-(O2Oc)2-VSNKYFSNIHW, named **HS-U11** (120 µL, 1 mg mL^{-1} in PBS) has been added and reacted for 2 h at room temperature. The colloidal dispersion has been concentrated in Amicon tubes (100 kDa filter cutoff) by centrifuging at 3500 rpm for 1 h. **MNP-U11** have been washed twice with deionized water (5 mL) and concentrated at the final volume of 1 mL and stored at 4°C for further experiments.

6.6.6 Synthesis of iron oxide nanoparticles functionalized with HALO (MNP-H)and HALO/U11 (MNP-H11) proteins

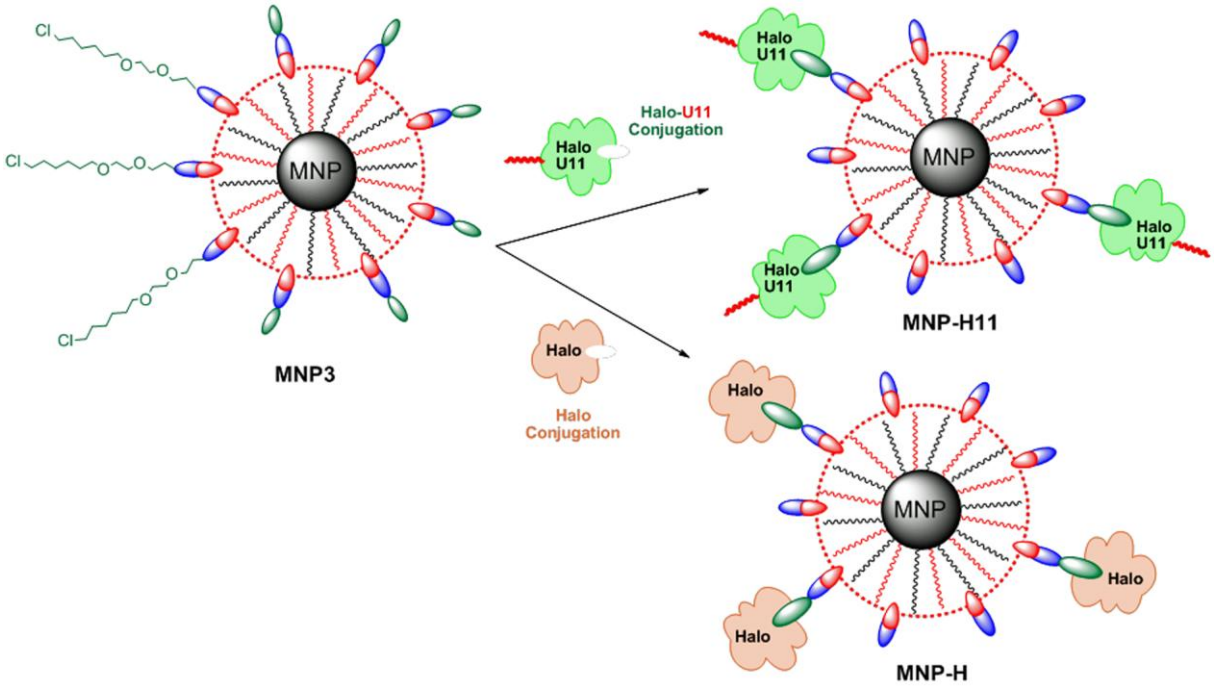

MNP3 (2 mg mL^{-1}, 1 mL) in 20 mM PBS have been incubated 1 h at RT under shaking with 2 mg of HALO-FITC labeled . Then, unconjugated HALO-FITC was removed by centrifugation of the sample with Amicon YM-100. Resultant **MNP-H** were washed three times in Amicon YM-100 with PBS buffer. The amount of dye labeled protein immobilized onto NPs has been determined by measuring fluorescence emission of the sample exciting at 488 nm, using the standard curve previously prerpared. In this context, it is possible to estimate 5 molecules of protein have been conjugated per particle.

With the same protocol and the same stoichiometric amount, the protein HALO/U11 have been attached to PMA-FITC coated MNP3 gaining **MNP-H11**, which have been used for biological experiments of uPAR recognition.

Related References

[1] Reuning, U.; Sperl, S.; Kopitz, C.; et al.; *Curr. Pharm. Des.* **2003**, *9*, 1529–1543.

[2] Wang, M.; Lowik, D. W.; Miller, A. D. and Thanou, M.; *Bioconjugate Chem.* **2009**, *20*, 32–40.

[3] Janssen, D. B.; *Curr Opin. Chem. Biol.* **2004**, *8*, 150–159.

[4] Los, G. V.; Encell, L. P.; McDougall, D. D.; et al.; *ACS Chem. Biol.* **2008**, *3*, 373–382.

[5] Pries, F.; Kingma, G. H.; Jeronimus-Stratingh, C. M.; Bruins, A. P. and Janssen, D. B.; *J Biol. Chem.* **1995**, *270*, 10405–10411.

[6] Algar, W. R.; Prasuhn, D. E.; Steward, M. H.; Jennings, T. L.; Blanco-Canosa, J. B.; Dawson, P. E. and Medinz, I. L.; *Bioconjugate Chem.* **2011**, *22*, 825–858.

[7] Park, K.; Lee, S.; Kang, E.; Kim, K.; Choi, K. and Kwon, I. C.; *Adv. Funct. Mater.* **2009**, *19*, 1553–1566.

[8] Kim, J.; Park, S.; Kang, K.; et al.; *Angew Chem.Int. Ed.* **2006**, *45*, 7754–7758.

[9] Yang, J.; Kim, E. K.; Lee, H. J.; et al.; *Biomaterials* **2008**, *29*, 2548–2555.

[10] Chen, S.; Reynolds, S.; Yu, L.; Weissleder, R. and Josephson, L.; *J. Mater. Chem.* **2009**, *19*, 6387–6392.

[11] Lewin, M.; Carlesso, N.; Tung, C. H.; Tang, X. W.; Scadden, D. T. and Weissleder, R.; *Nat. Biotechnol.* **2000**, *18*, 410–414.

[12] Thanh, N. T. K. and Green, L. A. W.; *Nano Today*. **2010**, *5*, 213–230.

[13] Casals, E.;Pfaller, T.; Duschl, A.; Oostingh, G. J. and Puntes, V. F.; *Small.* **2011**, *7*, 3479–3486.

[14] Colombo, M.; Mazzucchelli, S.; Montenegro, J. M.; Galbiati, E.; Corsi, F.; Parak, W. J. and Prosperi, D.; *Small*, **2012**, *8*. 1492–1497.

[15] Rivera-Gil, P.; Jimenez de Aberasturi, D.; Wulf, V.; et al.; *Acc. Chem. Res.* **2013**, *46*, 743–749.

[16] Avvakumova, S.; Colombo, M.; Tortora, P. and Prosperi, D.; *Trands. Biotechnol.* **2013**, DOI: 10.1016/j.tibtech.2013.09.006.

[17] Herd, H.; Daum, N.; Jones, A. T.; Huwer, H.; Ghandehari, H. and Lehr, C. M.; *ACS Nano.* **2013**, *7*, 1961–1973.

[18] Park, J.; An, K.; Hwang, Y.; et al.; *Nat. Mater* **2004**, *3*, 891–896.

[19] Lin, C. J.; Sperling, R. A.; Li, J. K.; et al.; *Small.* **2008**, *4*, 334–341.

[20] Pellegrino, T.; Manna, L.; Kudera, S.; et al.; *Nanolett.* **2004**, *4*, 703–707.

Chapter VII

Intracellular Drug Release From Curcumin-Loaded PLGA Nanoparticles Induces G2/M Block in Breast Cancer Cells

Contents

7.1 Curcumin: a drug model for Breast Cancer Therapy

Breast cancer is a heterogeneous disease that shows remarkably different biological characteristics and clinical behaviors [1]. Classification of these subtypes of breast cancer is generally based upon the presence or absence of three receptors: estrogen (ER) and progesterone (PR) receptors and HER2 [2]. More than 80% of breast cancers are positive for at least one of these three receptors [3] In Chapter IV, I have pointed out that the HER2/neu gene is generally over-expressed in 25−30% of breast cancer [4] and its amplification of the HER2/neu leads to activation of the cellular signaling pathways correlated to cell growth, invasion and metastasis leading to an aggressive breast cancer phenotype (see Chapter IV). Nowadays, the standard treatment options for early stage breast cancer therapy include surgery, radiation, and/or treatments with several anticancer drugs. Breast cancer has high metastatic disposition; for example, axillary or supraclavicular lymph nodes are often the most common sites for breast cancer metastasis [5,6] [Figure 7.1].

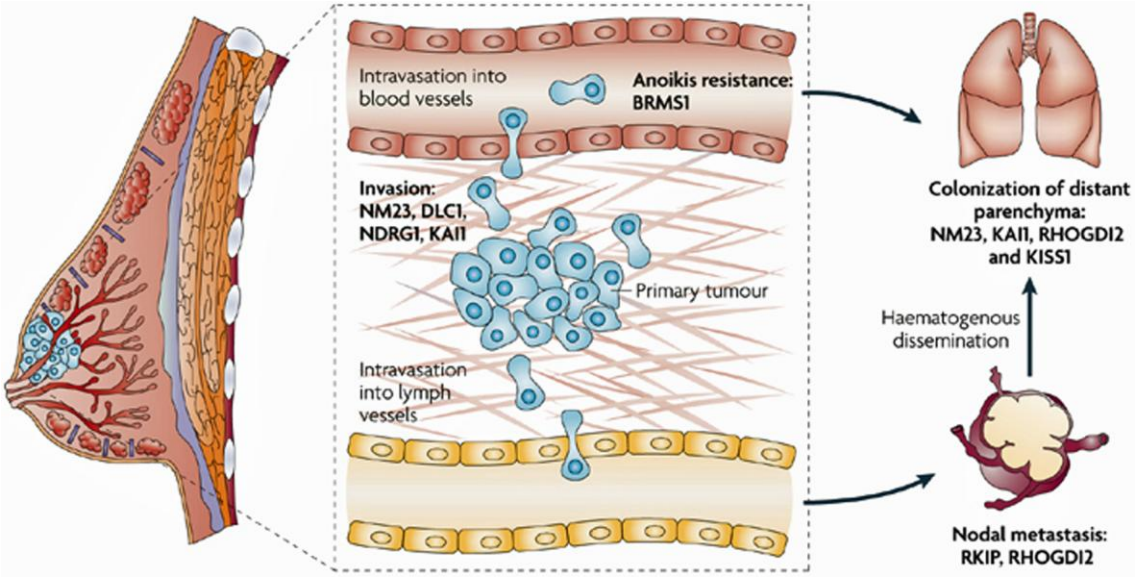

Figure 7.1: The biological process of metastasis in primary tumors.
The biological process of metastasis is a complex cascade with multiple steps in which suppressor activity may prevent clinically apparent metastasis. Given the prevalence and mortality of human breast cancer, it is focused here on this tissue type, although these principles apply to most solid malignancies. In the primary tumour, deregulation of oncogenes and tumour suppressor genes mediates the conversion of normal cells to a neoplastic phenotype. By definition, metastasis suppressor genes do not prevent these steps, but must function subsequently in the cascade as shown [6].

Distant sites of metastasis from breast cancer include the brain, bones, lungs, and the liver. Hormone receptor−positive breast cancers are usually treated with inhibitors of estrogen synthesis or modulators of estrogen receptor [7], however hormone receptor negative breast cancers are treated with cytotoxic chemotherapy [8]. Despite relatively large numbers of active agents available for the treatment of breast cancer, systemic therapy for metastatic disease still remains a serious concern. This raises the importance of identifying novel agents that can modulate resistance of breast cancer to cytotoxic agents.

Turmeric (*Curcuma longa L.*), the principal ingredient of curry powder, belongs to a member of the ginger family (*Zingiberaceae*). These plants are native to India and Indonesia and have been used for centuries as part of Indian Ayurvedic [9] and Chinese medicine [10]. Curcumin is the active ingredient of turmeric and is believed to be responsible for its therapeutic activity; indeed, this compound has been shown

to possess a wide range of pharmacological activities, including anti-inflammatory [11], antioxidant [12] and anticancer effects [13] (Table 8) (Figure 7.2).

Breast cancer cells	Effects	Refs
MCF7, SKBR3, T47D, BT20	Inhibit proliferation	[14,15]
MDA-MB-435	Inhibit metastasis	[16]
MDA-MB-231	Induce apoptosis	[17]
T47D,	Inhibit angiogenesis	[18]

Table. 8: Anti-breast cancerous effects of curcumin

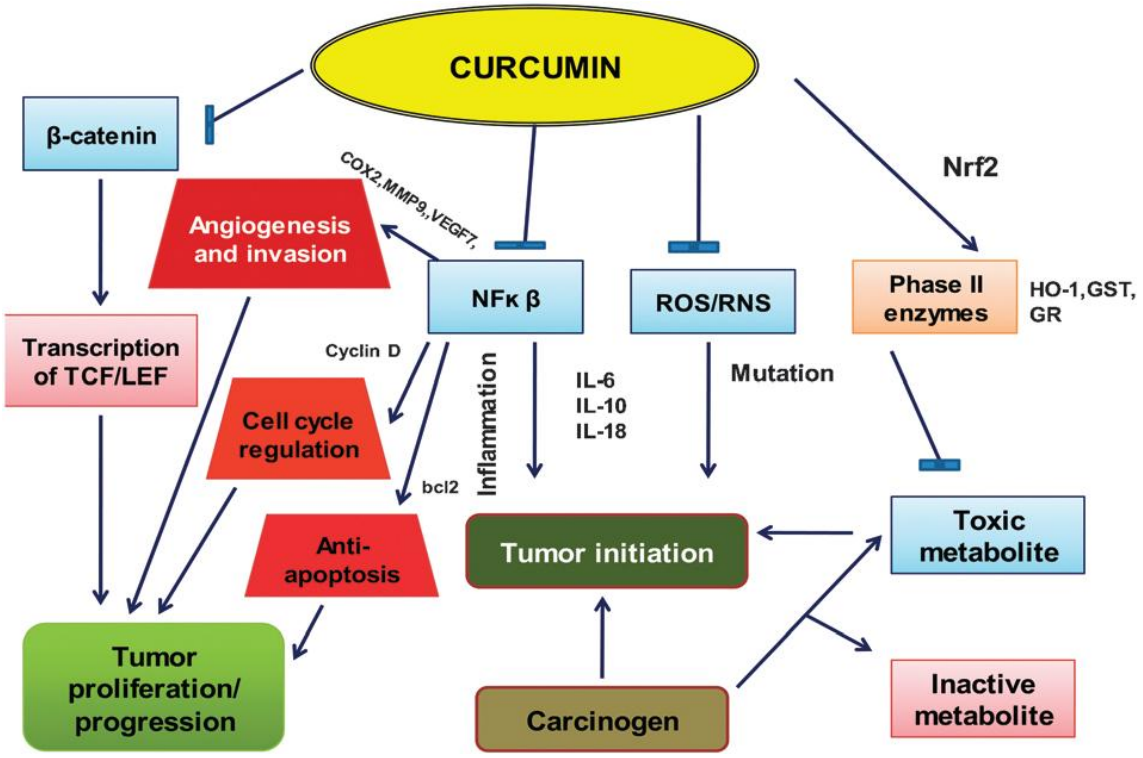

Figure 7.2: Targets associated with the anti-cancer activity of curcumin.
Curcumin exhibits chemopreventive and therapeutic response against breast cancer by targeting a variety of pathways that are associated with tumor initiation and progression. ROS: reactive oxygen species; RNS: reactive nitrogen species; NFkB: nuclear factor kappa B; Nrf2: (NF-E2)-related factor 2; HO-1: heme oxygenase-1; GST glutathione S-transferase; GR: glutathione reductase. COX: cyclooxygenase; MMP: matrix metalloproteinase; VEGF: vascular endothelial growth factor.

Phase I clinical trials reveled that curcumin could be safely administered at high doses (8 g per day) [19]. Curcumin and its metabolites have not been detected in plasma at doses lower than 3.6 g per day indicating low bioavailability when administered orally [20]. Other factors such as metabolic instability and poor aqueous solubility at basic and neutral pH values also impact on curcumin activity and therapeutic efficacy [21]. The limited tissue distribution and low plasma levels of

curcumin are attributed to its poor absorption and metabolism in the gastrointestinal tract and its rapid and extensive metabolism through reduction oxidation, sulfation, and glucuronidation, leading to less active metabolites. Several strategies were tested to overcome the pharmacokinetic limitations of curcumin. These approaches include testing piperine (like adjuvant) that interferes with glucuronidation, liposomal curcumin, curcumin nanoparticles, curcumin phospholipid complex, and structural analogues of curcumin [22,23]. Curcumin through its multiple cellular effects on apoptosis and its excellent safety profile may be an effective agent to combine with current available therapies. Curcumin may find application as a novel drug in the near future to control various diseases, especially breast cancer. The multiple molecular pathways modulated by curcumin may add to its therapeutic value in the treatment and prevention of breast cancer. Research on the nanotechnology-based formulations and delivery system of curcumin for breast cancer is in progress [24,25]. Different nanotechnologies are being applied to develop diverse or novel curcumin formulations that have improved pharmacokinetic profiles. These strategies include curcumin encapsulation with nanoparticles or curcumin conjugated to a ligand or antibody that specifically targets the cancer cell receptor or epitopes; moreover the inclusion of curcumin in polymeric micelles or liposomes/lipidic micelles [24,25]. Therefore, the use of these novel chemical analogs and nanotechnology-based formulations of curcumin may represent a potential alternative strategy for overcoming the principal factors limiting curcumin therapeutic effects when administrated orally.

7.2 New medicinal frontiers: Curcumin nanoformulations

Various types of NPs, such as polymer NPs, polymeric micelles, liposome/phospholipid, nano-/microemulsions, nanogels, solid lipid NPs, polymer conjugates, self-assemblies, and so on, are suitable for the delivery of an active form of curcumin to tumors [26]. Nano drug-crystals have a greater dissolution rate owing to a larger specific surface area; the development of successful nanocrystal formulation by any of these bottom-up approaches depends on the stabilization process. Curcumin crystal formation is a time-dependant process: after 90 min in a solution of alcohol and water [27] curcumin crystals start to aggregate and form a precipitate; the co-aggregation of surfactant molecules, including SDS, CTAB, Tween 80, Triton X-100 and pluronic polymers, form micelles at a CMC which can provide the required influence to stabilize curcumin molecules [28]. However, cationic micelles provide greater stability to curcumin even at elevated pH and are preferred for their medicinal implications; similarly, also plasma proteins have been documented as carriers for curcumin because of their ability to stabilize curcumin molecules [29].

Polymer–drug conjugates are considered to be alternative therapeutics from the nanoscale family. Two phenolic rings and active methylene groups are potential sites to conjugate any biomacromolecules onto curcumin. For example Kumar *et al.* designed nucleoside–curcumin bioconjugates to obtain high levels of glucuronide and sulfate curcumin conjugates in healthy human volunteers [30]. Novel polyethylene glycosylated (PEGylated) curcumin analogs have been also proposed to improve curcumin solubility. PEGylated curcumin conjugates sowed also a key role in growth inhibitory effects on a panel of human cancer cell lines [31]. In recent years, emerging products consisting of polymer–curcumin nanoconjugates have proved

useful for obtaining a higher cytotoxicity in cancer cells. The synergist activity is dependent on the type of terminal functionality and molecular weight of the linker chain. For example, a cationic poly(vinyl pyrrolidone)–curcumin (PVP–CUR) conjugate formulation with stable particle size and ζ-potential with a pH range of 3–9 has been shown by MTT assay to be more potent in L929 fibroblast cells in comparisons with free curcumin [32].

Microemulsions are isotropic nanostructural, stable solutions comprising surfactants, oil and water. Curcumin-based microemulsions are expected to improve curcumin delivery via local and transdermal routes for scleroderma, psoriasis and skin cancer. Eucalyptol-based curcumin microemulsions have very high permeability and flux with moderate solubility of curcumin compared with many oleic acid- and esteem oil-based microemulsions [33]. The enhanced penetration capacity of this applied curcumin microemulsion formulation, as well as its effect on the cellular structure of skin, has been observed.

Liposomes comprise artificial phospholipid vesicles, considered to be biologically safe, biocompatible and protect drugs from external stimuli. It has been known that an extended absorption capacity of curcumin can be attained by dissolving, mixing or complexing it with different types of phospholipids [34]. A recent pharmacokinetic study of solid lipid curcumin NPs in patients with osteosarcoma reported up to 31.42–41.15 ng mL^{-1} of curcumin within 4 h of 2000–4000 mg oral dose treatment [35]. More importantly, the patients did not experience any adverse effects.

Curcumin loaded into polymeric NPs has been an alternative choice to enhance the bioavailability of the drug exploiting the controlled release of such polymer matrix. For example different PLGA nanoformulations has been a

widespread choice in the production of a variety of biomedical devices owing to its biodegradability and biocompatibility. In an effort to create a safe carrier, several different types of PLGA NP for curcumin encapsulation have been explored by simple solid–oil–water solvent evaporation method [36,37], in which the particle size can be controlled by the surfactant concentration and sonication time. *In vivo* mice studies using this type of formulation resulted in a ten-fold increase in the concentration of curcumin blood, lungs and brain compared with curcumin dissolved in PEG_{400} formulation [38]. In a recent work, Tsai *et al.* [39] designed curcumin-loaded PLGA and demonstrated the half-life of curcumin in the cerebral cortex and hippocampus to be significantly increased from 2.32 to 19.9; additionally, retention time values of the cerebral cortex and the hippocampus have been increased approximately 2.0- and 1.8-fold, respectively. The curcumin plasma levels have been slightly higher with this nanoformulation compared to the normal administration vehicles.

The characteristics of these curcumin nanoformulations can be tailored according to the specific requirement for inducing cellular death by various mechanisms. Overall, our understanding from the available literature is that the use of curcumin nanoconstructs as drug for cancer treatment is a facile modality that improves existing curcumin therapies by targeting tumors and by reducing the dose required. Safe toxicological profiles of the various curcumin nanoformulations and their efficacy in the cell-line models highlight their potential for evaluation in *in vivo* models. Human trials need to be conducted to establish their effectiveness in clinical applications as an improved therapeutic modality. Therefore, future studies that combine curcumin delivery with other first-line anticancer chemotherapeutic agents or imaging, contrast, antibody or peptide-targeted delivery are going to achieve better-

targeted therapeutic modalities. Additionally, studies need be developed to estimate the efficacy and toxicity of curcumin NP formulations in both small and large cohorts, as well as in patients with cancer in phase I and II clinical trials. To this aim I have listed below (Table 9), a comprehensive list of commercially available curcumin NP formulations, which are trying to open new frontiers to the pharmacological market. Overall, these developed processes must be simple, efficient, continuous and suitable for large-scale convertible production that is acceptable by regulatory authorities.

Curcumin Formulations	Composition
NanoBioSphere™ complex (solid lipid nanocurcumin) Life Enhancement Products, Inc., USA	Vitamin E, sunflower oil, phospholipids, safflowerоil, ethanol, medium chain triglycerides,glycerin, curcumin C3 complex,
Curcumin C3 complex® vegetarian capsules BestVite, Inc., USA	Curcumin C3 complex, curcuminods and black pepper extract (*Piper nigrum*)
CurcuPlus D Ultra™ Advanced Orthomolecular Research, Inc., Canada	Curcumin (Longvida®), vitamin D3, ascorbyl palmitate, microcrystalline cellulose, soy lecithin, stearic acid, maltodextrin and silicon dioxide
Nanocurcumin (*N*-curcusorb) Konark Herbals & Health Care, India	Curcumin in nanosized particles
Nanocurcumin (in the scale-up process) SignPath Pharmaceuticals, Inc., USA	Liposomal curcumin formulation; PLGA-curcumin formulation
Nano curcumin/nano curcuma Nano Tech Miso-N, Korea	Nanocurcumin solution (colloid) products

Table. 9: Commercially available formulations containing curcumin

7.3 Synthesis of curcumin-loaded PLGA nanoparticles

The curcumin crude plant extract is commercially available as a mixture of three isomers: curcumin (70%), mono-demethoxy curcumin (20%), bis-demethoxy curcumin (10%); however, with the aim to perform the encapsulation inside PLGA NPs, only the pure active compound has been suitable. Difficult purification steps of Curcumin with silica gel chromatography have been avoided by the total synthesis of the active compound accomplished within a low cost total-synthesis in two simple steps.

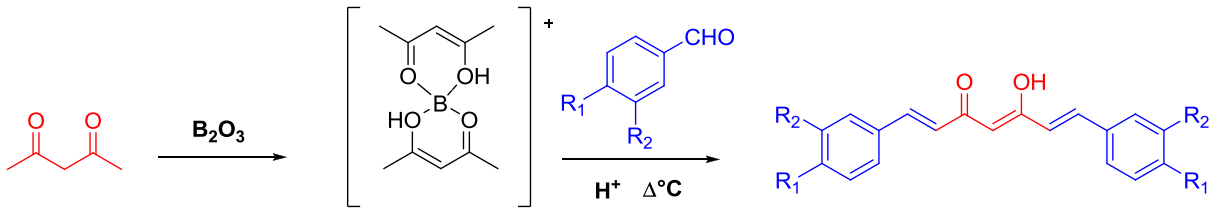

Figure 7.3: Total synthesis of curcuminoids.
First step is achieved by protection of acetylacetone while in the second step the appropriate benzaldheyde is condensed to the backbone. Finally the boron complex is hydrolyzed in acidic aqueous conditions.

The general procedure for synthesizing Curcumin is summarized in Figure 7.3, where the backbone starting material, 2,4-pentanedione, has been condensed with the appropriate benzaldehyde in DMF at 95°C using a slight modification of the Pabon method [40]. The main steps in this process are the protection of active methylene group (protection with a boron complex is necessary in order to avoid Knoevenagel condensation at C-3 of 2,4-pentanedione) by reacting with acetylacetone in the presence of boric oxide (B_2O_3) in order to get acetyl acetone–boric oxide stable intermediate complex which reacts through with less reactive methyls within the appropriate benzaldehyde group of 4-hydroxy-3-methoxy benzaldehyde using 1,2,3,4-tetrahydroquinoline (THQ) as catalyst. At the end of the reaction, the boron complex is cleaved by acidic hydrolysis, giving the desired product in 65 % yield with an excellent product quality.

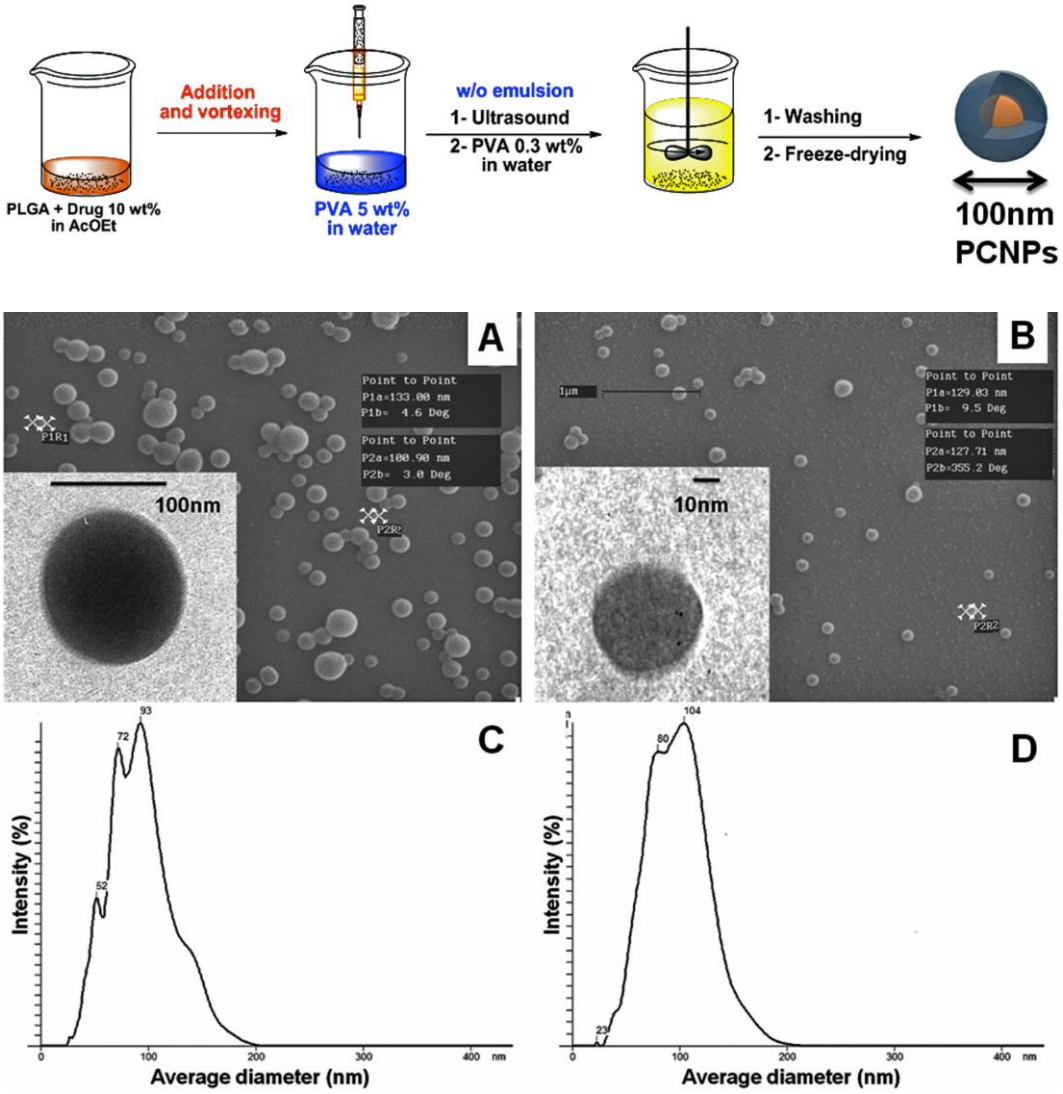

Figure 7.4: Synthesis of PLGA curcumin nanoparticles.
(Upper scheme) The organic phase containing the drug and the polymer is added to an aqueous surfactant solution to create a w/o emulsion; after emulsification, the organic solvent is allowed to evaporate and PLGA NPs are collected by freeze-drying process from the aqueous phase.
(Panels A, C) SEM and TEM pictures (inset) of VPNPs followed by the hydrodynamic size distribution (Nanosight analysis).
(Panels B, D) SEM and TEM pictures (inset) of PCNPs followed by the hydrodynamic size distribution (Nanosight analysis).

PLGA curcumin loaded nanoparticles (**PCNPs**) and the corresponding drug-free NPs (**VPNPs**) have been prepared using the "single-emulsion" process [41,42], which is also referred to as the "solvent evaporation" technique, an ideal method for the encapsulation of hydrophobic drugs (Figure 7.4). Within this technique, the organic phase containing curcumin and the polymer with an optimized stoichiometric proportion, has been mixed with an aqueous solution containing a surfactant partially

miscible with water (in this case polyvinyl-alcohol, PVA) which, on the basis of essential applied research [43], it has been established that the two most important parameters for steady-state nanoparticles dimensions are the composition ratio $C_{(surfactant)}\ C_{(polymer)}^{-1}$ and the chain-length of the polymer. PVA (5.0 and 0.3 wt %) has been used as surfactant to stabilize the nanoparticle emulsion during its formation, leading to an increase in the solubility of the drug without nanoparticle agglomeration. Within this method, at the same time, the maximum encapsulation efficiency and a narrow particle size distribution have been afforded. Indeed, no evidence of PCNPs and VPNPs alteration in their morphological surface and structure have been revealed by TEM and SEM analyses: images of VPNPs and PCNPs showed a spherical shape with diameters of 116.9 ± 13.8 and 128.37 ± 16.7 nm, respectively. Mean size distribution by Nanosight analysis confirmed nanoparticle diameters with a maximum in intensity of 93 ± 23 nm for VPNPs and 104 ± 28 nm for PCNPs. To follow their behavior in aqueous solution, the size distribution and surface charge of both kinds of nanoparticles in deionized water have been analyzed by DLS and ζ-potential before and after the freeze−drying process. Cryodessication could be a critical synthetic step because it is known that very low temperatures could affect negatively the colloidal stability during powder resuspension and, in the case of PLGA, this process is a necessary step due to the biodegradability of the polymer. From DLS analyses in cell culture DMEM (serum-free medium), initial hydrodynamic diameters of 99.6 ± 10.5 and 116.8 ± 18.2 nm have been measured for VPNPs and PCNPs, respectively, before freeze-drying. After lyophilization, values have been measured of 110.8 ± 12.4 and 133.2 ± 4.3 nm, respectively. The mean surface charge has been estimated to be −21.0 ± 1.9 mV for VPNPs and −30.2 ± 3.7 mV for PCNPs. No alteration of hydrodynamic diameters has been monitored up to 72 h of

incubation for both nanoparticle formulations following the freeze−drying step (Figure 7.5).

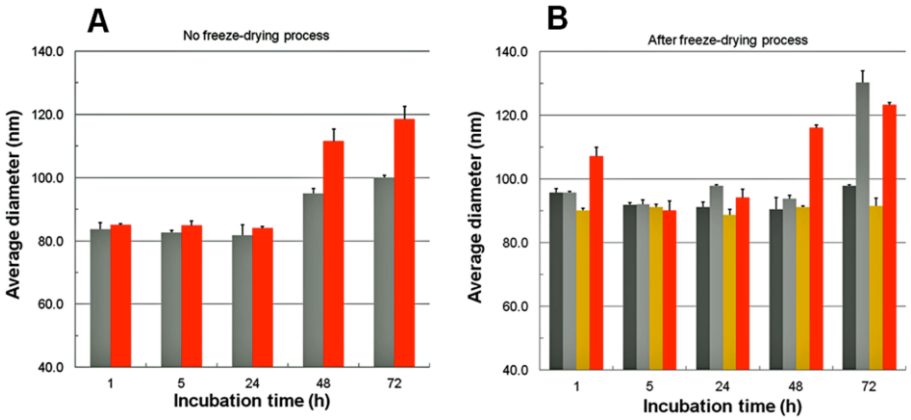

Figure 7.5: Aggregation kinetic of PLGA NPs in DMEM before and after lyophilization.
(Panel A) VPNPs (dark grey histogram) and PCNPs (red histogram).
(Panel B) VPNPs, 50 µg mL^{-1} (light grey histogram) and, 100 µg mL^{-1} (dark grey histogram); PCNPs, 50 µg mL^{-1}, (orange histogram) and 100 µg mL^{-1} (red histogram).

To find out the optimal concentration of nanoparticles and their potential use as drug delivery system, the critical micelle concentration (CMC) has been evaluated of VPNPs using pyrene as a fluorescent probe (Figure 7.6). This technique enables the opportunity to calculate the lower concentration limit of nanoparticles in aqueous solution. From the fluorescence graph, the mean intensity ratios (I_{338} / I_{334}) of pyrene excitation spectra increased by increasing polymer concentration. Since the increment in the

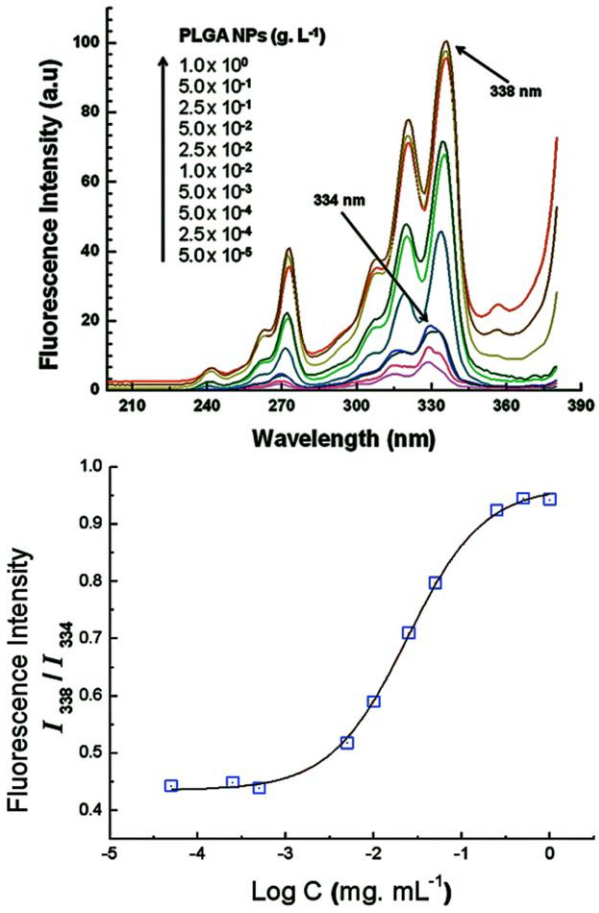

Figure 7.6: CMC evaluation of PLGA NPs.
(Upper level) Fluorescence excitation spectra using increasing amount of VPNPs
in a range between 5.0 x 10^{-5} g L^{-1} and 1.0 g L^{-1}.
(Lower level) Interpolation curve of the data.

intensity ratio indicates the aggregation of pyrene into the hydrophobic reservoirs of the polymers, CMC has been determined from the crossover point of the second derivative sigmoidal curve at low concentration ranges (9.07 ± 1.21 mg L^{-1}).

The amount of curcumin into the nanoparticle system has been calculated by both UV−vis and fluorescence spectroscopy. For this purpose, a calibration curve of the pure compound in a mixture of 9:1 chloroform/ethanol has been elaborated for the analysis. So, a known amount of PCNPs has been dispersed in aqueous solution under vigorous stirring. An organic phase composed by the same solvents has been poured for 3 h to form a biphasic system for the time necessary to dissolve the drug into the organic solvent, which has been later detected according to UV−vis (λ = 420 nm) and fluorescence spectroscopy ($\lambda_{emission}$ = 520 nm). The encapsulation efficiency has been calculated with the following equation (Equation 5):

$$E.E.(\%) = \frac{drug_{loaded}(\mu g_{drug} \cdot mg^{-1}{}_{NPs})}{drug_{initial}(\mu g_{drug} \cdot mg^{-1}{}_{NPs})} \cdot 100 \qquad \text{(eq. 5)}$$

In this way, it has been calculated that 80 ± 7 μg of drug have been encapsulated for each mg of PLGA nanoparticles (8.0 wt.%), corresponding to an 80% drug encapsulation into the polymer matrix.

A second important issue concerns the maintenance of the polymer shell, which should protect the drug from the solvent until the nanocomplex reaches the desired site of action. With the aim to demonstrate that curcumin is been able to maintain its chemical properties, series of fluorescence analyses in different physiological buffers commonly used both in cellular and clinical treatments have been further set up. For this experiment an acidic 20 mM sodium acetate buffer pH 4.75, a neutral 20 mM phosphate buffer pH 7.40, a basic 20 mM ammonium buffer

pH 9.25 and a complete cell culture medium DMEM, pH 7.40 (supplemented with FBS 10 wt.%) have been used a concentration of 5 μM of drug (Figure 7.7).

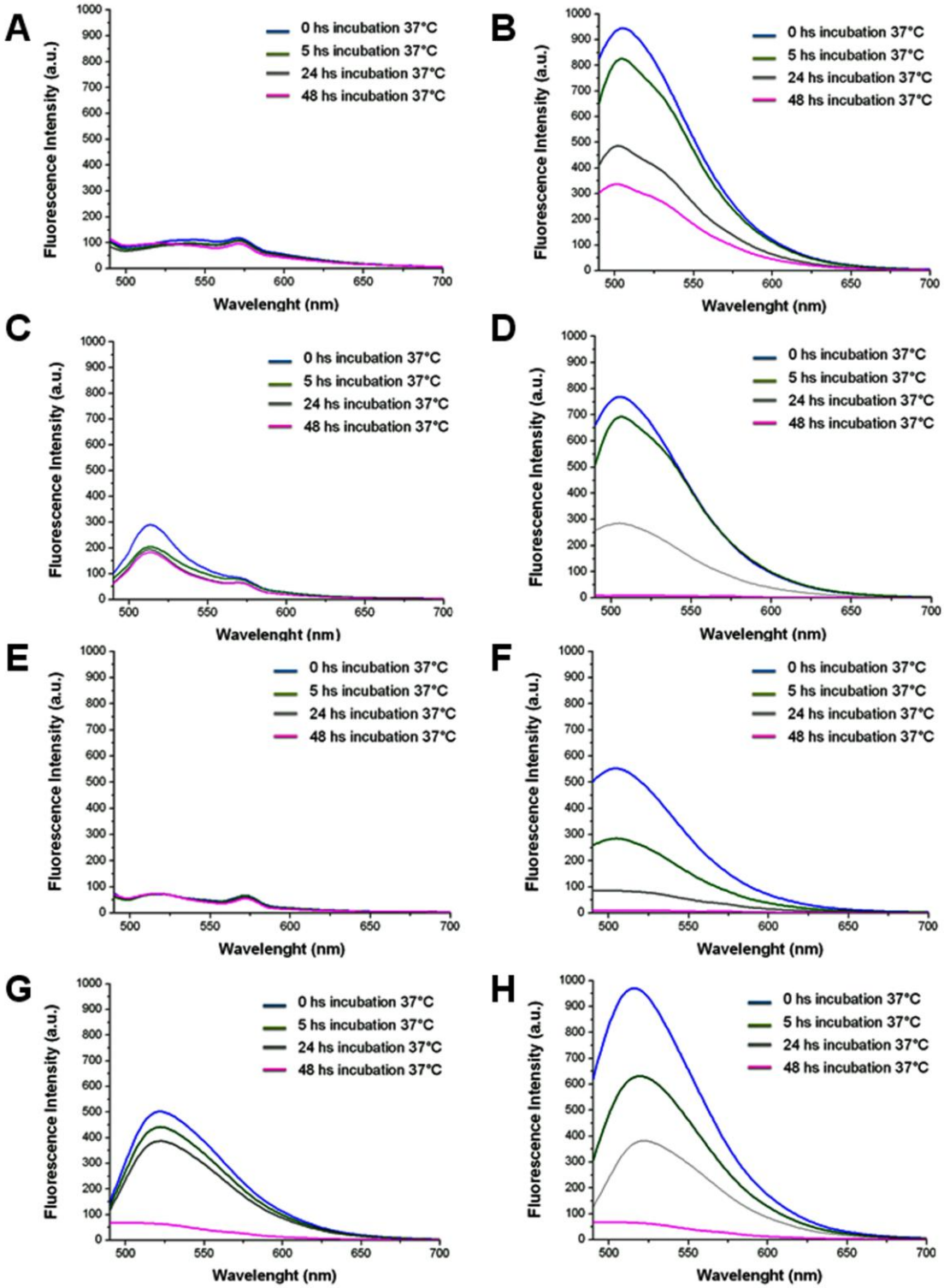

Figure 7.7: Fluorescence analysis of curcumin and PCNPs in different clinical buffers.
(Panel A, B) Free curcumin and PCNPs in acetate buffer up to 48 h of incubation.
(Panel C, D) Free curcumin and PCNPs in phosphate buffer up to 48 h of incubation.
(Panel E, F) Free curcumin and PCNPs in ammonium buffer up to 48 h of incubation.
(Panel G, H) Free curcumin and PCNPs in cell culture medium up to 48 h of incubation.

These analyses have revealed that in all cases, while the free drug suffers from structural changes and degradation of the molecule, the curcumin encapsulated has been detected showing a higher broad fluorescence peak.

The structural conservation of curcumin has been confirmed also with Raman spectroscopy (Figure 7.8). The basal spectrum of free curcumin is almost unchanged within the drug encapsulated inside PCNPs; this could explain that when the drug is efficiently encapsulated, is really protected by the polymer matrix. The only substantial change has been observed for the peak of the C-OH enolic of the backbone chain.

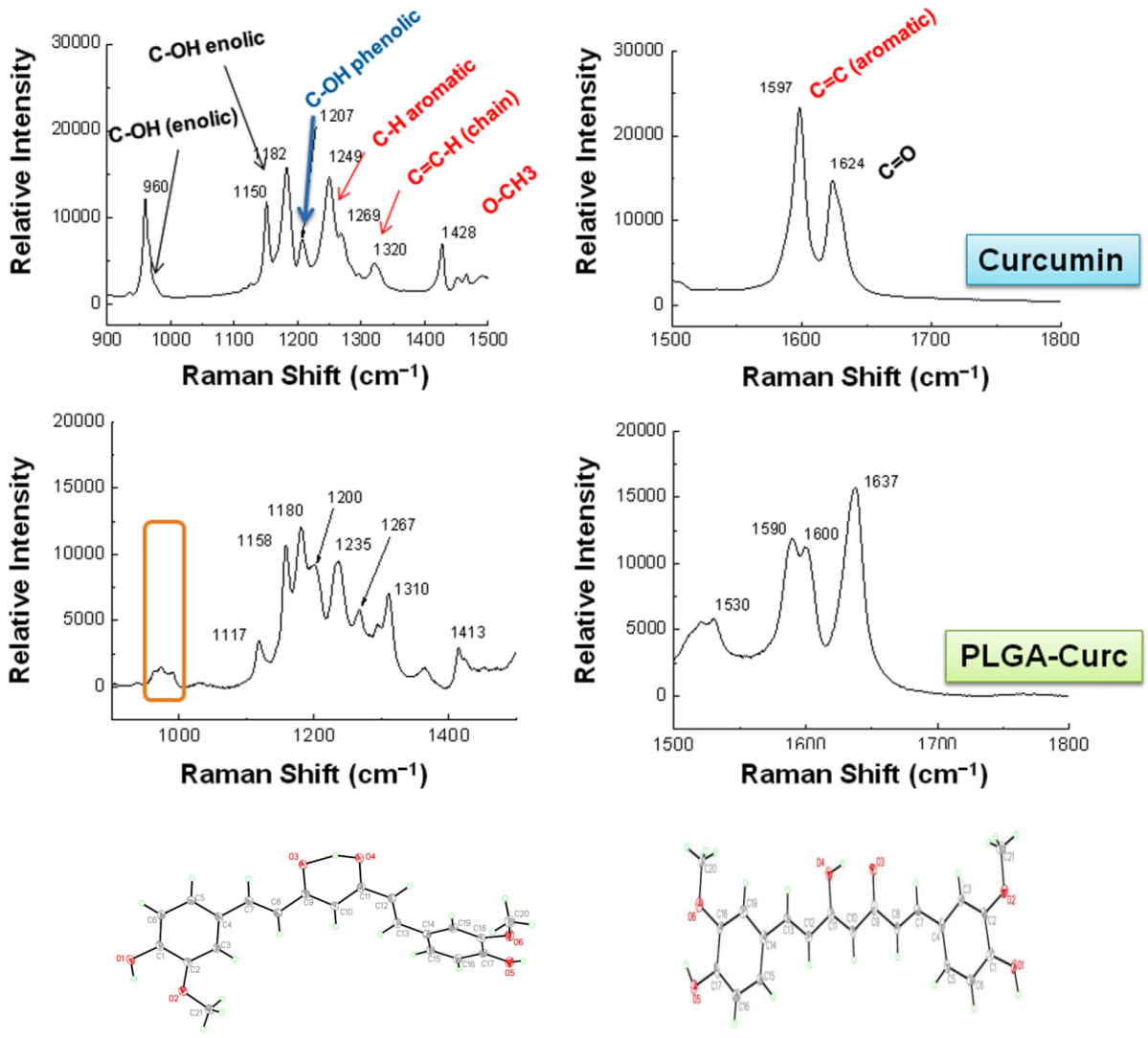

Figure 7.8: Raman spectroscopy of curcumin and PCNPs.
(Upper level) Free curcumin spectra from 900 to 1800 cm^{-1} Raman shift.

(Lower level) PCNPs spectra from 900 to 1800 cm^{-1} Raman shift.
(3D pictures) on the left the crystal structure of free curcumin and on the right a possible explanation of the conformational change occurred within the encapsulation of the drug inside PLGA NPs

Since it is explained in literature [44] that the enolic form of curcumin is predominant despite the diketonic structure because the former is enthalpy−favored due to the role of its hydrogen bond which leads to the formation of a pseudo six-membered ring in that specific position. The molecular nature of this flexible structure obliges the second aromatic ring to turn into a different plane with respect to the first aromatic ring. Instead, when curcumin is really encapsulated into PLGA, the structure of its enolic form turns into a more rigid and fully conjugated structure. For this reason, also the two aromatic rings are seized in the same plane. This circumstances can also strengthen the concept of the observed higher fluorescence intensity of drugs when they are protected by the polymer matrix.

7.4 *In vitro* drug release kinetics

Over recent years, drug release/dissolution from pharmaceutical dosage nanovectors has been the subject of intense and profitable scientific developments. Whenever a new solid dosage form is produced, it is necessary to ensure that drug dissolution occurs in an appropriate way; for this purpose the pharmaceutical industry and the registration authorities are focusing, nowadays, on the quantitative analysis of the values obtained in drug dissolution/release kinetics. In some cases, these mathematic models are derived from the theoretical analysis of the occurring process, but in most cases the theoretical concept is not applicable and some empirical equations have proved to be more appropriate (see for examples, drug dissolution profiles from Hixson-Crowell, Weibull, Higuchi, Baker-Lonsdale, Korsmeyer-Peppas and Hopfenberg) [45]. The kinetic of drug release has been described by these models in which the dissolved amount of drug (Q) is a function of the test time, t or $Q = f(t)$ where it represents the amount of drug dissolved in time t. Generally, for a water-soluble drug incorporated in a matrix, the active agent is mainly released by dissolution drug dissolution while for a low water-soluble drug, the self-erosion of the matrix is the principal release mechanism. To accomplish these studies, the cumulative profiles of the dissolved drug are more commonly used in opposition to their differential profiles. To compare dissolution profiles between two drug products model dependent (curve fitting) and statistical analysis can be used [46].

Based on these general considerations, our *in vitro* release kinetics has been performed to have access to fundamental implications about the porosity of our nanoformulation on a molecular level, possible interactions between drug and the external environment or the polymer matrix and their influence on the mechanism

and rate of drug release. The release study has been performed with the dissolution technique (see also “sample and separate methods”) as described in literature [46]. This is the most widely used technique; briefly, PCNPs have been introduced into a vessel containing media and release has been monitored over time. Media selection is based on drug solubility and stability over the duration of the release study and the container selection has been chosen on the basis of the volume of dissolution media necessary to maintain *sink* conditions without compromising the sensitivity of the assay in 150 mM PBS pH 7.4 supplemented with BSA 2.0 wt.% with the aim to enhance curcumin dissolution and mimic a biological environment. PCNPs suspension has been maintained at 37 °C with gentle stirring and small amounts of sample have been withdrawn at fixed times, NPs has been separated from supernatant and resuspended in the same volume of fresh medium to mimic a physiological *sink* condition. All samples have been analyzed by Uv-vis (λ = 420nm) and quantified according the calibration curve constructed previously with the same buffer. As expected, it has been observed an initial “*burst effect*” in drug release in the first 24 h of incubation (50.3 ± 6.5%); these values increased up to 73.3 ± 8.0% within the following 72 h (overall 4 days). Next, the release of residual cargo became very slow and the curve slope decreased to reach a plateau corresponding to a maximum after 10 days (81.3 ± 2.3%) (Figure 7.9). Thus, it was clear that the incorporation of curcumin in PLGA nanoparticles could significantly sustain its continuous and prolonged release. The data obtained from kinetic studies was fitted according to the Korsmeyer−Peppas model (Equation 6)

$$f_t = k \cdot t^n$$
$$\log f_t = \log k + n \cdot \log(t) + b \qquad \text{(eq. 6)}$$

Where f_t is the fractional drug release, k is the release constant, t is the time of release and n is the release exponent, which determines the type of kinetics.

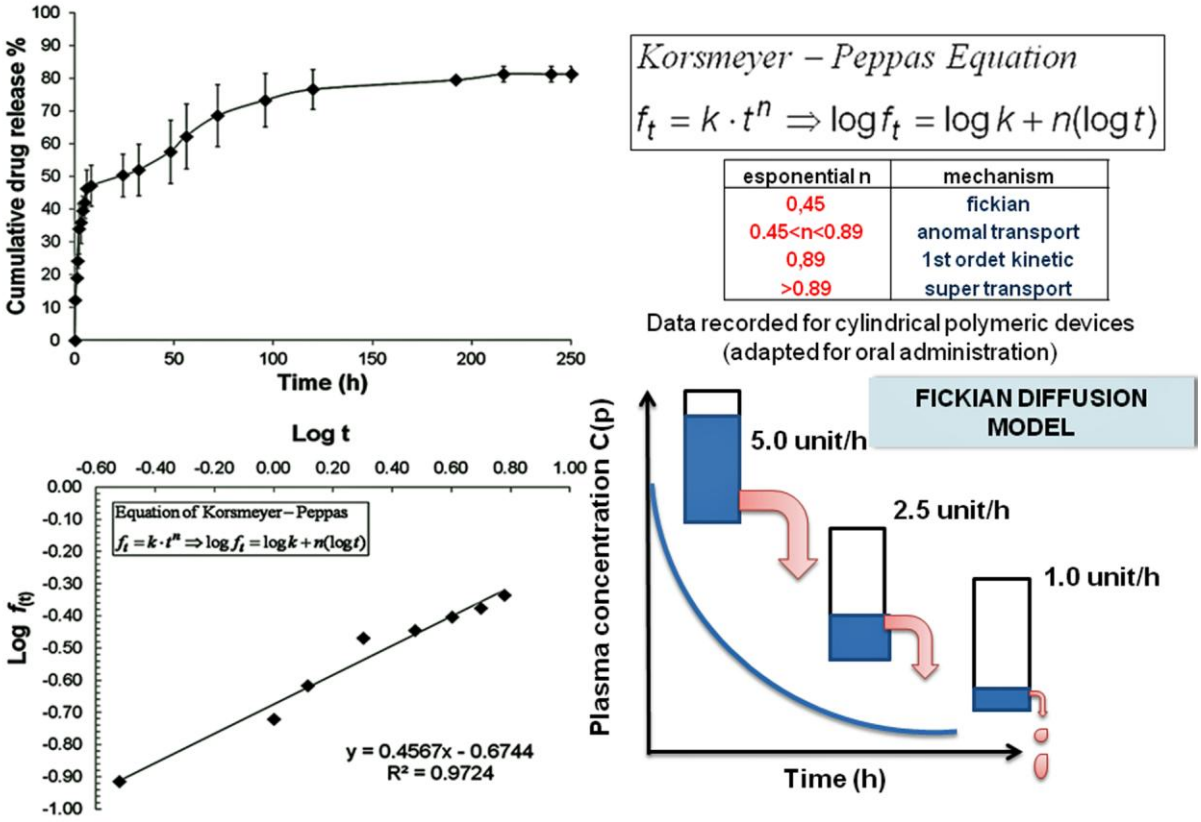

Figure 7.9: *In vitro* drug release kinetic.
(Left) Drug diffusion profile of curcumin from PCNPs using the dissolution technique Values represent mean ± SD of three batches (some error bars are too small to be shown). Below the Kinetic calculation of the drug release rate keeping into consideration the Peppas−Korsmeyes's model. (Right) The full equation used to build up the kinetic curve) and the data recorded to explain the Fickian Law diffusion model of our nanoformulation.

The regression coefficient of log f_t *vs.* log t has been calculated to be 0.972, with values of release exponent (n) and release constant (k) of 0.456 and 0.674, respectively. By this calculation, it has been demonstrated that our release follows a Fickian-law diffusion with a release exponent of 0.45, according to data recorded for cylindrical polymer devices adapted for intravenous administration. For the determination of the exponent (n), the linear portion of the kinetic curve until the fractional release amount reached 60% has been investigated.

7.5 Toxicity evaluation: Cancer Cell cycle arrest induced by curcumin-PLGA nanocarrier

MCF7 breast cancer cells have been chosen as a cellular model to study the effects of PCNPs and VPNPs (control). The cellular viability has been first investigated by measuring the cell proliferation by means of the MTT specific assay (Figure 7.10), after long-time NPs exposure on cells (72 h overall) at concentrations of 50 and 100 μg mL^{-1} (corresponding to 10 μM and 20 μM, respectively). Treatment with VPNPs has been showed not to alter cell proliferation, indicating that the PLGA vector is nontoxic even after prolonged exposure time. On the other hand, treatment with PCNPs (compared with direct biological effect of curcumin in these cells) has revealed a huge decrease of cellular proliferation in a dose- and time-dependent way. In contrast to VPNPs, MTT assay revealed that, ready after 24 h, the lower dosage of PCNPs efficiently triggered the inhibition of tumor proliferation and this value increased by

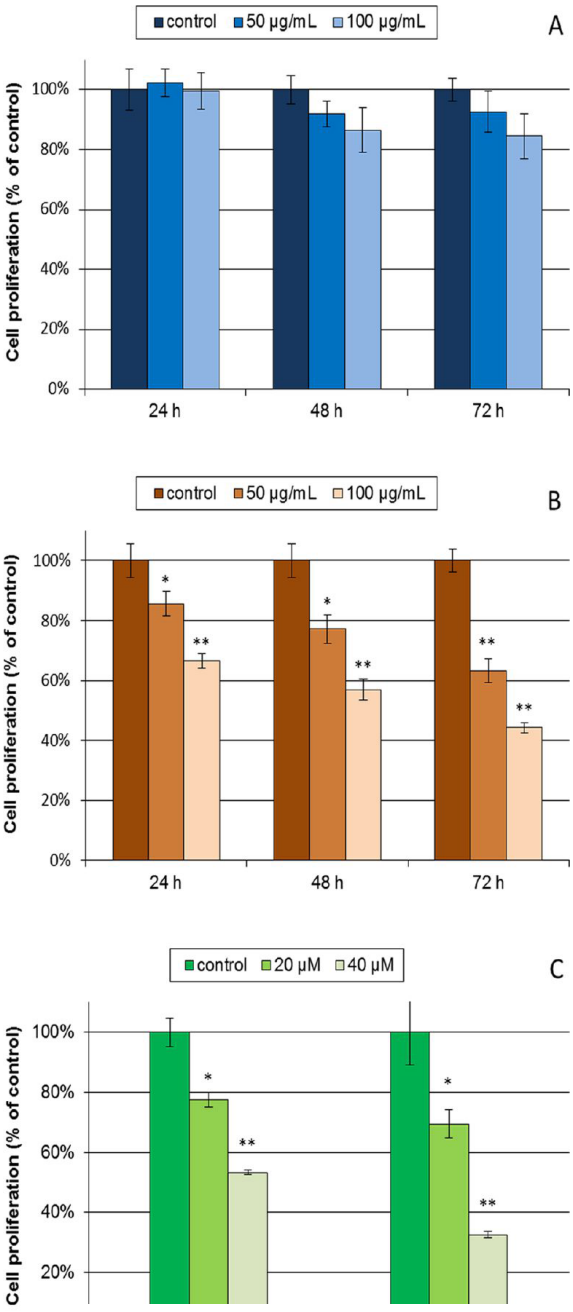

Figure 7.10: MTT assay of VPNPs, PCNPs and free curcumin

MCF7 breast cancer cells in the presence of: (Panel A) VPNPs (50 and 100 μg mL^{-1}) (Panel B) PCNPs (50 and 100 μg mL^{-1}) (Panel C) free curcumin (20 and 40 μM) Untreated cells were used as control 100% of the proliferation. Values are mean ± SD of three independent sets of experiments. Analyzed by one-way ANOVA, samples show statistical difference at *p ≤ 0.05 and **p ≤ 0.01.

over 50% after incubating the cells for 72 h with the highest NPs concentration. According to these preliminary results, it has been attempt to evaluate signs of apoptosis or necrosis processes at the basis of the reduced cell viability. The Annexin-V specific assay has been tested to find possible signs of cell death that the MTT was unable to detect (Figure 7.11). Exploiting high-affinity of Annexin-V for phosphatidylserine, apoptotic cells could be quantitatively determined by using fluorescently labeled Annexin-V in combination with a vital dye such as 7-amino-actinomycin (7-AAD) [47]. This assay allowed us to distinguish viable cells from early and late stages of apoptosis and from necrotic cells, for which all data could be quantitatively determined by flow cytometry.

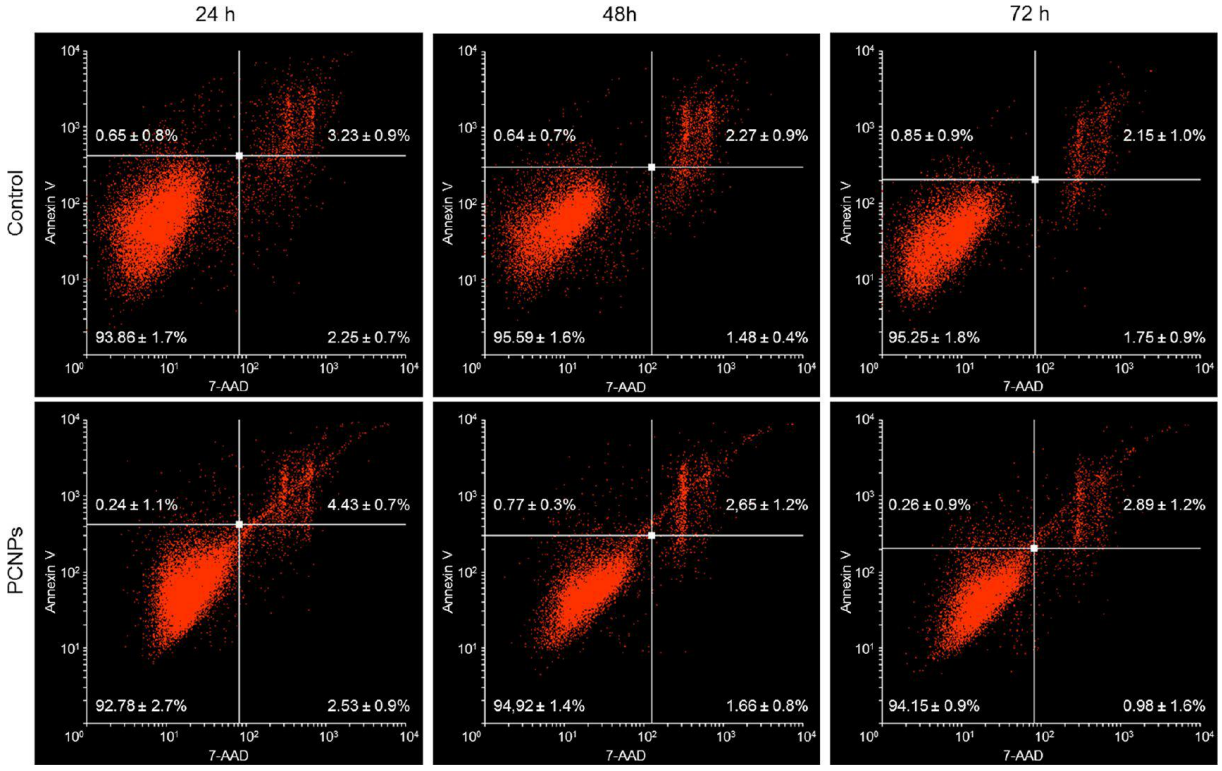

Figure 7.11: Apoptosis assay.
Cell death has been assayed by means of 7-AAD/annexin-V double staining on cells exposed to 100 mg L^{-1} of PCNPs up to 72 h, (Lower level) or left untreated as control (Upper level).
Viable cells could be distinguished (both annexin-V- and 7-AAD-negative) from early apoptotic (7- AAD−/annexin-V+), late apoptotic (7-AAD+/annexin-V+) and necrotic cells (7-AAD+/annexin-V−).

Surprisingly, by incubating cells with curcumin-PLGA nanoparticles for the whole time of exposure of the MTT, the same physiological basal apoptotic rate has

been recovered with untreated and NPs-treated samples, thus excluding apoptotic and/or necrotic events at the basis of the observed reduced proliferation.

Since that these two consequences have been discarded, it has been investigated whether the observed reduced proliferation has been indeed induced by a cell cycle arrest. For instance, the analysis of DNA content in cells treated with VPNPs and PCNPs, has been performed (Figure 7.12). Monoparametric DNA analysis with propidium iodide staining showed that pure PLGA treatment did not affect the cell cycle phases in comparison with control cells. In contrast, a significant alteration of the cell cycle has been demonstrated in samples treated with curcumin and PCNPs, leading to a reduction of S phase and to a G2/M block according with previous literature data [48]. This result indicates a specific biological effect owned by these nanoparticles related to its drug content. Taken together, MTT and cell cycle analysis suggest a specific cytotoxic activity of curcumin-loaded PLGA nanoparticles essentially attributable to the cell cycle

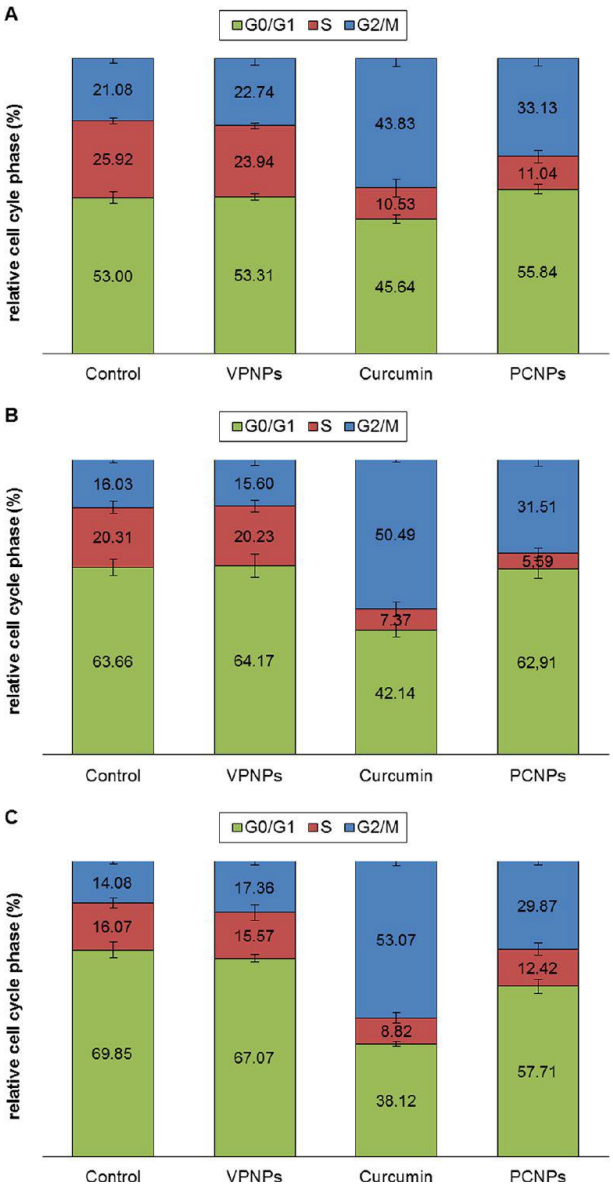

Figure 7.12: Cell cycle analysis
MCF7 cells have been treated with VPNPs, PCNPs (100 mg L^{-1}), free curcumin (20 μM).
At the end of each time (Panel A, 24h), (Panel B, 48h), (Panel C, 72h) cells have been ethanol fixed, stained with propidium iodide and the DNA analysis have been assessed with FACS. Values are meas of three independent sets of experiments (10 thousand events collected each sample)

arrest induced by curcumin release. To demonstrate that the biological effects of PCNPs could be actually correlated with the drug release from the cargo, the fluorescent properties of the curcumin has been exploited by considering the whole increase of cell fluorescent population due to curcumin upon its release into the cellular environment (Figure 7.13).

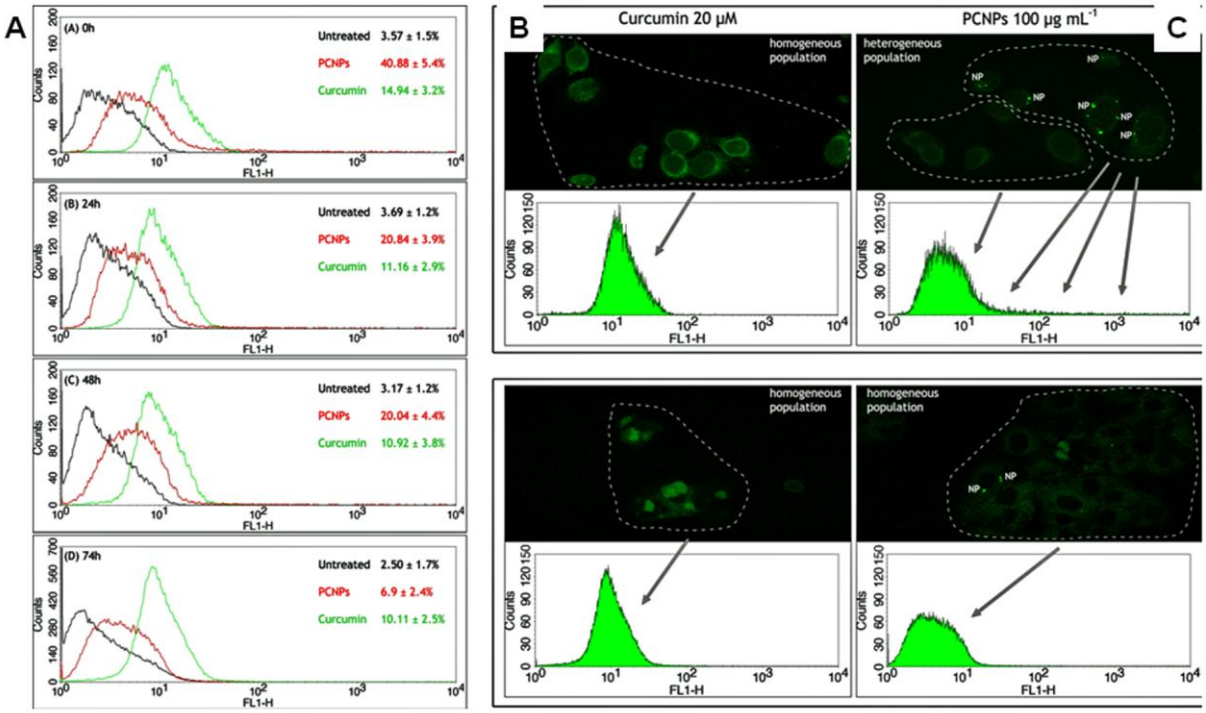

Figure 7.13: Sustained drug release in tumor cells.
(Panel A) FACS analysis of curcumin release by PCNPs (100 mg L^{-1}) from zero-time (first level) up to 72 h (lowest level).
(Panel B and C) Correlation of FACS and CLSM analyses. Curcumin samples treated have been analyzed 24 h (upper panel, B) and 72 h (lower panel, B) after removal of curcumin medium. PCNPs samples treated have been analyzed 24 h (upper panel, C) and 72 h (lower panel, C) after removal of NPs containing medium.

After 24 h incubation of MCF7 cells with PCNPs, the cell culture containing nanoparticles has been completely replaced by fresh medium without NPs; the whole cell fluorescence has been then monitored for the next three days and analyzed by FACS every 24 h. As illustrated in figure 7.13 (Panel A) the total fluorescence of PCNP-treated cells undergoes a strong increase in comparison with untreated cells, particularly noticeable at zero-time (after the 24 h of exposure). The levels of whole fluorescence remain higher as compared with samples treated with the free curcumin

for the following two days but decrease drastically from the third day. Of particular interest are the fluorescence profiles that greatly differ each other. Therefore, the fluorescence curve of curcumin-treated cells exhibits a narrow shape indicating a homogeneous distribution of the molecule inside the cell population, while cells treated with PCNPs have a broader fluorescence profile, suggesting a marked heterogeneity of the population.

To visually confirm this hypothesis, the same sample (at each time point) has been observed by laser scanning confocal microscopy (Figure 7.13, Panels B and C). While curcumin treated cells confirm a homogeneous cellular fluorescence, in curcumin-PLGA samples, cells exhibit a wider spectrum of fluorescence intensity as two main populations can be distinguished. One is homogeneous (corresponding to many cells with a low intensity level of fluorescence) whereas the second is heterogeneous (corresponding to a small number of cells exploiting high levels of fluorescence) mainly due to bright spots representing nanoparticles agglomerates. It has been interestingly observed that, over time, the main population (Panel C) remains almost unaltered, whereas bright spots gradually disappear. This suggests that the NPs system has been dissolved and the total amount of drug has been diluted by cell proliferation and metabolism.

7.6 Conclusions and outlooks

Among the different biodegradable polymers developed to formulate polymeric nanoparticles, PLGA has attracted nowadays considerable attention due to its attractive properties: (i) biodegradability and biocompatibility; (ii) FDA and European Medicine Agency approval in drug delivery systems for parenteral administration; (iii) formulations and methods of production adapted to various types of drugs (e.g. hydrophilic or hydrophobic small molecules or macromolecules); (iv) protection of drug from degradation; (v) capability of sustained release; (vi) possibility to modify surface properties to provide better interaction with biological materials and (vii) possibility to target nanoparticles to specific organs or cells.

Within this project, PLGA bearing the naturally available nutraceutic agent curcumin, have been synthesized and characterized. Their effects related to the drug release have been investigated *in vitro* in MCF7 breast cancer cells. This study has demonstrated that, while PLGA nanoparticles proved to be completely innocuous toward cells in absence of drug, our drug-nanoformulation is able to release curcumin intracellularly inducing time- and dose-dependent inhibition of proliferation as a consequence of a G2/M block of the cell cycle.

This preclinical example clearly demonstrates that PLGA based nanoparticles have proven potential for the treatment of breast cancer and our future perspective is to modify the surface of the polymer with biomolecules in order to enhance specific recognition of malignancies, making these polymeric devices a useful tools for controlled and prolonged drug delivery system with the aim to help new generations to prevent the widespread diffusion of severe tumor−associated diseases.

7.7 Nanomaterials Experimental section

7.7.1 Procedure for the total synthesis of Curcumin

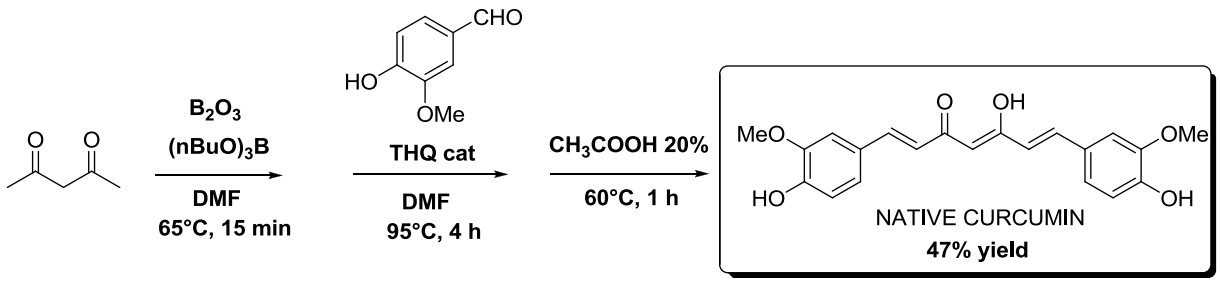

Synthesis of [1,7-bis-(4-hydroxy-3-methoxyphenyl)-1,6-heheptadiene-3,5-dione (**Curcuma**)

In a round bottom flask a solution of boric oxide (350 mg, 5.0 mmol) in freshly distilled DMF (1.0 mL) has been prepared and acetylacetone (0.51 mL, 5.0 mmol) has been added under gentle stirring followed by tributyl borate (2.7 mL, 10 mmol). The colorless mixture has been kept at 65°C for 15 min to form the borate complex. To the complex, 4-hydroxy-3-methoxybenzaldehyde (1.52 g, 10 mmol) has been added and stirred for 5 min at 65°C. Into a small glass container a mixture of the catalyst 1,2,3,4-tetrahydroquinoline (0.1 mL) and glacial acetic acid (0.3 mL) in DMF (1 mL) previously prepared, has been added to the reaction mixture. The temperature has been raised to 95°C and the reaction has been kept under vigorous stirring for 4 h (the color of the reaction turns from colorless to yellow trough orange and finally dark red). After cooling the mixture to 15°C, a solution of aqueous acetic acid 20 vol.% (50 mL) has been added in the reaction mixture and stirred at 70°C for 1 h. The solution turns black and an dark orange precipitate is formed. The mixture has been cooled to 4°C and the formed solid has been filtered, washed with water (50 mL), hexane (25 mL), and finally dried overnight under vacuum pump. The crude curcumin has been passed through a small silica gel column using chloroform/methanol (95:5) as eluent followed by recrystallisation from the same solvent (precipitation at 4°C overnight) to give pure curcumin as an orange solid (2.20 g, 5.97 mmol). ^{1}H NMR data are consistent with literature data [49].

^{1}H NMR ($CDCl_3$) δ= 7.64 ($d_{(J,\ 16\ Hz)}$, 2H, Ar), 7.09 ($dd_{(J,\ 16\ Hz)}$, 2H, Ar), 7.04 ($d_{(J,\ 16\ Hz)}$, 2H, Ar), 6.91 ($d_{(J,\ 8\ Hz)}$, 2H, $H_{1\text{-}7}$ backbone), 6.46 ($dd_{(J,\ 8\ Hz)}$, 2H, $H_{2\text{-}6}$ backbone), 5.70 (s, 1H, H_4 backbone), 3.65 (br s, 6H, Ar-O-CH_3) ppm.

7.7.2 Synthesis of Curcumin-Loaded PLGA NPs (PCNPs)

In a glass vial a drug/polymer organic mixture has been prepared dissolving PLGA (50 mg, 1.5 μmol) and curcumin at 10 wt.% of the polymer (5 mg, 13.6 μmol) in ethyl acetate (500 μL). The mixture has been allowed to dissolve for 45 min with intermittent stirring and quick sonication. Into another glass tube the aqueous surfactant solution composed of 5 wt.% PVA solution (2 mL) has been prepared. The drug/polymer organic phase has been added dropwise to the surfactant solution under vortexing and then it has been left under vigorous stirring for additional 30 s. To create an oil-in-water emulsion, the formulation has been treated with 3 cycles (30 s) of sonication and vortexing. Ultrasounds have been generated by a tip-sonicator S15H Elmasonic Apparatus from Elma GmbH (Singen, Germany). At the end of the cycles, the formed emulsion has been quickly poured into diluted aqueous surfactant solution of 0.3 wt.% PVA (25 mL) under vigorous stirring for 3−4 h for NPs hardening and the organic solvent evaporation. At the end of reaction, curcumin loaded nanoparticles (**PCNPs**) have been collected by centrifugation at 8000 rcf for 15 min and washed three times with deionized water (20 mL). The supernatant has been analyzed by DLS establish to exclude PCNPs remained in solution. Nanoparticulate pellets have been resuspended in water (5 mL) and finally dried by lyophilization using a Christ Alpha 1−2 D freeze-dryer. A fine yellow powder has been obtained (38 mg).

Control drug-free nanoparticles (**VPNPs**) have been synthesized by the method described with the exception of the drug molecule.

Related References

[1] Hergueta-Redondo, M.; Palacios, J.; Cano, A. and Moreno-Buono, G.; *Clin. Transl. Oncol.* **2007**, *10*, 777–785.

[2] Dent, R.; Trudeau, M.; Pritchard, K. I.; Hanna, W. M.; Kahn, H. K. and Sawka, C. A.; *Clin. Cancer. Res.* **2007**, *13*, 4429–4434.

[3] Sekine, C.; Shimizu, C.; Nishio, K.; Saijo, N. and Tamura, T.; *J. Clin. Oncol.* **2009**, *14*, 112–119.

[4] Pohlmann, P. R.; Mayer, I. A. and Mernaugh, R.; *Clin. Cancer. Res.* **2009**, *15*, 7429–7491.

[5] Volinia, S.; Galasso, M.; Sana, M. E.; et al.; *Proc. Natl. Acad. Sci.* **2012**, *109*, 3024–3029.

[6] Smith, S. C. and Theodorescu, D.; *Nat. Rev. Cancer.* **2009**, *9*, 253–264.

[7] DeCremoux, P.; *Bull. Cancer.* **2011**, *98*, 1311–1319.

[8] Lambrechts, S.; Decloedt, J. and Neven, O.; *Acta. Clin. Belg.* **2011**, *66*, 283–292.

[9] Aggarwal, B. B.; Banerjee, S.; Bharadwaj, U:; et al.; *Biochem. Pharmacol.* **2007**, *73*, 1024–1032.

[10] Itokawa, H.; Shi, Q.; Akiyama, T.; Morris-Natschke, S. L. and Lee, K. H.; *Chin. Med.* **2008**, *3*, 1–13.

[11] Sandu, S. K.; Pandey, M. K.; Sung, B.; et al.; *Carcinogenesis.* **2007**, *28*, 1765–1773.

[12] Ak, T. and Gülcin, T.; *Chem. Biol. Interact.* **2008**, 1*74*, 22–37.

[13] Batthacharyya, B.; Mandal, D.; Sen, G. S.; et al.; *Cancer Res.* **2007**, *67*, 362–370.

[14] Maeshwari, R. K.; Singh, A. K.; Gaddipati, J. and Srimal, R. C.; *Life Sci.* **2006**, *78*, 2081–2087.

[15] Zhou, H.; Beevers, S. C. and Huang, S.; *Curr. Drug Targets.* **2011**, *12*, 332–347.

[16] Tamvakopoulos, C.; Dimas, K.; Sofianos, Z. D.; et al.; *Clin. Cancer Res.* **2007**, *13*, 1269–1277.

[17] Rowe, D. L.; Ozbay, T.; O'Reagan, R. M.; et al.; *Breast Cancer.* **2009**, *3*, 61–75.

[18] Kunnumakkara, A. B.; Anand, P.and Aggarwal, B. B.; *Cancer Lett.* **2008**, *269*, 199–225.

[19] Bayet-Robert, M.; Kwiatowski, F.;Leheurther, M.; et al.; *Cancer Biol. Ther.* **2010**, *9*, 8–14.

[20] Sharna, R. A.; Steward, W. P. and Gescher, A. J.; *Adv. Exp. Med. Biol.* **2007**, *595*, 453–470.

[21] Dhillon, N.; Aggarwal, B. B.; Newman, R. A.; et al.; *Clin. Cancer Res.* **2008**, *14*, 4491–4499.

[22] Anand, P.; Kunnumakkara, A. B.; Newman, R. A. and Aggarwal, B. B.; *Mol. Pharrnaceutics.* **2007**, *4*, 807–818.

[23] Mosley, C. A.; Liotta, D. C. and Snyder, J. P.; *Adv. Exp. Med. Biol.* **2007**, *595*, 77–103.

[24] Mohanty, C. and Sahoo S. K.; *Biomaterials.* **2010**, *31*, 6597–6611.

[25] Yallapu, M. M.; Jaggi, M. and Chauhan, S. C.; *Drug. Discov. Today.* **2012**, *17*, 71–80.

[26] Muqbil, I.; Masood, A.; Sarkar, F. K.; Mohammad, R. M. and Azmi, A. S.; *Cancers..* **2011**, *3*, 428–445.

[27] He, Y.; Huang, Y. and Cheng, Y.; *Cryst. Growth. Des.* **2010**, *10*, 1021–1024.

[28] Wang, Z.; Leung, M. H.; Kee, T. W. and English, D. S.; *Langmuir.* **2010**, *26*, 5520–5526.

[29] Mandy, H. M.; Leung, M. H. and Kee, T. W.; *Langmuir.* **2009**, *25*, 5773–5777.

[30] Vareed, S. K.; Kakarala, M.; Ruffin, M. T.; et al.; *Cancer Epidemiol. Biomarkers Prev.* **2008**, *17*, 1411–1417.

[31] Li, J.; Wang, Y.; Yang, C.; et al.; *Mol Pharmacol.* **2009**, *76*, 81–90.

[32] Manju, S. and Sreenivasan, K.; *J Pharm. Sci.* **2011**, *100*, 504–511.

[33] Lui, C. H. and Chang, F. Y.; *Chem Pharm. Bull.* **2011**, *59*, 172–178.

[34] Sou, K.; Inenaga, S.; Takeoka, S. and Tsuchida, E.; *Int. J. Pharm.* **2008**, *352*, 287–293.

[35] Gota, V. S.; Maru, G. B.; Soni, T. G.; et al.; *J Agric. Food. Chem.* **2010**, *58*, 2095–2099.

[36] Yallapu, M. M.; Gupta, B. K.; Jaggi, M. and Chauhan S. C.; *J. Colloid. Interface. Sci.* **2010**, *351*, 19–29.

[37] Mukeriee, A. and Vishwanantha, J. K.; *Anticancer Res.* **2009**, *29*, 3867–3875.

[38] Shahani, K.; Swaminathan, S. K.; Freeman, D.; et al.; *Cancer Res.* **2010**, *70*, 4443–4452.

[39] Tsai, Y. M.; Chien, C. F.; Lin, L. C. and Tsai, T. H.; *Int. J. Pharm.* **2011**, *416*, 331–338.

[40] Pabon, H. Y. Y.; *Recl. Trav. Chim. Pays-Bas.* **1964**, *83*, 379−381.

[41] Mathew, A.; Fukuda, A.; Nagaoka, T.; et al.; *PloS One.* **2012**, *7*, e32616.

[42] Nava-Arzaluz, M. G.; Pinon-Segundo, E.; Ganem-Rondero, A. and Lechuga-Ballestros, D.; *Recent. Pat. Drug. Deliv. Formul.* **2012**, *6*, 209−223.

[43] Filippov, S. K.; Panek, J. And Stepanek, P.; Chapter 10; in *"Nanotechnology and Nanomaterials,"Smart Nanoparticles Technology".* DOI: 10.5772/33772, INTECH© publisher.

[44] Sanphui, P.; Goud, N. R.; Khandavilli, U. B. R.; Bhanoth, S. and Nangia, A.; *Chem. Commmun.* **2011**, *47*, 5013−5015.

[45] Costa, P. and Lobo, J. M. S.; *Eur. J. Pharm. Sci.* **2001**, *13*, 123−133.

[46] D'Souza, S. S. and DeLuca, P. P.; *Pharm. Res.* **2006**, *23*, 460−474.

[47] van Tilborg, G. A. F.; Mulder, W. J. M.; Chim, P. T. K.; et al.; *Bioconjuate Chem.* **2006**, *17*, 865−868.

[48] Sa, G. and Das, T.; *Cell. Div.* **2008**, *3*, 1−14.

[49] Venkateswarlu, S.; Ramachandra, M. S. and Subbaraju, G. V.; *Bioorg. Med. Chem.* **2005**, *13*, 6374–6380.

Acknowledgements

My first acknowledge is dedicated to my supervisor Dr. Davide Prosperi for giving me the opportunity to develop the work of this thesis and to give me all directions to learn the fundamental nanobiochemical knowledge in order to focus my research.

Another important person who I would like to acknowledge is Prof. Kenneth Dawson; he allowed me to attend the Centre for Bionano Interactions (CBNI) in Dublin for more than six months, in particular to introduce myself in his own ongoing projects

A special thanks to our financial supports: all subprojects have been supported by Fondazione Regionale per la Ricerca Biomedica (FRRB), NanoMeDia Project (Hosp. “L. Sacco” and Regione Lombardia) and finally the “Fondazione Romeo ed Enrica Invernizzi” and CMENA “Centro di Microscopia Elettronica e Nanomedicina”.